THE UNIVERSITY *of* EDINBURGH

Separating polar ionospheric and lithospheric magnetic signals in satellite data

Ashley Robert Andrew Smith

Submitted for the degree of Doctor of Philosophy
The University of Edinburgh
2019

Abstract

Both the interior of the Earth and near-Earth space contain a variety of interacting magnetic field sources, which together make up the "geomagnetic field". When a magnetic field measurement is made, either on Earth or in space, a superposition of these sources is observed. In order to study each source in isolation, it is therefore necessary to process these collected data to separate the superposed signals. Over the past two decades, the volume of data available has increased tremendously, in particular due to a number of satellite missions carrying high quality magnetometers. This has motivated the development of new techniques to make greater use of the available data. This thesis uses data from the contemporary European Space Agency mission, Swarm, to investigate sources primarily within the ionosphere and lithosphere, focusing on the polar regions where their mutual contamination is most extreme. I also use data from older missions: CHAMP, Magsat, and POGO.

Of the ionospheric field sources, the auroral electrojets are one of the strongest and most variable. These are horizontal electric currents that flow within the auroral regions (at high latitudes). Their magnetic signal is not only an important aspect of auroral studies, but is also particularly difficult to separate from lithospheric field models derived from satellite data. I use a combination of satellite field intensity measurements from the past 50 years to examine their climatology, investigating their average behaviour in relation to solar wind, solar cycle, local time, and seasonal factors. I identify inter-hemispheric asymmetries, solar cycle modulation, and a secular shift in their location due to the variation of the core field. I also discover features which indicate incomplete removal of the lithospheric signal, showing that studies of the weakest ionospheric currents are still contaminated by lithospheric sources. This can be remedied by improved lithospheric models.

In the latter part of the thesis, I create a lithospheric field model with a new cor-

rection technique to reduce the effect of ionospheric noise. As part of this process, I demonstrate a bias field over the poles due to the noise introduced by the auroral oval. The technique involves stacking signals onto two global icosahedral hexagonal grids, one in geographic coordinates and one in local time coordinates, respectively organising lithospheric and ionospheric sources in their appropriate reference frames. The signals on the ionospheric grid are then removed from the input data and the reduced (stacked) data in geographic coordinates are inverted for a spherical harmonic model. This is demonstrated with Swarm data and shows a beneficial effect, but more work is needed to bring the model to the precision of the current state-of-the-art models.

These two studies are directed toward two different physical systems but the observations are derived from the same data. In each case, attempts are made to remove the opposing "noise" from the target signal. In this way, the data are interrogated from both perspectives, where that which is considered as "noise" in one case is used as "signal" in the other.

Lay summary

Magnetic fields surround and permeate Earth, from the core and out into interplanetary space. These fields arise from a wide array of processes: fluid motion and electric currents within the metallic outer core; magnetisation of rocks in the crust (more broadly, the *lithosphere*); electric currents flowing through the upper layers of the atmosphere (the *ionosphere*); great circulations of currents in space, in Earth's *magnetosphere*, which have a complex interaction with emissions from the Sun; and so on. Measurements of these fields not only provide us with much scientific information about these sources, but also are a vital tool for society, supporting navigational systems, for surveying and exploitation of natural resources, and playing a key role towards understanding *space weather* risks. For this reason, there is a network of permanent magnetic observatories around Earth, as well as several space missions dedicated to making magnetic measurements, the latest of which is the multi-satellite *Swarm* mission developed and operated by the European Space Agency.

In order to access the wealth of information provided by magnetic fields, collected data must first be processed to extract the constituent signals, separating them according to the different physical sources from which they originate. This involves the creation of empirical models which are able to predict the magnetic field vector at different locations and times. This thesis focuses on the usage of satellite data to address this problem, mainly targeting the fields from the lithosphere and the ionosphere, whose signals often overlap in the polar regions causing strong cross-contamination in models. There are two main studies presented, each focusing on these two sources separately, with connections drawn between them.

The first study is of the *auroral electrojets*. These are ionospheric electric currents which flow around the magnetic poles and are associated with the aurora. They are both a key component of space weather and also a large noise source within models of the

lithospheric magnetic field. The second study is the development of a novel technique for lithospheric field modelling which aims to account for the ionospheric contamination by processing the data on spherical grids. I demonstrate asymmetries in ionospheric behaviour between hemispheres, seasonal and longer-term variations, and a bias that can leak into lithospheric models if not accounted for.

Declaration

I declare that this thesis has been composed solely by myself, and that it contains only my work except where otherwise specified, or where the work is explicitly indicated below to have formed part of a jointly-authored publication. This work has not been submitted for any other degree or professional qualification.

Chapter 5 is based on work published as Smith et al. (2017).

Ashley Smith

December 2019

Acknowledgements

Foremost I thank my supervisors, Kathy Whaler, Ciarán Beggan, and Susan Macmillan, for all their encouragement, understanding, and feedback along the way. I also thank friends and colleagues across the School of GeoSciences for the convivial atmosphere, particularly Hannah Rogers for help with proof-reading.

I would also like to give a general "thank you" to the open source community, particularly developers of Python and Latex and associated libraries, and to the contributors to online resources such as the StackExchange online fora, and to the teams behind free productivity tools such as GitHub, Mendeley, and Overleaf. Creating programs and documents would be a lot more painful without these resources.

Contents

List of Figures

List of Tables

Glossary

AEJ Auroral electrojet.
ASM Absolute Scalar Magnetometer (Swarm instrument).

C (Z) Centre (downwards) component of the magnetic field.
CD Centred dipole magnetic coordinate system.
CI Swarm comprehensive inversion chain.

DISC Swarm data, innovation, and science cluster.
DP(Y/1/2) The disturbance, polar, magnetic signals.

E (Y) Eastwards component of the magnetic field.
EEJ Equatorial electrojet.

F10.7 The 10.7cm solar activity index.
FAC Field-aligned current.

GEO The geographic binning system.
GSE Geocentric solar ecliptic coordinate system.
GSM Geocentric solar magnetospheric coordinate system.

IAGA International association of geomagnetism and aeronomy.
IGRF International geomagnetic reference field.
IMF Interplanetary magnetic field.
IMF-B(x/y/z) The IMF components in the GSM frame.

LEO Low-Earth orbit: ∼200-1000km altitude.

MAG (CD) magnetic coordinate system.
MCO Swarm core field model.
MIO Swarm ionospheric field model.
MJD Modified Julian Day.
MLI Swarm lithospheric field model.
MLT (Quasi-dipole) magnetic local time.
MMA Swarm magnetospheric field model.

N (X) Northwards component of the magnetic field.
NEC North/East/Centre geocentric frame.

QD Quasi-Dipole coordinate system.
QDLat Quasi-Dipole latitude.
QDLon Quasi-Dipole longitude.
QDMLT The QDLat/MLT binning system.

R(0/1/2) The region-0/1/2 field-aligned current systems.

SCARF Swarm satellite constellation application and research facility.
SH (of a model) spherical harmonic.
SHA Spherical harmonic analysis.
SM Solar magnetospheric coordinate system.
Sq The solar quiet ionospheric current system, or its magnetic effect.
STR Star tracker.

VFM Vector Field Magnetometer (Swarm instrument).

X (N) Northwards component of the magnetic field.

Y (E) Eastwards component of the magnetic field.

Z (C) Centre (downwards) component of the magnetic field.

Chapter 1

Introduction

Earth and its environment in space contain many magnetic field sources (see Figure 1.1), which together represent the *geomagnetic field*. By far the strongest of these sources originates in Earth's fluid outer core through a process referred to as the geodynamo (e.g. Roberts and King, 2013; Stevenson, 2008). This field dominates over the others, influencing, and providing the setting for, a wide range of phenomena. When we make magnetic measurements, we find a superposition of magnetic fields which vary over all spatial and temporal scales, with each source occupying different but overlapping scales according to their physical origins (Olsen et al., 2002; Olsen and Stolle, 2012). These sources range from the remanent magnetism frozen into the rock of the lithosphere (Purucker and Whaler, 2006; Thébault et al., 2010), to the fields produced from electric currents flowing through Earth's magnetosphere and ionosphere as they interact with the solar wind (Keiling et al., 2018; Milan et al., 2017). These fields are rich and complex, providing a fascinating way to probe geophysical processes, revealing both Earth's deep interior and its intimate connection with the Sun.

Magnetic measurements have proven very valuable, both scientifically and economically. They are a key tool for gathering remote information on inaccessible regions, below and above ground, with a wide range of applications, including navigation (Chulliat et al., 2015), geophysical exploration for natural resources (Purucker and Clark, 2011), in monitoring and mitigating the effects of space weather (Eastwood, 2008; Lotko, 2017; Mandea and Purucker, 2018), and links with Earth's climate (Friis-Christensen, 2018). This has motivated the growth of a global network of observatories and surveys spanning the previous few centuries, and in recent years supported by satellites (Chulliat et al., 2016b). Permanent observatories provide high quality continuous measurements

at fixed locations, while surveys (on ground, at sea, and by air) provide spatial coverage though with less temporal information. A few satellites in Low Earth Orbit (LEO), i.e. between 300 and 800 km altitude, have provided near global coverage during their respective periods of operation (Olsen et al., 2010a), the latest of which are the (originally three, currently four) *Swarm* mission satellites developed and operated by the European Space Agency (ESA) (Friis-Christensen et al., 2006; Olsen et al., 2013).

Dis-entangling the magnetic effects of different sources is a difficult and ongoing task (Backus, 1970; Finlay et al., 2017; Gauss, 1838; Langel and Hinze, 1998), and the separation of these signals and attribution to their respective sources is a necessary step before they can be accurately studied. The lithospheric and ionospheric fields are very hard to separate due to their often similar magnitudes and spatial scales (i.e. it is hard to distinguish between them in any given measurement). This is particularly the case in polar regions where even during geomagnetically quiet conditions, the ionospheric field can be much stronger than the lithospheric field and is highly variable (Olsen and Stolle, 2017). The usage of satellite data to understand and separate these fields in polar regions is the main target of this thesis.

To more fully separate lithospheric and ionospheric signals, and hence derive less mutually contaminated models of each, the main limiting factor is the need for a detailed description of the polar ionospheric currents and their complex coupling with the solar wind. I explore this coupling through a study of the auroral electrojets (Smith et al., 2017), horizontal ionospheric electric currents which flow around Earth's poles and which are associated with the aurora. This study is in connection with recent research on hemispheric asymmetries in ionospheric behaviour (e.g. Laundal et al., 2017; Østgaard et al., 2016) and on seasonal and long term variations (e.g. Cnossen, 2017; Tsyganenko, 2019). I also develop a new method to derive global lithospheric field models, aiming to remove the bias field which is otherwise introduced by the auroral electrojets. The basis of this method can also be used to study solar wind-ionosphere coupling.

Chapter 2 reviews the physical origins of Earth's magnetic field sources, and Chapters 3 & 4 review measurement techniques and models used to study and describe these sources. Chapter 5 contains the study of the auroral electrojets and Chapters 6 & 7 present the lithospheric modelling method, with a discussion of the connections between these two studies and potential future research in Chapter 8.

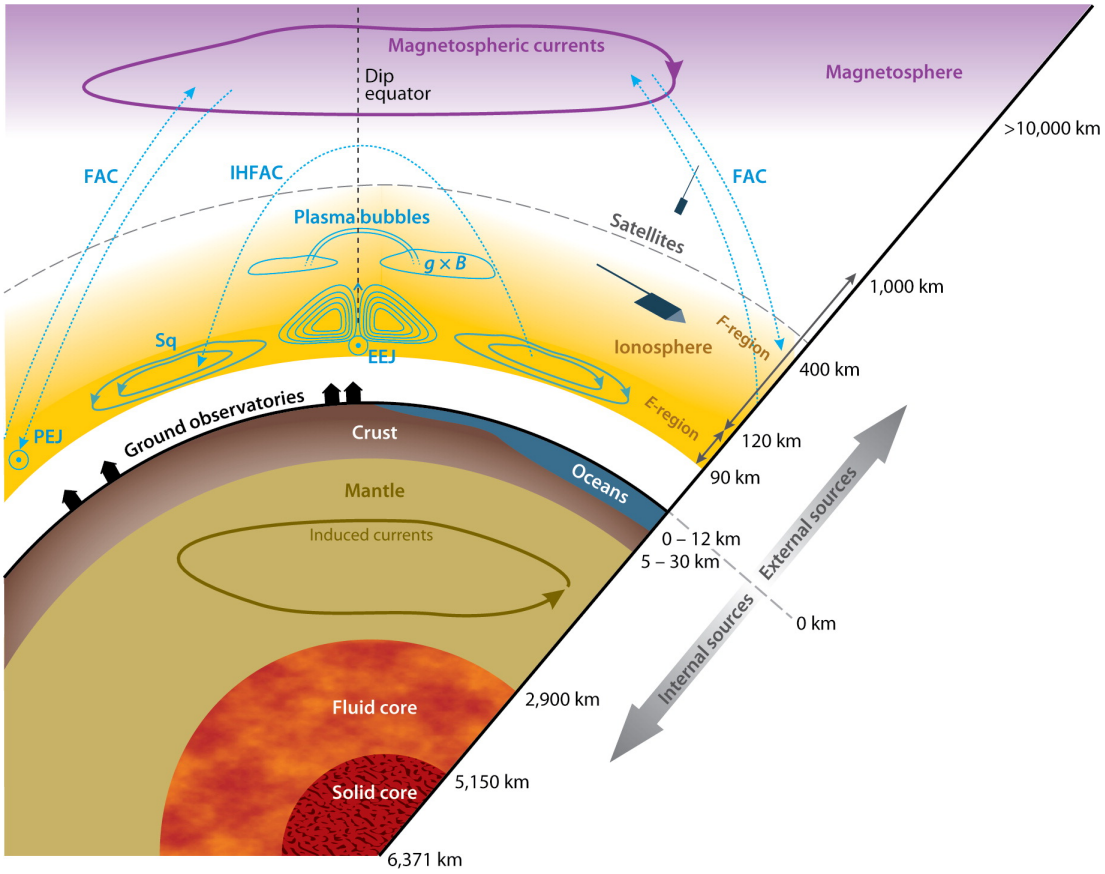

Olsen N, Stolle C. 2012.
Annu. Rev. Earth Planet. Sci. 40:441–65

Figure 1.1: Sketch of some of the near-Earth magnetic field sources, from Olsen and Stolle (2012)

Chapter 2

The geomagnetic field

Before discussing the origins of the magnetic fields in and around Earth, it is useful to define some of the terms we use to refer to regions of Earth and its environment:

- *geospace*: the space around Earth controlled by Earth's magnetic and gravitational fields
- *inner core*: the solid, predominantly iron, centre of Earth
- *outer core*: fluid, mainly iron and nickel, electrically conductive and convecting
- *mantle*: the solid bulk, composed of silicate minerals, unmagnetised and only weakly conductive
- *lithosphere*: the rocky rigid outer layer, can be magnetised and conductive
- *ionosphere*: the upper part of the atmosphere between about 60km and 1000km altitude, which is electrically conductive due to ionisation by sunlight and energetic particle precipitation
- *magnetosphere*: the cavity around Earth created by Earth's magnetic field deflecting the flow of the solar wind, bounded by the *magnetopause* at about $10R_E$ on the dayside and extending to about $100R_E$ on the nightside (highly variable), containing several plasma populations
- *heliosphere*: the Sun's magnetosphere, extending well beyond the solar system planets, to >100 A.U.
- *solar wind*: the material which defines the heliosphere, a collisionless plasma moving radially out from the Sun and carrying the so-called interplanetary magnetic field which is tied to the Sun's surface

2.1 Internal fields and external fields

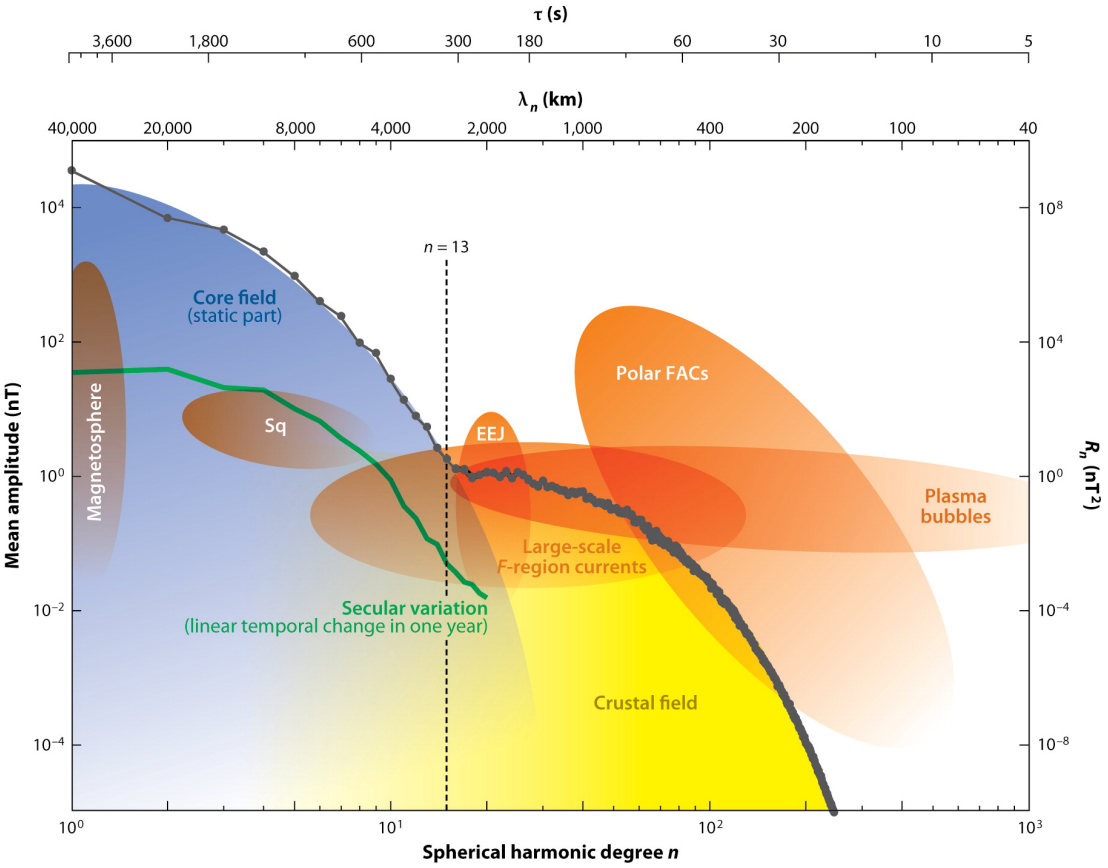

Olsen N, Stolle C. 2012.
Annu. Rev. Earth Planet. Sci. 40:441–65

Figure 2.1: Schematic of the power spectra of field sources at satellite altitudes (300km), from Olsen and Stolle (2012)

It is common to make a distinction between internal and external fields, e.g. Olsen et al. (2010b), following the original analysis by Gauss (1838) (see a recent translation by Glassmeier and Tsurutani, 2014). Internal fields, those originating from beneath the Earth's surface, are typically the realm of the geophysicist (e.g. Backus et al., 1996; Parkinson, 1983). External fields are typically the realm of the ionospheric and space physicist (e.g. Russell et al., 2016). Magnetic measurements contain both of these signals and so "geomagnetism" spans these disciplines. The various sources and their spatial extents and intensities are indicated in Figure 2.1.

Internal sources include the geodynamo, induced electric currents in the mantle, lithosphere, and oceans, and remanent and induced magnetisation in the lithosphere. External sources include electric currents that close within the ionosphere, largely con-

trolled by insolation and atmospheric effects, and large current circuits within the magnetosphere, out to the magnetopause, which can close through the ionosphere or out into interplanetary space, largely controlled by the solar wind (e.g. Baumjohann and Nakamura, 2007).

2.2 Electromagnetism

2.2.1 Remanent and induced magnetisation

Magnetisation arises from the coherent orientation of electron spins, appearing in materials in three main forms: diamagnetism, paramagnetism, and ferromagnetism (and similar flavours such as ferrimagnetism and antiferromagnetism), (e.g. Lowrie, 2007, Section 5.2.6). Both diamagnetism and paramagnetism only produce magnetic fields when an external magnetic field is applied, i.e. they are forms of *induced* magnetisation. Ferromagnetic materials retain their magnetism in the absence of external magnetic fields, resulting in *remanent* magnetism. The most common naturally-occurring significantly magnetic minerals are magnetite (ferrimagnetic) and haematite (antiferromagnetic), (Dunlop and Özdemir, 2007, Section 5.08.3).

Remanent magnetism is where a material acquires a magnetic field related to that of its environment and can happen through a number of processes (Dunlop and Özdemir, 2007, Section 5.08.6). The dominant process is thermoremanent magnetisation, which occurs when a hot material drops below its Curie temperature, the temperature above which the thermal energy disrupts the self-alignment of magnetic moments and remanent magnetism is not present. The material acquires a magnetisation which is related to the strength and direction of the magnetic field applied when it dropped below the Curie temperature. In nature there are some additional ways that materials can gain a remanent magnetisation, including detrital and chemical and isothermal remanent magnetisation.

Materials can exhibit both remanent and induced magnetisation and so the magnetic field of a material is the sum of both of these. This is further complicated when materials are also electrically conductive, because electric currents will flow when a time-changing magnetic field is applied, themselves producing an additional magnetic field.

2.2.2 Magnetohydrodynamics

Magnetohydrodynamics is the description of processes occurring in magnetised fluids, such as the tenuous plasma present in space, and the dense but fluid metal in Earth's outer core. It describes the interrelation of the motion and the magnetic field of such fluids. Derivations and much more detail can be found in texts such as Baumjohann and Treumann (1997), Russell et al. (2016), and Parkinson (1983), but some important points are highlighted here.

Maxwell's equations can be written as

$$\nabla \cdot \boldsymbol{E} = \frac{\rho}{\epsilon_0}, \tag{2.1}$$

$$\nabla \cdot \boldsymbol{B} = 0, \tag{2.2}$$

$$\nabla \times \boldsymbol{E} = -\frac{\partial \boldsymbol{B}}{\partial t}, \tag{2.3}$$

$$\nabla \times \boldsymbol{B} = \mu_0 \left(\boldsymbol{j} + \epsilon_0 \frac{\partial \boldsymbol{E}}{\partial t} \right), \tag{2.4}$$

where $\boldsymbol{E}$ and $\boldsymbol{B}$ are the electric and magnetic fields, ρ is the charge density, $\boldsymbol{j}$ is the electric current density, and ϵ_0 and μ_0 are the electric permittivity and magnetic permeability of free space.

Ohm's law can be written as

$$\boldsymbol{j} = \sigma \boldsymbol{E}', \tag{2.5}$$

relating the current density, $\boldsymbol{j}$, to the electrical conductivity, σ, and electric field, $\boldsymbol{E}'$, in the rest frame of the fluid.

From equations 2.3, 2.4, and 2.5, the "induction equation" can be derived:

$$\frac{\partial \boldsymbol{B}}{\partial t} = \nabla \times (\boldsymbol{u} \times \boldsymbol{B}) + \eta \nabla^2 \boldsymbol{B} \tag{2.6}$$

where $\eta = \frac{1}{\mu_0 \sigma}$ and $\boldsymbol{u}$ is the velocity of the fluid. This describes how $\boldsymbol{B}$ changes with time in response to a combination of two terms, $\nabla \times (\boldsymbol{u} \times \boldsymbol{B})$ being the *advective* term describing the joint movement of magnetic field and fluid, and $\eta \nabla^2 \boldsymbol{B}$ the *diffusive* term describing the diffusion of magnetic field through the fluid. The relative influence of each term is indicated by the magnetic Reynolds number,

$$R_m = \frac{uL}{\eta}, \tag{2.7}$$

where L is the length scale being considered. When $Rm \gg 1$, the advective term is dominant and we are in the regime where flux is said to be "frozen-in" to the flow. This is stated mathematically by *Alfvén's theorem* as

$$\int_S \boldsymbol{B} \cdot d\boldsymbol{S} = constant, \tag{2.8}$$

meaning that the magnetic flux passing through a surface within the fluid is conserved. This means that either the magnetic field lines are dragged along by the motion of the fluid, or that the magnetic field dictates the allowable movement of the fluid. This is the basis of the behaviour we observe within the changing core magnetic field configuration due to its fluid motion, within the solar wind flow transporting its magnetic field, and the formation of the barrier provided by Earth's magnetosphere. When Alfvén's theorem breaks down, a process called *magnetic reconnection* occurs, allowing the transport of material and energy between two "frozen-out" regions. As shall be seen later, this is an important process within the magnetosphere.

2.3 Internal fields

The field of internal origin largely comprises that from the core, and from the lithosphere. Our knowledge and understanding of these sources is driven primarily by the collection of data from different sources, and the combination of these data to produce empirical models (Hulot et al., 2007). The origins of the core field and the lithospheric field are summarised here.

2.3.1 The core field

The core magnetic field, originating from the action of the geodynamo, is the largest component of the geomagnetic field. It is responsible for the large-scale shape and strength as the field extends out into space. It is predominantly dipolar, and, since the higher order components decay away when viewed further from the source, can be approximated very accurately as such when far from the Earth. However, the interaction with the solar wind distorts the shape, as we shall see in section 2.4.1. The radial magnetic field at the core surface and an example of the flow inferred from it is shown in Figure 2.2.

Geodynamo theory was first proposed by Larmor (1919) and later developed by

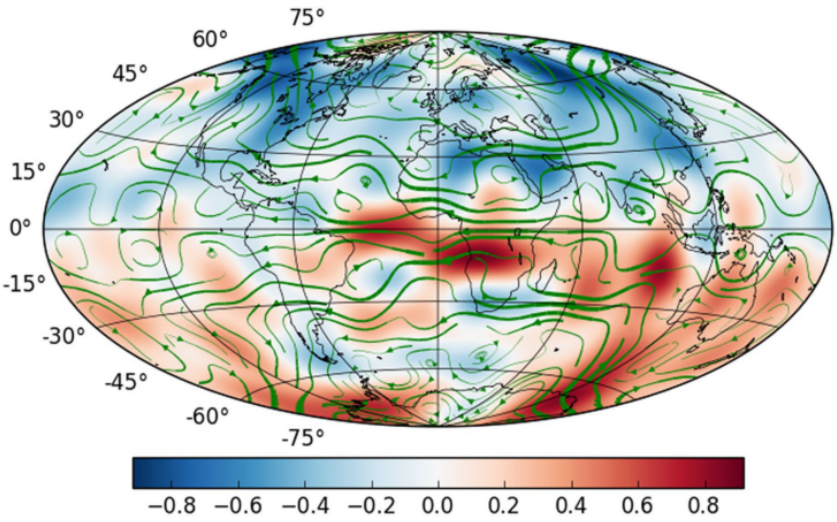

Figure 2.2: The radial magnetic field at the core surface in mT, from the CHAOS-6 magnetic field model. Green lines are tracers of the core flow (average flow velocity is 20 km/year). Image from Finlay et al., 2016

Parker (1955) and many others, also in relation to the solar dynamo (the source of the Sun's magnetic field and its activity cycle, see e.g. Jones et al., 2010). It describes how electric currents and flow of material in the outer core act in such a way as to create a self-sustaining dynamo (Cowling, 1976; Roberts and King, 2013) which we can remotely observe through the magnetic field that it creates. Measurement of this magnetic field therefore gives us information about the conditions and physical behaviour of the core. This is one of the few tools we have to probe planetary cores, along with seismology, geodesy, laboratory experiments, and computer simulations (Glatzmaier and Olson, 2005; Hardy and Wong, 2019; Whaler, 2007).

Various scenarios were initially considered for the origin of the field, but it is now understood that the only possible source for such large magnetic field strength is from electric currents in the outer core. This is a result of what is known of the properties (such as density and conductivity) of the crust, mantle, and outer and inner core. These electric currents are being sustained by a complicated convectional motion in the fluid outer core controlled by magnetohydrodynamics and the rotation of the core, and thermodynamic flow (Finlay et al., 2010). The combined effect is self-sustaining, in that the presence of the magnetic field drives the dynamo which is then responsible for creating new magnetic field sources. Observation of the so-called "secular variation", the long-term (months to years and longer) variation of the magnetic field, reveals the flows on the surface of the outer core and their change over time (Beggan and Whaler, 2008;

Gillet et al., 2010). In practice, information is hidden from us because of shielding by the slightly conductive mantle over the distance to the core from the surface (> 3000km), as well as because of contamination by other magnetic sources. Our interpretations are also limited by knowledge and assumptions of physical conditions in the core and mantle.

Geodynamo theory allows us to describe, and even predict, the secular variation, and allows for reversal of the dipole (being one of two quasi-stable states). However, simulating and and understanding the details remains a great challenge as the dynamo process is inherently complex. See e.g. Roberts and King (2013) for a recent review.

Our knowledge of the core magnetic field and support for core flow theories is built upon a solid foundation of measurements from observatories, satellites, and palaeomagnetism (Hulot et al., 2010). Recently, with the increased capabilities afforded with the inclusion of new satellite measurements, there has been more focus on short-lived (such as secular acceleration and jerks, e.g. Chulliat and Maus, 2014) and localised (such as jets, e.g. Livermore et al., 2016) features. There has also been a renewed interest in novel ways to exploit satellite data (such as the virtual observatory method, e.g. Mandea and Olsen, 2006).

2.3.2 The lithospheric field

The magnetic field of the lithosphere has three main sources: from remanent and induced magnetisation, and from electric currents. There are several natural origins of remanent magnetism, the most dominant of which (when considering the large scale lithospheric field) is thermoremanent magnetisation as discussed in Section 2.2.1, whereby grains in igneous rocks acquire magnetic moments related to the strength and direction of the ambient magnetic field (i.e. mostly the core field) when they cool below their Curie temperature. By inspecting remanent magnetisations we are able to reconstruct the past main magnetic field (palaeomagnetism, see. e.g. Chapter 5 of Lowrie, 2007). A particularly important result from this is the knowledge of reversals of the field, most prominent in the alternation of sea floor spreading features (as visible in Figure 2.3).

The variations in magnetic field across a region are also referred to as magnetic anomalies. As well as providing a record of the past field, they help us to probe the subsurface since different mineralogies exhibit different levels of magnetisation. Global surveying of the lithospheric field is a particular driver for the Swarm mission and has

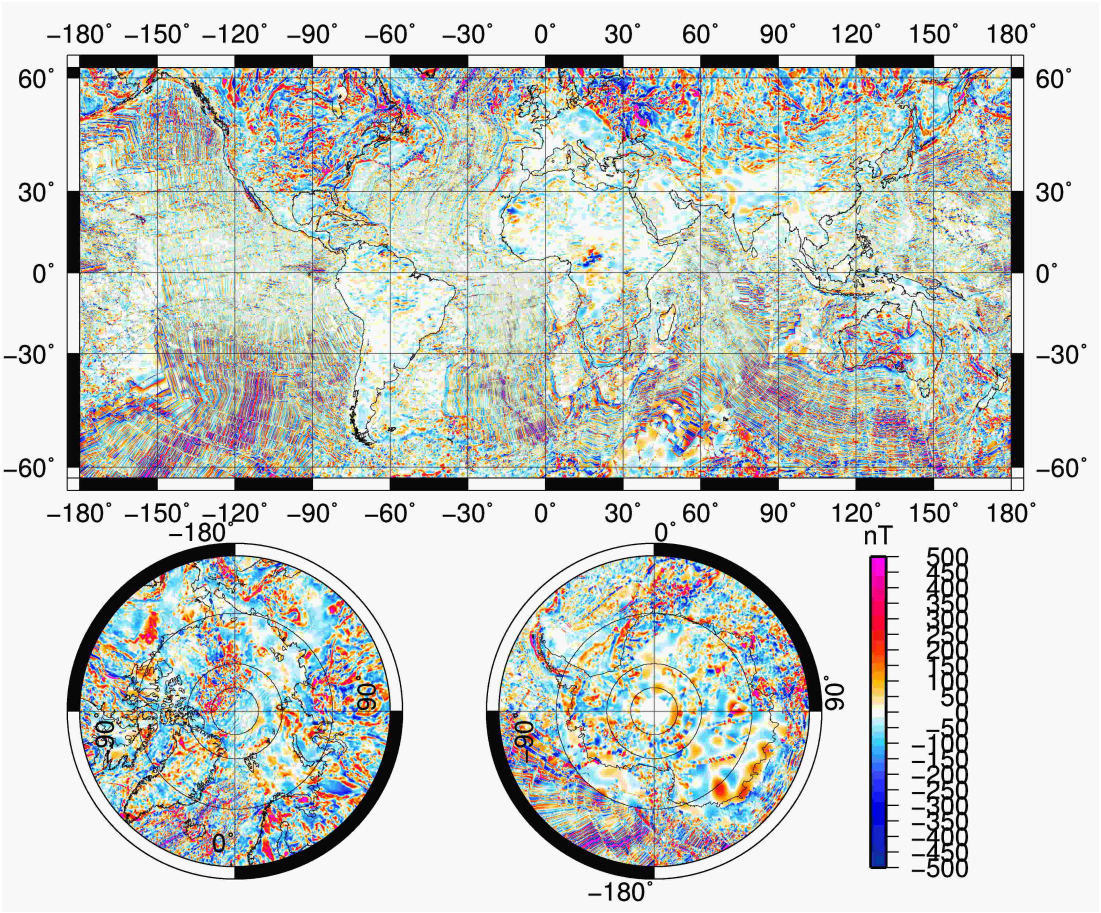

Figure 2.3: Total field anomaly from the World Digital Magnetic Anomaly Map (WDMAM) v2 (Lesur et al., 2016)

its key contribution from magnetic LEO satellites in general (Langel and Hinze, 1998). In addition to satellites, aeromagnetic and marine surveys provide localised information (the shorter wavelength features) and are invaluable in geophysical exploration, with the three approaches supplementing and complementing each other. Data are compiled together to create global maps, such as the World Digital Magnetic Anomaly Map (WDMAM v2, Lesur et al., 2016) as shown in Figure 2.3.

The magnetic field observable by large-scale surveys results from the integrated effect of rock magnetisations, with significant variations both laterally (from region to region) and with depth. This inhomogeneity is caused by variation in lithospheric composition, structure, and heat flow, with the magnetic depth varying substantially across Earth though not extending significantly in the mantle because here minerals are above their Curie temperature (Wasilewski et al., 1979). The distribution of magnetisation itself is a combination of both remanent and induced magnetisations. Total magnetisation is therefore dependent on the mineralogical compositions of rocks, their thermal history and the history of the main field (giving rise to the remanent component), and their magnetic susceptibilities and the current main field (giving rise to the induced component). The relative strengths of these components is described by the *Koenigsberger ratio*, $Q = |\boldsymbol{M}_r|/|\boldsymbol{M}_i|$, for which representative values for different minerals can be found in Clark (1997).

Determining magnetisation maps from magnetic field measurements is a very difficult inverse problem since a given magnetic field can arise from an infinite number of different distributions of magnetisation, with some configurations producing no external magnetic field. Moreover, separating the contributions of remanent and induced magnetisations is challenging. Nevertheless, such information is invaluable for geological investigations so there are many techniques developed to tackle these problems to deduce maps of the magnetisation and susceptibility (e.g. Vervelidou and Lesur, 2018, and references therein).

Continental and oceanic crust are very different in composition and structure, yielding very different magnetic properties (Hinze et al., 1991). The oceanic crust is denser, younger, and thinner and composed mainly of mafic rock (igneous rocks rich in magnesium and iron, such as basalt), whereas continental crust is generally much thicker and more felsic (rocks containing more silicate minerals which are lighter, such as granite). The more mafic nature of oceanic crust results in a larger relative contribution

from remanent rather than induced magnetisation (i.e. a high Koenigsberger ratio), whereas continental crust often exhibits stronger induced magnetisation. These differences motivate different treatment of continental and oceanic regions when inferring magnetisations from field measurements. For example, making the assumption that the field originates fully from induced magnetisation is more reasonable over the continents than over the oceans.

Purucker and Whaler (2006) and Thébault et al. (2010) provide reviews of crustal magnetism, describing its utility, and methods to measure and model it. Langel and Hinze (1998) give a more detailed review which focuses on the application of satellite data, brought up to date by Thébault et al. (2017).

2.4 External fields

External field sources are electric currents in the ionosphere and magnetosphere, with a complicated coupling between the two, and into the solid Earth. These cover a large volume of space from just 65 km above the Earth's surface (where the atmosphere becomes ionised enough to be electrically conducting), out to many Earth radii (Chapters 2 & 10 of Russell et al., 2016). They create magnetic disturbances over a range of time scales, from rapid variations at the millisecond scale, to current systems that evolve over a few hours or days (see Sections 4.4 to 4.6 of Parkinson (1983), and Baumjohann and Nakamura (2007)). There are longer scale variations, in relation to the seasons, the 11-year solar activity cycle, and even longer due to secular variation in solar output as well as in the geomagnetic field shape and strength (Cnossen and Matzka, 2016; Lockwood et al., 2018a). Magnetic fields measured by satellites are strongly influenced by these external sources and so it is a challenge to separate out the external sources in order to retrieve the internal field from satellite measurements. From another perspective, satellites are an ideal platform with which we can study these external sources.

2.4.1 The solar wind and the magnetosphere

The solar wind is a fast (typically 400-800km/s) flow of plasma moving mostly radially outwards from the Sun's corona (Russell et al., 2016, Chapter 5), with structures within it being twisted into the *Parker spiral* (after Parker, 1958) by the rotation of the Sun, including the *interplanetary magnetic field* (IMF) which is frozen into the flow. This

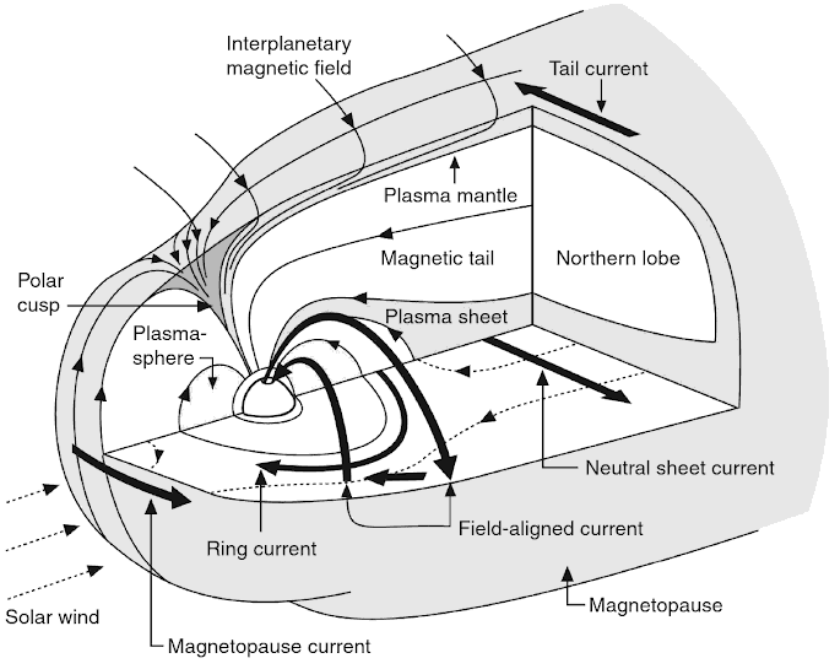

Figure 2.4: A cut-away diagram of the magnetosphere from Russell et al. (2016). The major regions and persistent current systems are indicated.

flow changes constantly due to the chaotic processes at the Sun's surface and within the flow itself, and we quantify it in terms of its particle density, temperature, bulk velocity, and magnetic field vector.

The solar wind is interrupted when it meets solar system bodies, magnetised or not (Russell et al., 2016, Chapters 7 & 8), where a variety of complex interactions occur. In the case of the Earth, the geomagnetic field creates a cavity in the solar wind (see Figure 2.4), compressed on the dayside to about $10R_E$ and extended out into the magnetotail on the nightside to about $100R_E$, held in an equilibrium between the dynamic pressure of the flow and the internal (geo-)magnetic pressure. The IMF carried by the solar wind cannot penetrate the geomagnetic field lines and the two regimes are said to be "frozen-out". Since this interaction distorts the overall shape of the geomagnetic field lines, electric currents are flowing along the magnetopause (called "Chapman-Ferraro currents" after Chapman and Ferraro (1931)). The magnetosphere shape has been modelled empirically from analysis of spacecraft magnetopause crossings (e.g. Shue et al., 1997; Tsyganenko, 1995).

Energy can enter the magnetosphere from the solar wind, in the form of particles crossing the magnetopause during magnetic reconnection events, feeding magnetospheric processes. Energy also enters at the polar cusps, effectively 'gaps' in the shield,

where the field lines are practically vertical and extend out into the solar wind and polar ionospheric processes can be driven directly by the solar wind, within the so-called *polar cap* region. Solar wind conditions that are conducive to magnetic reconnection are said to be "geoeffective" and there are a number of patterns within this behaviour (Lockwood et al., 2016).

Plasma within the magnetosphere is divided into a number of different regions with different densities and temperatures, which are controlled by the shape and strength of the geomagnetic field (ranging from about 50μT at Earth's surface down to 10nT in the tail). The material is sourced from entry of the solar wind, and from evaporation from the ionosphere (Chappell, 2015). The main regions are identified as the *plasmasphere*, the *Van Allen radiation belts*, the *plasma sheet*, and the *magnetotail lobes*. Each region is characterised by its different plasma properties and the way in which they are governed by the geomagnetic field. Magnetospheric physics is a very active area of research with some clear outstanding questions to be answered (Denton et al., 2016) and has motivated several space missions as well as coordinated observations from ground (Lotko, 2017).

Motion of the plasma around the Earth can conspire to create electric currents which we can observe from Earth by their magnetic fields. This is the case for the azimuthal drift of radiation belt particles, where electrons and protons move in opposite directions, creating the *ring current*. These fields are weak most of the time (as felt at Earth) compared to the fields originating internally and from the ionosphere, usually contributing only a few nT, but vary with geomagnetic activity. Ganushkina et al. (2018) give a concise overview of the magnetospheric current systems for the geophysicist. Their effects at LEO in relation to geomagnetic field modelling are reviewed by Lühr et al. (2017).

The complex interaction arising from solar wind energy input and eventually resulting in ionospheric currents and even atmospheric phenomena is referred to as solar wind-magnetosphere-ionosphere-atmosphere coupling. Explanations of electric currents within geospace inevitably require understanding from all aspects of this system; Chapter 9 of Russell et al. (2016), and Milan et al. (2017) give useful reviews of this coupling.

Consideration of the coupling between the solar wind and the geomagnetic field has been fruitful for gaining knowledge of the long-term behaviour of the Sun. Historic geomagnetic data have been used to reconstruct heliospheric conditions from before the space era (Lockwood, 2013). Together with sunspot records and cosmogenic radionuclides, a surprisingly broad understanding of space climate has been achieved (Lockwood

et al., 2017, 2018b).

2.4.2 The ionosphere

The base of the magnetosphere merges into the ionosphere, which is the transition region between the fully ionised magnetospheric plasma and the neutral gas of the atmosphere (Section 4.2 of Parkinson (1983) and Chapter 2 of Russell et al. (2016)). Electron density and collision frequency vary with altitude, producing a vertical gradient in conductivity. It so happens that conductivity peaks within what is called the *E-layer* at around 110km, so electric currents are strongest here.. The electron/ion density is mostly explained by the combined action of ionising solar radiation and deionisation by collisional recombination. This results in a diurnal variation with ion densities, and therefore currents, being generally higher on the day side.

Sq and the EEJ

There is a stable ionospheric current system, the *solar quiet (Sq)* variation, that follows a diurnal oscillation that is stronger during the day, being modulated by the daily cycle in atmospheric tides due to the Sun's heating. It is driven by a dynamo where current-driving electric fields are produced by winds moving ionised gas across the geomagnetic field. This has been well studied since the late 19th century (Yamazaki and Maute, 2017). It takes the form of two circular current systems, one over each hemisphere (on the day side), and also produces a strong eastward current along the equator, the equatorial electrojet (EEJ). There are also other current systems driven by the pressure and gravity gradients within the atmosphere - these are typically weaker (Alken et al., 2016).

The auroral oval

Aside from the effect of insolation, the other significant source of ionisation is magnetospheric particle precipitation, which is most important at high latitudes where magnetospheric electrons of a few keV are channelled in along the field lines. It is this process that produces the aurorae, in both the Northern and Southern Hemispheres, through collisions of the electrons with atmospheric particles pumping them to higher energy levels, which subsequently relax and emit visible and UV radiation at particular transition levels (Chapter 11 of Russell et al., 2016)). It is stronger during increased

geomagnetic disturbance (when the magnetosphere has been driven by solar wind energy), typically giving brighter emission and extending to lower latitudes. The aurora forms an oval around the magnetic pole with the lowest latitude and most intense part over the night side, while the day-side aurora is weaker and closer to the pole. There is also precipitation directly from the solar wind into the magnetic cusps over the poles, within the "polar cap" (e.g. Friis-Christensen and Wilhjelm, 1975).

The aurora is associated with electric currents due to the conductivity provided by the ionisation. These comprise the *auroral electrojets* (AEJ) running horizontally (parallel to the Earth's surface) and *field-aligned currents* (FAC) that source/sink these currents in the magnetosphere (see Figure 2.6). These FACs are also referred to as Birkeland currents, as they were first envisaged by Birkeland, 1908, and they are joined by Hall currents (which are the electrojets) and Pederson currents (which are additional weaker horizontal currents perpendicular to the Hall currents). The electrojets flow within the E-layer and are modulated by geomagnetic disturbance and so cause varying contributions to the magnetic field. The magnetic field variation from them is sometimes called the disturbed polar (DP) variation and varies over a time scale of minutes to a few hours (Nishida, 1968).

2.4.3 The Dungey cycle and magnetosphere-ionosphere coupling

Dungey (1961) laid the foundations of our modern understanding of the magnetosphere, describing the origin of the auroral zones in terms of geomagnetic field lines open to the solar wind which advect across the poles from the dayside to the nightside, following the solar wind bulk motion. The field lines are opened and closed again respectively at the dayside magnetopause and in the nightside magnetotail, through the process he coined as *magnetic reconnection*. The newly closed magnetic field lines at the nightside are then a source of magnetic pressure which causes a movement of lower latitude magnetic flux back to the dayside. This repeating process has become known as the Dungey cycle and the concept has been a very successful basis of more advanced theories in the decades since (Lockwood, 2016; Southwood et al., 2015).

Magnetic reconnection occurs when a magnetic gradient becomes too high and the frozen-in flux assumption breaks down. This happens when magnetic field lines are oppositely oriented, which in the case of the dayside magnetopause is when the IMF is southwards (compared to the northwards geomagnetic field lines there). It is indeed

found that auroral activity is strongly correlated with southwards IMF, i.e. during increased reconnection and thus driving of the Dungey cycle. The reconnection rates at the front and the back of the Dungey cycle can be used to determine the energy throughput of the magnetosphere (Milan et al., 2006), with energy input from the solar wind ultimately either being dissipated through Joule heating in the ionosphere or lost out the magnetotail.

The magnetic field line convection of the Dungey cycle has its ionospheric footprint forming two cells over each pole, continuously driving electric currents around these cells. The other major process providing energy to the auroral oval is the rapid unloading of magnetospheric energy on the nightside through the *auroral substorm* (Akasofu, 1964). In this way, energy transfer from the magnetosphere to the ionosphere, i.e. through electric currents coupling them, can be characterised as originating through two types of mechanism / current system: *directly driven*, and *unloading* (Akasofu, 2017).

Substorms and storms

Enhanced auroral activity usually follows some particular patterns that are part of the process known as the auroral substorm, accompanied by its magnetic counterpart, the magnetic substorm (Akasofu, 1964, 2017). Following a period of increased dayside reconnection, the Dungey cycle produces a build up of flux on the nightside, resulting in an expansion of the auroral oval (substorm growth phase). Excess energy is released when reconnection occurs in the magnetotail, resulting in currents driven into the auroral oval (substorm break-up), and contraction of the auroral oval. Described by Cowley and Lockwood (1992), this is known as the expanding/contracting polar cap (ECPC) paradigm, and can be considered as the dynamic extension to the original Dungey cycle concept.

Substorms can be studied by observing the auroral processes they produce, and by mapping out the electric currents that carry the energy transfer. The substorm current system is classically envisaged as a loop of current flowing between the magnetosphere and the ionosphere along the geomagnetic field lines (Horning et al., 1974; McPherron et al., 1973). This *substorm current wedge* maps between magnetically conjugate locations in the magnetotail and the auroral oval. See Kepko et al. (2014) for more recent advances.

Geomagnetic storms have been known about for more than two centuries (Lakhina

and Tsurutani, 2016). These are the largest geomagnetic disturbances and their signatures can be seen in observatories across the globe. This is because they are characterised by a large increase in the ring current strength which can last for several days (Sandhu et al., 2019). Storms are driven by intense periods of solar wind energy entry into the magnetosphere, typically caused by more geoeffective solar wind structures such as coronal mass ejections (Rostoker and Fälthammar, 1967; Tsurutani and Lakhina, 2014).

2.4.4 Field-aligned currents and auroral electrojets

Iijima and Potemra (1978) described the large scale structure of the field-aligned currents (FAC) in terms of two main regions, "region 1" and "region 2", which differ as to their magnetospheric origin and latitudinal footprint in the ionosphere. These are indicated in Figure 2.5. This arrangement is the most important component of magnetosphere-ionosphere coupling, which is joined by a complex system of currents within the ionosphere as shown in Figure 2.6. The ionospheric footprint of each region is a ring around the pole, with the region 1 being poleward of region 2, and both being stronger in the dusk and dawn sectors. Region 1 currents sink and source in the ionosphere on the dawn and dusk sides respectively, whereas region 2 currents are the opposite. Current closure is provided by Pedersen currents linking the region 1 and 2 currents, and by the Hall currents (the auroral electrojets, flowing anti-Sunwards due to the Sunwards Dungey cycle return convection), both within the auroral region which lies within the annulus of region 1 and 2. Some current closure also occurs through weak Hall and Pedersen currents flowing across the polar cap.

The substorm current wedge forms in addition to the continual region 1 and 2 currents, which, due to more intense particle precipitation from magnetospheric unloading, drives a more intense *substorm* electrojet across the midnight sector. There is also a "region 0" FAC which flows on the dayside, around the magnetic cusp, with its polarity dependent on the IMF direction.

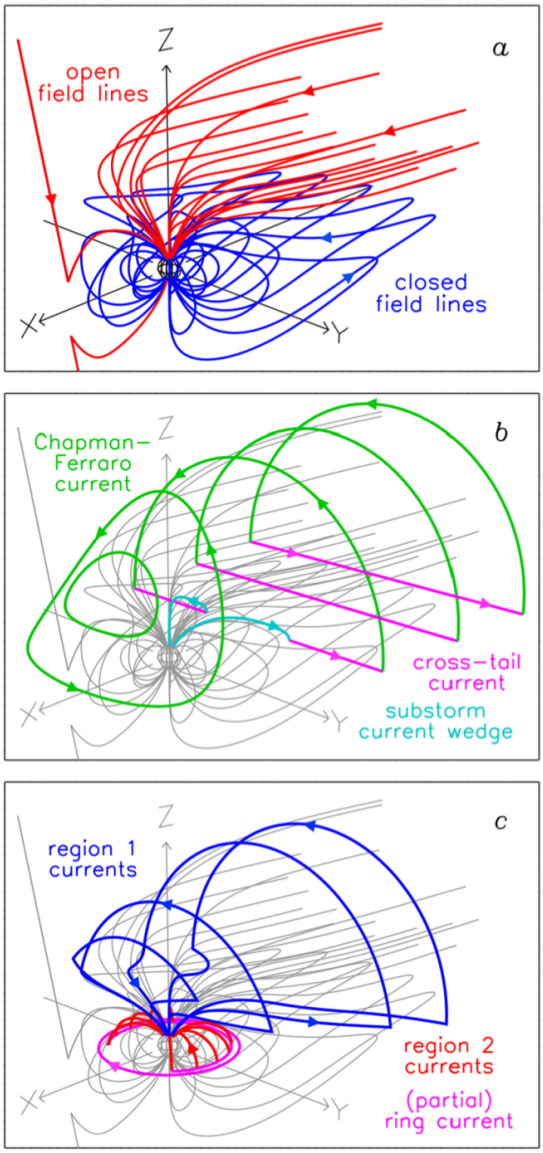

Figure 2.5: Geomagnetic field lines and magnetospheric currents, from Milan et al. (2017). (a) "Open" and "closed" field lines as envisaged in the Dungey cycle; (b) Chapman-Ferraro currents along the magnetopause surface, cross-tail currents across the magnetotail, and the substorm current wedge; (c) region 1 and region 2 field-aligned currents (FACs), and the ring current. Auroral electrojets can be sourced from the region 1 and 2 currents, the substorm current wedge, and along the open field lines ("region 0" or cusp currents).

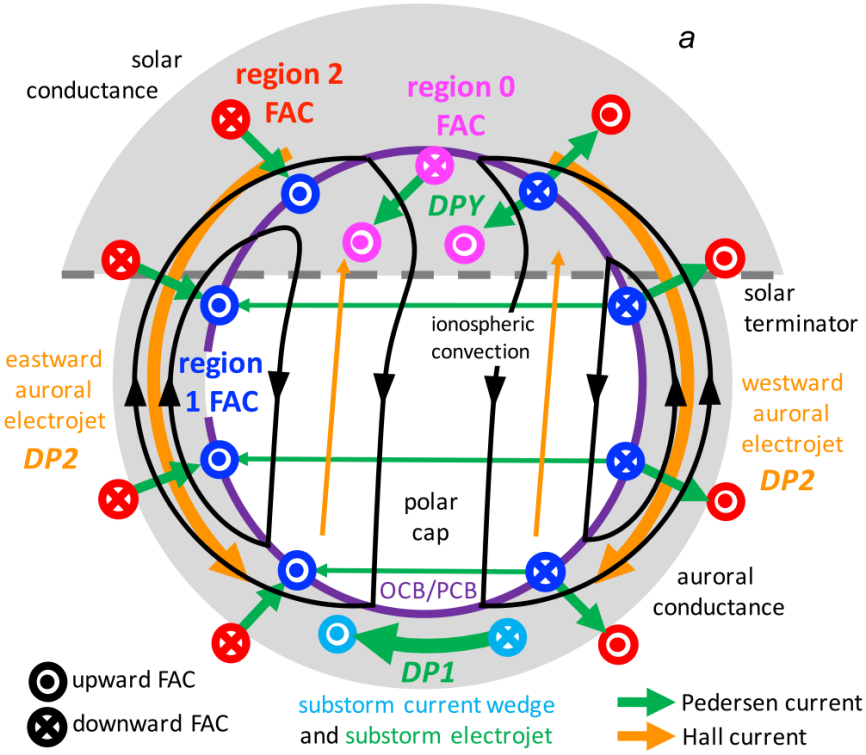

Figure from Milan et al. (2017) DOI: 10.1007/s11214-017-0333-0

Figure 2.6: A view over the Northern Hemisphere of the polar ionospheric currents, flowing horizontally within a spherical cap over the pole, from Milan et al. (2017). The North pole is at the centre, noon is at the top, dawn to the right, and dusk to the left. Grey shading indicates more conductive regions. The black lines show the path of convection due to the Dungey cycle. Coloured lines represent electric currents. Region 0 (pink), 1 (blue), 2 (red) FACs, and the substorm current wedge (light blue) link radially (more accurately, along magnetic field lines) out to the magnetosphere as shown in Figure 2.5. These magnetospherically-sourced/sinked currents close horizontally within the ionosphere in the currents shown here in green and orange: these produce the magnetic disturbances termed DP1, DP2, DPY. The purple circle shows the open/closed field line boundary (OCB/PCB), the boundary between the field lines shown in red and blue in Figure 2.5(a).

2.4.5 Geomagnetic pulsations and other waves

As well as the current systems outlined above, the magnetosphere and atmosphere carry many electromagnetic wave phenomena. Some of these lie within the ULF and VLF bands, and have been observed since the 19th century (see reviews by McPherron (2005), Pilipenko (1990), and Troitskaya and Gul'elmi (1967)). In magnetospheric physics, the ULF band covers frequencies of 1mHz to 1Hz and VLF up to several kHz. ULF waves are also termed *(geo)magnetic pulsations* or *micropulsations*, and are assigned a range of categories according to waveform morphology and frequency: pulsations continuous, Pc1-5, are quasi-sinusoidal, and pulsations irregular, Pi1-2, have more irregular waveforms. These waves have a range of origins, both from the solar wind and generated internally within the magnetosphere, and affect and are affected by the current systems, with the magnetosphere acting as a resonant cavity.

As well as pulsations, there are a number of other wave phenomena at higher frequencies which propagate within the ionospheric wave cavity, including *Schumann resonances*, and *whistlers*, produced by lightning (Section 10.4.4 of Russell et al., 2016). There are also waves of human origin, such as radio transmissions and *powerline harmonic radiation* (Werner et al., 2005). The various external electromagnetic wave sources, in addition to the magnetospheric and ionospheric current systems, can be used to probe the conductivity in the interior of the Earth by measuring the induced response in *magnetotellurics* (Unsworth, 2007). This is achieved by measuring the electric and magnetic fields produced beneath the surface due to induction from the external sources, i.e. measuring their response to the external sources and hence deducing the conductivity. In addition to its effect on the magnetic field, the state of the ionosphere is of particular commercial interest for communications as it affects radio wave propagation. For the same reason, GNSS measurements are affected because the signal delay time is a critical part of position determination.

2.5 Induced fields

Currents are induced within the Earth by time-changing magnetic fields which may be internal, i.e. from the core, or external, i.e. from the ionosphere and magnetosphere. This includes currents generated both within the mantle and the crust, and within the oceans. Measurement of these currents in reaction to the natural magnetic field

changes allows us to determine the conductivity structure within Earth's interior (with the earliest attempt by Schuster, 1889). It is possible to use a range of different external sources for induction studies (Olsen, 2007). Similarly, it is also possible to extract the oceans' tides and currents (Sabaka et al., 2016; Tyler et al., 2003).

Chapter 3

Data and observation platforms

Geomagnetic observations have a long history and in some cases represent some of the longest running geophysical time series that have been continuously measured. The earliest magnetic observatories were established in the early 19th century, following the legacy of Gauss (Garland, 1979). These observatories monitor and record the magnetic field in one location and so measurements must be drawn from the global network of observatories in order to study the global magnetic field. Initially, these observatories were concentrated in Europe, but the network has since expanded to sample the field across the planet (Macmillan, 2007a; Rasson et al., 2011). However, observatory data are still limited by an uneven and sparse distribution, and so the advance of satellite coverage strongly complements the ground network as well as extending the range of phenomena that can be investigated (Chulliat et al., 2016b).

The evolution of magnetic measurements over the previous two centuries has driven major innovations in our understanding of the Earth system and its environment in space. This chapter highlights the key aspects upon which this thesis depends. First, I describe the fundamentals of magnetic measurements and the instrumentation used, in the context of ground observatories and satellite missions. This is followed by an introduction to geomagnetic activity indices, solar wind data, and relevant coordinate systems.

3.1 Ground observatories

Observatories are operated by many different organisations across many countries, using different instruments and procedures. This variety introduces challenges in drawing to-

gether the disparate data sources in an effective and consistent manner. Currently there is a focus on bringing together observatories to a common standard (INTERMAGNET, see e.g., Reay et al., 2011), and extending the network on land and even to the sea floor (Rasson et al., 2011). There is also a drive to draw data sources together in a more directly usable manner, e.g. SuperMAG (Gjerloev, 2012), which, as well as providing data compiled into one location and format with new baseline corrections, is providing added value through novel approaches such as network analysis to provide new activity indicators. However, the SuperMAG network includes variometers that only provide measurements of relative changes in the magnetic field, in contrast to observatories which provide the absolute values at high precision over long time periods. This makes observatory data crucial for secular variation and climatological studies.

Since the distribution of observatories is not uniform and spatial coverage is incomplete, they are supplemented by ground measurements at other locations (repeat stations). Measurements are also obtained from airborne and marine surveys (Hamoudi et al., 2011), which provide high resolution lithospheric measurements over localised regions. These are particularly driven by commercial interests in mineral and hydrocarbon exploration. Since it is difficult to accurately orientate vector measurements on these platforms, the measurements are almost exclusively of just the field intensity (i.e. scalar measurements).

Measurements are made of several different vector field quantities (Figure 3.1). These are declination (D), inclination (I), horizontal intensity (H), total intensity (F), and the vector components, X (northwards), Y (eastwards), Z (downwards). Declination is the angle of the magnetic vector from geographic North in the horizontal plane and inclination is its angle from the horizontal.

Modern observatories typically make continuous measurements of the field using two instruments. The first is a triaxial fluxgate magnetometer, which measures variation of the three components of the magnetic field vector. The second is one of several types of absolute scalar magnetometer, relying on quantum mechanical properties such as proton precession or the Overhauser effect to make highly sensitive measurements of the absolute intensity of the field. The absolute magnetometer is necessary to perform a baseline correction of the vector measurements which are subject to drift. Additional calibration is performed by periodic manual observations, particularly of the declination and inclination (Chulliat et al., 2016b) using a fluxgate theodolite, usually on a weekly

basis.

Observatory records are supplemented by repeat stations, where an additional set of locations are revisited every few years in order to provide a greater geographical coverage to better track secular variation. At these repeat stations, similar measurements are carried out as at observatories, over a few hours, and external field contaminations (diurnal variation and storms) are corrected for (Macmillan, 2007b). Example observatory data is shown in Figure 3.2

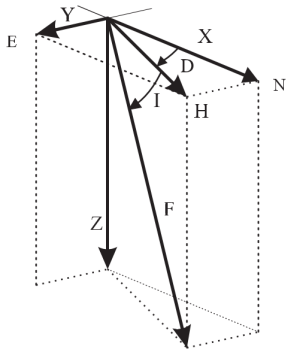

Figure 3.1: The conventional magnetic vector quantities, from Glassmeier et al. (2009)

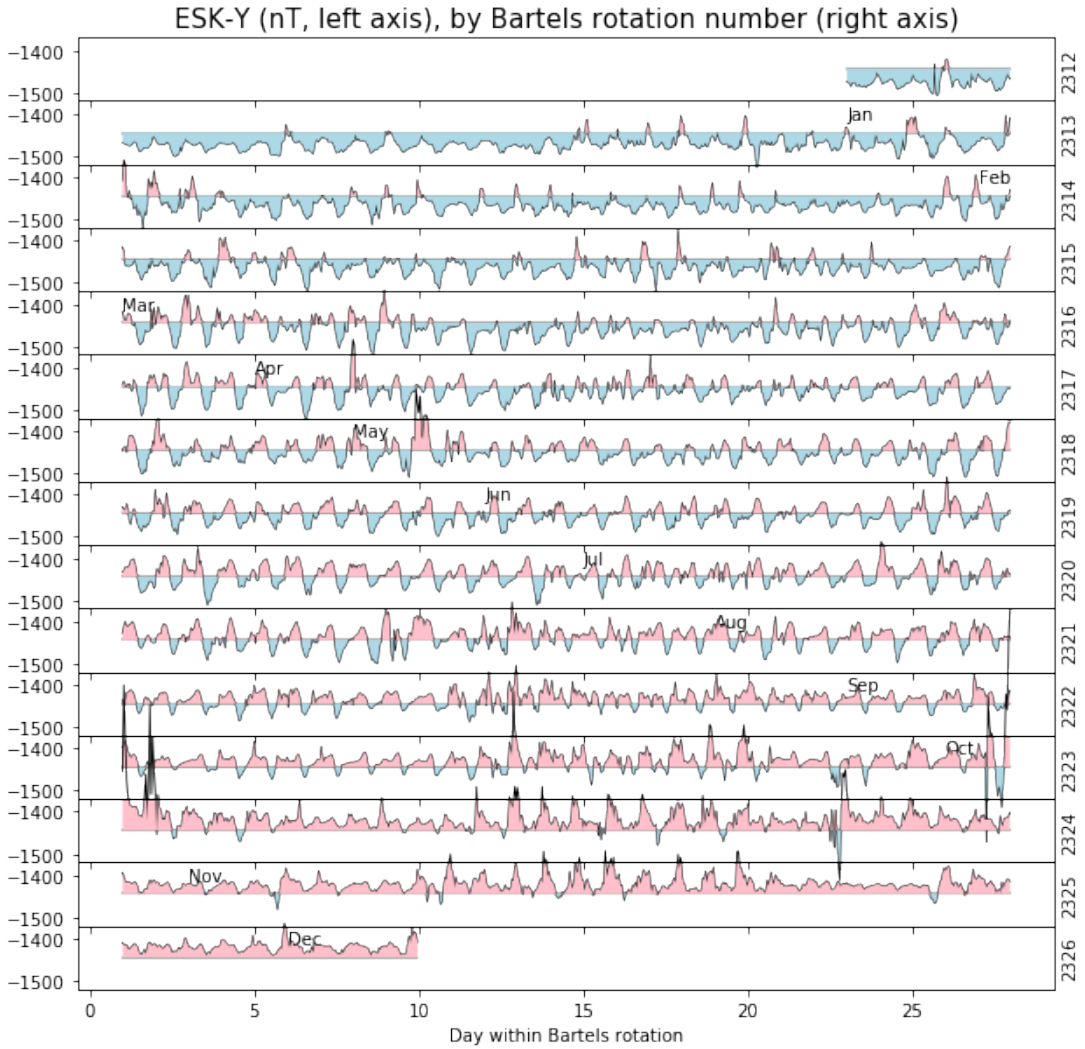

Figure 3.2: The Eastwards (Y) component measured at Eskdalemuir observatory during 2003 (hourly means). The horizontal line is the annual mean, so that the change in the shaded area over the year shows the secular variation. The effect of the Sq system is visible as a daily variation, and large jumps are produced by geomagnetic storms. The year is partitioned into Bartels rotations (according to the rotation period of the Sun) so that cyclic disturbances due to persistent coronal holes (active areas of the Sun) line up.

3.2 Satellite missions

	Operation	Inc.	Altitude	Data
OGO-2	10/1965 - 09/1967	87°	410-1510 km	Scalar
OGO-4	07/1967 - 01/1969	86°	410-910 km	Scalar
OGO-6	06/1969 - 06/1971	82°	400-1100 km	Scalar
Magsat	11/1979 - 05/1980	97°	325-550 km	Vector
Ørsted	02/1999 - 01/2014	97°	650-850 km	Vector
CHAMP	07/2000 - 09/2010	87°	260-450 km	Vector
SAC-C	01/2001 - 12/2004	98°	698-705 km	Scalar
Swarm (ABC)	11/2013 -	88°	530/<450 km	Vector

Table 3.1: Summary of high precision LEO magnetic satellites (Olsen and Stolle, 2012)

Some of the earliest satellites started to provide geophysical information from magnetic measurements, but precision (preferably vector) magnetometers with global coverage, as well as precise orbit and attitude information, are required for the purposes of geomagnetic field modelling. The notable missions providing such platforms are listed in Table 3.1. The first three of these, OGO-2, OGO-4, and OGO-6, were part of the Polar Orbiting Geophysical Observatory (POGO) series which provided only scalar data from elliptical orbits between 1965 and 1971. Magsat, launched in late 1979, was the first satellite providing vector magnetic data and was able to map lithospheric anomalies, motivated by the discoveries of the earlier POGO satellites. Unfortunately Magsat was only in orbit for about half a year and was followed by a twenty-year absence of high precision measurements in LEO. More information on these and other magnetic satellites can be found in Langel and Hinze (1998, Chapter 3), and a later review by Olsen et al. (2010a) which describes the relation of satellites to field modelling in the lead-up to the launch of Swarm.

Between 1999 and 2001, Ørsted, CHAMP, and SAC-C were launched, providing a decade of high precision coverage which inspired many new field models probing the sources in greater detail. Their success provided a clear motivation for the Swarm mission which was selected in 2004 as ESA's 5th Earth Explorer (Friis-Christensen et al., 2006). The Swarm spacecraft design is heavily based on the designs of Ørsted and CHAMP.

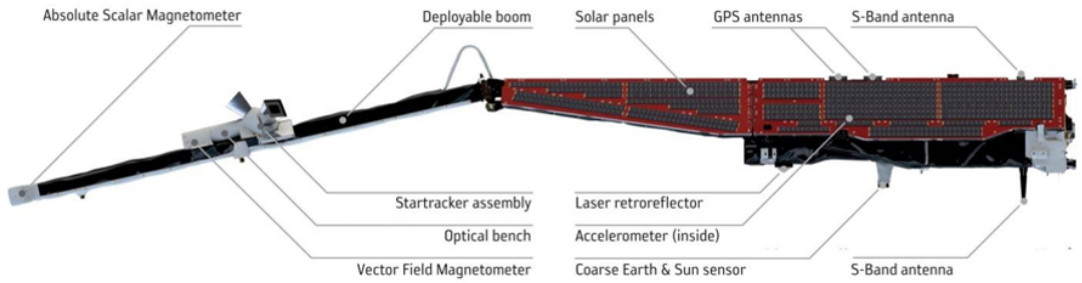

Figure 3.3: The *Swarm* spacecraft (ESA). The magnetic measurements are made by the Absolute Scalar Magnetometer (ASM) and the Vector Field Magnetometer (VFM).

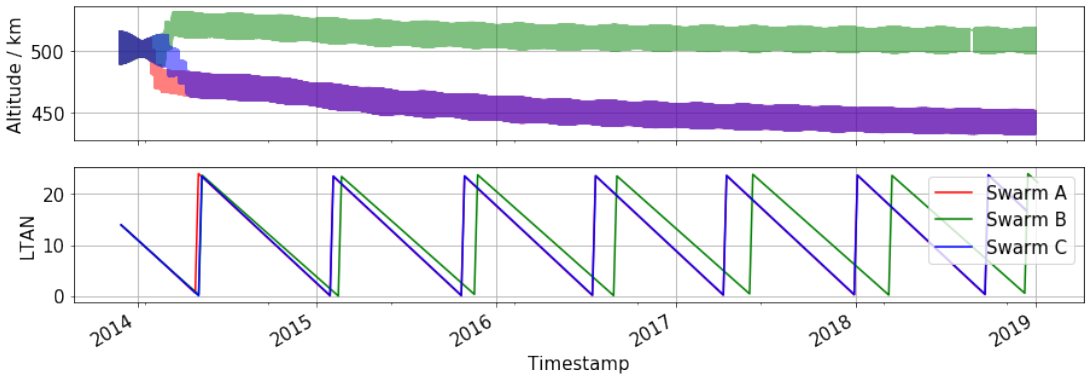

Figure 3.4: Altitude and local time of ascending node (LTAN) of the Swarm trio since launch in 2013 until end of 2018

3.2.1 Swarm

Swarm launched in November 2013 as a constellation of three identical satellites providing magnetic gradiometry measurements in LEO for the first time. Analogously to ground observatories, measurements are made by a duo of the Vector Field Magnetometer (VFM) and the Absolute Scalar Magnetometer (ASM) - see Olsen et al. (2013). These sensors are kept distant from the magnetic fields generated by the spacecraft by being mounted on a boom (see Figure 3.3). As with other Earth observation missions, precise orbit determination (accurate knowledge of the spacecraft position at the time of each measurement) is provided by GNSS and a laser retroreflector.

The ASM (Fratter et al., 2016) is positioned furthest from the spacecraft body in order to obtain the most pristine measurements of the scalar field, which is used for in-flight calibration of the VFM data. This calibration procedure is based on experience from previous missions (Olsen et al., 2003; Yin and Lühr, 2011). The orientation of the vector measurements are derived from the star tracker (STR) orientation, and so the VFM is colocated with the STR to minimise offsets, but distortions still occur because of thermal effects. Rotations are applied to transform the vector measurements from the VFM frame to the STR frame and to the geocentric frame, but accurately determining the Euler angles is challenging and has previously been achieved by comparing with independently determined geomagnetic main field models. For this reason, the Euler angles are co-estimated with the core field models which are derived as part of the Swarm mission processor chain. Corrections are also applied to the data to account for stray fields introduced by the instrument and spacecraft setup, so for this reason successively improved data versions are released as these fields are better characterised as the mission progresses. The primary magnetic data product, `SW_OPER_MAGx_LR_1B`, contains the vector and scalar measurements sampled at 1Hz (DTU, 2019).

The three original satellites of the Swarm mission (Alpha, Bravo, and Charlie) were deployed together and manoeuvred into their current constellation configuration over a few months until May 2014 (see Figure 3.4). From this point onward, Bravo orbits at an altitude below 530 km, and Alpha and Charlie orbit almost side by side at below 480 km, separated by about 1.5° longitude at the equator. Altitude (above the reference radius) varies over each orbit by about 20 km. The satellites sweep through all local time sectors over about 4 months. The gradual separation in local time of the orbital planes of A/C and B is such that they were perpendicular around 2018.0.

Other spacecraft are being added under the umbrella of the Swarm mission. In 2018, the Canadian Space Agency's CASSIOPE satellite and its instrument, e-POP, were added as "Swarm Echo", providing another sampling point primarily for space weather research (ESA, 2018). The French space agency, CNES, is working on a new nano-satellite with a miniaturised Swarm-like ASM that can also provide vector data (Hulot et al., 2018). This is hoped to become "Swarm Delta". Other missions are also becoming involved, with synergies and potential future operational support from ESA being explored. These include the Chinese National Space Agency's "China Seismo-Electromagnetic Satellite" (CSES) and other ESA missions, Cryosat and GOCE, and NASA's GRACE (Bouffard et al., 2019).

3.3 Geomagnetic indices

Geomagnetic activity levels are characterised by various indices which are derived from observatory data. Each of the indices are designed to capture activity in different external current systems. This is achieved by careful algorithm design and application to appropriate observatories according to their geographic location and ability to respond to the current system in question. These indices are key parameters used in solar-terrestrial research and space weather monitoring and are widely applied in many studies, including geomagnetic internal field modelling (Kauristie et al., 2017). Some of the most important ones are introduced here: "Kp", "Dst", and "AE". For more details see reviews by Mayaud (1980) and Menvielle et al. (2011).

The so-called K indices (for "Kennziffer", meaning "reference number") were introduced by Bartels et al. (1939) and are regularly calculated at observatories. They are based off the maximum deviation of magnetic D (declination) and H (horizontal intensity) over a three-hour period after accounting for the quiet-time diurnal variation. The calculation was later standardised by Bartels (1949) and an averaging of K indices from 13 chosen mid-latitude observatories used to define the Kp (planetary) index. The Kp index is thus a three-hourly index representing the global disturbance.

The Dst index (disturbance, storm-time, Sugiura, 1964) is derived from the deviations of the H components measured at four near-equatorial observatories and is calculated hourly . This measure responds strongly to the ring current because of its geometry, and so Dst is a good index to track the evolution of geomagnetic storms

due to to the characteristic pattern of energisation and subsequent decay of the ring current. Because of difficulties in determining the absolute baseline of the Dst index, more recently efforts have been made to derive indices which are better able to describe the quiet-time ring current, such as the RC index (Olsen et al., 2014).

The AE index (auroral electrojet, Davis and Sugiura, 1966) is derived from H component deviations at 12 observatories in the northern auroral oval. At each observatory, the H deviations are calculated by subtracting a determined monthly baseline value. These values from the 12 observatories are superposed and the largest and smallest values at each given time are picked, defining upper (AU) and lower (AL) envelopes. AE is then calculated as AU - AL, at 1-minute resolution. AU represents the strongest current intensity of the eastward auroral electojet, and AL the westward, so AE aims to represent the overall activity of both. The AE index has several deficiencies, as shall be explored in Chapter 5, and so there are some recent developments to define better indices to describe electrojet activity. One of these initiatives is the SME index, as part of the SuperMAG project (Gjerloev, 2012; Newell and Gjerloev, 2011). Another is an orbit-by-orbit measure of the strength and location of the auroral electrojets based on Swarm data (Swarm DISC Invitation to Tender 1.2, SD-ITT-1.2), which will soon be released as a Swarm mission product.

3.4 Solar wind data

Measurements of the solar wind are available from a small number of spacecraft located upstream from Earth's magnetosphere. These spacecraft carry magnetometers and particle analysers, providing a typical array of plasma measurements: particle densities and temperatures, the magnetic field vector (i.e. the IMF), and the bulk flow velocity. These data are available as homogenised time series, time-shifted from the spacecraft locations to the solar wind's arrival time at the magnetosphere bow shock, through NASA's OMNI service (`https://omniweb.gsfc.nasa.gov`). In this thesis I use the common convention that, when referring to IMF Bx,y,z, this refers to the IMF components in the GSM frame (see next section), unless stated otherwise.

Related to these data are various measurements of the Sun. A measurement that is commonly used in geomagnetism is the solar radio flux at the 10.7cm wavelength. This is referred to as the F10.7 index and is indicative of the overall radiative output of the

Sun, and is particularly useful due to its continuous availability and long record.

3.5 Coordinate systems

There are a number of coordinate systems relevant to geomagnetism (Hapgood, 1992; Laundal and Richmond, 2017). The systems that are used in this thesis are introduced here.

3.5.1 Geocentric and geodetic

As is common practice, I use "geocentric" (GEO) to refer to the Earth-centred Earth-fixed coordinate system with its z axis along the rotation axis, and x axis pointing to the intersection of the Greenwich meridian and the equator. GEO co-latitude and longitude are spherical coordinates, θ_{GEO} and ϕ_{GEO}, which, together with the radial distance from the geocentre, r, describe a position vector. If unspecified, θ and ϕ refer to these coordinates in this thesis. This is not to be confused with *geodetic* coordinates which are defined with respect to the ellipsoid surface (of e.g. the World Geodetic System 1984 [WGS84]), accounting for the oblateness of the Earth.

A local Cartesian system is also used, called NEC (for North, East, Centre). These are defined geocentrically, with C pointing to the geocentre. This is a natural reference system for satellite measurements and is the principle system that the Swarm data are provided in. Note that these are different from the X, Y, Z components described in Section 3.1, which are defined geodetically, with Z pointing perpendicular to the local surface of the ellipsoid. Later in this thesis, I refer to the "C" direction using either "C" or "Z" but in these cases I am instead referring to the same *geocentrically* defined direction.

3.5.2 Geocentric solar ecliptic (GSE) and Geocentric solar magnetospheric (GSM)

Both the Geocentric solar ecliptic (GSE) and Geocentric solar magnetospheric (GSM) systems have their x axis pointing towards the Sun on the Earth-Sun line. The GSE z axis points perpendicular to the ecliptic plane and the y axis therefore points retrograde along Earth's orbit (i.e. duskward). GSM is similar but it is rotated about the x axis (the Earth-Sun line) such that the z axis points along the projection of the magnetic

dipole in the plane perpendicular to the x axis (see Figure 3.5). GSM is therefore an appropriate frame in which to consider solar wind-magnetosphere coupling, since at the magnetosphere "nose" the geomagnetic field points in the z_{GSM} direction.

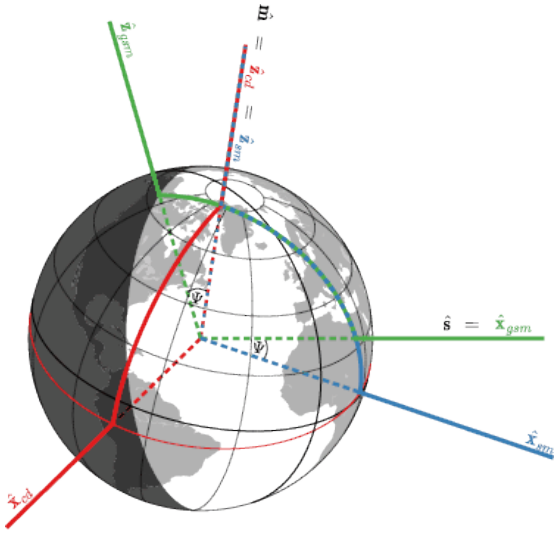

Figure 3.5: Illustration of CD (red), GSM (green) and SM (blue) coordinate systems, from Laundal and Richmond (2017). SM (solar magnetic) is often used to define magnetic local time in the outer magnetosphere.

3.5.3 Centred dipole (CD) and Quasi-dipole (QD)

The centred dipole (CD) is often referred to simply as magnetic (MAG) coordinates. It is Earth-fixed and its z axis points along the dipole. Its x axis is along the intersection of the (dipole) magnetic equatorial plane and the plane containing the great circle that passes through the northern geographic and geomagnetic poles.

Quasi-dipole (QD) is one of several non-orthogonal systems which account for more of the complexity of the real geomagnetic field. Its coordinate axes are close to the CD axes but vary across the Earth according to the shape of the main field as defined by the full IGRF (see Figure 3.6). CD depends on the first order terms (i.e. the dipole) of the IGRF which dominate at higher altitudes, so CD approximates QD at large distances away from Earth's surface. However, the higher order terms produce significant structure at low altitudes and influence ionospheric activity, so QD is a more appropriate coordinate system to describe ionospheric current systems. QD is one of two magnetic apex systems (Emmert et al., 2010; Richmond, 1995) based on tracing along IGRF field lines to their apex.

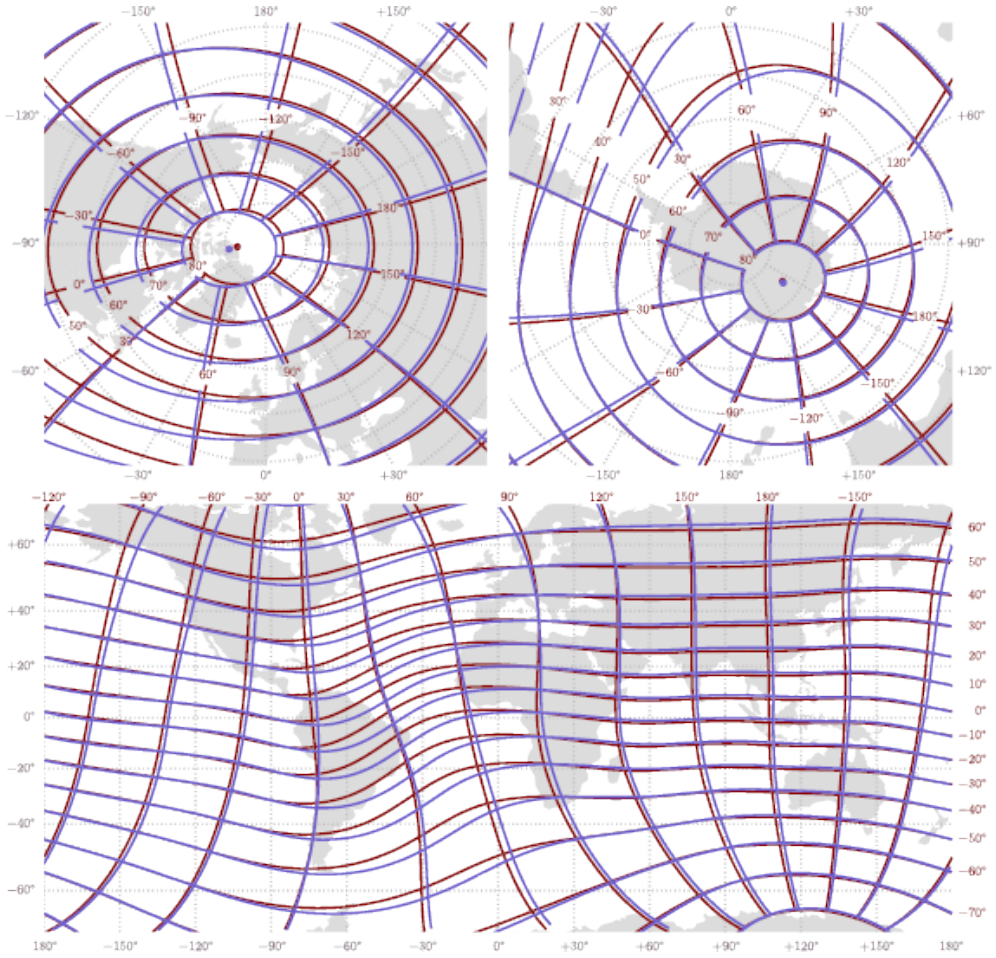

Figure 3.6: Quasi-dipole (QD) coordinate grids, from Laundal and Richmond (2017). QD grids for epochs 1985 (blue) 2015 (red). They are offset and distorted from geographic latitude and longitude, and vary in time.

3.5.4 Magnetic local time (MLT)

Magnetic local time (MLT) organises measurements with respect to the local time of day and the geomagnetic main field. There are several ways to define MLT (Laundal and Richmond, 2017) but the one used here is based on QD longitude, ϕ_{QD}, and the subsolar point:

$$\text{MLT [hours]} = (\phi_{QD} - \phi_{CD,\hat{\boldsymbol{s}}})/15 + 12, \tag{3.1}$$

where $\phi_{CD,\hat{\boldsymbol{s}}}$ is the CD longitude of the subsolar point, both in degrees (see Laundal and Richmond (2017) for how to calculate these quantities). The factor of 15 converts between degrees and hours (i.e. 360° being equivalent to 24 hours) and the offset of 12 hours provides a rotation so that the MLT at the subsolar point (at $\phi_{QD} = \phi_{CD,\hat{\boldsymbol{s}}}$) is 12 noon.

Chapter 4

Geomagnetic field models

There are many ways in which one can approach modelling geomagnetic field sources so, naturally, many competing models have arisen, each with different advantages and disadvantages as their focuses, and intended applications, differ. In this chapter, the mathematical apparatus of spherical harmonic analysis is introduced and some of the important models are summarised, including the Swarm mission products.

4.1 Spherical harmonics

Spherical harmonic analysis (SHA), as first developed by Gauss (1838), is the most widely used method to produce and describe global magnetic field models. Spherical harmonics have a number of useful properties that suit them to this purpose. One such property is that they allow for a natural separation of internal and external magnetic fields (see e.g. Garland, 1979; Olsen et al., 2010b). The fundamental assumption that is required for the use of spherical harmonic analysis is that measurements are taken in a region free of electric currents / magnetic sources. In this case, the magnetic field can be simply expressed as the gradient of its scalar potential, $\boldsymbol{B} = -\nabla V$, and, following from Maxwell's equations, the divergence of the magnetic field is zero, $\nabla \cdot \boldsymbol{B} = 0$. Combining these, we find that the potential must be a solution to $\nabla^2 V = 0$ (Laplace's equation). It can be shown (e.g. Backus et al., 1996; Parkinson, 1983) that solutions of Laplace's

equation can be expressed as sums of spherical harmonic terms of the following form:

$$\begin{aligned} V &= V^{int} + V^{ext} \\ &= R_E \sum_{l=1}^{N} \sum_{m=0}^{l} \left(g_l^m \cos m\phi + h_l^m \sin m\phi\right) \left(\frac{R_E}{r}\right)^{l+1} P_l^m(\cos\theta) \\ &\quad + R_E \sum_{l=1}^{N} \sum_{m=0}^{l} \left(q_l^m \cos m\phi + s_l^m \sin m\phi\right) \left(\frac{r}{R_E}\right)^{l} P_l^m(\cos\theta) \end{aligned} \tag{4.1}$$

where R_E is the reference radius for Earth, (r, θ, ϕ) are the spherical coordinates of radial distance, geocentric colatitude, and longitude, $P_l^m(\cos\theta)$ are the associated Schmidt semi-normalised Legendre polynomials, and the coefficients (g_l^m, h_l^m) and (q_l^m, s_l^m) are spherical harmonic coefficients (or Gauss coefficients) that describe the strength of the magnetic field, usually in nanoTesla (nT). This elegant formulation is a summation of ever-higher degree harmonics (as l increases) where higher degree terms (increasing l) describe variation over smaller angular scales. In this way, the field is approximated by the earlier terms in the summation, and is made more and more accurate by adding more terms. The coefficients can be determined from data by, for example, least-squares fitting. Theoretically the summation extends to infinity but practically must be truncated at some maximum degree, N, which depends on the noise present in the data.

The lower degree terms are dominated by the core field and the higher degree terms are determined by the crustal field, while the external field contributions occur over a range of scales. The global field (as far as the core and crustal sources are concerned) is thus compactly described by the coefficients g_l^m and h_l^m. Secular variation of the main field can be described by making the coefficients time-dependent, $g_l^m, h_l^m = g_l^m(t), h_l^m(t)$. The more rapid time-varying components (external and induced fields), on the other hand, must be described in a more complex manner which includes considerations of local time and geomagnetic activity etc.

The internal and external contributions are described together in equation 4.1 where internal sources, at $r < R_E$, are separated from external sources, at $r > R_E$, with the first line (with g_l^m and h_l^m) and second line (with q_l^m and s_l^m) representing the internal and external contributions respectively. See, e.g. Parkinson, 1983, for more details. This separation of internal and external sources holds true for measurements taken within a shell at around R_E devoid of sources, which presents an issue when

interpreting measurements from satellites which in fact orbit above, and sometimes within, ionospheric sources (e.g. Lowes, 2007).

A useful construction from spherical harmonics is the Mauersberger–Lowes power spectrum (Lowes, 1974; Maus, 2008). This gives the mean squared field strength of degree l (the amount of power contained within each degree), at a given radial distance from the centre, r:

$$R_l = (l+1)\left(\frac{R_E}{r}\right)^{2l+4} \sum_{m=0}^{l} (g_l^m)^2 + (h_l^m)^2, \tag{4.2}$$

(for internal fields) and thus provides a compact way to characterise and compare models and field sources (see Figure 2.1). This can be defined similarly for the secular variation and acceleration, to describe the change in power per degree.

4.2 Summary of current models

The geomagnetic field is complex and it is natural to think of it in terms of a sum of the fields from different sources, each of which behaves differently as they originate from different physics. For this reason, models often describe one of these fields in isolation using parameterisations that make sense for each source. A more complex model that describes multiple sources can be thought of as a collection of individual models that have been prepared in some consistent way, such as by co-estimation. For example, an internal field model representing the core and crustal field may be derived from a high degree SHA which is split at a chosen degree (usually near l=15) with the lower degree part being time dependent to represent the core field and the higher degree part being a static crustal field contribution. In cases where ionospheric or magnetospheric fields are modelled, the analysis is typically done in suitable reference systems that are not Earth fixed (e.g. GSM, QD/MLT etc.).

Where models attempt to capture only a particular source in isolation, they must aim to remove the effect of the other sources from the data being used to produce the model. For example, for a regional crustal field survey, the main field can be subtracted from the data using an existing main field model, each pass can be line-levelled to remove the effect of long wavelength trends, and remaining noise assumed minimal or average to zero. This can be referred to as the "sequential" approach. Other models describe

more aspects of the field simultaneously, by parameterising the known sources sensibly and co-estimating them: the "comprehensive" approach. In both cases, it is important to consider the unmodelled fields and perhaps employ careful data selection to reduce their effect. There are also choices to be made about the appropriate mathematics used to describe the models, which depend on source field morphology, on the typical use case for the model, and on the nature and quantity of the data used in constructing the model.

Some contemporary near-Earth magnetic field models are listed in Table 4.1 and are now introduced.

Model	Core	Lithosphere	Ionosphere	Magnetosphere	Reference
CM5	✓	✓	✓	✓	(Sabaka et al., 2014) [NASA]
CIY4	✓	✓	✓	✓	(Sabaka et al., 2018)
CHAOS-6	✓	✓		✓	(Finlay et al., 2016) [DTU]
POMME-11	✓	✓		✓	(Maus et al., 2010) [CIRES/NCEI]
MEME	✓	✓		✓	(Hamilton et al., 2015; Thomson et al., 2010) [BGS]
IGRF12	✓				(Thébault et al., 2015) [IAGA]
WMM2015	✓				(Chulliat et al., 2015) [NOAA/BGS]
EMM2017	✓	✓			[NOAA]
GRIMM	✓				(Lesur et al., 2008) [GFZ]
COV-OBS	✓				(Gillet et al., 2015) [DTU]
gufm1	✓				(Jackson et al., 2000)
NGDC-720		✓			(Maus, 2010b) [CIRES/NCEI]
MF7		✓			(Maus et al., 2008) [CIRES/NCEI]
LCS-1		✓			(Olsen et al., 2017) [DTU]
DIFI-3			✓		(Chulliat et al., 2013) [CIRES/NCEI]
AMPS			✓		(Laundal et al., 2018) [pyAMPS]
EMAG2v3*		✓			[Global] (Meyer et al., 2017) [NOAA]
WDMAM*		✓			[Global] (Lesur et al., 2016) [IAGA]
ADMAP-2*		✓			[Antarctic] (Golynsky et al., 2018)
CAMP-M*		✓			[Arctic] (Gaina et al., 2011)

Table 4.1: A selection of contemporary near-Earth magnetic field models. *These are grids rather than models.

4.2.1 Main field and joint models

The International Geomagnetic Reference Field

The International Geomagnetic Reference Field (IGRF; Macmillan and Finlay, 2011) is a time-dependent model of the main field up to degree 13 (in recent years; older versions do not go this high due to lack of data) and is updated every 5 years to provide a definitive model for international standardisation, with its starting epoch at 1900.0. It has been produced by the International Association of Geomagnetism and Aeronomy (IAGA) since 1965, and its latest release is IGRF-12 (Thébault et al., 2015). It is parameterised by a set of Gauss coefficients at each 5-yearly sample point, and the prediction at intermediary times is given by a linear interpolation of these coefficients. Similarly, a predictive secular variation for the upcoming 5-year interval is given in units of nT/year.

Rather than being the most scientifically accurate model of the core field (since such a goal is inevitably subjective, and different models may be deemed "accurate" for different reasons), the goal of the IGRF is to be a consistent reference standard upon which many scientific or operational systems are built. A typical example usage is as the basis of magnetic coordinate systems. The IGRF is therefore built from a weighted combination of a number of candidate models submitted by various modelling groups. These candidate models are in turn built from various combinations of observatory, repeat station, and satellite data. The World Magnetic Model (WMM, Chulliat et al., 2015) has a similar role, being used in many navigation systems.

CHAOS models

The CHAOS series of models, of which the latest is CHAOS-6 (Finlay et al., 2016), is named after the satellite missions which originally contributed data to it: CHAMP, Ørsted, and SAC-C. Since CHAOS-5 (Finlay et al., 2015), these have been joined by Swarm. Monthly means of observatory data are also used in the inversion, and ground based activity indices are used for data selection to identify quiet times. CHAOS-6 covers the period from 1999.0 onward, being periodically extended as new data becomes available, with the most recent available at the time of writing being CHAOS-6-x9 which includes data up to the end of April 2019. The primary motivation is to represent the core field at high time resolution. The contributing data are inverted for a spherical

harmonic model using an iteratively reweighted least-squares algorithm which makes use of Huber weights (Huber, 1964), attempting to fit fields resulting from the core, lithosphere, and magnetosphere. The resulting model gives time-dependent Gauss coefficients for main field up to degree 20, and the (static) lithospheric field up to degree 110. The magnetospheric field (both external and induced) is given up to a maximum of degree 2, parameterised by the RC index which is derived from observatory data as part of the model production. For the core field over longer durations, the COV-OBS (Gillet et al., 2015) and gufm1 (Jackson et al., 2000) models are available. COV-OBS spans 1840 to 2010, and gufm1 spans 1590 to 1990.

Comprehensive Models

"Comprehensive Inversion" is the approach used by the series of "Comprehensive Models", the latest of which are CM5 (Sabaka et al., 2014) and CIY4 (Sabaka et al., 2018), and their derivatives as Swarm mission products. Their aim is to use as much of the data as possible by parameterising the known field sources and solving for them simultaneously, rather than attempting to filter out the unmodelled fields as is the case in other approaches. The parameterisation is necessarily complex, involving different spatial and temporal resolutions for each source. Ionospheric fields and their induced counterparts are described in the quasi-dipole frame. The model represents the best attempt to account for all sources together in one inversion process, and so the complete model probably reproduces the total geomagnetic field better than would be achieved by adding together other models. However, imperfect separation of the sources means that the individual components of CM5 are not generally the most accurate estimates of the source fields.

4.2.2 Lithospheric models

Two recent satellite-derived lithospheric field models are MF7 (Maus et al., 2008; Maus, 2010b) and LCS-1 (Olsen et al., 2017). These are spherical harmonic models representing the static lithospheric field between degrees 16 and 133, and 16 and 185, respectively. These both benefit from the final two years of CHAMP's operation at low altitude, which enabled higher sensitivity to the lithospheric features than with previous satellites. The higher resolution achieved by LCS-1 is due to the addition of the hitherto unique Swarm constellation data, even though they are gathered at a higher altitude than CHAMP.

LCS-1 employs the along-track and cross-track sums and differences of measurements, which provide a higher signal-to-noise ratio by being less sensitive to the large-scale external field "noise" while being more sensitive to the small-scale crustal features (Olsen et al., 2017). A significant advantage here is that it enables modelling without the use of orbit-by-orbit filtering of noise, of the kinds described by Thébault et al. (2017), which tend to also remove some of the desired signal.

Higher resolution lithospheric models require the addition of marine, aeromagnetic and ground magnetic surveys, the data from which are typically compiled on a grid. As part of the compilation process, the longer wavelength components can be replaced with satellite-derived models (as in e.g. Lesur et al., 2016). This is necessary because regional surveys cannot resolve these because of their limited spatial extent. The compilation of these measurements, and correction of them to a common reference field model, is a complex process and the large regional and global compilations are the result of large collaborations. Global grids include WDMAM (Lesur et al., 2016) and EMAG2v3 (Meyer et al., 2017). NGDC-720 (Maus, 2010a) is a degree 720 ellipsoidal harmonic representation to allow prediction of the lithospheric magnetic field anywhere close to and above the Earth's surface. Other options include recent anomaly grids which focus on the Arctic (CAMP-M, Gaina et al., 2011) and Antarctic (ADMAP-2, Golynsky et al., 2018).

4.2.3 Ionospheric models

The ionospheric field is complex and is the result of many different processes with different drivers, and the current systems necessarily overlap and interact. This means that it would be difficult to produce a single model describing all the aspects simultaneously with an accuracy and resolution (both spatial and temporal) suitable for all applications. This situation has led to a number of models which are parameterised very differently as they capture different current systems and have different applications.

Ionospheric fields are by their nature global (or at least very large scale) so satellite data are invaluable for measuring them due to their global coverage, and understanding these fields is crucial for making use of satellite data for other purposes. It is no surprise then that some of the models I introduce here are being adopted as official Swarm products, as will be described in the following section.

The daytime mid-latitude (i.e. below 55°) field is fairly predictable (i.e. the Sq

system) and is a large and regular disturbance. In order to use data taken during the daytime for lithospheric field surveys, it is necessary to account for this field. The CM5 model (see above) is therefore popular for this purpose because it incorporates a prediction of this field. As described by Sabaka et al. (2018), the field is parameterised in spherical harmonics as a function of magnetic local time, season, and location in quasi-dipole coordinates, as well as a scaling by the $F_{10.7}$ solar radiation index to account for insolation increasing the strength of the Sq system. The induced counterpart is based on estimates of the mantle and ocean conductivity structure (Kuvshinov, 2008).

Complementing the models from the comprehensive approach, a similar model of the ionospheric field has been produced using the sequential, or "dedicated", approach: DIFI (Dedicated Ionospheric Field Inversion; Chulliat et al., 2013; Chulliat et al., 2016a), and the related EEF model (Equatorial Electric Field; Alken et al., 2013), both as Swarm products.

The ionospheric field in polar regions is strongly driven by solar wind conditions, so for this reason the AMPS model (Average Magnetic field and Polar current System; Laundal et al., 2018) is based on Gauss coefficients which are dependent on the IMF components, solar wind speed, and Earth's dipole tilt.

The models above are derived from inversions of satellite data with suitable parameterisation in order to give global predictions given different input conditions, and therefore represent the *average* response. This means that they do not necessarily well represent the true field at any given moment, since they are inherently limited by the unrealistic simplicity of their parameterisations and the occurrence of (currently) unpredictable "noise". Other models exist, particularly targeting the polar ionospheric and field-aligned currents, which synthesise ground or satellite data during a given time period to describe the current system at that time. Some of these are based on the "Spherical Elementary Current Systems" (SECS) method developed by Amm (1997), such as a study by Pulkkinen et al. (2003) using ground magnetometers, and by Juusola et al. (2006) using CHAMP data. Juusola et al. (2016) provide a comparison of related methods. Olsen (1996) described a method to determine the horizontal ionospheric currents flowing directly below a satellite as it passes overhead (the "line currents" method), and this was subsequently developed by Aakjær et al. (2016) and will soon be released as a Swarm mission product.

4.3 Swarm mission magnetic field products

As well as the calibrated data releases from ESA (the "Level 1b" data), e.g. the magnetic vector and scalar measurements, there are a number of "Level 2" (L2) products which are produced by institutions which contribute to the Swarm Satellite Constellation Application and Research Facility (SCARF; Olsen et al., 2013) and a larger group, DISC. Many of these L2 products are magnetic field models, some of which are summarised in Table 4.2. These products are categorised into three groups: Fast track (`F`), Dedicated (`D`), and Comprehensive (`C`).

Fast track models are produced rapidly. In the case of the field aligned currents (`FAC_TMS_2F`, Ritter et al., 2013) and magnetospheric models (`MMA_SHA_2F`, Hamilton, 2013), these are produced daily as soon as data are available, as the algorithms only depend on relatively short windows of data to derive the models. The fast track core field model (`MCO_SHA_2F`) is updated every three months.

Dedicated models include models of the core (`MCO_SHA_2D`, Rother et al., 2013), ionosphere (`MIO_SHA_2D`, Chulliat et al., 2013; Chulliat et al., 2016a), and lithosphere (`MLI_SHA_2D`, Thébault et al., 2013). These are updated yearly and are produced by algorithms that are designed to isolate the field in question and model them in a robust way (i.e. better than the fast track models). The fast track products are used to derive some of the other products: for example `MMA_SHA_2F` is used in the production of `MCO_SHA_2F` and the `_2D` models. The inter-relation of the models and their processing chains is complex (see Olsen et al., 2013).

Comprehensive models are produced in the "Comprehensive Inversion" chain following the method used in the CM series of models (Sabaka et al., 2013, 2018). The individual products are in actuality the different components of a larger parent model where each source is co-estimated. These comprise `MCO_SHA_2C`, `MLI_SHA_2C`, `MMA_SHA_2C`, `MIO_SHA_2C`, for the core, lithosphere, magnetosphere, and ionosphere respectively.

Model name	Source field	Notes
Comprehensive inversion		*Updated yearly with 6 week latency*
MCO_SHA_2C	Core	SH l=1-18
MIO_SHA_2C†	Ionosphere (Sq)	SH l=1-60, m=1-12 *
MLI_SHA_2C	Lithosphere	SH l=16-150
MMA_SHA_2C†	Magnetosphere	SH l=1; 1 hour cadence
Dedicated inversions		*Updated yearly with 6 week latency*
MCO_SHA_2D	Core	SH l=1-18
MIO_SHA_2D†	Ionosphere (Sq)	SH l=1-60, m=1-12 *
MLI_SHA_2D	Lithosphere	SH l=16-150
Fast track		
MCO_SHA_2F	Core	SH l=1-18; updated every 3 months with 1 week latency
MMA_SHA_2F†	Magnetosphere	SH l=1; 1.5 hour cadence; updated daily
FAC_TMS_2F	Field-aligned currents	Time series along the orbit
AMPS	Polar ionosphere	SH model also parameterised by solar wind

Table 4.2: Summary of relevant Swarm Level 2 data products (Swarm data handbook). *SH in QD coordinates, modulated by seasonal and daily wavenumbers; valid within ±55° QDLat. †In two parts, "primary" and "secondary" for external and internal (induced) fields respectively.

4.4 Methods used to improve lithospheric models

I focus here on recent advances and possible directions in improving lithospheric field models in particular. This inevitably involves aspects of modelling the other fields due to the entwined nature of separating the field sources from measurements. The current state of internal field modelling techniques and the growth in the amount and variety of data available is such that knowledge of the external field "noise" sources, particularly in the polar regions, is now the limiting factor (Finlay et al., 2017). Accurately modelling, or otherwise accounting for, the quiet-time external field sources is a delicate process. For example, something that has not been studied before is the effect of external field variations due to secular variation of the main field (Cnossen, 2017).

4.4.1 Data selection

Models typically are derived from data that have been carefully selected according to some set of criteria that minimise the presence of noise. Each modeller chooses selection criteria according to prior knowledge of the noise behaviour and according to the quality of the generated model (as compared to other models and to theoretical properties). There are a variety of such criteria that have been used but they typically follow the pattern of using data acquired on the Earth's dark side and when below threshold values of geomagnetic activity indices. Sometimes only scalar data are used in polar regions in order to reduce the effect of FACs. Such strategies have worked well for obtaining reasonable models of both the core and lithospheric fields (see Lesur et al., 2011, for details on selection procedures used by CHAOS, GRIMM, and BGS models). For lithospheric models, these criteria can be more stringent in order to remove as much as possible the external field noise from the weak lithospheric signal, without concern about the resultant sampling rate since the signal is constant in time.

Some of the quantities commonly used to identify geomagnetic active conditions are:

- Activity indices:
  - Kp and am: globally disturbed periods (Mayaud, 1980)
  - Dst and $dDst/dt$: ring current size and changes, or refined variants such as RC and dRC/dt (Olsen et al., 2014)
  - AE: auroral electrojet activity (Davis and Sugiura, 1966; Menvielle and Marchaudon, 2007)

  - *PC*: polar cap convection (Stauning, 2013; Troshichev and Andrezen, 1985)
- Solar wind conditions:
  - IMF B_z, B_y
  - dayside merging electric field (MEF) (Newell et al., 2007)

Kauristie et al. (2017) discuss in detail the usage of these activity indices in field modelling, including the effect of baseline biases, observatory coverage, and generally the ability of indices to capture the complexity of geomagnetic activity. Determining an appropriate baseline for the *Dst*-like indices is a challenge because it requires separating out a dipole term into contributions from the core, and the magnetosphere and its induced internal counterpart, but progress has been made on this with the *RC* index and with other approaches. Mid-latitude activity can therefore be well removed on the nightside, and even with some success on the dayside when the *Sq* system is accounted for. However, it remains a greater challenge to select quiet periods in the polar regions, and to adequately describe the remaining ever-present quiet-time external fields.

Another general issue is that most indices are derived from ground-based data and don't necessarily describe well the field as seen by satellites, which are instead above the ionospheric sources rather than below. The combined action of the magnetic fields produced by horizontal and radial currents produce a different observable equivalent current system when viewed from below (the Fukushima theorem; Fukushima, 1976), and satellites are flying through some of the current systems in question.

There are numerous issues with the usage of the *AE* index to describe quiet polar conditions, associated with its design capturing only part of the electrojet system and accuracy only in average conditions. Any single index will struggle with this because of the complex structure and variability in polar currents. Merging electric field (MEF) was designed by Kan and Lee (1979) to characterise the dayside magnetopause reconnection rate with the solar wind. A revised version by Newell et al. (2007) is used in contemporary internal field modelling:

$$\mathrm{MEF}_N = 0.33 V^{4/3} B_T^{2/3} \sin^{8/3}(|\theta|/2), \tag{4.3}$$

where V is the solar wind bulk velocity, $B_T = \left(B_z^2 + B_y^2\right)^{1/2}$ is the transverse component of IMF, and θ is the IMF clock angle, the angle between B_T and the GSM z axis, i.e. $\arctan(B_y/B_z)$ (see Figure 4.1). Appropriately time-averaged, it indicates the level of

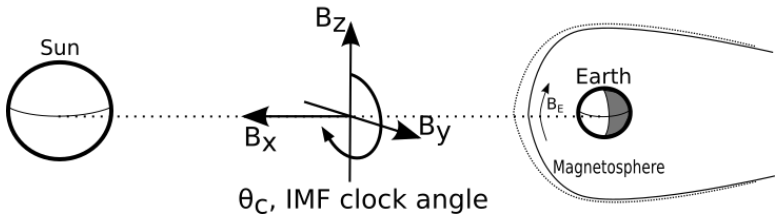

Figure 4.1: Illustration of the definition of IMF clock angle, with IMF in the GSM frame and the direction of the geomagnetic field indicated as B_E.

magnetospheric convection and driving of geomagnetic activity particularly over the polar caps.

4.4.2 Filtering techniques

Several techniques have been used which process satellite data along the orbital tracks to filter out the effect of external fields. Thébault et al. (2017) reviewed some recent advances: Fourier filtering, polynomial filtering, high-pass spherical harmonics, singular spectral analysis, and line-levelling. They showed that these techniques do indeed reduce the level of external field power, but result in artefacts in the output data as well as loss of some of the lithospheric signal. Nevertheless, the application of such techniques has been successful in extending lithospheric field models to higher degree, albeit with a lower power level than unfiltered models (e.g. Maus et al., 2008). However, Thébault et al. (2017) point out that the stepwise application of complex correction techniques means that it is difficult to cleanly assess their effectiveness and the accumulated error budget.

4.4.3 Gradiometry and other techniques

Older field models were built using data from single-satellite missions that provide only the vector field measurements. The Swarm constellation can measure cross-track differences between Swarm A and C, effectively providing the East-West gradient. The use of gradients rather than vector measurements provides better information content for retrieving the lithospheric field (e.g Kotsiaros and Olsen, 2012; Kotsiaros, 2016). This has led to the LCS-1 model (Olsen et al., 2017) which surpasses the resolution of MF7 without need for any filtering. Gradiometry techniques will likely be improved upon to make full use of Swarm, and is a clear motivation for a future mission that

could retrieve the full magnetic tensor.

4.5 Summary of current state-of-the-art and direction of this thesis

Satellite and ground magnetic data have some fundamental differences. With ground data, separation of internal and external sources can in principle be performed naturally by spherical harmonic analysis (SHA). Satellite data on the other hand are recorded within a shell enclosing (most of) the ionospheric sources so SHA would see these as "internal" and hence the determined internal field Gauss coefficients would contain ionospheric signals. More problematically, currents exist within the shell where satellite measurements are taken, violating the source-free assumption of SHA. Geometric factors of the external current configurations also affect which parts of the currents are even visible at ground or by satellite, as well as the different source-measurement distances affecting relative signal levels of different sources. These issues mean that satellite and ground data "see" different signals, complicating any comparisons or joint treatment. To make better usage of satellite data for internal field modelling, new techniques are needed to account for the external field contamination.

Many field modelling strategies have been developed to tackle the mutual contamination of field sources, including data selection and filtering, subtraction of prior models (the "sequential" approach), and co-estimation of sources (the "comprehensive" approach). Subsequently, field models vary in effectiveness and cross-compatibility, depending on the precise problem they are being applied to. A common defect among all internal field modelling schemes is an overly simplistic treatment of polar currents, typically handled by rejecting data deemed to be "noisy", various forms of filtering, and model regularisation. Consequently, there is not much evidence of what their remaining effect is on models. To approach this problem, we need better descriptions of the polar current systems themselves and their physical origins (Finlay et al., 2017).

The lithospheric field, being much weaker than the main field, is particularly hard to retrieve from satellite data due to the low signal to noise ratio. Many techniques exist that are able to build reasonable models of the lithospheric field, as well as filtering techniques that can better isolate it from external field noise (Thébault et al., 2017). Data selection routines to identify quiet times where data are least contaminated by

external fields have also made incremental progress over recent years, but there are still improvements to be made in polar regions (Kauristie et al., 2017). Progress in these domains improves internal field modelling in general. However, handling polar regions is continually a problem and remains extremely challenging. A particular challenge is to accurately describe quiet-time current systems, i.e. the weak currents that are always present and must have some seasonal and longer time scale variation, as well as small-scale and weak currents that are currently impossible to isolate from the lithospheric field.

In general, advances in internal field modelling are likely to come from more sophisticated treatment of external fields, and so we need new types of studies into external system behaviour specifically within this context. Most studies of the external systems are made from the perspective of space physicists and so are focused on understanding individual phenomena, characterised by single-event studies and simplified physical models, while there are few studies into long-term trends and quiet-time currents. There are hidden and unquantified effects on internal field models due to such externally-driven biases. Conversely, measurements of the weakest external currents will be limited by the accuracy of internal field models. These issues are emblematic of the difficulty of magnetic source separation.

The rest of this thesis firstly investigates the behaviour of polar ionospheric currents, whose severe effect on internal field modelling efforts is then demonstrated with an exploration of lithospheric field modelling. I aim to first demonstrate some of the complexity and variations (climatology) of the polar currents. This is achieved in Chapter 5 with a study of the auroral electrojets, which are indicative of the overall behaviour of the polar ionosphere, as well as being the strongest coherent signal that leaks into lithospheric field models. The climatology is related to physical origins, to provide insight into both the behaviour of this system and how it might be treated in the context of internal field modelling. In Chapters 6 & 7 I outline a new technique to derive lithospheric field models using some of the information from the auroral electrojet chapter.

Chapter 5

Climatology of the auroral electrojets

In this chapter, the behaviour of the auroral electrojets (AEJ) is studied, using data from Swarm and its predecessors. The focus is on average responses and long-term trends, hence the choice of the word "climatology", where I analyse a large number of events statistically without looking into the detail of individual events. This approach is useful to identify and demonstrate statistical trends which may be otherwise neglected in space weather research. In particular it uncovers weak tendencies which are also intimately related to internal field studies, as shall be explored in the later chapters.

Among the various ionospheric and magnetospheric currents, the auroral electrojets (AEJs) are perhaps the most troublesome to describe and predict. This reflects their origin in the complex solar wind-magnetosphere interaction and subsequent magnetospheric unloading processes and coupling to varying ionospheric conductivity structure. They are highly variable with several different types of drivers, from partly stochastic variations in the solar wind, to seasonal effects caused by Earth's orbit and its rotational and magnetic axes, to the longer term modulation by the solar cycle. As a key component of space weather, understanding them is important both in terms of furthering space and geophysical research and for practical applications due to their role in geomagnetically induced currents (GICs) in power grids, changes in ionospheric total electron count (TEC) altering radio wave propagation and negatively affecting GNSS, atmospheric heating increasing drag on satellites, and disturbances to magnetic navigation systems (Gaunt, 2016; Pirjola, 2005).

The AEJs, and the associated field-aligned currents (FACs) which feed them, are challenging to deal with when modelling the internal fields (from the core and the crust). This is because they represent a large disturbance field which is both highly spatially and temporally variable and difficult to predict. This makes it difficult to either reject periods of data contaminated by these external fields, or to model their effect. As they introduce noise to core and crustal field models, Cnossen (2017) and Finlay et al. (2017) point out that models of the core secular variation could be seriously contaminated in the polar regions by time-varying biases in external fields, depending on the data selection criteria used in building the models.

5.1 Physical origin of the auroral electrojets (AEJs)

It is well known that when the interplanetary magnetic field (IMF) is oriented southwards in the geocentric solar magnetospheric (GSM) reference frame, i.e. GSM IMF-$B_z < 0$, it causes enhanced reconnection at the front of the magnetopause and so energy entering and driving the magnetosphere, as first proposed by Dungey (1961). Although southwards IMF is the strongest driver of reconnection, the transverse IMF component (GSM B_y), and solar wind velocity and density also have an effect. This has led to the development of "coupling functions" which aim to quantify the amount of energy transfer into the magnetosphere in terms of solar wind parameters (Finch and Lockwood, 2007). As well as affecting the amount of energy entering, the B_y component also has the effect of twisting the magnetosphere such that magnetically conjugate points in each hemisphere get displaced longitudinally relative to each other (Østgaard et al., 2011). This has consequences for the release of energy from the magnetosphere to the ionosphere and back-coupling through the spatial distribution of ionospheric conductivity.

In addition to these variations in solar wind-magnetosphere coupling, there are various lag times involved between the energy input and the ionospheric response. On the day side there are more direct responses through energy entry along the magnetic cusps, whereas on the dawn/dusk and night sides convection-driven and substorm currents will lag due to the duration of energy build-up and unloading from the magnetotail. These lag times can be affected by the direction of the IMF (e.g. Browett et al., 2017) as well as its time history. Such issues complicate the local time pattern of the AEJs, which are also being driven by daily cycles in insolation-dependent conductivity.

The AEJs have seasonal patterns which are related both to the axial tilt providing a yearly oscillation in the amount of insolation in each hemisphere, and to the effect, identified by Russell and McPherron (1973), of the projection of the typical IMF direction into the GSM frame increasing the activity around the equinoxes. This, and other issues arising from the behaviour of the solar wind, are reviewed by Lockwood et al. (2016). There is also an approximately 11-year periodicity due to the solar cycle.

At high altitudes (above the ionosphere) the non-dipole components of the geomagnetic field can often be ignored, but at ionospheric altitudes they remain important and the interhemispheric differences (in terms of magnetic pole location, field intensity, and field inclination) play a role in magnetosphere-ionosphere coupling. This can be through several effects, including field intensity influencing ionospheric convection and precipitating particles (associated with both current sources and ionisation), and different insolation patterns over magnetically conjugate regions. Issues of North-South asymmetries due to the shape of Earth's magnetic field are reviewed by Laundal et al. (2017).

It is to be expected that the external current systems (in the magnetosphere and ionosphere) have long-term trends which reflect changes in the core field over time, being affected by its intensity and orientation, and by the different temporal variation across Earth. Cnossen (2017) used theoretical considerations and simulations to derive scaling relations for external current systems as the dipole moment changes, and reviewed how changes in dipole orientation and the non-dipolar contributions could non-trivially affect the current systems and how they relate to North-South differences.

5.2 Previous measurements of the AEJs

Ground-based magnetometers can be used to study the AEJs. This has been done extensively by utilising the auroral electrojet (AE) activity index (Davis and Sugiura, 1966) and other indices, which are useful for their long-term availability and continuity. More complex usage of the data can be made from certain groupings of magnetometers (e.g. Pulkkinen et al., 2003) which is better suited to detailed regional studies. Recent advances with the SuperMAG project (Newell and Gjerloev, 2011), and studies which use this dataset, show promise in making better use of the data. However, these approaches will ultimately be limited by spatial distribution of the ground stations with an uneven

and incomplete coverage, particularly the bias towards the Northern Hemisphere. Satellite data on the other hand provide us with almost complete global coverage (with the exception of the polar gaps of about 3°) and good latitudinal resolution, although they lose the advantage of continuous coverage that ground magnetometers have at given locations.

The AEJs have been estimated from several satellite magnetic data missions: Olsen (1996) using Magsat; Moretto et al. (2002) using Ørsted, CHAMP, and SAC-C; Ritter et al. (2003), Juusola et al. (2009), and Vennerstrom and Moretto (2013) using CHAMP; and Aakjær et al. (2016) using Swarm; among others. Vennerstrom and Moretto (2013) developed a method which tracks the estimated activity of the AEJs orbit-by-orbit. They applied it to five years of CHAMP data to produce statistical synthesis plots which show the response of the AEJs to different levels of geomagnetic activity and seasonal variation. However, in their analysis they combined the results from the Northern and Southern Hemispheres, even though hemispheric differences are identifiable using their method.

5.3 Methodology for monitoring the AEJs

The procedure I have adopted from Vennerstrom and Moretto (2013) is outlined here. Following the previous approaches (Moretto et al., 2002; Olsen, 1996), I use just the scalar magnetic field data, $F = |\boldsymbol{B}|$, rather than the full vector field, $\boldsymbol{B}$. The total magnetic field at a point combines internal and external sources (perturbations), $\boldsymbol{B} = \boldsymbol{B}_{int} + \boldsymbol{B}_{ext}$, with $\boldsymbol{B}_{int} \sim 40,000\text{nT}$ and $\boldsymbol{B}_{ext} \sim 100\text{nT}$ at altitudes of satellites in low Earth orbit when above 50° latitude, as in this study. This means that by separating the total field, $\boldsymbol{B}$, into components parallel ($\boldsymbol{B}_{\parallel}$) and perpendicular ($\boldsymbol{B}_{\perp}$) to the internal field, we get $\boldsymbol{B}_{\perp} \ll \boldsymbol{B}_{\parallel}$ and so $\boldsymbol{B}_{\parallel}$ can be approximated by the magnetic field total intensity (scalar), F:

$$F = |\boldsymbol{B}| = \left(\boldsymbol{B}_{\parallel}^2 + \boldsymbol{B}_{\perp}^2\right)^{\frac{1}{2}} = |\boldsymbol{B}_{\parallel}| \left(1 + O(10^{-5})\right)^{\frac{1}{2}} \tag{5.1}$$

This means that perturbations to the parallel field component can be observed from the scalar measurements, F. Of the two main perturbing fields, that which is produced by the electrojet and that which is produced by the FAC, the FAC-field effect on F is much smaller as it acts perpendicular to $\boldsymbol{B}$. Perturbations to F are therefore due primarily to

the electrojet. To isolate this perturbation, δF, an internal field model, F_{int}, must be subtracted: $\delta F = F - F_{int}$, i.e. isolating the ionospheric field from the core and crustal fields. As will now be discussed, I use the along-track gradient of F near the poles, to which the large-scale magnetospheric field has only a minimal contribution, so it is not necessary to subtract a model of this field.

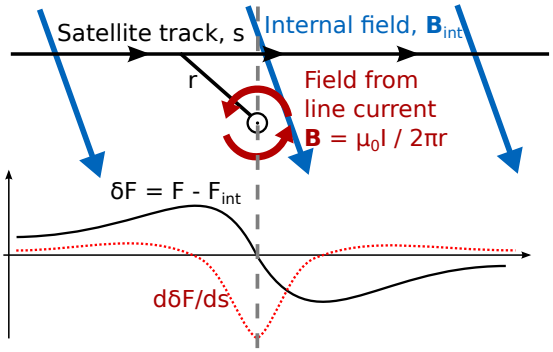

Figure 5.1: Summary of detection scheme. An internal field model is subtracted from the observed scalar field, $\delta F = F - F_{int}$. The electrojet contribution then has the demonstrated characteristic signature, with a maximum in $\frac{d\delta F}{ds}$ near the electrojet latitude. This maximum (either negative or positive) over each auroral region pass is picked as the electrojet latitude, and the magnitude of the maximum is used to estimate the electrojet current modelled as an infinite line current placed at that latitude.

As illustrated in Figure 5.1, the electrojet can be modelled as a single horizontal line current perpendicular to the satellite track (aligning approximately with the contours of magnetic latitude along which the currents flow since the satellite motion is essentially North-South). Due to the motion of the satellite, the time derivative of δF, $\frac{d\delta F}{dt}$, is equivalent to the along track gradient, $\frac{d\delta F}{ds}$, where ds is the distance travelled by the satellite during time dt. By assuming the electrojet remains static during a satellite pass ($\sim$ five minutes), the peak in $\frac{d\delta F}{ds}$ therefore indicates the latitudinal location of the current, with its sign depending on the direction of the current. The size of the peak is used to calculate the strength of an equivalent infinite line current placed perpendicular to the satellite track at a height of 110km (the peak of conductivity in the ionospheric E-layer). I additionally include a small correction which accounts for the inclination of the main field away from the vertical, shifting the location of the peak (see Vennerstrom and Moretto, 2013).

It is important to note that the current estimated in this way really indicates the location of peak intensity, and more accurately represents the true current when the flow is concentrated in a narrow range in latitude compared to when the current system is more complicated. The real magnetic signature is wider than that produced from an

infinite line current, so this will underestimate the true current. There can also be false positives and ambiguous situations when the magnetic signature does not conform to the idealised "single line current" form (e.g. when there is more than one large peak in $\frac{d\delta F}{ds}$, indicating multiple currents at different latitudes), leading to a wide range of latitude and current estimates. To screen out other non-electrojet contributions at very low current strengths, electrojet detections are only accepted above a minimum threshold of 10kA (inferred AEJ current) for CHAMP and Swarm measurements, consistent with Vennerstrom and Moretto (2013). A given detection alone does not represent the full complexity of the electrojet but the method is sufficient to indicate the activity statistically under different conditions when large numbers of detections are considered.

5.4 Application to Swarm, CHAMP, Magsat, and POGO

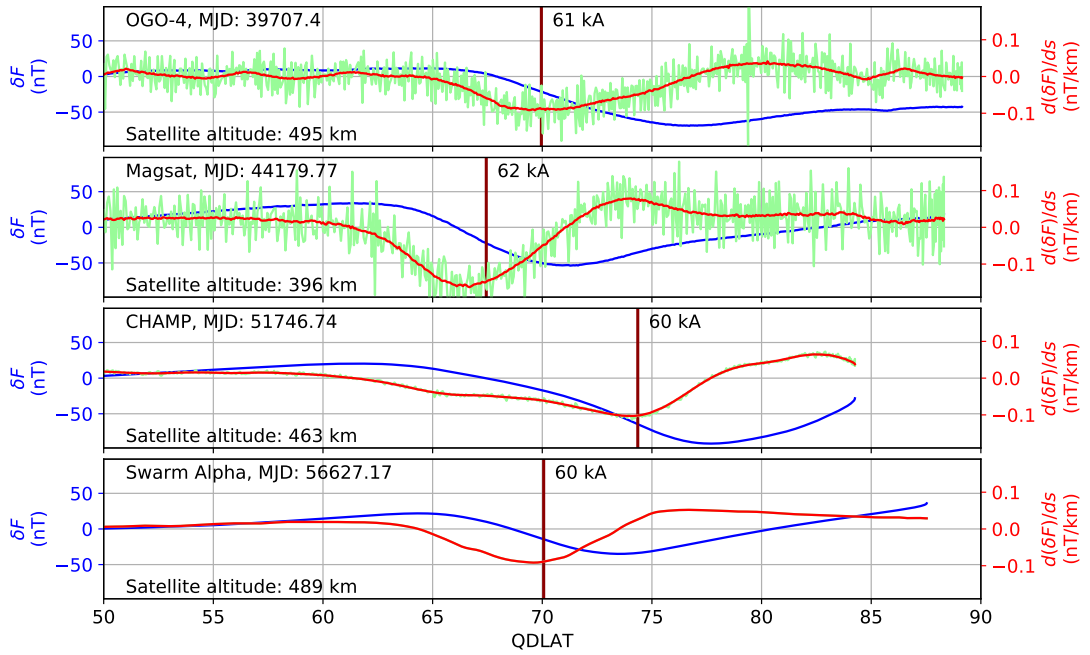

Figure 5.2: Examples of detections from OGO-4, Magsat, CHAMP, and Swarm Alpha. The blue line shows δF, the measured scalar field residual to the internal field model. The green line shows $\frac{d\delta F}{ds}$ and the red line shows it smoothed, except for Swarm where smoothing is not applied. The vertical line marks the determined electrojet latitude and the estimated current strength is indicated.

The method has been applied successfully to data from Swarm, CHAMP, Magsat, and POGO. Examples of detections are shown in Figure 5.2 for one pass from each satellite missions. In each case I show an ascending pass over the Northern Hemisphere, from 50° quasi-dipole latitude (QDLAT) towards the pole. Smoothing is applied to

$\frac{d\delta F}{ds}$ as described in the following section. As already mentioned, the peak in $\frac{d\delta F}{ds}$ may be negative or positive depending on the direction of the current. For the analysis presented here, I do not distinguish between Eastward and Westward currents and only use the current magnitude. Vennerstrom and Moretto (2013) demonstrated that this electrojet estimate tracks well over consecutive orbits, showing latitudinal expansion and contraction patterns associated with strengthening and weakening current strength during geomagnetic activity, and a good correlation with the AE index.

The data are segregated into passes over the Northern and Southern auroral regions, $> |50°|$ QDLAT, and further into the ascending and descending phases (toward and away from the pole), and so up to four electrojet signals can be detected on each orbit, as shown in Figure 5.3. A problem arises due to the offset of the geographic axis (the orbital convergence region) from the magnetic poles (the centre of the auroral oval) and the polar gap in coverage, leading to incomplete and biased sampling of the electrojets. To help preserve the true oval shape within the collected detections (see Figure 5.4), a criterion is employed that essentially excludes the region between the geographic and magnetic poles, that is the polar passes are split (into the ascending and descending phases) such that I exclude the section of the polar pass between the orbit's maxima in geographic (GLAT) and magnetic latitudes (QDLAT). The ascending phase begins at 50° MLAT and ends at the maximum of GLAT or MLAT, whichever the satellite arrives at first. The descending phase begins where both GLAT and MLAT are decreasing again and ends at 50° MLAT.

To adequately sample the AEJs, low-altitude ($\lesssim$600 km) polar-orbiting magnetic satellite data are required. This requirement is satisfied by the POGO missions, OGO-2, 4, and 6 (over parts of their orbits), Magsat, CHAMP, and Swarm. OGO-2 operated from October 1965 to September 1967 at 413-1510 km altitude, OGO-4 from July 1967 to January 1969 at 412-908 km, and OGO-6 from June 1969 to July 1971 at 397-1098 km, each providing data at all local times. For POGO data, I use only those when the satellites are below 600 km. OGO-2 is in a more elliptical orbit so only contributes a relatively small amount of useful data. Magsat operated from November 1979 to May 1980 in a dawn/dusk orbit at 325-550 km, CHAMP from July 2000 to September 2010 at 454-270 km altitude. Swarm launched in November 2013 and is a trio of satellites: after the three-month commissioning phase Alpha and Charlie flew side-by-side at ∼450 km altitude, and Bravo at ∼530 km; they have increasing local time separation. I therefore

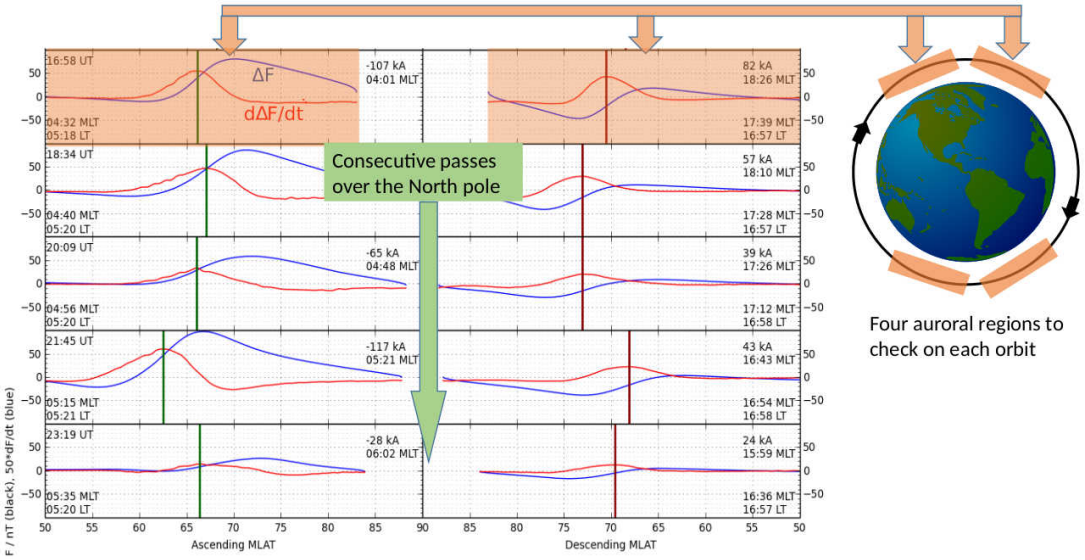

Figure 5.3: Example demonstrating how four segments are extracted from each orbit. The Northern Hemisphere segments are shown over five consecutive Swarm Alpha orbits, showing the AEJ signal in two local time sectors, around 05:00 (left) and 17:00 (right).

use data from Alpha and Bravo (since Charlie detects the same electrojet signal as Alpha with my method) up until the end of 2014 to match the end point of the internal field model used.

In each case, I use 1 Hz scalar datasets where available, or resample the original data to 1 Hz. I then apply a smoothing using a running average over a window of 30 seconds to filter out high frequency noise, except in the case of Swarm where the data are of high enough quality that this is not necessary. CHAMP data are from the Level 3 reprocessed set and Swarm data are from version 0408 of the Level1b MAGx_LR set.

To isolate the ionospheric field from the measured magnetic field, the contribution from the core and the crust is subtracted using a consistent field model for each date period studied. For this I use a combination of the COV-OBSx1 core field model (Gillet et al., 2015) up to degree 14 (which spans years 1940.0 to 2015.0) and a static contribution from degrees 15-110 of CHAOS-6 (Finlay et al., 2016) respectively.

Values for the AE and Kp indices and the IMF conditions are drawn from the hour-averaged and minute NASA OMNI 2 databases which draw data together from a number of sources, with solar wind conditions time-shifted to the magnetosphere bow shock. The SuperMAG auroral electrojet index (SME) was obtained on 18 April 2017 and is produced from many ground stations (Gjerloev, 2012).

I also make use of the quasi-dipole (QD) coordinate system which is the most appro-

priate for organising data representing ionospheric currents (Laundal and Richmond, 2017). I refer to QD latitude as QDLAT and magnetic local time (calculated from QD longitude and the subsolar point) as MLT. To calculate QD coordinates I use a Python library, apexpy, based on Emmert et al. (2010).

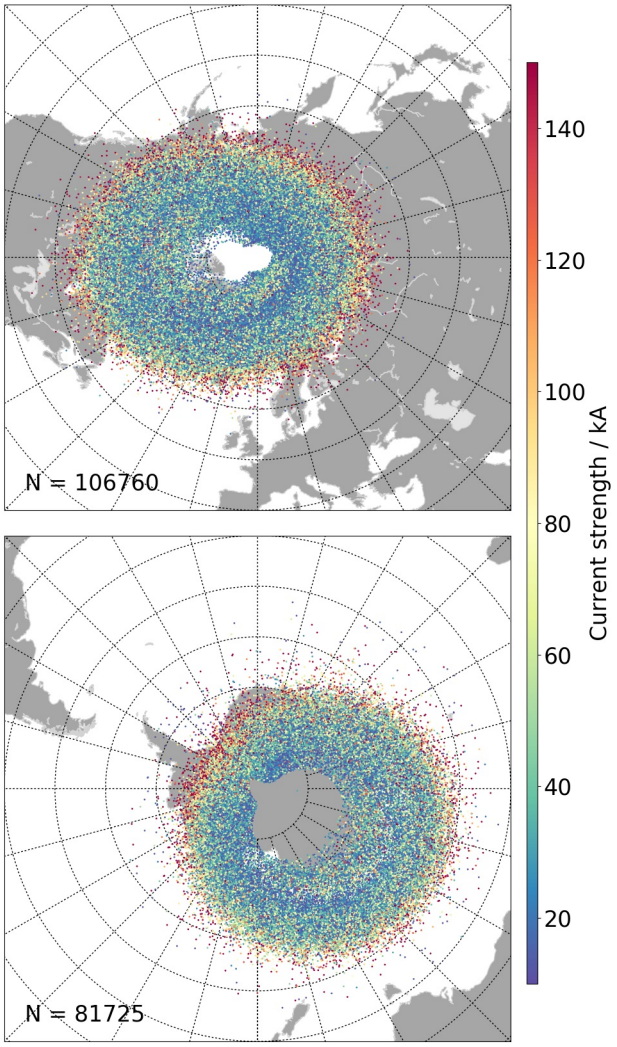

Figure 5.4: All detections collected from the CHAMP and Swarm-2014 data, coloured by inferred current strength. The upper plot is for the Northern and the lower for the Southern Hemisphere; the graticule is segmented by 10° in geographic latitude and 15° in longitude. The total number of detections, N, is indicated.

Figure 5.4 shows the collection of all detections from CHAMP and Swarm Alpha and Bravo together (using just the data from 2014 for compatibility with the COVOBS model). Familiar features can already be seen. The auroral ovals are centred around the magnetic poles, with a more elliptical form in the Northern Hemisphere following the

horizontal intensity contours of the main magnetic field. Lower latitude signals tend to have stronger current strengths, and a higher latitude inner ring can be seen separate from the main oval which corresponds to detections on the dayside due to cusp currents. I initially used only a core field model subtraction but in that case I observed clustering of detections around known crustal magnetic features, motivating the inclusion of a high degree crustal field model which resolved this issue. There still may be small issues of crustal field contamination, particularly in the South where the crustal field is less well known, but the results are not strongly dependent on the particular core and crustal field models chosen.

Orbital effects produce uneven sampling. Orbital convergence produces a higher density of detections close to the poles. The offset of the magnetic poles from the geographic poles produces a longitudinal bias in the number of detections, which is not significant in the North but is in the South due to the greater offset. However, the effect of the longitudinal bias is reduced when I consider activity as a function of MLT. The greater offset in the South also leads to a greater loss of detections over the polar gap. This contributes to a lower number of detections overall in the South and a bias towards lower latitudes (which would typically be of higher current strength). The lower number of detections could also be partly due to hemispheric asymmetries in the current strengths and fewer detections due to the current detection threshold (i.e. very small currents are ignored). These issues make it difficult to directly compare the average current strengths and positions between hemispheres, but comparisons between different MLT sectors in the same hemisphere are not strongly affected.

5.5 Response to IMF direction and season

Figures 5.5 and 5.6 show the response of the AEJs as a function of MLT, separately for each hemisphere for different IMF directions and different seasons, for CHAMP and Swarm-2014 data. I use the hour-averaged IMF direction at the time of each detection, with direction split into four quadrants according to the sign of B_z and B_y. I denote $B_z > 0$ as B_z^+, $B_z < 0$ as B_z^-, and similarly for B_y. The detections are collected in bins of 1 hour MLT and for each MLT sector, the mean and standard deviation of QDLAT are indicated by the oval position and half width, and the mean current strength is indicated by the colour. Well-known features are produced: stronger substorm- and convection-

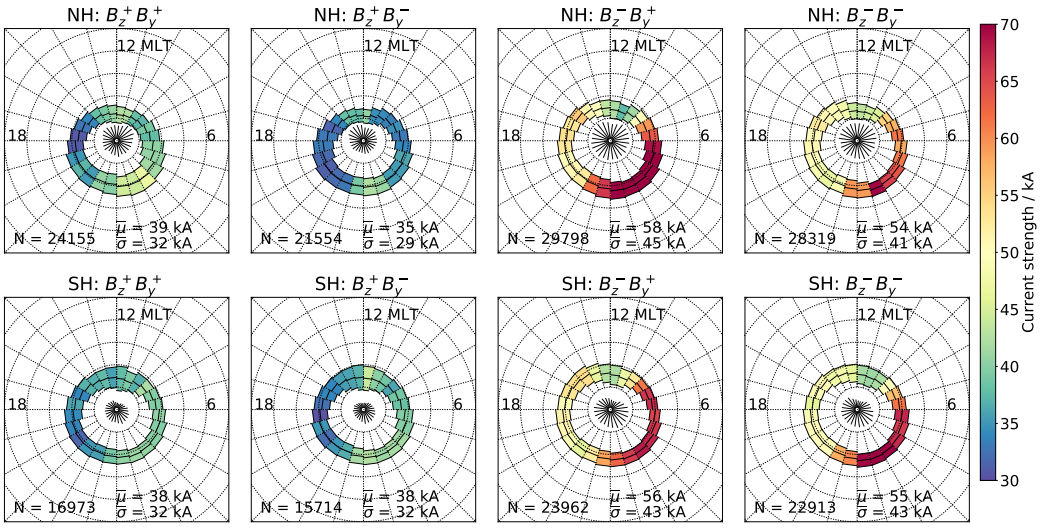

Figure 5.5: Collected detections from CHAMP and Swarm-2014 data in bins of 1 hour MLT. The latitudinal position and half width of each bin mark the mean and standard deviation of QDLAT, and the colour indicates the mean current strength. Data are split by hemisphere and by IMF direction. NH: Northern Hemisphere, SH: Southern Hemisphere, $B_z^{+/-}$: $B_z > 0$ / $B_z < 0$ etc. The mean current strength, $\overline{\mu}$, and mean of the standard deviations of current strengths in each bin, $\overline{\sigma}$, are indicated. The graticule is spaced by 10° in QDLAT. The numbers of detections in each bin are indicated by the lengths of the lines in the centre, and are between 766 and 1371 in the NH, and 383 and 1302 in the SH.

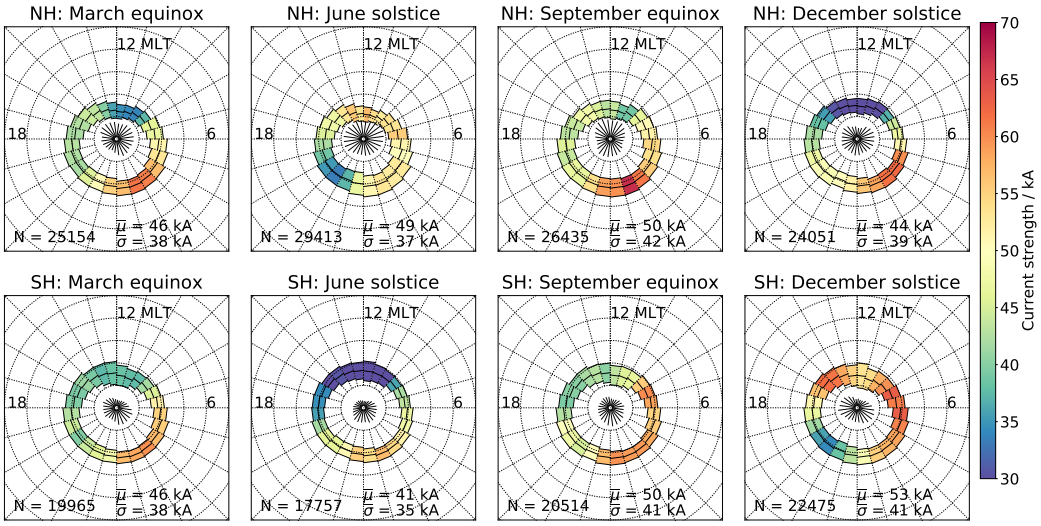

Figure 5.6: As for Figure 5.5, but data are instead split according to season. Each season selection is composed from data taken 45 days each side of each solstice/equinox. The number of detections in each bin is between 755 and 1476 in the NH, and 411 and 1202 in the SH.

associated currents on the nightside; high-latitude cusp currents on the dayside; stronger response during southward IMF (B_z^-); stronger response around the equinoxes due to the Russell-McPherron effect (Russell and McPherron, 1973); stronger response dur-

ing local summer compared to winter due to increased conductivity and cusp currents (particularly on the dayside).

In Figure 5.5, all seasons are considered together so the seasonal effects are not visible. Mean dayside currents are between 35 kA and 45 kA and do not vary much between different IMF directions. The dawn currents are stronger than the dusk currents in all cases. Both dawn and dusk currents are strongly increased by southwards IMF (B_z^-), increasing from 30-45 kA (B_z^+) to 50-70 kA (B_z^-). The nightside currents are yet more strongly affected, increasing from 35-50 kA to 60-70+ kA.

There are also differences in the response to the sign of B_y. For the Northern Hemisphere during B_z^+, the dayside, dawn, and nightside currents are slightly stronger for B_y^+ than for B_y^-, with an increase of the mean current around the full oval from 35 kA to 39 kA; during B_z^-, the dawn, dusk, and nightside currents are stronger for B_y^+, with an increase of the mean current from 54 kA to 58 kA. Conversely, in the Southern Hemisphere, for B_z^+ or B_z^-, the current strengths are more similar for each sign of B_y.

In Figure 5.6, all IMF directions are considered together so we can only see the seasonal variations. The mean dayside currents are most strongly affected, varying from 30 kA in winter to 55 kA in summer, for both hemispheres. The peak in current strength during local summer is around 12 MLT for the Northern Hemisphere. For the Southern Hemisphere, however, there are two peaks, one in the afternoon sector and one around dawn, where the mean current strength increases to 60 kA. This gives rise to a larger overall mean current strength of 53 kA in the Southern summer compared to 49 kA in the Northern summer. As in Figure 5.5, dawn currents are stronger than dusk currents, and are not so strongly affected by season as the dayside currents. Outside of local summer, similar nightside current strengths are observed which are slightly stronger than during summer, and slightly stronger for the Northern Hemisphere than the Southern.

Figure 5.7 compares the current strengths from the full oval for each hemisphere for both varying IMF direction and season. This separates the effects of IMF direction and season, since the effect of IMF direction is expected to be season-dependent. Response to IMF is split according to the sign of B_z, and each further split according to the sign of B_y and its magnitude, $|B_y| < 3$ nT or $|B_y| > 3$ nT. Box plots show the distribution of current strengths in each bin. The number of samples in each is also indicated and ranges from 1225 to 5331, typically being lower in the SH. In all seasons, currents

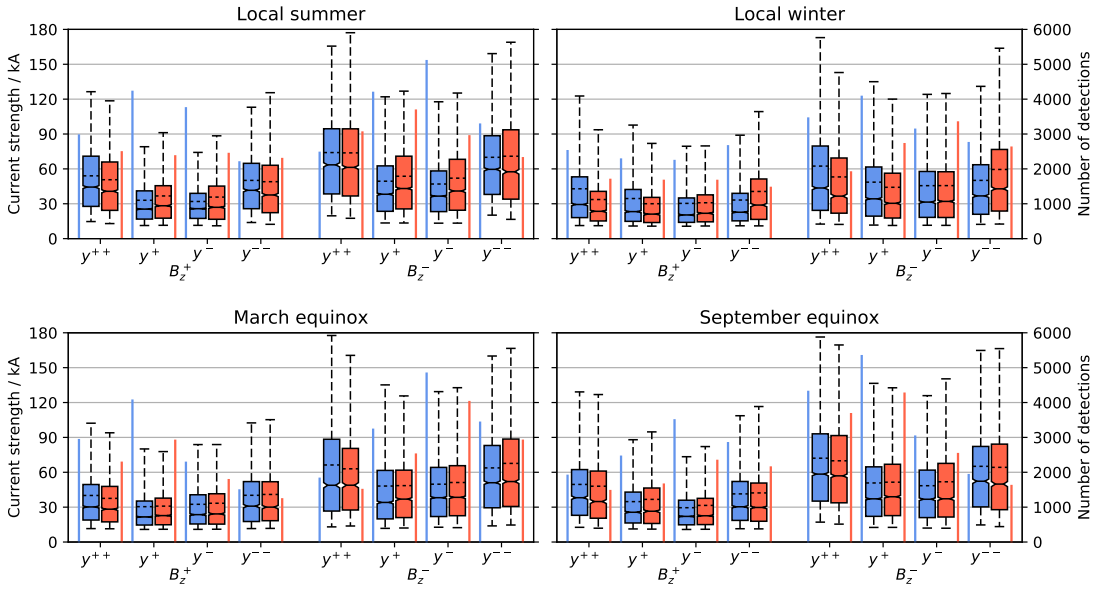

Figure 5.7: Box plots of current strengths from all detections around the full oval in MLT, from all the CHAMP and Swarm-2014 data, split according to hemisphere, season, and IMF direction. Local summer/winter means 45 days either side of the June/December solstice, depending on hemisphere. In each season, IMF conditions are split between $B_z > 0$ (indicated by B_z^+) and $B_z < 0$ (B_z^-), and further divided by $B_y > 3$nT (y^{++}), $0 < B_y < 3$nT (y^{+}), -3nT$< B_y < 0$ (y^{-}), $B_y < -3$nT (y^{--}). The Northern Hemisphere measures take blue boxes, and the Southern Hemisphere red boxes. For each box, the median current strength is indicated by the solid line with notches, the mean by the dashed line, the 25th and 75th percentiles by the boundaries of the solid box, and the 5th and 95th percentiles by the vertical whiskers. The number of detections contributing to each is indicated by the vertical line beside each box.

are stronger for $B_z < 0$, and stronger for $|B_y| > 3$nT than $|B_y| < 3$nT, indicating the increased magnetopause reconnection for southwards IMF and for IMF of greater magnitude. Current strengths in summer tend to be higher in the SH than the NH for $|B_y| < 3$nT, for both signs of B_z, but are more similar in each hemisphere for $|B_y| > 3$nT, which indicates the increased role of insolation rather than IMF driving hemispheric asymmetry during summer. In winter, increasing magnitude of B_y shows an asymmetry in the hemispheric response: currents are stronger in the NH for $B_y > 0$ than for $B_y < 0$, but stronger in the SH for $B_y < 0$ than for $B_y > 0$, for both signs of B_z, with an increasing disparity at $|B_y| > 3$nT. This effect is unclear around the equinoxes and during summer.

5.6 Response to solar cycle

Figure 5.8 shows the mean current strength and QDLAT in each hemisphere from consecutive two-year periods. By combining data from two years, MLT and seasonal

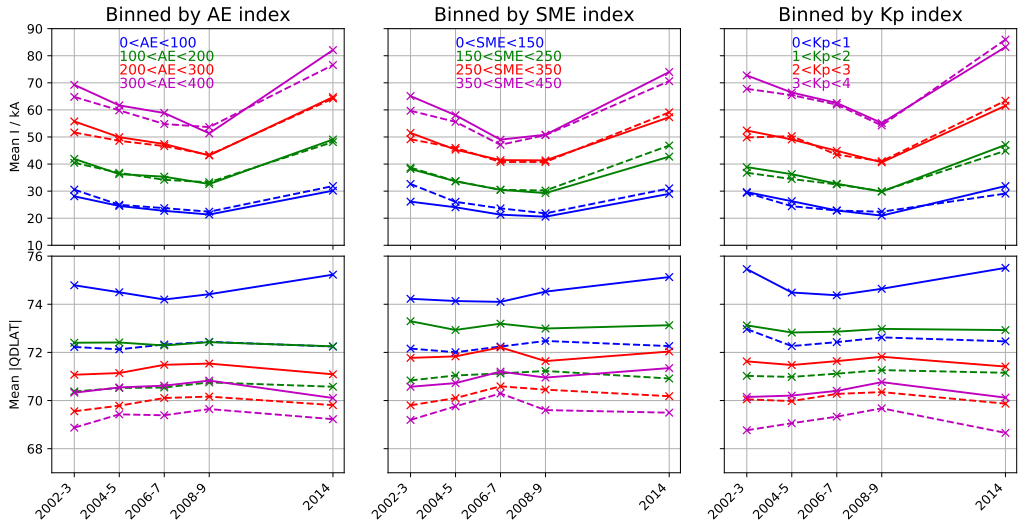

Figure 5.8: Mean current strengths for the full oval split according to the AE, SME, and Kp indices at the time of each detection, and split into consecutive two-year periods, from CHAMP, and for just 2014 from Swarm. Solid line: Northern Hemisphere, dashed line: Southern Hemisphere. The effect of the solar cycle (decreasing activity from 2002 to 2010, and increased again at 2014) is visible, even after grouping the data into similar levels of geomagnetic activity as determined by ground-based measurements.

variation are similarly sampled between each two-year period, smoothing out the effect of the variable solar wind geoeffectiveness that a particular individual year carries. Data are split according to the AE (1 minute), SME (1 minute), and Kp (3 hour) indices at the time of each detection. The mean latitudes for the Southern Hemisphere (SH) are lower than the Northern (NH) due to the bias in the detections arising from the greater polar gap. Selecting SH data from only the geographic longitude sector which is most accurately sampled ($\sim 105^\circ - 160^\circ$) reveals that this is the case, with very similar mean |QDLAT| as the NH measure (not shown here). For all three indices, there is the expected shift to higher current strengths for higher activity levels, but also a trend which corresponds to the solar cycle maximum around 2002, minimum around 2008, and increasing again at 2014. For the mean latitude, there appear to be similar but more complicated trends related to the solar cycle. In each case, for the two higher activity levels, there is a trend to higher latitudes at the solar minimum, while the trend is reversed for the lowest activity level selection. The solar cycle trend has implications for main field modelling, and also demonstrates the issue of variation associated with the solar cycle (or even longer term trends in solar activity) facing measurement of secular variation of the AEJs.

5.7 Secular variation of the auroral oval

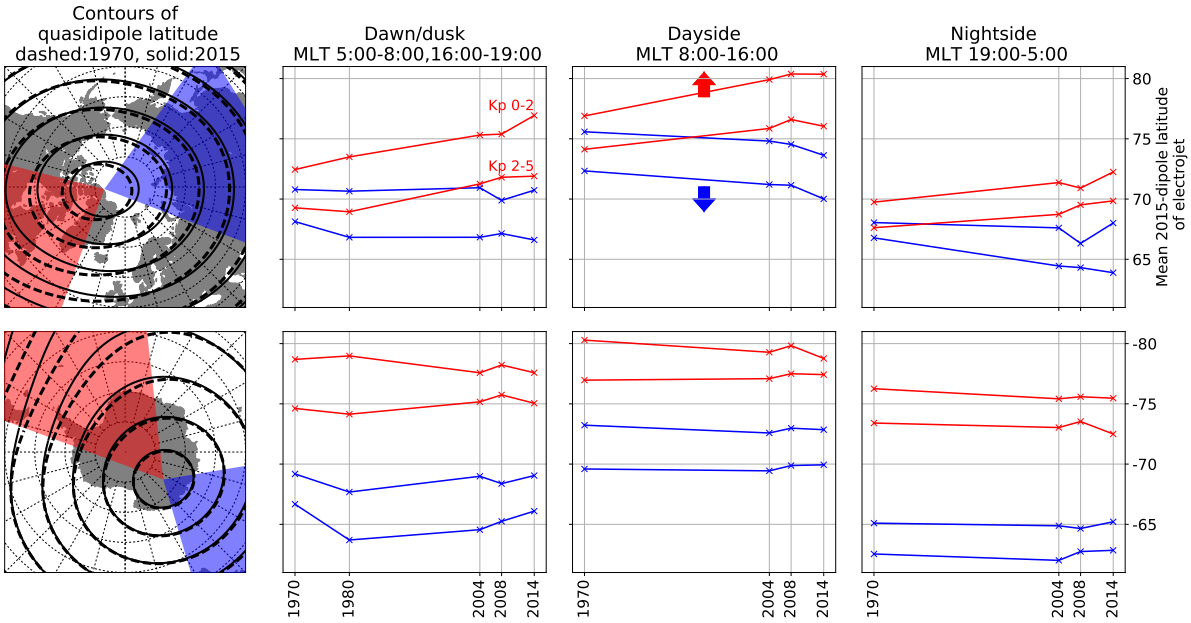

Figure 5.9: Left panels: Contours of QDLAT for 1970 and 2015 over each hemisphere, with divisions into two sectors of differing change (shifting to either higher or lower latitudes) coloured red and blue. Other panels (top for Northern Hemisphere, bottom for Southern Hemisphere): Each shows the latitudinal responses of the AEJs in different MLT sectors. Mean latitudes of all detections are compared from OGO-2, 4, 6 (combined into one period marked 1970), Magsat (marked 1980), CHAMP (split 2002-5 and 2006-9), and Swarm (2014). Data are split into the two sectors marked in the maps (the red and blue colouring of lines indicate which sector they refer to). Responses during low Kp (0-2) and high Kp (2-5) are shown. The arrows indicate the poleward shift of the AEJs in the Northern Hemisphere sector coloured red (red lines) and the equatorward shift for the sector coloured blue (blue lines).

As we have seen, there are several variations in the AEJs associated with different physical drivers: MLT and seasonal responses due to Earth's rotation and orientation (affecting both insolation-driven conductivity and solar wind-magnetosphere coupling); main field morphology and hemispheric asymmetries; responses to solar wind conditions and the solar cycle. This makes it challenging to observe long term variation in the electrojets. Such a variation would be in the form of a shift in position of the oval due to shift of the magnetic poles (and more subtle change in the morphology), and change in intensity (and latitudinal extent) due to variation both in the main field dipole strength (and so the amount of solar wind energy entry) and in long term trends in solar activity. Tsyganenko (2019) demonstrated how models predict such a change between 1965 and 2020.

In Figure 5.9 I attempt to identify variation in the electrojet position due to the

main field secular variation over the period 1970-2015. Electrojet position estimates are made from 7 satellites: collectively OGO-2,4,6 (∼1967-1971), Magsat (∼1980), CHAMP (2002-2009), and Swarm Alpha and Bravo (2014). The results derived from POGO and Magsat data, with plots analogous to Figures 5.4 to 5.6, can be found in Appendix A. I select two sectors from each pole (coloured red and blue), according to the differing main field variation in each sector as seen by the shift in contours of QDLAT, in order to compare latitudinal variation of the electrojets in each sector separately. I further split by MLT, roughly corresponding to electrojets with different origins: dawn/dusk convection, dayside cusp currents, nightside convection and substorms. Mean latitudes are compared for low and high Kp index. The reason for this separation by MLT and Kp index is to attempt to account for variation of solar wind forcing, so that remaining trends are isolated from this. For each satellite, I show the mean dipole latitudes (fixed to the 2015 dipole) of the electrojets detected in each sector.

The data points for 1970 and 1980 are both close to solar maxima, whereas the datapoints for 2004 and 2008 are for periods moving away from solar maximum (around 2000/2001), and 2014 is again solar maximum (albeit an atypically weak maximum). Due to increased activity near solar maxima, we would expect AEJs at lower latitudes at these times, which holds true more for periods during which Kp $>$ 2, as in Figure 5.8. There is not a consistent trend in the datapoints to this effect so I do not believe solar cycle effects are strongly influencing these results.

Although the earlier data are very noisy and there are many complicating factors (the highly variable nature of the AEJs, varying data quality, varying biases introduced by the satellites' orbits), expected patterns are reproduced: dayside electrojets are at higher latitudes; nightside electrojets (which include substorms) at lower latitudes; dawn/dusk electrojets at intermediary latitudes; and higher levels of the Kp index are associated with lower latitude electrojets. In the Northern Hemisphere sector coloured red we see the largest variation in QDLAT, with a shift to higher latitudes over time from 1970 to 2015. The Northern Hemisphere sector coloured blue has a slightly smaller shift, but to lower latitudes over time. Although certainly not conclusive, there are corresponding trends in the measured electrojet positions for these sectors for all three MLT sectors, while the sectors in the South are more constant.

5.8 Discussion

The results presented are consistent with the previous results of Vennerstrom and Moretto (2013): the AEJs increase in intensity and extend equatorwards with increasing geomagnetic activity, are typically stronger in the dawn sector with a weaker peak in the afternoon sector, and are stronger on the dayside during local summer. However, with the application to more data and separation by hemisphere, I have shown that there are subtle asymmetries in the way in which the AEJs in each hemisphere respond to solar wind and seasonal drivers, as well as the longer term asymmetry associated with core field change which is hidden by the use of QD coordinates.

The seasonal changes in the MLT patterns compare favourably with recent studies of the FACs (e.g. Laundal et al., 2016a), driven by the variations in sunlight and particle precipitation. In winter, currents are stronger on the nightside and weaker on the dayside; in summer the dayside currents are stronger. The dusk sector has stronger currents in the winter than the summer, which is consistent with stronger/weaker FACs here measured by Laundal et al. (2016a), who attribute this to suppression of auroral precipitation in sunlight (Newell et al., 2010). The same effect should also cause stronger dawn currents in summer. However, I find stronger dawn currents in the winter for the NH in the range 0-6 MLT, while in the SH dawn currents are stronger in winter for 0-2 MLT but stronger in summer for 2-6 MLT. This may be due to increased effect of the substorm current in my measure, which is most noticeable during winter and the equinoxes, while the SH may be more insolation-driven in the summer than the NH is.

Laundal et al. (2016a) also measured the horizontal equivalent currents, finding that the overall summer-time currents are stronger in the South than in the North (during conditions of $B_z < -1\text{nT}$) by 6% and that this is reversed in winter with stronger currents in the North than the South by 16%. I find the same asymmetry, with hemispheric differences of 8% and 7% in summer and winter respectively. Differences in the values determined by each study arise because the measures are very different: measurements of the full current distribution over the whole polar region, versus an average of the individual AEJ estimates made at different positions and times. This is in contrast with studies using the AMPERE dataset (e.g. Coxon et al., 2016) in which the summer FACs are significantly stronger for the Northern Hemisphere. This may be due to poorer AMPERE data quality since it is derived from magnetometers of much

lower sensitivity.

The disparity between mean current strengths in summer compared to winter is greater in the SH than in the NH (29% summer/winter difference in the SH compared to 11% in the NH), with a different MLT pattern in intensity, and not strongly related to IMF direction. I suggest that this may be a result of the different insolation pattern over the Southern oval due to the increased geographic offset of the Southern magnetic pole. The Southern oval experiences longer periods with more sunlight than the Northern, but also periods with less sunlight (but these are shorter than the periods with more sunlight). There is also an increase in insolation around January due to perihelion, which is also a driver for stronger Southern summer currents. However, there is a systematic bias towards stronger current strength measurements in the South due to the loss of higher latitude detections (which are typically weaker) due to the polar gap in satellite coverage. Conversely, there is potentially a greater underestimation of the true current strength from each satellite pass in the South than the North because there is a greater deviation of the QDLAT contours from the perpendicular to the satellite track along which the model line current flows. Despite these issues, the comparison of current strengths between different conditions for the same hemisphere is quite robust due to the large number of detections considered in each case, and because the conditions are unrelated to the sampling by the satellites.

I have been able to show seasonal tendencies because there is sufficient sampling from ∼10 years of data which averages out contributions from the solar wind variation between individual seasons. The seasonal variations are further complicated by hemispheric differences in the reaction to solar wind conditions (and indeed in tendencies of the IMF toward particular orientations). I have explored the seasonal response, in each hemisphere, to the signs of the IMF B_z and B_y components. The observed increase in current strength for $B_y > 0$ in the Northern Hemisphere winter agrees with previous results from ground-based studies (Friis-Christensen and Wilhjelm, 1975; Friis-Christensen et al., 2017; Laundal et al., 2016b). The asymmetric B_y response between hemispheres is likely to be associated, on the dayside and dawn/dusk, with modification of the polar convection cells (Tenfjord et al., 2015) and, on the nightside, to twisting of the magnetotail (Østgaard et al., 2016).

The solar cycle's appearance within the AEJs, even after grouping by similar levels of geomagnetic activity, demonstrates an issue in main field modelling: although geo-

magnetic activity may have been "accounted for" by index-based data selection, there are likely still solar-cycle trends in external-field noise within data used for modelling. This is confounded by the fact that more data will be used at solar minimum because there are more periods of low activity. The solar-cycle trend appears in the satellite data when contrasting with the ground data (in the case presented, with the AE, SME, and Kp indices), indicating that satellite data contain trends not seen in ground data. I therefore suggest that the geomagnetic index based data selection used in internal field modelling (Kauristie et al., 2017) may be enhanced by the use of a satellite-based index when selecting satellite data. The appearance of these trends in the along-track gradient in polar regions is particularly pertinent as it represents one of the largest noise sources in internal field modelling (Olsen and Stolle, 2017).

5.8.1 Application to space weather hazards

The climatological behaviour which I have shown is relevant to the development of improved geomagnetic activity indices monitoring the AEJs. The underlying quiet-time trends in activity, whether through seasonal or solar cycle drivers, need to be accounted for. For a satellite-based activity index, these trends should be removed in order to be comparable to the existing ground-based indices which remove these trends by the monthly changing baseline. I have identified some of these trends but further work is needed to properly quantify them. Such an index would be useful in conjunction with the ground-based indices and could be deployed in near real time, subject to data down-linking constraints, for space weather monitoring purposes.

The trends in the AEJ response to solar wind conditions, together with the seasonal and longer term variations, will influence GICs and atmospheric heating. To assess this influence, an empirical model of the AEJs would be useful which necessarily must include these trends and a more realistic current distribution than that presented here. By including these effects (long term behaviour and interhemispheric differences not visible in the traditional activity indices) better understanding may be reached about the cumulative effect that they have. For example, cumulative atmospheric heating influences satellite lifetime through increasing drag, and the real baseline will affect real-time predictions of drag. Likewise, GICs influence the lifetime of pipelines through increased corrosion.

The location and intensity of the AEJs indicate levels of radiation entering the

ionospheric polar cap. With the increase in the number of polar flights, radiation effects on personnel and passengers need to be better quantified. High latitude directional drilling is also affected by the AEJs due to reliance on magnetic navigation systems. Both of these could benefit from better baseline data of the AEJs.

I investigated the effect of IMF clock angle (B_z and B_y), as the largest driver of change, but not other solar wind parameters. To more fully parameterise the driving of the AEJs, time-of-year and solar wind coupling functions could be used along with appropriate MLT-dependent time averaging to account for the solar wind time history and the different magnetospheric unloading processes. The ongoing Swarm mission will be invaluable in providing data for this purpose.

5.9 Summary

By tracking peaks in the along-track field intensity gradient over each auroral region satellite pass, after subtracting an internal field model, I have obtained practical estimates of the AEJ strength and location and have demonstrated the utility of this approach for studying their behaviour in response to a number of drivers. I have used it to show broadly the response of the system to drivers from IMF direction and season, within the context of hemispherical differences due to the core field asymmetry, using the high quality data provided by CHAMP and Swarm (with reasonable results obtainable from Swarm data without smoothing).

I found that, during local winter, AEJ currents are on average stronger in the Northern Hemisphere than the Southern Hemisphere for IMF $B_y > 0$ and stronger in the Southern Hemisphere for $B_y < 0$. This asymmetry tends to disappear during summer, and instead I see stronger average currents in the South regardless of IMF direction. I attribute this partly to the increased role of insolation during summer and the different Southern auroral oval insolation pattern due to the greater Southern geomagnetic pole offset. I have also compared results with older satellites, POGO and Magsat, to show the AEJ response to secular variation of the core field and validity of QD coordinates for controlling the morphology the AEJs.

I highlighted the issue of separating the ionospheric field from the core and crustal fields, finding that it was essential to remove the crustal field to obtain results that are not obviously contaminated by crustal field signals. This is indicative of the mutual

contamination of magnetic field measurements from the crust and from the ionosphere, which often have similar magnitudes and scale lengths when measured from LEO satellites. I also demonstrated some of the solar cycle related trends that presumably contaminate internal field models of the secular variation in as yet unknown ways, and that should be considered for the development of AEJ activity indices or models.

Chapter 6

Creating a lithospheric field model

The previous chapter showed that there are many patterns within the behaviour of the auroral electrojets (AEJs). It is difficult to attribute any particular observed behaviour to a particular driver because there are many interacting processes. This presents a challenge both for understanding the full system, and how best to account for it when attempting to use AEJ-affected data for other purposes, where the AEJ "signal" is considered "noise".

In this chapter, I use Swarm data to derive a lithospheric field model. I will show how this process uses stringent data selection to reduce the effect of the highly variable external field, models to remove other "known" fields, and a careful inspection of remaining data to avoid biases due to other signals which have not been accounted for. The appearance of AEJs and FACs within candidate data used to construct lithospheric models will be made clear using a new technique I developed which stacks the signals spatially. The motivation for this technique is firstly to provide a convenient way to visualise the data, and secondly as a simple way to produce an effective model. It will be elaborated on in the following chapter to further remove the effect of the AEJs.

The chapter proceeds first with an overall description of how to build a lithospheric model, then an exploration of correcting data using various models of the core, magnetosphere, and ionosphere. This is followed by an explanation of my new technique and how this is applied to data. Finally this is used to derive a spherical harmonic lithospheric model, as well as a novel application to the (quasi) radial gradient of the measured field.

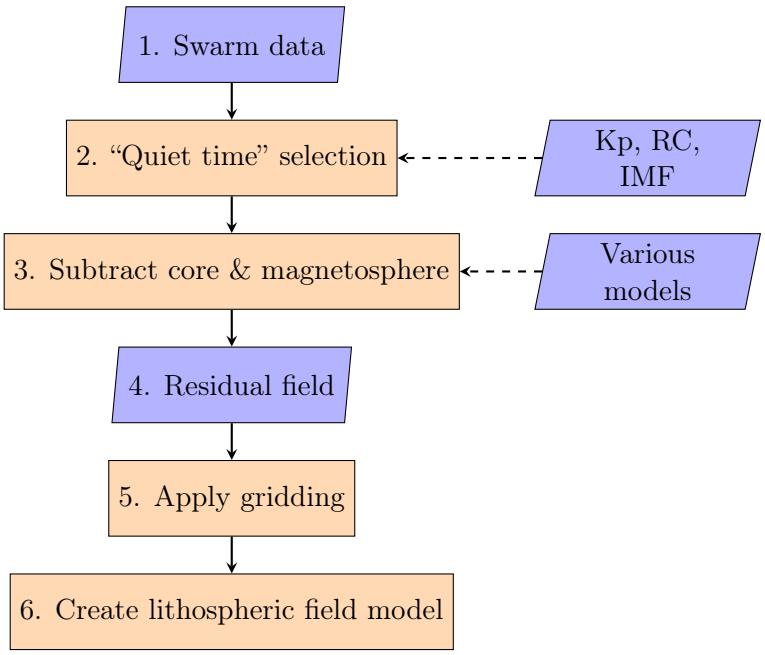

Figure 6.1: Flow chart showing the overall procedure used to reduce Swarm data to create a lithospheric field model

6.1 Overview of creating a lithospheric field model

The general process through which I extract a lithospheric field model from Swarm data is outlined here. Details of each step are expanded upon in later sections. Figure 6.1 shows the steps in the procedure:

1. Swarm data: This is the Level 1b 1Hz VFM time series of the vector magnetic field components, X, Y, Z (in the NEC frame), and ASM magnetic field intensity, F.
2. "Quiet time" selection: The data are decimated to retain only those during geomagnetically quiet times (Kp$\leq$3, $|\frac{d(RC)}{dt}|$ <3nT/hr, IMF-Bz>0, using a 20-minute time average of IMF) and in darkness (the solar zenith angle is greater than 100°). The data are now less noisy and describe the "quiet" state of the magnetic field, with less contamination by the rapidly changing parts of the field.
3. Subtract core & magnetosphere: The smoothly varying strongest component (from the core) and the large-scale magnetospheric component are subtracted using existing models, which are relatively well-determined.
4. Residual field: The remaining data now contain signals predominantly from the lithosphere but also from several sources which may be thought of as "noise". In order of decreasing contribution, these are:

(a) "Quiet-time" ionospheric field:

i. Along the auroral oval and outside the polar cap:

A. Continual (convective) direct driving by the solar wind / IMF

B. Sporadic substorms by a lagged effect of solar wind / IMF through magnetospheric loading/unloading

ii. Inside the polar cap: Direct driving by the IMF through the field lines open to the solar wind

(b) Internal field:

i. Remaining contamination from the core field

ii. Long time scale induced fields from the unmodelled long term trends in external fields (long wavelength, long duration, and deep), from tides and from the ring current

iii. Induced counterparts of sporadic auroral activity (short duration and shallow)

5. Apply gridding procedure to reduce the data to an equal-area grid. This is the novel part of the procedure.
6. Create lithospheric field model: A spherical harmonic model is fitted to the data.

6.2 Removing the non-lithospheric contributions

6.2.1 Data residuals to the Swarm Comprehensive Inversion products

In this section I explore the usage of different field models (and combinations thereof) for isolating the lithospheric field. In general we can isolate the contribution of a particular component of the total geomagnetic field to the magnetic measurements by subtracting models of the other components. That is, we obtain the data-model residual, which contains the desired field contribution plus noise/contamination associated mainly with the accuracy/completeness of the model(s) used.

There are many options of field models to use. First I investigate the usage of the series from the comprehensive inversion (CI) Swarm product line (Sabaka et al., 2018), i.e. `Mx_SHA_2C` where `Mx` = (`MCO`, `MMA`, `MIO`, `MLI`) for the core, magnetospheric, ionospheric, and lithospheric components respectively, as listed in section 4.3. The vector residuals from a single pass from South pole to North pole are shown as a function of QD latitude in Figure 6.2, for combinations of the models. The first line shows the residual

to the core field model (MCO), the second line the residual to core field plus magnetospheric field (MCO+MMA) and so on, adding the ionospheric (MCO+MMA+MIO), and lithospheric (MCO+MMA+MIO+MLI) fields. I include here the lithospheric field as an ultimate goal would be to produce a combination of models to which the data residuals fall to zero if we were able to eliminate all contamination. It also demonstrates that the lithospheric field is typically much smaller than the other fields we are aiming to remove, as it is not visible at this scale. The actual model values are shown in Figure 6.3.

Once the main field has been subtracted from the data, it becomes very clear that the largest residuals are around the poles, in the auroral oval. The signal from the magnetospheric Southwards-pointing dipole field is visible as a decrease in X around the equator and a decrease/increase in Z in the Southern/Northern hemisphere (i.e. a hemispheric bias). Much of this strong signal is removed by subtracting the MMA model.

Subtracting the MIO model appears to reduce the effect of an Sq-like disturbance at mid-latitudes in the Z component, but its effectiveness on different passes is likely not always beneficial. This is because of the nature of the model as an averaged large-scale response which does not necessarily provide a good match to any particular orbit. It is also less accurate in the dark-side region we are interested in due to the difficulty in fitting the much smaller scale dark-side field compared to the day-side. It is also not at all accurate at high latitudes as the model is set up to reproduce the mid-latitude field, and the high latitude field originates from different physical systems. For these reasons, Thébault et al. (2017) do not include the MIO model (from either the dedicated or comprehensive chain) in their analysis of the lithospheric field and prefer instead to apply dedicated corrections to account for the ionospheric field. In contrast, Barrois et al. (2018) do include an ionospheric field model correction (from CM4) when defining their Virtual Observatories for core field studies, which they reason is a necessary though imperfect procedure in the absence of any other type of correction for these fields.

In Figures 6.4 & 6.5, the residuals and model values for one day are shown, i.e. $\sim$ 15 orbits, along with their mean and interquartile range (IQR). The same patterns described above are also visible, indicating that these are persistent features. The wide spread in residuals at high latitudes shows how variable they are from one pass to the next, and is suggestive of the complexity of modelling the field here. By including

MMA, a large reduction in the spread of residuals is achieved in the X component. This is because the ring current changed significantly during this day and MMA is able to accurately account for its change.

In Figure 6.6, the residuals are collected from one year (2016), filtered for geomagnetically quiet times (Kp $\leq$ 3), and the mean and spread shown as before. This is shown separately for data taken during sunlight and during darkness. This shows that during darkness a smaller spread is achieved and the mean is closer to zero, and using a full year of data should help to average out seasonal effects. The Z residual is less strongly contaminated than the X and Y residuals. If we describe the magnetic effect of the auroral oval as the combination of the magnetic fields produced from the FACs (i.e. close to vertical), the electrojets (horizontal, mostly East/West), then we can posit that the FACs more strongly contaminate the Y component and the electrojets the X and Z components. Because of the greater relative rotation of the geomagnetic and geographic frames near the poles, the X component is also contaminated by the FACs similar to the Y component. The Z component is thus the one with the smallest residuals, resulting mainly from the electrojets and not the FACs. This is less true further away from the poles, where the field lines are less radial, but here the effect of the FACs is lesser since they are concentrated in the auroral oval (more so during quiet times). After electrojets, the Z component is also contaminated by weaker cross-cap currents.

The residuals achievable are lower during darkness at mid latitudes because the ionosphere has weaker electric currents flowing and is more stable than under insolation, while the residuals are always large around the poles because of the complex auroral activity. Subtracting the MIO model is able to correct much of the disturbance due to the Sq system during sunlight, with just a small localised disturbance due to the equatorial electrojet remaining. Figure 6.7 shows that subtracting the MIO model tends to over-correct the ionospheric effect at mid latitudes during darkness.

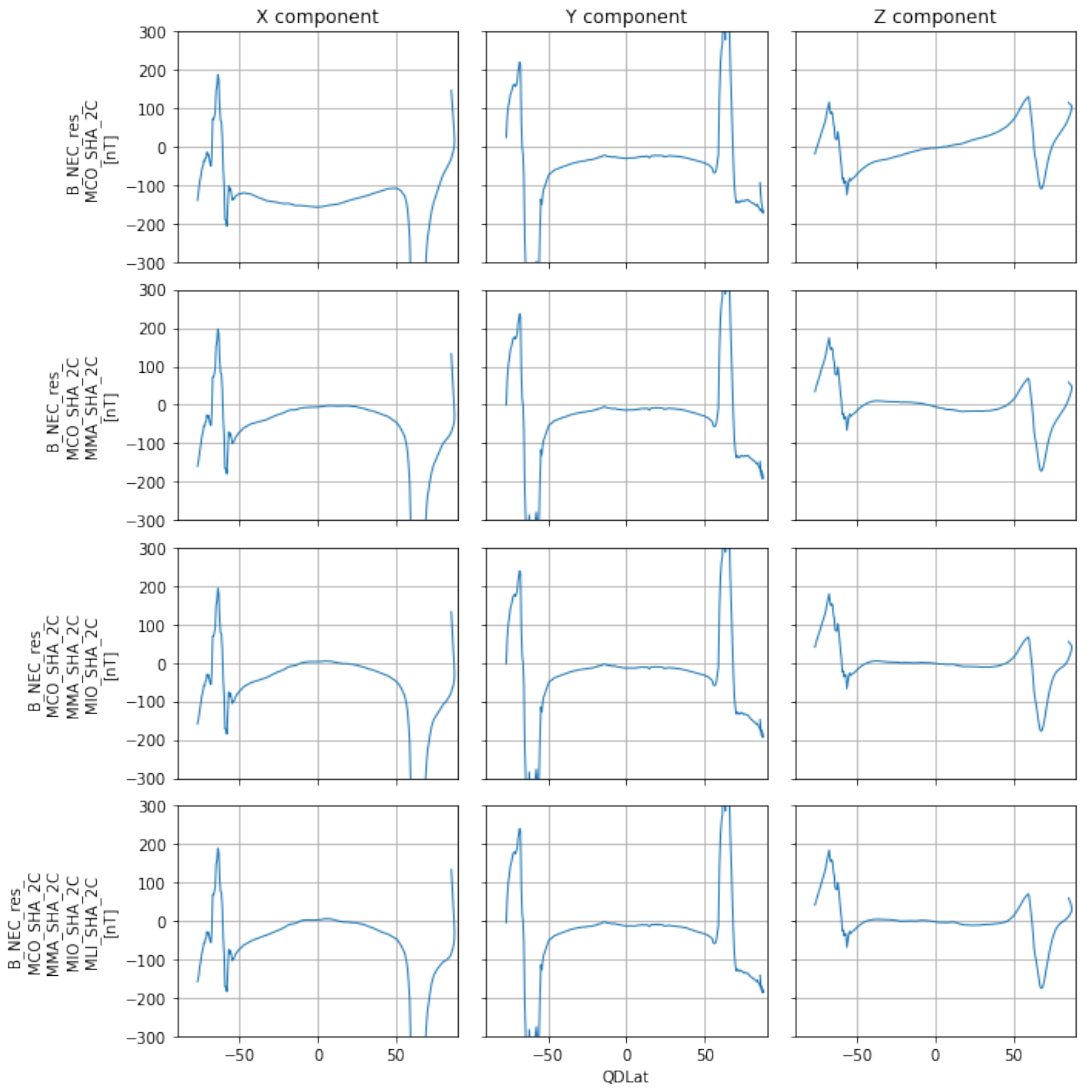

Figure 6.2: Vector residuals to combinations of the Comprehensive Inversion Swarm models (`Mx_SHA_2C`), for half an orbit. Recall that (X, Y, Z) refer to (North, East, Centre) components (Section 3.5).

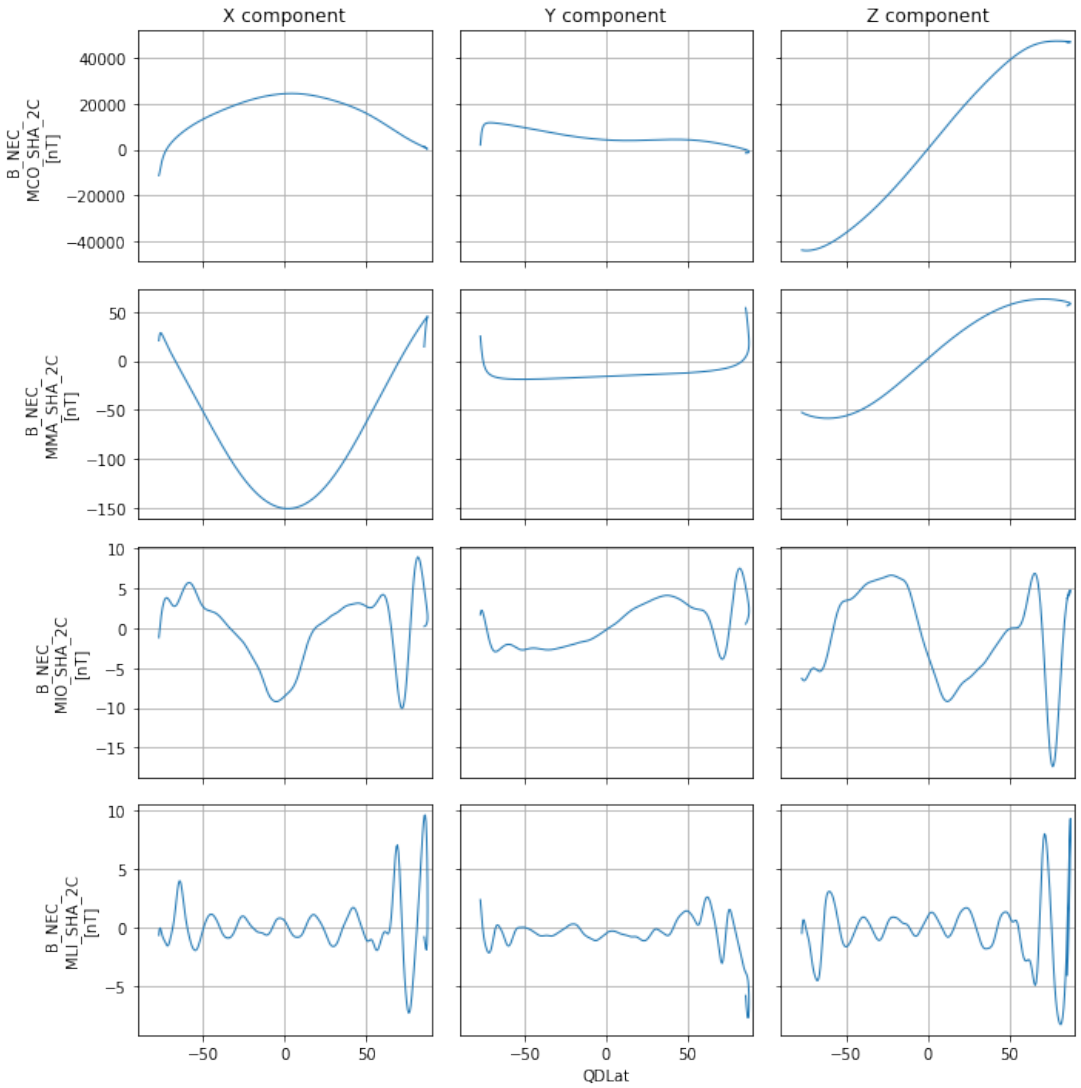

Figure 6.3: The model values from the same pass as Figure 6.2

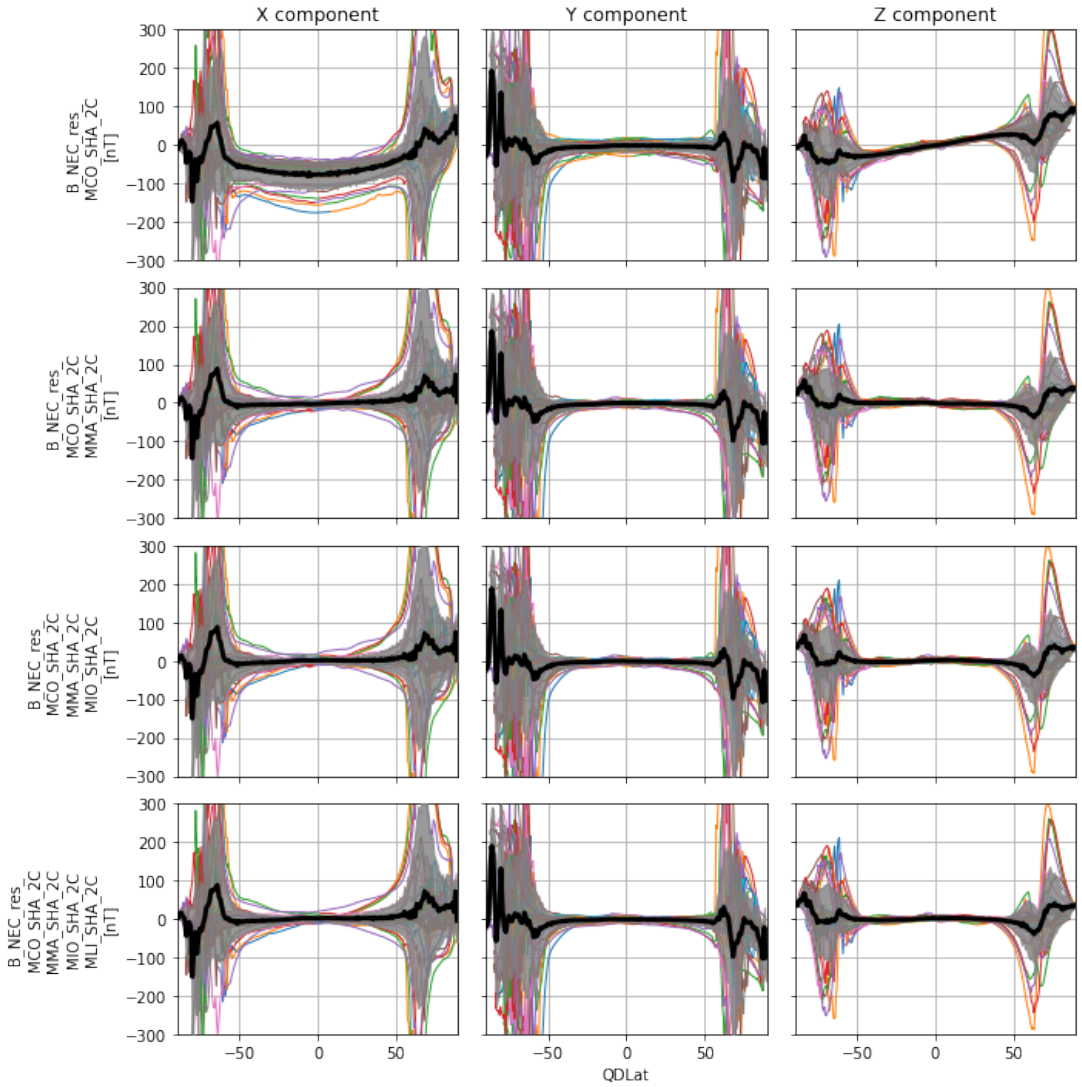

Figure 6.4: Vector residuals to combinations of the Comprehensive Inversion Swarm models, for orbits from one day. The mean is shown in black, and the IQR is shown in grey.

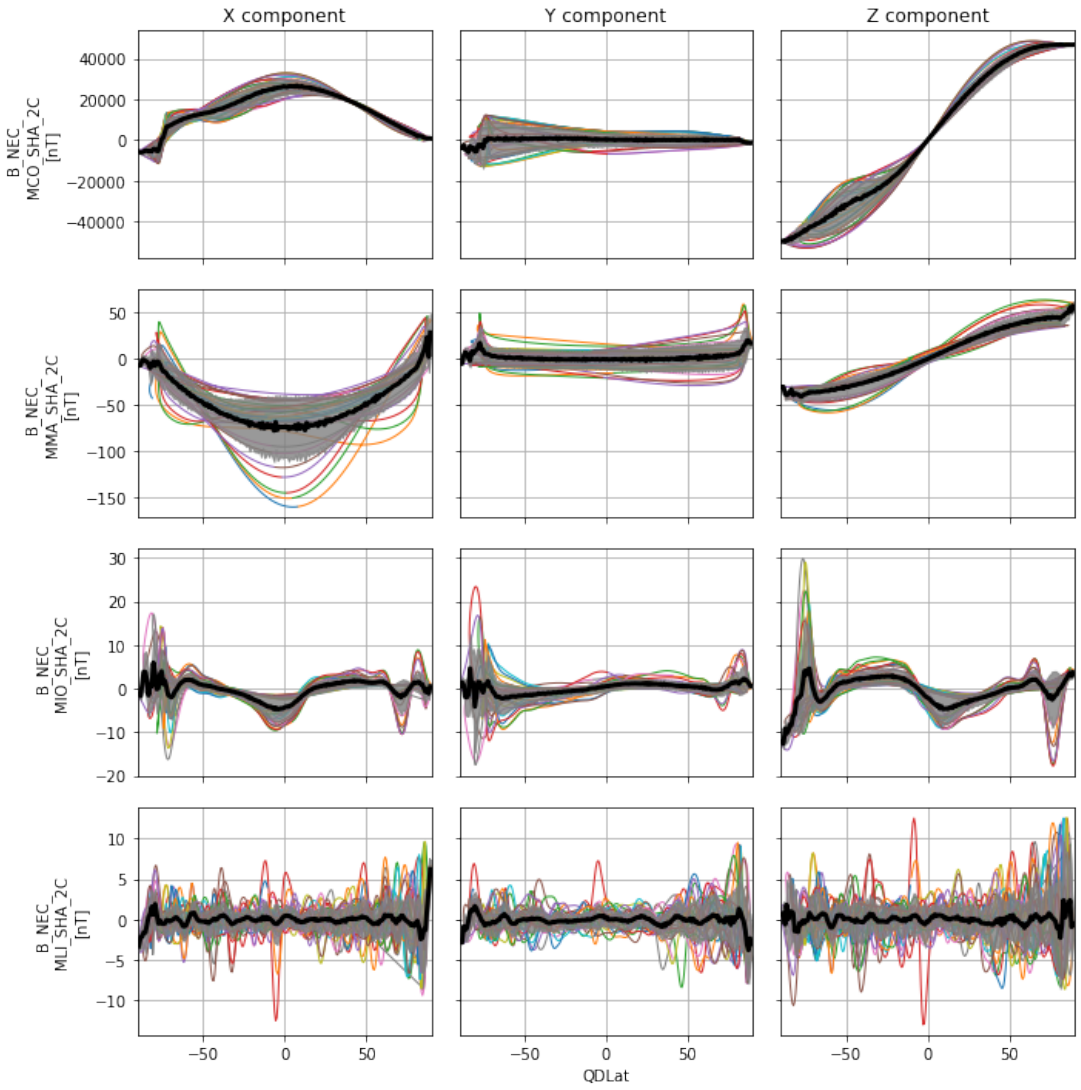

Figure 6.5: The model values from the same day as Figure 6.4

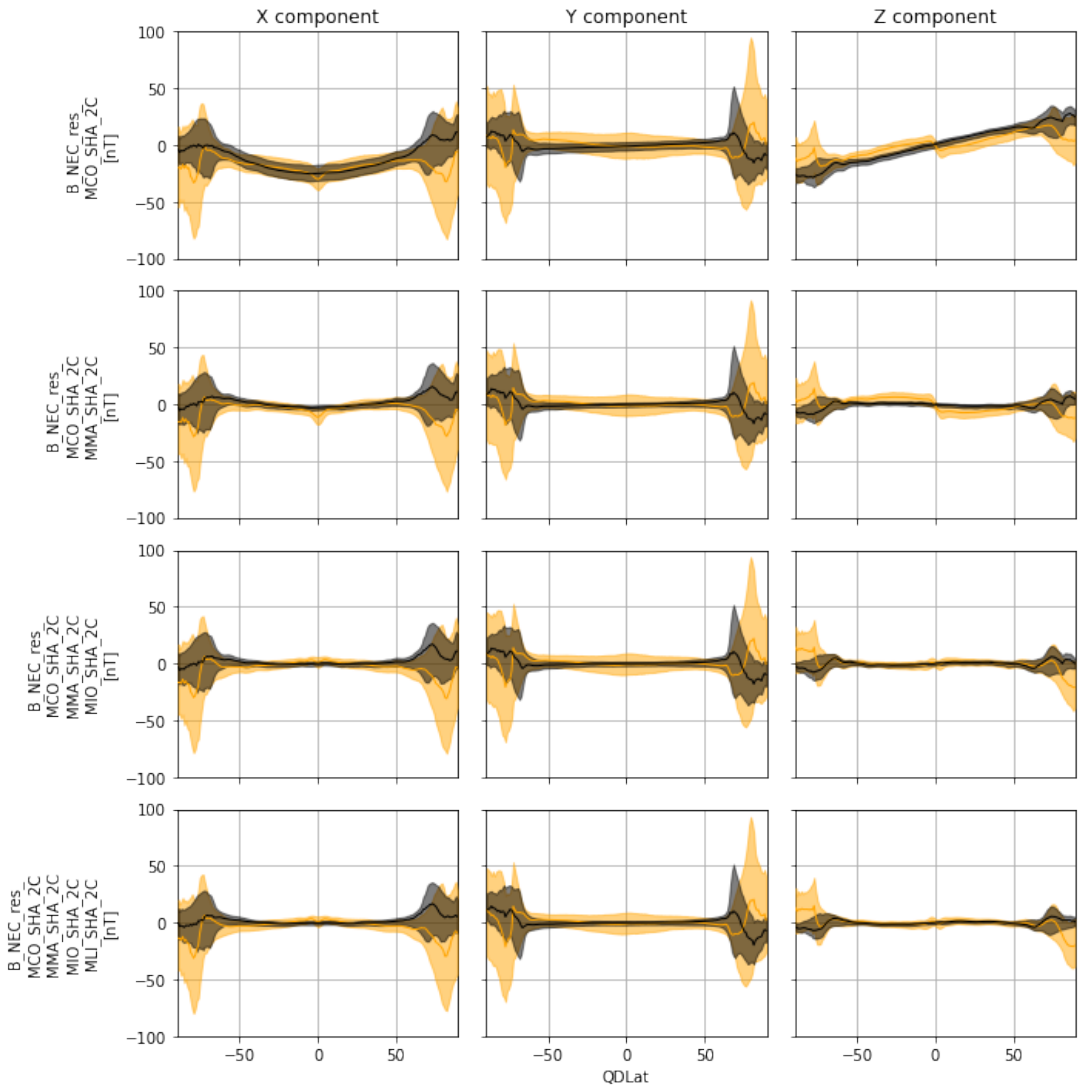

Figure 6.6: Vector residuals to combinations of the Comprehensive Inversion Swarm models, during Kp ≤ 3 from the year 2016. The mean and the IQR are shown separately for the data taken during darkness (black) and during sunlight (orange).

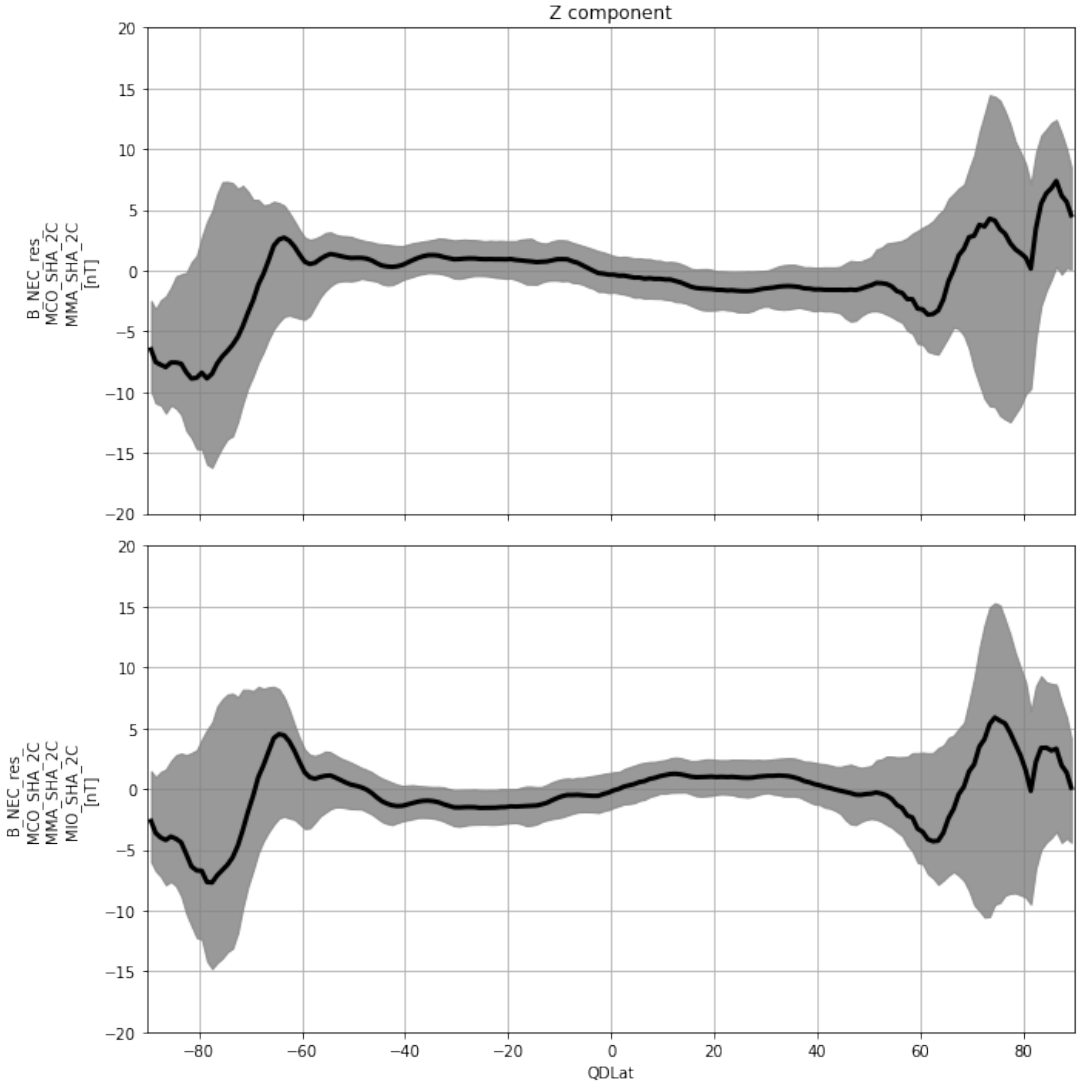

Figure 6.7: Closer view at the panels of Figure 6.6, showing the effect of including MIO during darkness.

6.3 Equal-area binning method (gridding)

As part of the process of separating the spatial and temporal components of the field, I decided to reduce the residual data to a regular grid. The result of this approach is a spherical shell of (mostly) equally spaced data points. This grid is initially in geographic coordinates and is of a resolution such that it is similar to the scale of the lithospheric field wavelengths that can be resolved at satellite altitude. The equidistribution of grid points is described in this section.

The rationale behind the gridding approach is that it provides a natural way of performing point-wise corrections to data to reduce the effect of external currents, in contrast to the orbit-by-orbit along-track corrections which are more usual (as reviewed by Thébault et al., 2017). These corrections can be agnostic of the particular orbit which the data were collected from and instead related to their grid location in a relevant coordinate system. It also simplifies the spherical harmonic inversion by reducing the problem to a smaller set of evenly spaced "data" which have already been processed to reduce noise.

Baumgardner and Frederickson (1985) describe how the surface of a sphere can be discretised into a mesh of triangular faces whose edges are geodesics (see also Teanby, 2006). The dual of this shape is a mesh of hexagonal faces, which provide optimal bins to which to assign data. The nodes of the mesh of triangles are the centroids of the hexagonal bins, and these bin perimeters can be found by Delaunay triangulation (Teanby, 2006). This "spherical triangular tesselation" is the same as that used by Stockmann et al. (2009), but I only make use of the vertex locations (the hexagon centres). To construct this shape, first, a regular icosahedron is set up with its vertices on the surface of the sphere to be discretised (left of Figure 6.8). By definition, it has twelve vertices and twenty equal area triangular faces bounded by thirty edges. The vertices of this icosahedron are equally spaced and form the basis of the higher resolution grid. To increase the resolution, the midpoints of all the edges of the icosahedron are calculated and these form an additional set of vertices to be added to the original set of vertices to form a higher resolution mesh. This can be alternatively stated as subdividing each triangular face into four new triangles. I fixed the new vertices to the face of the original bounding sphere by using the spherical linear interpolation ("slerp";

Shoemake, 1985) between the original vertices (p_0 and p_1) to be bisected:

$$\text{slerp}(p_0, p_1; t) = \frac{\sin[(1-t)\Omega]}{\sin\Omega} p_0 + \frac{\sin[t\Omega]}{\sin\Omega} p_1 \tag{6.1}$$

where Ω is the angle between them at the origin, and t is a positional parameter $0 \leq t \leq 1$ along the arc between them (which is in this case set to $t = 0.5$ for bisection). This process of subdivision is repeated until the desired resolution is reached as shown in Figure 6.8. The number of vertices produced by k iterations is given by $V = 2+10(2^{2k})$. The resulting shape has icosahedral symmetry and can be referred to as a spherical grid or an *icosphere*.

I use six iterations of the above procedure, which results in a set of 40,962 points. These points are the centroids of bins in a spherical grid to which each magnetic measurement is assigned, with the majority of the bins being identical hexagons except for at the original 12 vertices where the bins are pentagonal. The resolution achieved with this number of points gives bins of side length $\sim$ 110km and would theoretically allow a spherical harmonic analysis up to degree $L \sim 200$. The assignation of the measurements to their grid locations is done with a nearest neighbour search that finds the nearest grid location (bin centroid) for each data point, by making use of a k-d tree (in Python: `scipy.spatial.cKDTree`). Each grid point, the distribution of which is illustrated in Figure 6.9, is then associated with a number of data collected at different times as shown in Figure 6.10.

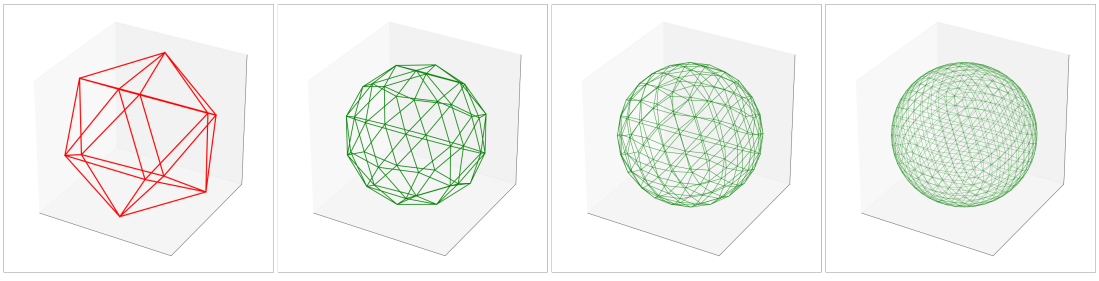

Figure 6.8: Refining the icosphere. Left to right: the base icosahedron and repeated subdivisions

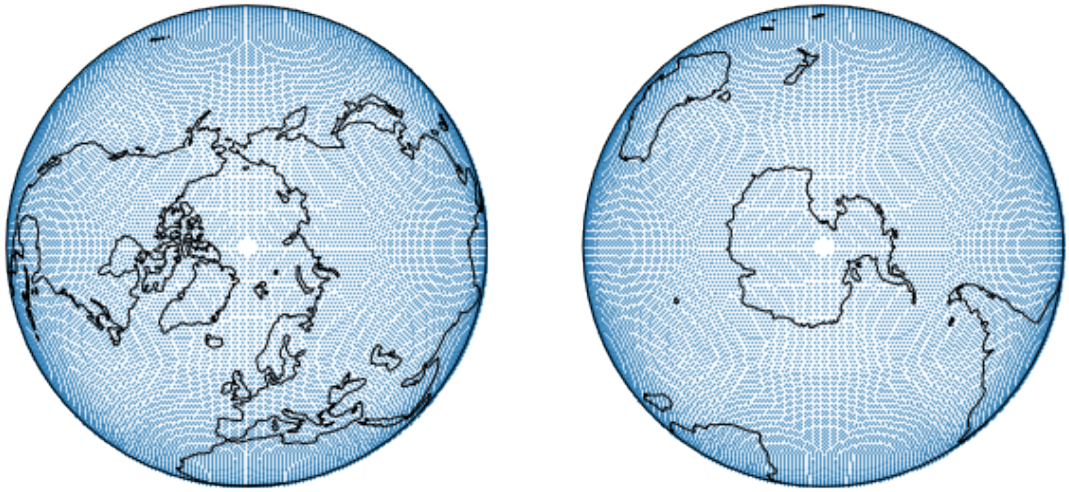

Figure 6.9: Orthographic views of the resulting grid points, after applying to Swarm data. Note the polar gaps are present.

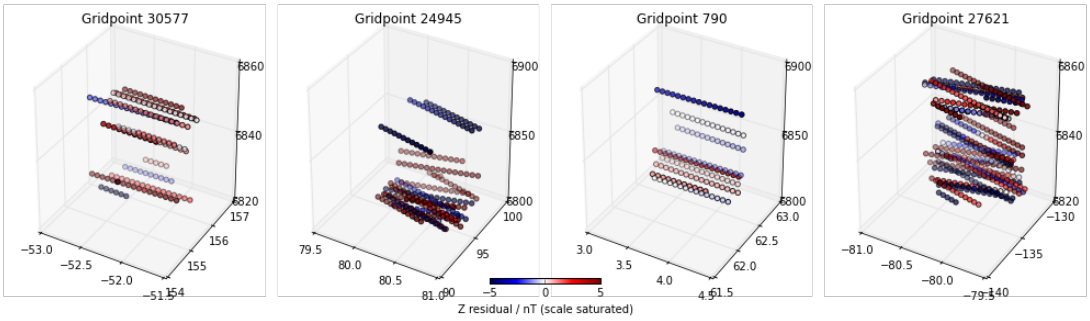

Figure 6.10: Examples of data that have been assigned to particular grid points. The horizontal axes are latitude and longitude in degrees and the vertical axis is geocentric radius in km.

6.4 Model choice and application of gridding

6.4.1 Application to the CI model residuals

The binning method was applied separately to each of the CI residual combinations as in Figure 6.6, for the same quiet and dark conditions but extended to four years of data from May 2014 to May 2018 from Swarm Alpha. For each field component, X, Y, Z, the median value was calculated at each grid point, and these are shown in Figure 6.11. This gives more detail to the observations made in section 6.2.1. In the second row, the field produced by the Sq system (even during night) is quite pronounced in the X and Z components. Subtracting the MIO field (the third row) successfully reduces its effect at mid-latitudes, although it over-corrects for the hemispheric bias in the Z residual (albeit reducing the absolute size of the bias). These figures still do not show the effect

of the higher degree terms of the MIO model but they are likely to be unhelpful due to them being less well-determined than the lower degree terms, even more so because we are only considering the night-side. The remaining residuals after subtracting the full CI model must be due to the incompleteness of the model, and their length scales are troubling if we are to use the CI residuals for lithospheric field modelling as they indicate contamination of the wavelengths we are seeking.

6.4.2 Application to the CHAOS model residuals

To compare with Figure 6.11 based on the CI models, Figure 6.12 shows the results using the CHAOS-6 models instead. Similarly, I evaluate the residuals to the core field part (I used degrees 1-14), the core field plus magnetospheric field, and the full model (core + magnetosphere + lithosphere). We see notable differences from the CI model residuals. Removing the core and magnetospheric components leaves relatively little regional/hemispheric contamination compared to the same from the CI model. This is due to the different approach to modelling used in the CI models, where the attempt is made to separate all known fields into their physical origins. This means that to describe the field, all components should be taken together, and the usage of individual or combinations of components is not appropriate in some use cases as the separation is imperfect. By contrast, the CHAOS core field model, and likely all models that don't follow the CI approach, will be contaminated by signals from the induced part of the ionoospheric variations which the CI approach attempts to clean out (see the discussion of this issue by Olsen et al., 2005). Taking the CHAOS core + magnetosphere residual provides the best estimate of the lithospheric field, although there will still be contamination from the ionospheric fields which depend on the data selection used. Subtracting the full CHAOS model leaves some large scale residuals which I attribute to using a different data selection than was used in the CHAOS model derivation, and thus a different contamination from the external fields.

The residuals to the CHAOS (core + magnetosphere) model will be used in the following sections, but it is noted that there are other options available.

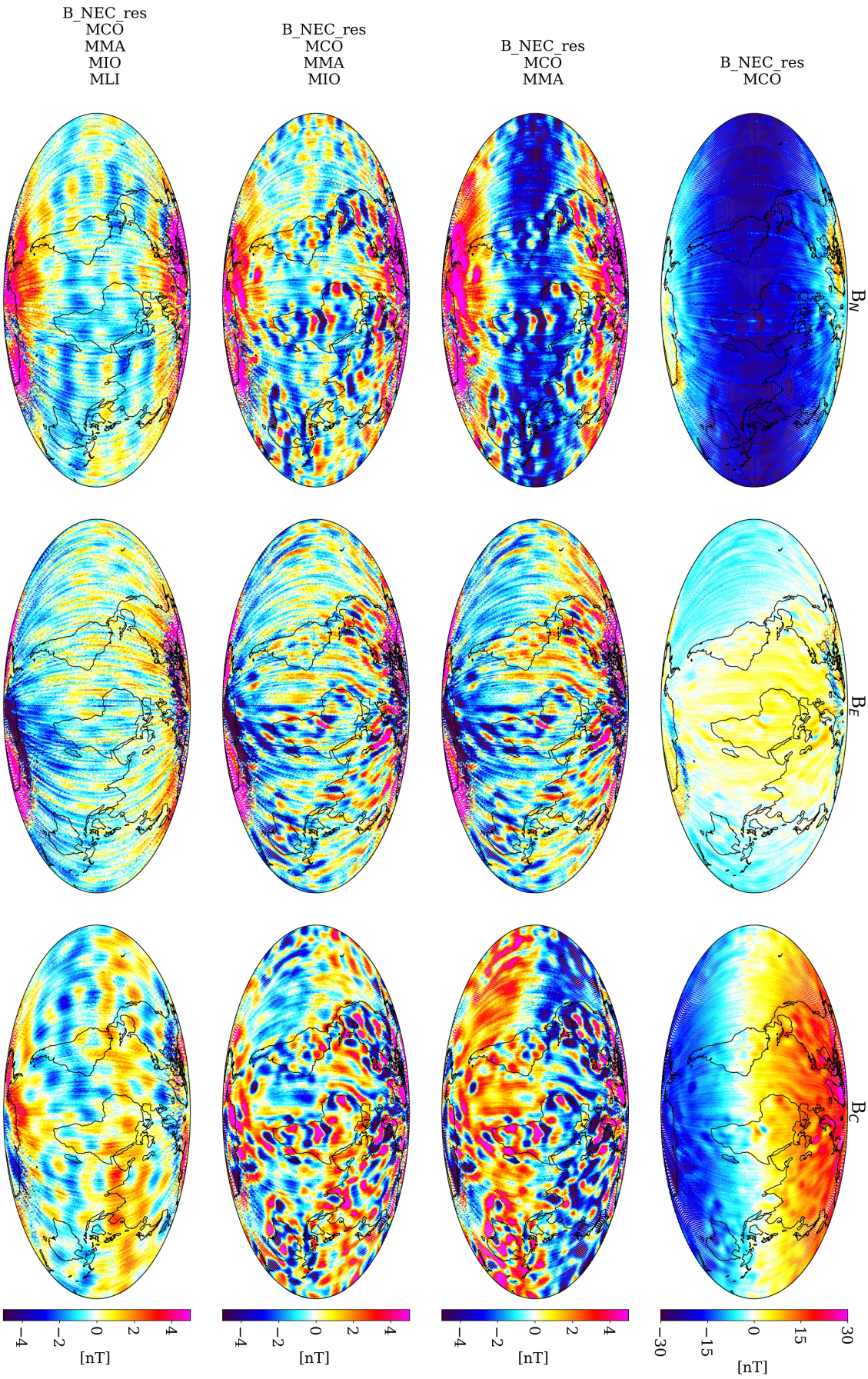

Figure 6.11: Four years of Swarm data from May 2014 to May 2018; filtered for darkness and geomagnetic quiet times; residuals to combinations of field models as in Figure 6.6; reduced to the icosphere grid by evaluating the median at each grid point.

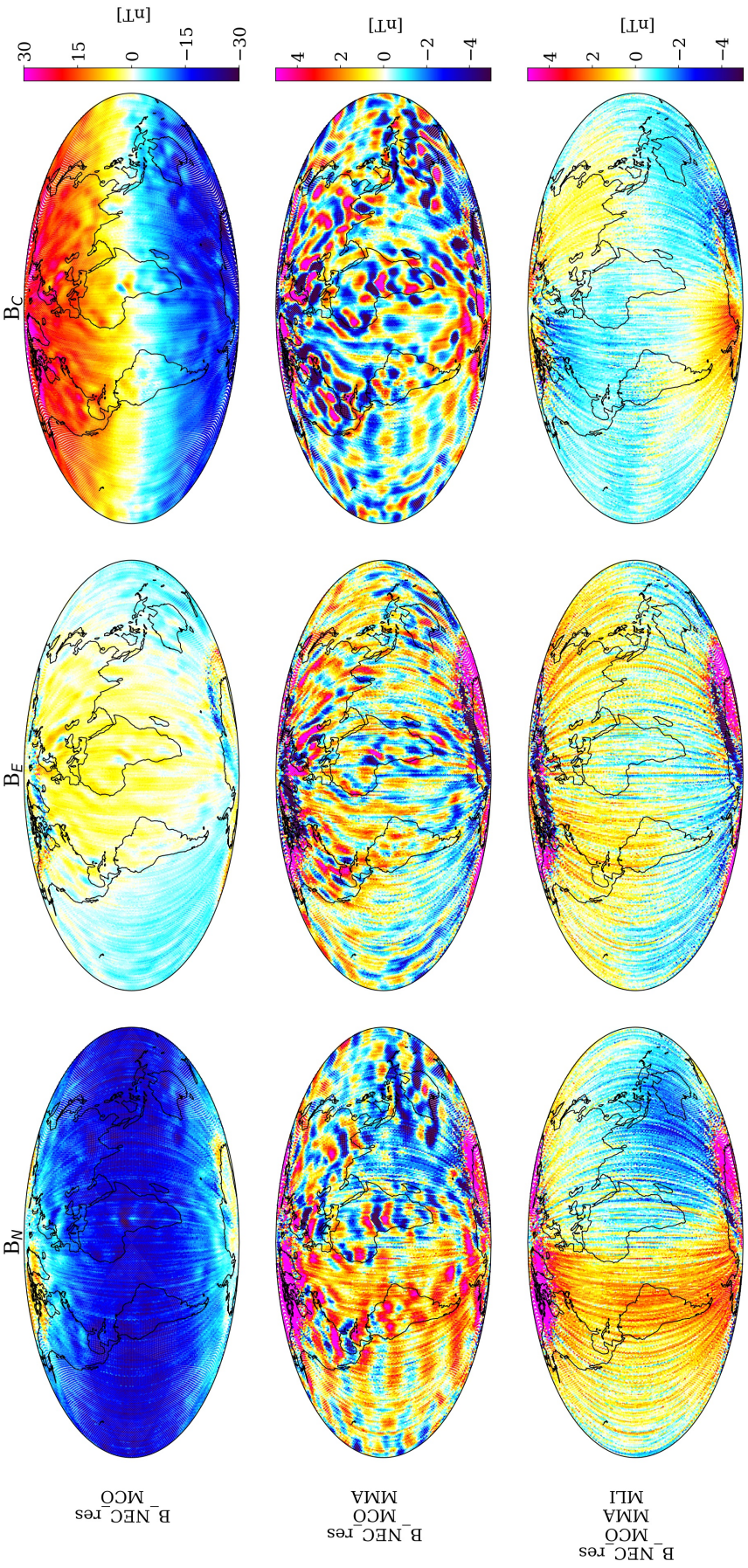

Figure 6.12: As in Figure 6.11 but using CHAOS instead. Four years of Swarm data from May 2014 to May 2018; filtered for darkness and geomagnetic quiet times; residuals to combinations of the CHAOS model components; reduced to the icosphere grid by evaluating the median at each grid point.

6.5 Investigation of the gridded dataset

Further details of the sampling provided with the reduced dataset are provided in Figures 6.13 through 6.16, respectively, the derived (X, Y, Z, F) median field components, the standard deviation of input data contributing in each bin, the variation in sampling density and altitude, and the sampling density as a function of time. I found that use of the data at the original 1-second sampling rate, rather than a 10-second subsampling, did not improve the results (in fact introducing more along track striping), so the results presented in this chapter and the following one are based on 10s subsampling.

Figure 6.14 reveals the increased auroral oval contamination in the X and Y components (due to FACs) is also much more variable than in the Z component (predominantly due to the auroral electrojet), which makes it harder to model than the more steady contamination in the Z component. This figure also reveals strong contamination from particular satellite tracks, also visible as streaks in Figure 6.13. At mid latitudes, this type of feature is likely due to poor removal of the magnetospheric field, so is more prominent in the X component. At high latitudes, it is likely due to the effect of substorms, or otherwise short-lived auroral oval activity, that is not captured by the long-period activity indices that we use to filter the data. It would be advantageous to remove these particular tracks.

Figure 6.15 shows both the sampling density and altitudes of measurements. The altitudes are higher over the Northern Hemisphere, which may bias results in some way, but should be taken care of by the spherical harmonic inversion. This figure highlights the much higher density of sampling over the poles, which could justify more extreme rejection of data in these regions if the remaining data are cleaner. It also shows a smaller number of remaining data in the North, presumably due to higher levels of geomagnetic activity during Northern winters as can be seen in Figure 6.16. It is notable that the sampling of each hemisphere is not uniform through time, with significant data gaps, which is particularly problematic for modelling time-varying fields such as from the core. This should not cause too much trouble for retrieving the static lithospheric contribution, although it could introduce biases due to the time-varying fields that are not accounted for.

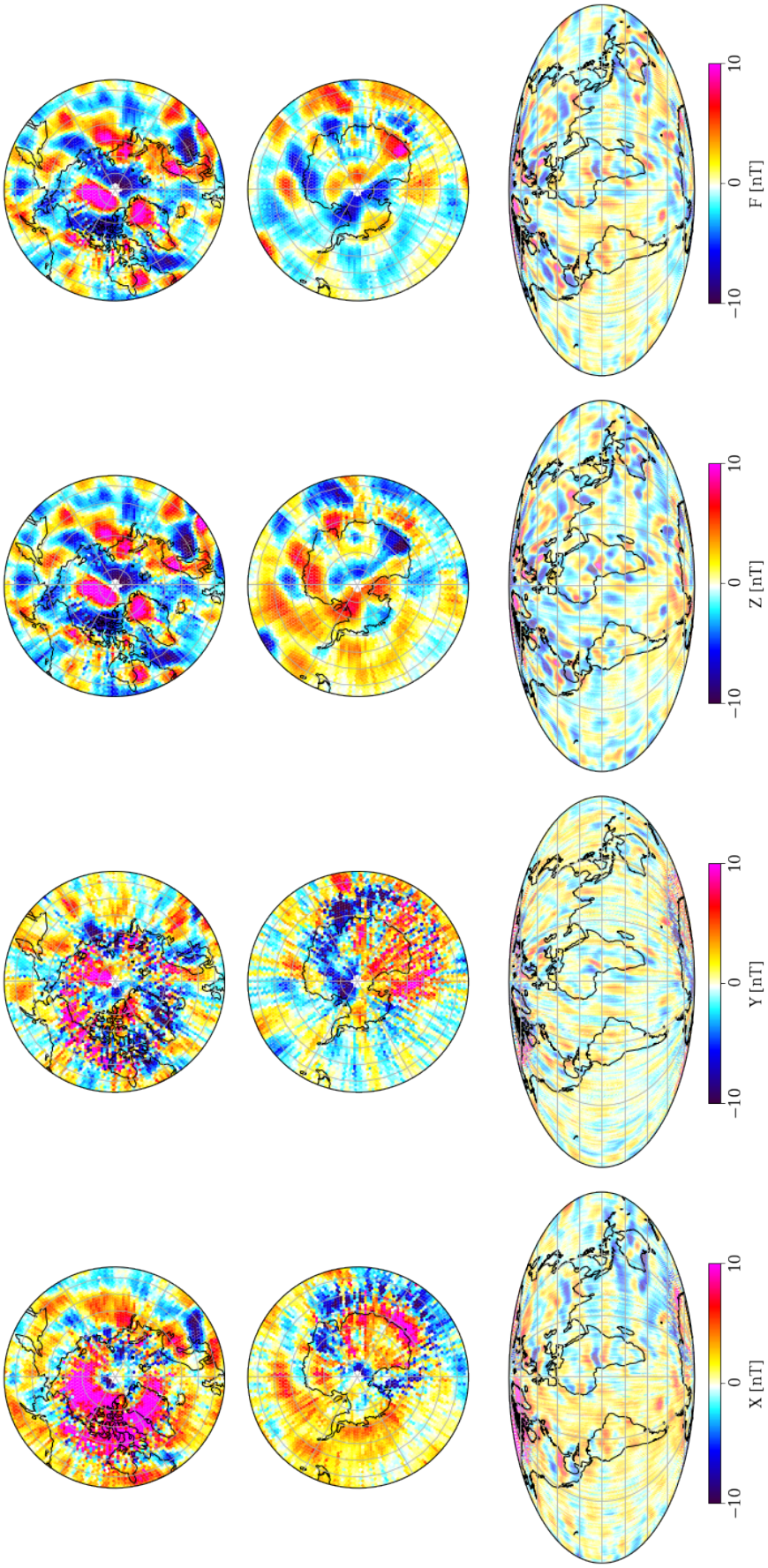

Figure 6.13: The vector field components resulting from the stacking of the residuals to the CHAOS (core + magnetosphere) model, derived from four years of Swarm Alpha data, as in Figure 6.12.

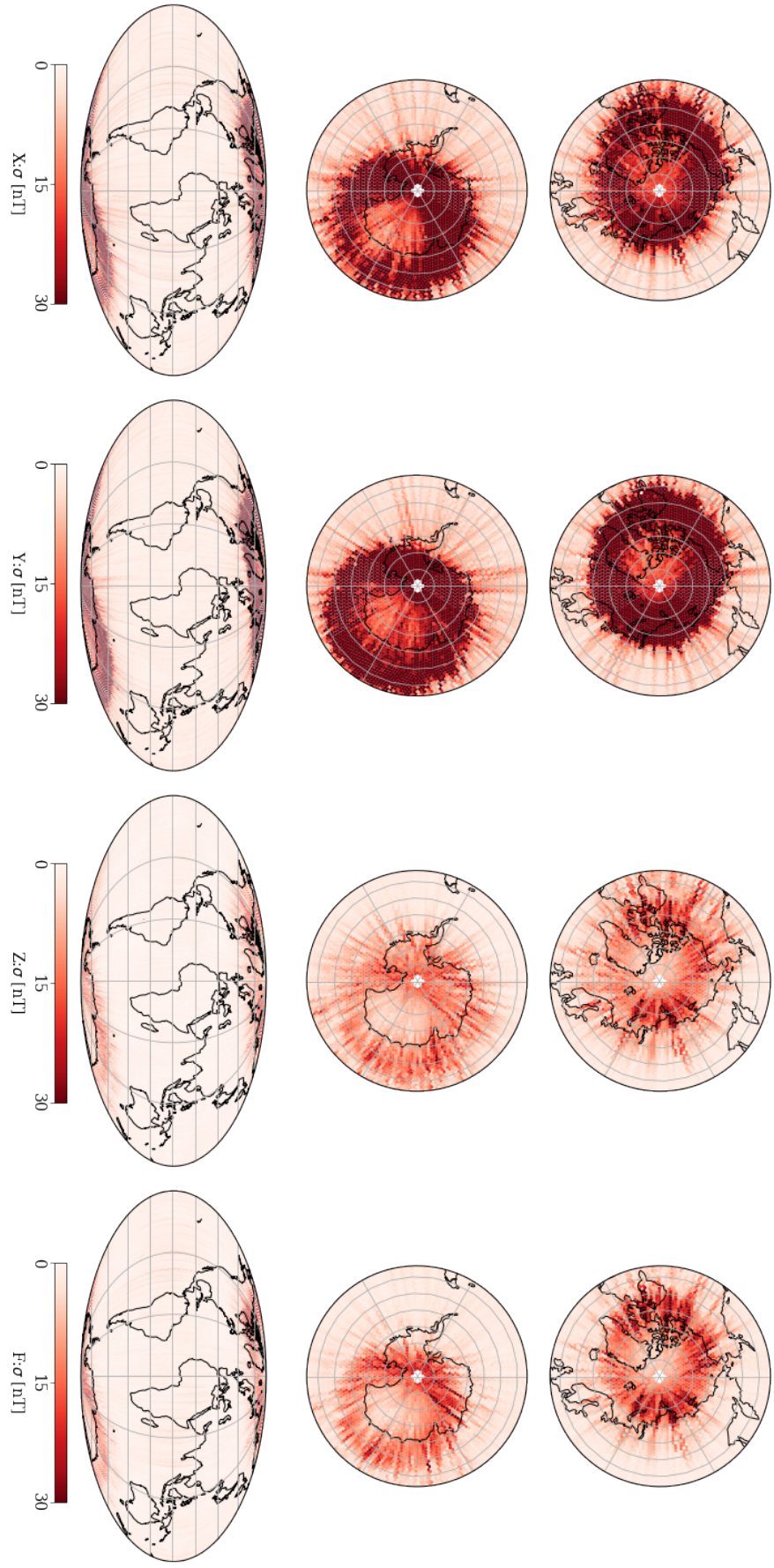

Figure 6.14: As Figure 6.13, but instead showing the standard deviation of the stacked data at each grid point. The effect of the auroral oval noise is very strong in the X and Y components, while the Z component has smaller uncertainties (but still heavily contaminated).

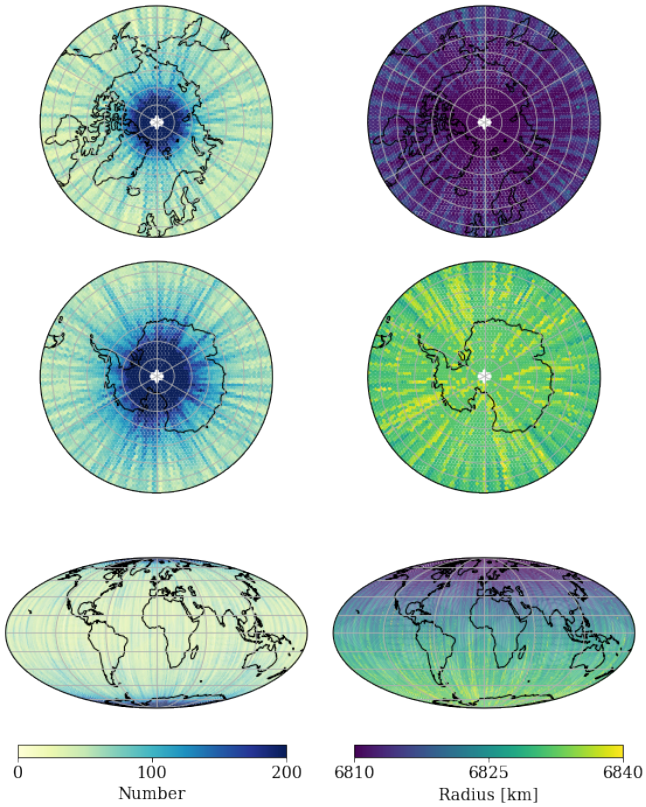

Figure 6.15: As for Figures 6.13 and 6.14, but instead showing (left) the number of samples and (right) median radius at each grid point. The lesser sampling of the Northern Hemisphere (NH) is due to the coincidence of high geomagnetic activity, and thus rejection of data, during Northern winter (see Figure 6.16). The perigee of the orbit occurs over the NH, meaning that data are collected at ∼30 km lower altitude in the NH.

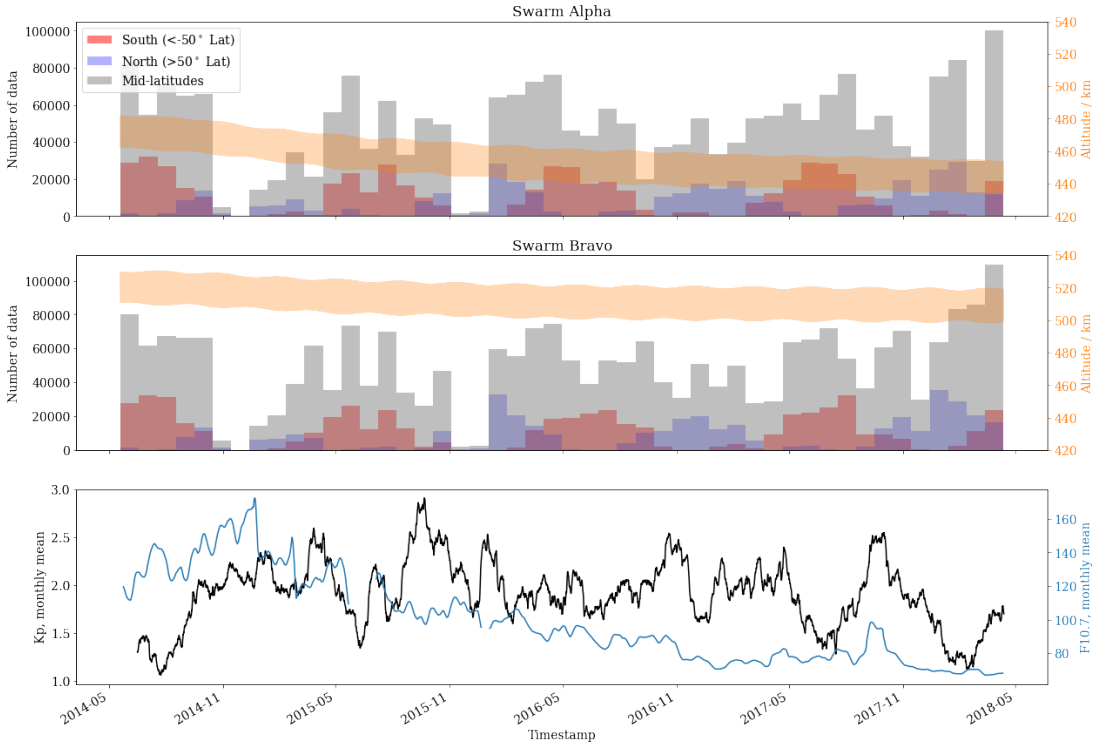

Figure 6.16: Sampling through time for the input data. The top two panels show monthly-binned histograms of the number of data contributing, split between each hemisphere and mid latitudes. The lower panel shows monthly moving averages of the Kp and F10.7 indices.

6.6 Spherical harmonic analysis of the gridded data

The gridded residuals can be used to determine a spherical harmonic model. This follows the standard procedure where data, $\boldsymbol{d}$, and model, $\boldsymbol{m}$, are related by the linear equation,

$$\boldsymbol{d} = \boldsymbol{G}\boldsymbol{m}, \tag{6.2}$$

where $\boldsymbol{G}$ is the design matrix which relates the Gauss coefficients stored in the vector $\boldsymbol{m}$ (i.e. $\{g_n^m, h_n^m\}$) to the magnetic field components stored in $\boldsymbol{d}$. In this case, $\boldsymbol{d}$ contains the reduced measurements (median values) made at each grid point - the angular position is fixed at the grid cell centre and the radius fixed at the median radius of the data within each cell. This means that the inverse problem is smaller than in many existing models where the original measurements (usually sub-sampled) are used directly in the inversion.

Denoting the magnetic field components $(B_r, B_\theta, B_\phi) = (-Z, -X, Y)$ as B_i, which are related to the potential as $V = -\partial_i B_i$, and using equation 4.1, seeking internal

sources only,

$$
\begin{aligned}
B_i = & -\partial_i \left(R_E \sum_{n=1}^{N} \sum_{m=0}^{n} \left(g_n^m \cos m\phi + h_n^m \sin m\phi\right) \left(\frac{R_E}{r}\right)^{n+1} P_n^m(\cos\theta) \right) \\
= & -\partial_i \begin{bmatrix} R_E \sum_{n=1}^{N} \sum_{m=0}^{n} \left(\cos m\phi\right) \left(\frac{R_E}{r}\right)^{n+1} P_n^m(\cos\theta) \\ R_E \sum_{n=1}^{N} \sum_{m=0}^{n} \left(\sin m\phi\right) \left(\frac{R_E}{r}\right)^{n+1} P_n^m(\cos\theta) \end{bmatrix} \begin{bmatrix} g_n^m & h_n^m \end{bmatrix}. \qquad (6.3)
\end{aligned}
$$

Note that ∂_i here is a shorthand which should be replaced by the derivatives in spherical polar coordinates,

$$\partial_r = \frac{\partial}{\partial r}, \qquad (6.4)$$

$$\partial_\theta = \frac{1}{r}\frac{\partial}{\partial \theta}, \qquad (6.5)$$

$$\partial_\phi = \frac{1}{r\sin\theta}\frac{\partial}{\partial \phi}. \qquad (6.6)$$

Equation 6.3 can be compared to equation 6.2 to generate $\boldsymbol{G}$, depending on which magnetic field component measurements are to be used in the inversion.

As has been discussed, the magnetic field components, X, Y, Z, are contaminated differently by the auroral oval noise. The Z component is most weakly affected, and with less variation (low σ). It is therefore reasonable to construct a model from the Z component alone, assuming the extra information added by X and Y is not particularly valuable given their increased noise. Many previous models use just the scalar residual, F, over the polar regions for this same reason, but also because the scalar data are less noisy and more available, particularly with older missions than Swarm. However, using only F is problematic as it introduces the Backus effect (Backus, 1970), and employing different procedures over the polar region introduces edge effects.

Due to the resolution of the grid resulting in 40,962 "data" points, the maximum degree model attainable before the problem becomes under-determined is at $l_{max} = N = 202$ (the number of model parameters is $N(N+2)$). However, due to the altitude of Swarm measurements, it is not possible to resolve features of such small wavelength and so degree $N <\approx 100$ is a reasonable target. The actual truncation level used is decided depending on where noise starts to dominate the model coefficients so should be lower than this.

Since we have evaluated the variances, σ^2, of the original data contributing at each

grid point, it is natural to weight the inversion by σ^{-2} so that more unstable points contribute less. We can define a vector of weights, $\boldsymbol{W^\sigma}$, where each term is σ^{-2}, corresponding to terms in $\boldsymbol{d}$. Minimising the L2 norm (see e.g. Chapter 6 of Gubbins, 2004), the model coefficients can then be evaluated as

$$\boldsymbol{m}_0 = \left(\boldsymbol{G}^T\boldsymbol{W^\sigma}\boldsymbol{G}\right)^{-1}\left(\boldsymbol{G}^T\boldsymbol{W^\sigma}\boldsymbol{d}\right). \tag{6.7}$$

This results in a model which begins to be dominated by noise above about degree 60, which is seen by comparing the power spectrum to other lithospheric field models. To reduce this effect a damping parameter is introduced at high degrees, along with an iterative re-weighting by the data-model residuals to reduce the effect of outliers. Denoting the i-th model as $\boldsymbol{m}_i$, a weighting matrix is defined as

$$\boldsymbol{W}_i^{\boldsymbol{r}} = \frac{\sqrt{2}}{|\boldsymbol{d} - \boldsymbol{G}\boldsymbol{m}_i|}. \tag{6.8}$$

The damping is introduced by a regularisation matrix which affects model coefficients between a chosen starting degree, l_s, and l_{max}:

$$\boldsymbol{\Lambda} = \lambda\left(\frac{(l+1)^2}{2l+1}\right)\widetilde{\boldsymbol{I}}, \tag{6.9}$$

where $\widetilde{\boldsymbol{I}}$ is a diagonal matrix matching the shape of $\boldsymbol{G}$, having zeros up to $l = l_s$ and linearly increasing with l from 0 at $l = l_s$ and 1 at $l = l_{max}$ in order to ramp up the damping effect at higher degrees. λ is a parameter chosen to set the strength of the damping desired, and l_s is chosen according to where noise starts to dominate the model. The $(i+1)$-th model is then given by

$$\boldsymbol{m}_{i+1} = \left(\boldsymbol{G}^T\boldsymbol{W}_i^{\boldsymbol{r}}\boldsymbol{G} + \boldsymbol{\Lambda}\right)^{-1}\left(\boldsymbol{G}^T\boldsymbol{W}_i^{\boldsymbol{r}}\boldsymbol{d}\right), \tag{6.10}$$

which is iterated until the residuals do not change significantly. This implements the L1 norm (as in e.g. Farquharson and Oldenburg, 1998; Walker and Jackson, 2000). The power spectra of the resulting models at each iteration, and for different λ, are shown in Figure 6.17 in comparison to LCS-1.

The model resulting from the CHAOS residuals, with $\lambda = 10$ and 3 iterations, is shown in Figure 6.18 (the radial component at ground level). Comparing to other

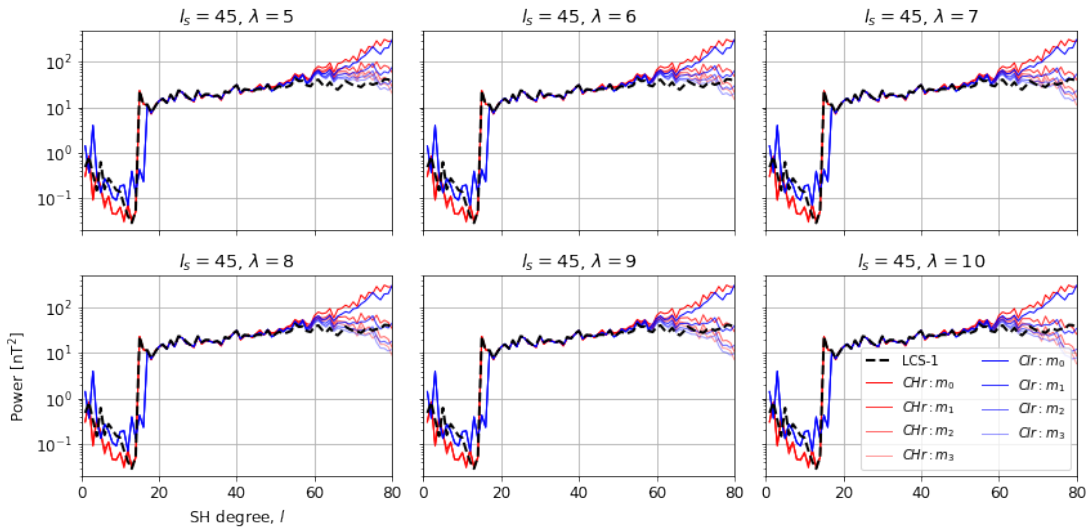

Figure 6.17: Comparisons of power spectra of candidate lithospheric field models derived from the Z residual. CHr denotes models derived from residuals to the CHAOS (core + MMA) model, and CIr denotes models derived from residuals to the CI (MCO_2C + MMA_2C) model. m_i denotes successive iterations of the model following equation 6.10. The LCS-1 model is shown for comparison. All models are truncated at degree 80.

lithospheric field models, this model clearly picks up the strongest lithospheric features, but severely suffers from longitudinal banding in relation to the satellite orbits. This is particularly noticeable over the oceans in the absence of the stronger continental signals. Figure 6.19 shows the model residuals to the gridded data. It highlights that the model struggles to fit the data in the auroral regions, where the granularity of the noise is smaller than the smoothness of the spherical harmonics being fitted. Interestingly, this appears to be much more the case in the Northern Hemisphere, perhaps because of lower sampling resulting in poorer median values.

The model is derived from the gridded dataset from only Swarm Alpha. It was found that using a combination of Swarm Alpha and Bravo data (i.e. a SHA of two grids of data, each at a different altitude) did not result in a significantly different model (not shown). This indicates that more work is necessary to improve the approach before simply including more data. Swarm Charlie, being in essentially the same position as Alpha for our purposes, is not useful except for marginally improving the statistics of the data contributing to the "Alpha grid". The generation of two grids of data at different altitudes does however provide an interesting opportunity to look at the vertical differences between them, as is explored next.

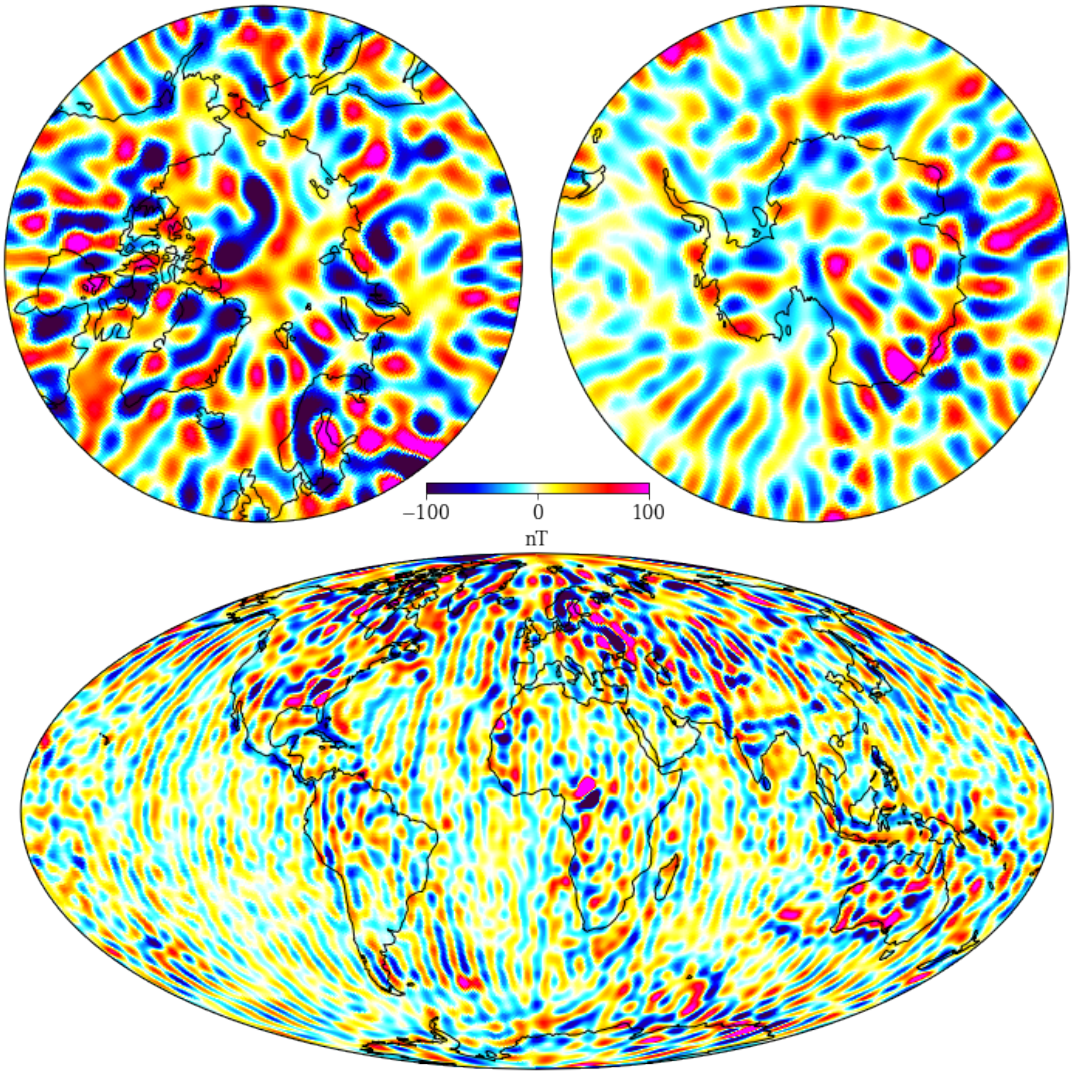

Figure 6.18: The radial component at ground level evaluated from the final lithospheric field model, c.f. "$\lambda = 10$, CHr:m_3" in Figure 6.17. Generated from only Swarm Alpha data.

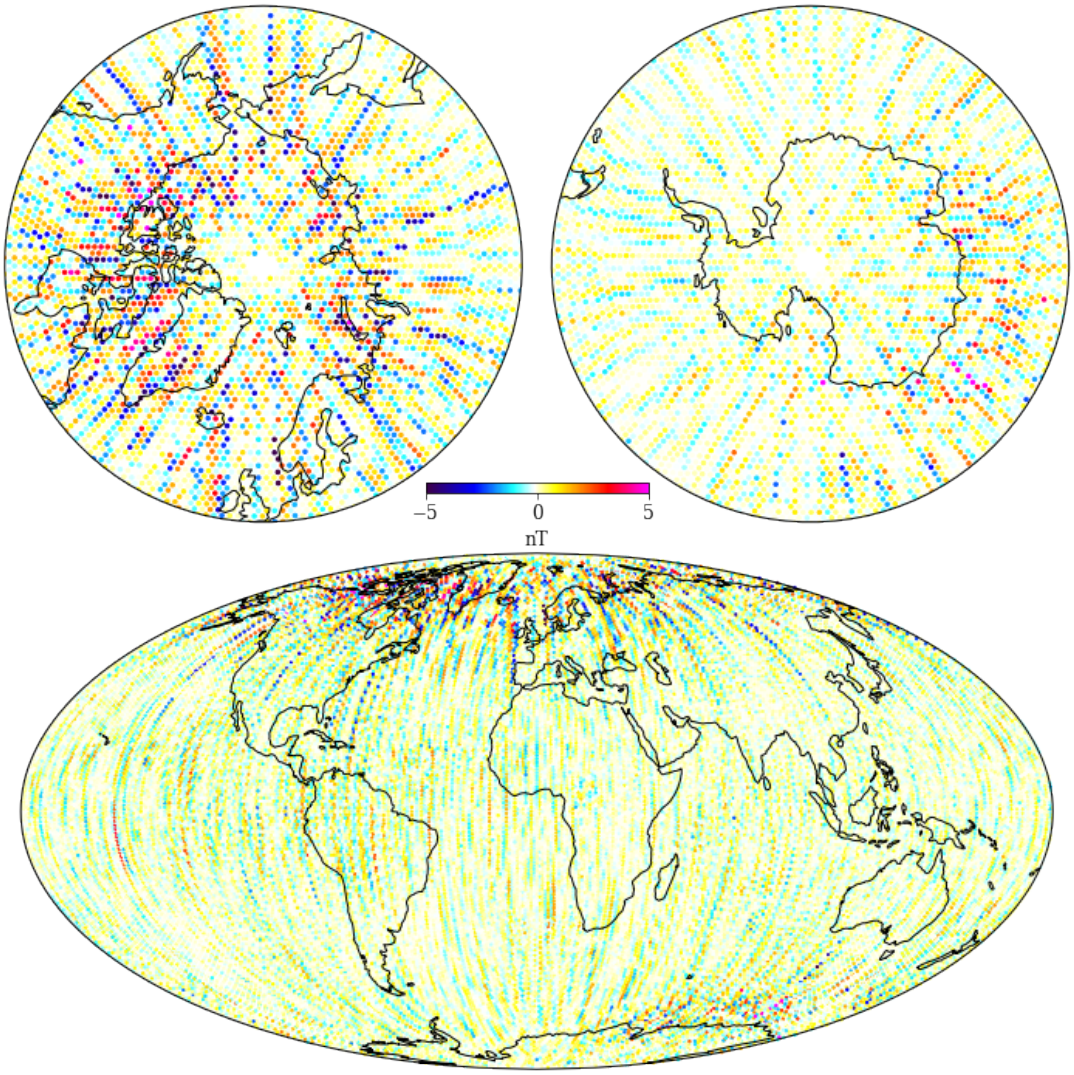

Figure 6.19: Following Figure 6.18, showing the residual between the model values and the gridded input data.

6.7 Using the vertical gradient

Measurements from Swarm Alpha and Bravo are within different altitude ranges (see Figure 6.16), resulting in two spherical grids of data with Bravo's enclosing Alpha's. From these, we can get a rough estimate of the vertical gradient of the magnetic field by looking at the difference between values at the corresponding grid points at the two altitudes. This is of course with the caveats that the input data are actually gathered across a range of altitudes, at different times, and with a large separation (50 km) between the two sample points.

Again, the Z components of the gridded data are taken, this time derived on two grids, one from Swarm Alpha and one from Swarm Bravo. The vertical gradient at the radial midpoints between the two grids is estimated, by calculating $\frac{Z_B - Z_A}{\Delta h}$ at each grid point, to give a grid of quasi-$\partial_r B_r$ values. It is then possible to perform a SHA of these derived data, although strictly it only applies to actual gradient measurements.

Reproducing from Kotsiaros (2016), the magnetic field gradient tensor elements are written as

$$[\nabla \boldsymbol{B}]_{jk} = \mathbb{R}\left\{\frac{1}{R_E}\sum_{n=1}^{N}\sum_{m=0}^{n}\gamma_n^m\left(\frac{R_E}{r}\right)^{n+3}Y_{nm}^{jk}\right\} \tag{6.11}$$

where $\{j,k\} = \{r,\theta,\phi\}$, $\gamma_n^m = g_n^m - ih_n^m$, and Y_{nm}^{jk} are modified spherical harmonics (using the more compact complex number formulation of spherical harmonics, with $\mathbb{R}$ denoting the real component). I use just the radial-radial component, for which

$$Y_{nm}^{rr} = -(n+1)(n+2)e^{im\phi}P_n^m(\cos\theta). \tag{6.12}$$

These equations allow us to generate the design matrix, $\boldsymbol{G}^{(0)}$, to perform the inversion of

$$[\nabla \boldsymbol{B}]_{rr} = \boldsymbol{G}^{(0)}\boldsymbol{m}. \tag{6.13}$$

The power spectrum and radial component of the model resulting from this procedure is shown in Figures 6.20 and 6.21. Real physical features are picked up but the model is rapidly dominated by noise. There is a large degree-1 noise signal.

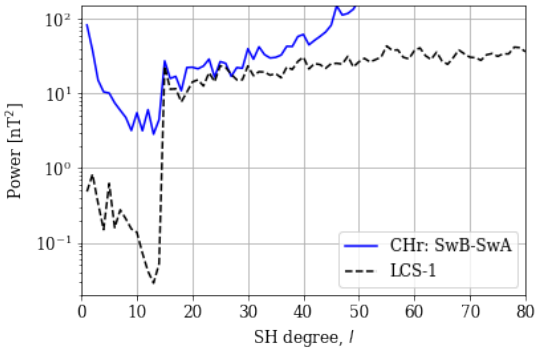

Figure 6.20: The power spectrum from the model resulting from the radial-radial differences.

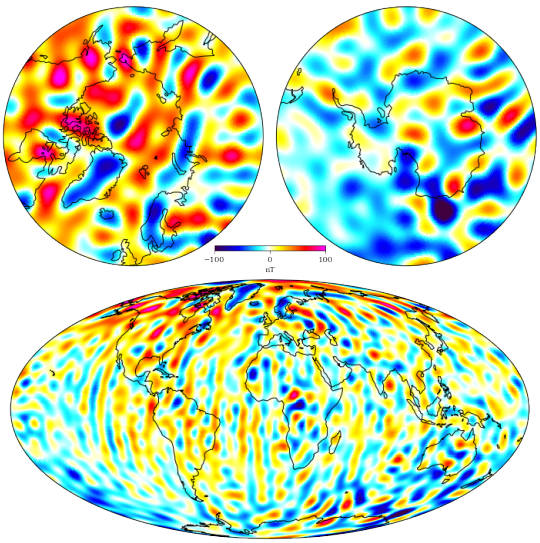

Figure 6.21: The radial component of the model shown in Figure 6.20, calculated up to degree 40

Chapter 7

Removing the ionospheric field from the lithospheric model

In this chapter, the gridding procedure described in the previous chapter is extended to also consider a grid in quasi-dipole latitude (QDLAT) and magnetic local time (MLT) in place of geographic latitude and longitude. This organises the data into ionospheric structures instead of lithospheric structures. With this new grid, the average ionospheric field is described for the same data selection criteria as those used to derive the lithospheric field (quiet, night time). The bias that this field produces within the lithospheric field model is thus demonstrated and accounted for in deriving a new lithospheric field model.

7.1 Binning residuals by QDLAT and MLT

7.1.1 Medians and standard deviations

The geographic grid (abbreviated GEO) in the previous chapter is defined just by spherical coordinates, (θ, ϕ), so we can re-use this grid for the QDLAT/MLT grid (abbreviated QDMLT). In the new grid, θ (originally colatitude) instead represents QD colatitude, and ϕ (originally longitude) is mapped to MLT as ϕ (in degrees) $= 15 \cdot$ MLT (in hours). Roughly half the cells in the grid are empty since we only consider night side data, and there is asymmetric coverage between hemispheres due to the different offsets of the North and South magnetic poles. The input data are the same as before, but in this instance the residuals are now calculated to the full CHAOS model (core + magneto-

sphere + lithosphere), so that the residuals we are binning are an estimate of the polar ionospheric field alone, with the lithospheric field removed. The resulting estimate of this field is shown in Figure 7.1.

In the previous chapter we observed greater contamination of the lithospheric field signal in the X and Y components than the Z. Here the source of this difference is made clear, with a stronger and more variable pattern (as also indicated by larger standard deviations, shown in Figure 7.2) visible in X and Y components in QDMLT, reflecting the nature of FACs. This figure also shows a large scale contamination at mid latitudes which is presumably due to not only weak ionospheric currents but also to the far-field effect of Region 1/2 currents (as described by Olsen and Stolle, 2017), which could be tested for by investigating the IMF dependence. The shape of the magnetic perturbations is controlled by the geometry and typical positions of the current systems during the quiet-time conditions that we select for, which, depending on the way in which these contributions are collected within geographic coordinates, drive a bias in the lithospheric field model.

7.1.2 Reaction to solar wind conditions

Figure 7.1 displays data which contain the gross average of the auroral oval over many different conditions, but this can be separated out somewhat by applying different additional filters to the input data. Figure 7.3 shows the result of splitting the input data into four parts according to the quadrant of the IMF clock angle. Here only the Z residual is shown, as it is the least noisy and easiest to interpret (in terms of horizontal currents, i.e. predominantly auroral electrojets).

The differing patterns in Figure 7.3 can be viewed in connection with the key findings from Chapter 5 about the hemispheric asymmetries in the auroral electrojets in reaction to IMF angle. More intense electrojets were found for $B_y > 0$ than $B_y < 0$ in the Northern Hemisphere, while the reverse is true for the Southern Hemisphere. The effect of this can be seen here in the substorm sector (post-midnight) but it is hard to compare directly without more quantitative analysis. What can be observed here is the rotation of the cells and modification of their shape in reaction to B_y, with opposite effects in each hemisphere. This behaviour is explained by Tenfjord et al. (2015) (their Figure 6 in particular), amongst others, in terms of the modification of the convection cells by asymmetric loading of flux to the magnetosphere lobes. This has been observed

many times before, using a range of different ground and space based measurements (e.g. Cowley and Lockwood, 1992; Friis-Christensen and Wilhjelm, 1975; Grocott et al., 2012; Haaland et al., 2007; Huang et al., 2000).

Ionospheric conditions are driven by IMF (and more generally solar wind) conditions. Whatever data selection or filtering has been applied to data for lithospheric field modelling, biases will remain which are dependent on solar wind conditions. It is therefore reasonable that data correction techniques should take solar wind conditions into account.

Since the core and magnetospheric fields have been removed using models, it would seem natural to use other models to remove the remaining external field sources which are themselves typically parameterised by solar wind conditions (i.e. climatological). Such models include MFACE (He et al., 2012) for the FACs, and others which describe both ionospheric currents and FACs together: Juusola et al. (2014) using the SECS method (Amm, 1997), AMPS (Laundal et al., 2018) using spherical harmonics, and others. Other options are track-by-track models such as that by Aakjær et al. (2016) of the auroral electrojets (AEJs).

Climatological models are successful in producing useful insight into the external fields themselves, but, due to their limitations in capturing the full complexity of the systems and their lack of sensitivity for the weakest currents, are less suitable for isolating the lithospheric signal. Conversely, track-by-track models may capture more complexity for a particular track or time, but, since they are dedicated to a particular source, do not account well for other sources. It is also a problem to combine models in a consistent way, as was seen in the previous chapter with the usage of the CI and CHAOS models. This produces the necessity to co-estimate sources in one inversion process or to use dedicated correction techniques. However, adequately parameterising many different sources simultaneously and devising an inversion scheme which can produce effective models of the sources is a major challenge. This motivates the point-based correction technique introduced in this chapter, which gives some suitable (but limited) parameterisation relevant to the ionospheric sources (i.e. the QDMLT grid) without the constraint of having to produce a smooth model of them.

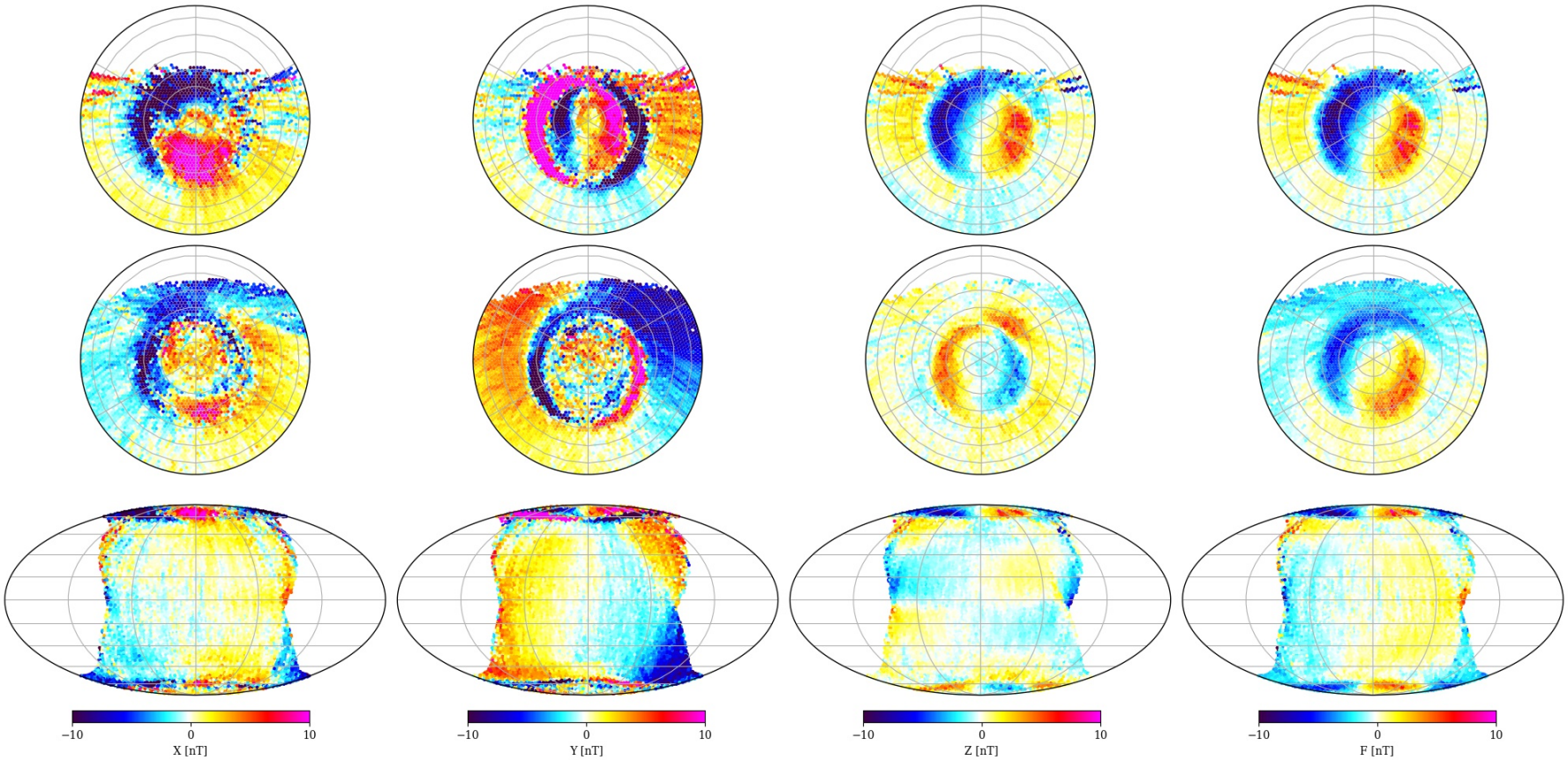

Figure 7.1: The vector field component medians resulting from the stacking of the residuals to the CHAOS (core + magnetosphere + lithosphere) model, derived from four years of Swarm Alpha data, as in Figure 6.13 but instead in coordinates of QDLAT and MLT. Each column shows a different component (X, Y, Z, F / North, East, downwards, intensity); the top row shows the Northern Hemisphere and the second row the Southern Hemisphere with midnight at the bottom and dawn to the right; the bottom row figures show the nightside centred on midnight.

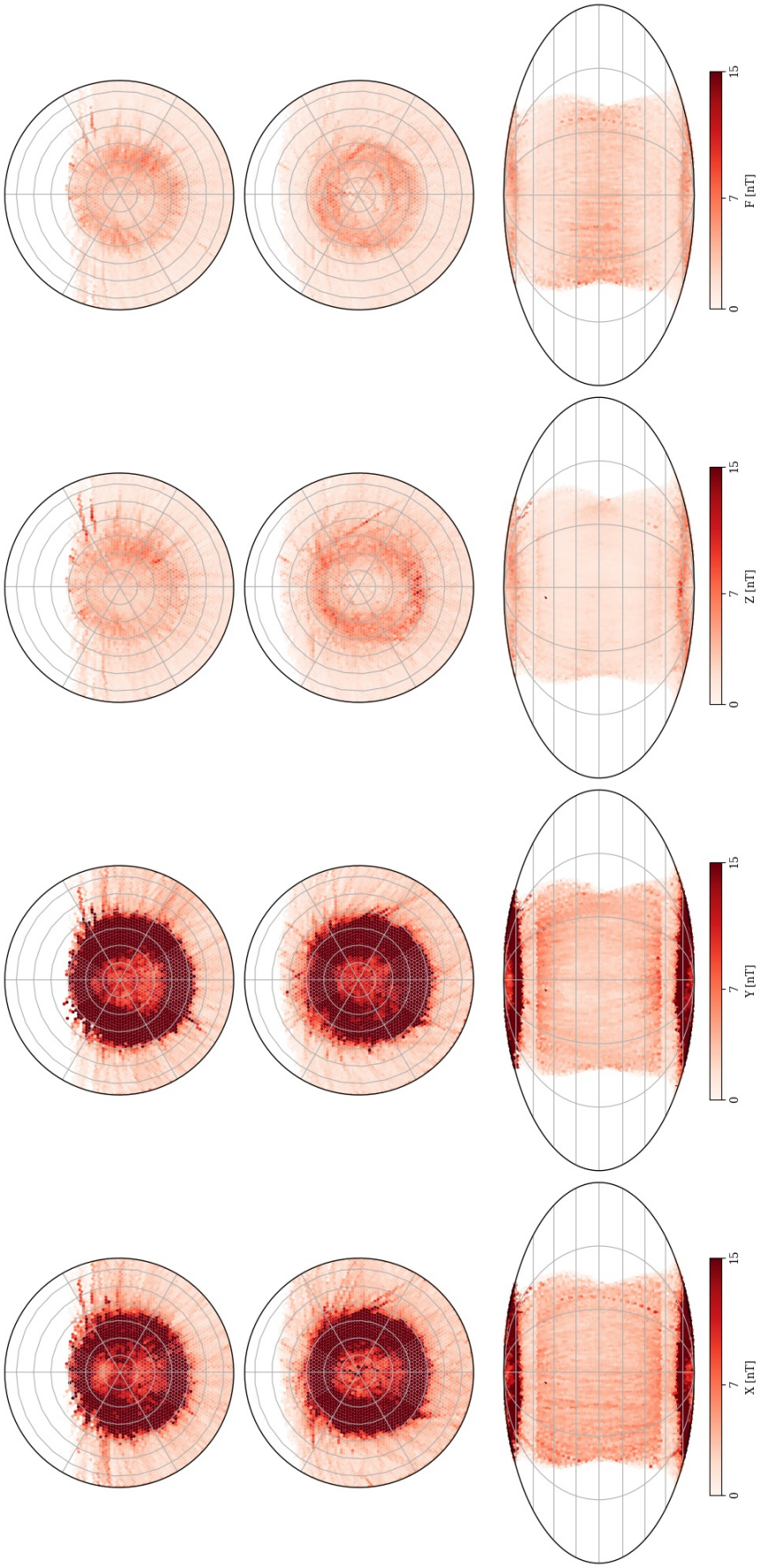

Figure 7.2: The corresponding standard deviations for the data shown in Figure 7.1

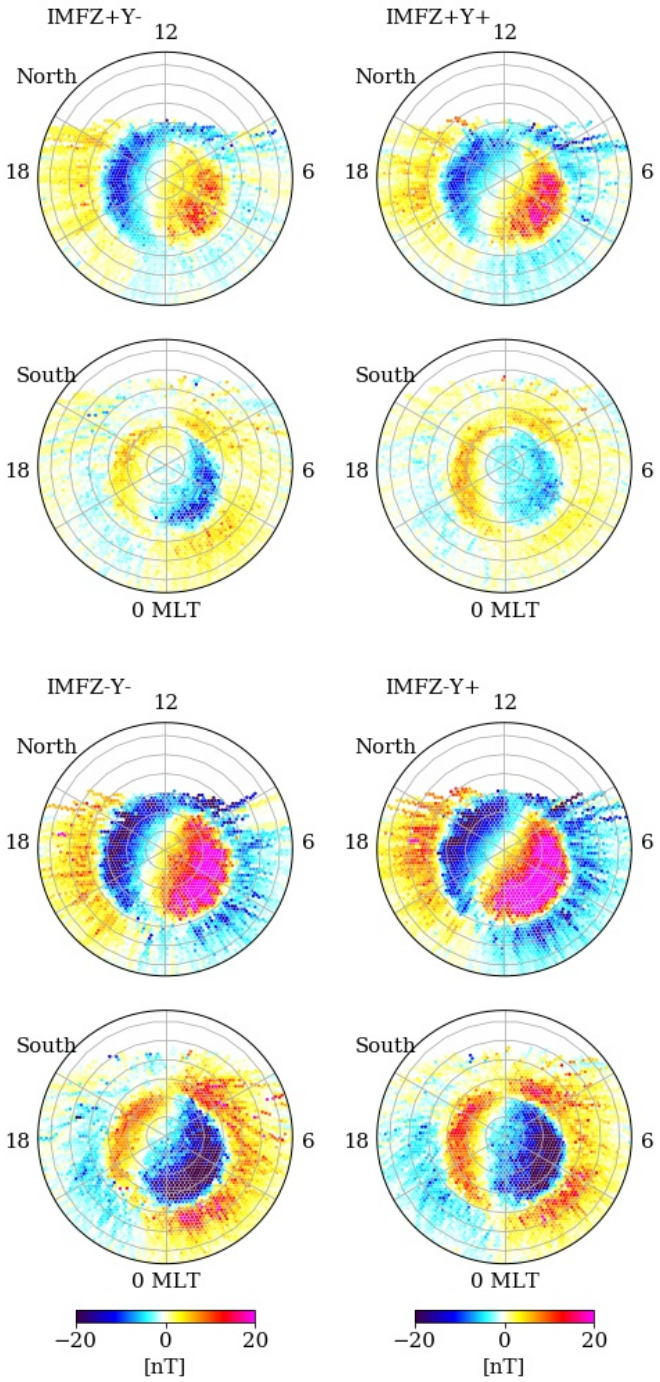

Figure 7.3: The vertical (Z) component residual medians in QDMLT coordinates over the Northern and Southern Hemispheres, for data segregated into four bins depending on the quadrant of the IMF clock angle ($\theta = \arctan B_y/B_z$). This shows the stronger currents present during $B_z < 0$ and the differing rotation of the system in each hemisphere due to the sign of B_y.

7.1.3 Notation

The handling of the gridded residuals is more complex in this chapter, so some notation is adopted to help describe this.

The CHAOS model components, core, magnetosphere, and lithosphere, are denoted as $\boldsymbol{m}_C + \boldsymbol{m}_M + \boldsymbol{m}_L = \boldsymbol{m}_{C,M,L}$. GEO grid points are $\{i\}$, and QDMLT grid points are $\{j\}$, i.e. $\{i\}$ is the set of latitude and longitude coordinates and $\{j\}$ the set of QDLAT and MLT coordinates. The input data vector, $\boldsymbol{d}$, is thus split into a set of vectors at each grid point, $\boldsymbol{d}_i$, or, $\boldsymbol{d}_j$. The median values of the vector, $\boldsymbol{v}$, derived on the grid at positions i, are denoted as $(\boldsymbol{v})_i\,|_{med}$, with the standard deviation likewise: $|_{std}$. The lithospheric estimate derived in the previous chapter, LITH_0, then becomes, at the i-th grid-point,

$$(\mathrm{LITH}_0)_i = (\boldsymbol{d} - \boldsymbol{m}_{C,M})_i \Big|_{med}. \tag{7.1}$$

A QDMLT grid point estimate, at positions j, where the CHAOS lithospheric field is also subtracted, is similar:

$$(\mathrm{IONO}_0)_j = (\boldsymbol{d} - \boldsymbol{m}_{C,M,L})_j \Big|_{med}. \tag{7.2}$$

LITH_0 is a function of the position vectors of the GEO grid: $\mathrm{LITH}_0 = f(\mathrm{LAT}, \mathrm{LON}, \mathrm{RAD})$, where LAT and LON are fixed at the equidistant spacing of the grid points, but RAD is the median radius of the data within each bin. The same follows for IONO_0, with instead $\mathrm{IONO}_0 = f(\mathrm{QDLAT}, \mathrm{MLT}, \mathrm{RAD})$.

7.2 Further data rejection

The previous sections have demonstrated the large strength and variability of the auroral oval contamination at this point still present in the candidate data for the lithospheric field model. This motivates the usage of further data selection, since the criteria are not yet as stringent as in other contemporary models. Following LCS-1 (Olsen et al., 2017) and others, here I select data according to merging electric field (MEF). I also introduce a new selection criterion which screens out the polar passes containing strong AEJ signatures.

7.2.1 Rejection by merging electric field (MEF)

MEF is a quantity that estimates the amount of energy transfer between the solar wind and the magnetosphere, and the form adopted in recent studies was derived by Newell et al. (2007) (there are earlier forms):

$$MEF = E_m = 0.33 v^{4/3} B_t^{2/3} \sin^{8/3}(|\theta|/2), \tag{7.3}$$

where v is the solar wind speed, B_t is the transverse IMF component (i.e. $(B_z^2 + B_y^2)^{1/2}$) and $\theta = \arctan B_y/B_z$ is the IMF clock angle. v is in $\mathrm{km\,s^{-1}}$ and B_t in nT, to yield E_m in units of $\mathrm{mV\,m^{-1}}$, where the values are scaled dimensionlessly since the factors and exponents are derived empirically. The form of MEF is therefore physically motivated and its precise value is tuned by empirical observations so it is a reliable tool to predict solar wind energy input. In order for it to better correlate with the response of ionospheric currents, it should be suitably time averaged to account for the lagging effect of magnetospheric processes.

The precise application I adopt to apply MEF follows the description by Olsen et al. (2014). IMF data are taken from the OMNI 1-minute resolution dataset, and then time averaged over the preceding 2-hour period using a weighted average with weights of $w_k = \exp(-k\Delta t/0.75h)/\sum w_k$ which give more importance to the more recent data points. Data are then rejected where $E_m > 0.8\mathrm{mV\,m^{-1}}$ but only over the polar regions (QDLAT $> 50°$), following Olsen et al. (2017).

7.2.2 Rejecting anomalous passes by AEJ activity

The second new selection criterion rejects polar passes according to the strength of the AEJ estimated following the procedure in Chapter 5. On each pass, all the data (at QDLAT>50°) are either rejected or retained according to the AEJ strength being below a threshold value. This threshold was set to reject the noisier 50% of the passes (of all passes, before data selection was applied). The reason for introducing this criterion was to remove particular outlier passes where a strong perturbation occurred even within the conditions that otherwise predict generally quiet conditions. This has a similar effect to the more common procedure of rejecting data having anomalously large residuals to existing field models.

7.2.3 Effect of data rejection

The effects of these two selection procedures are shown in Figures 7.4 (GEO) and 7.5 (QDMLT). The numbers of data remaining in each bin are shown in Figure 7.6, and indicative distributions of data are shown for nine of the GEO bins in Figure 7.7. The procedures produce a very clear reduction in the spread of input data, with typical standard deviations within the auroral oval dropping from >15 nT to <7 nT and a reduction in the magnitude of the auroral oval perturbation from >20 nT to <10 nT. The AEJ selection successfully removes periods when the AEJ is stronger and a number of spurious passes when it is particularly strong, although some do still remain. It is not feasible to reject more passes, however, as then there would be some unpopulated bins (see Figure 7.6).

Before the selection, much of the strong variation is in the post-midnight sector which can be attributed to the more sporadic substorm activity which occurs during the Kp<3 conditions already imposed (substorms continue to occur, driving strong magnetic perturbations, even during quiet times). This structure in the variability is mostly suppressed by these new selection procedures and so the remaining auroral oval signal is more stable. This makes it easier to more consistently remove this remaining ionospheric contamination from the lithospheric signal.

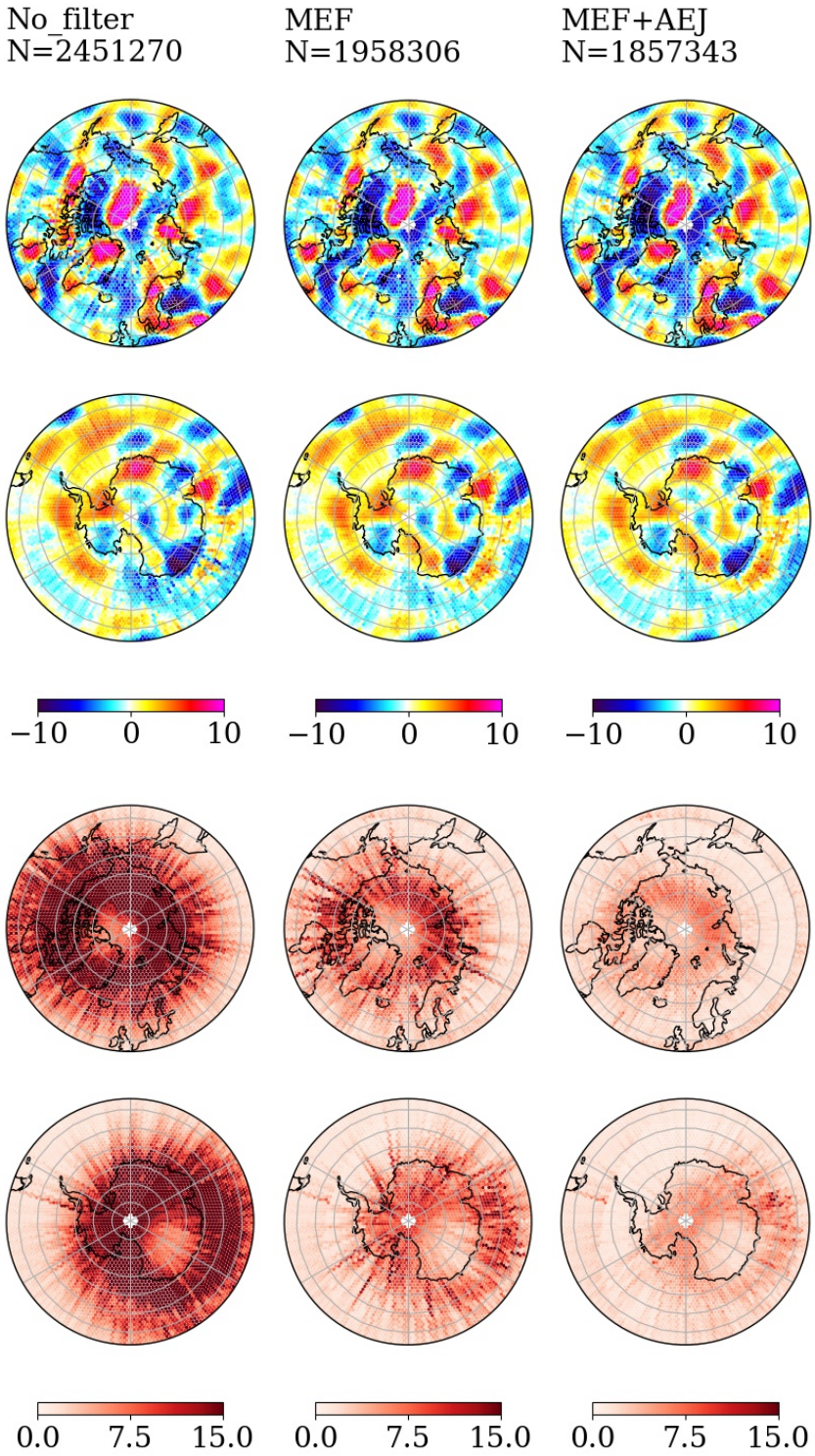

Figure 7.4: Z component medians (top) and standard deviations (bottom) of the stacked data without further data rejection (left), filtering by merging electric field (centre), and by additionally rejecting passes with a strong auroral electrojet signature (right). Units are nT.

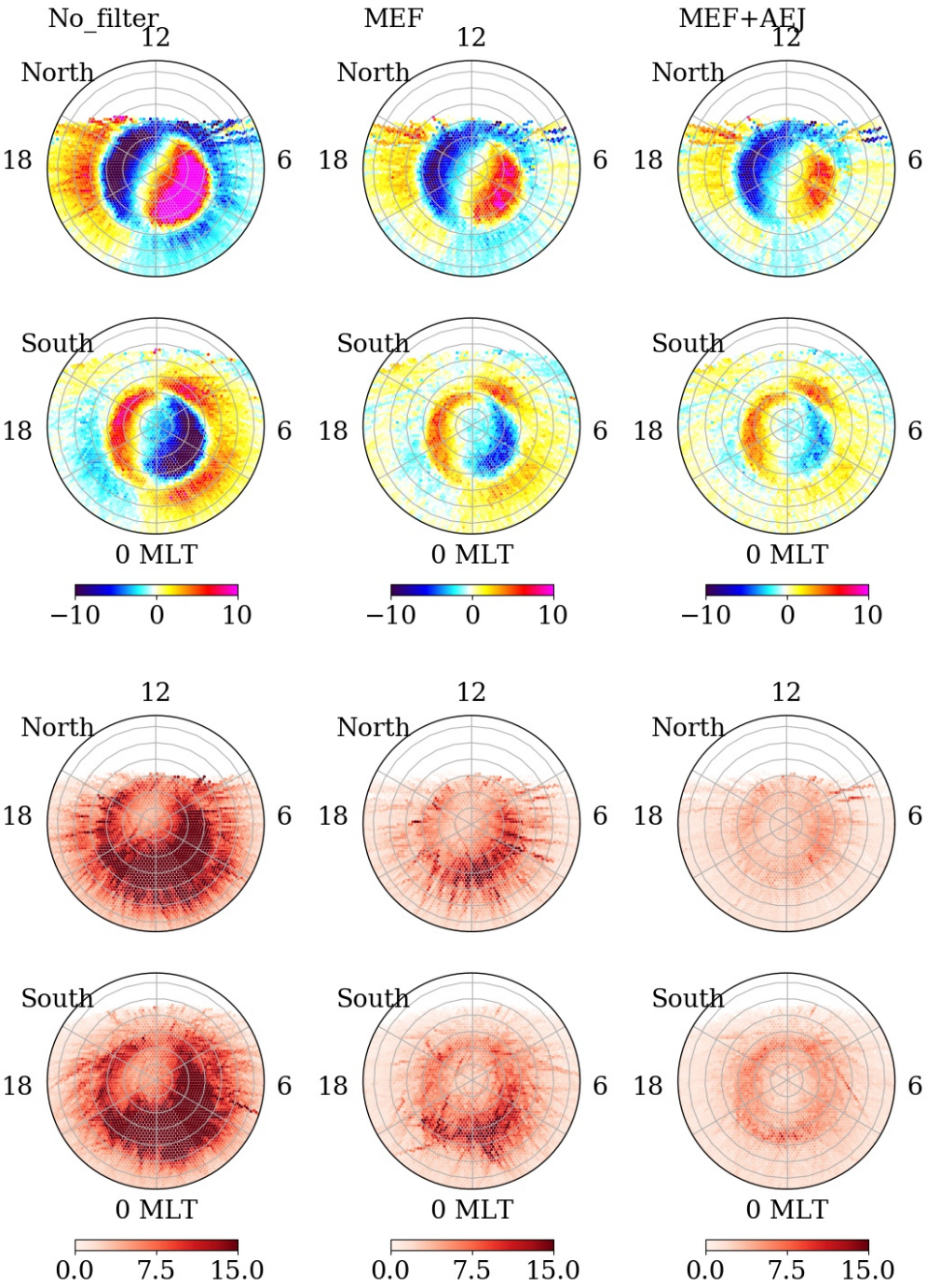

Figure 7.5: As in Figure 7.4 but in QDMLT coordinates, after also removing the CHAOS lithospheric field.

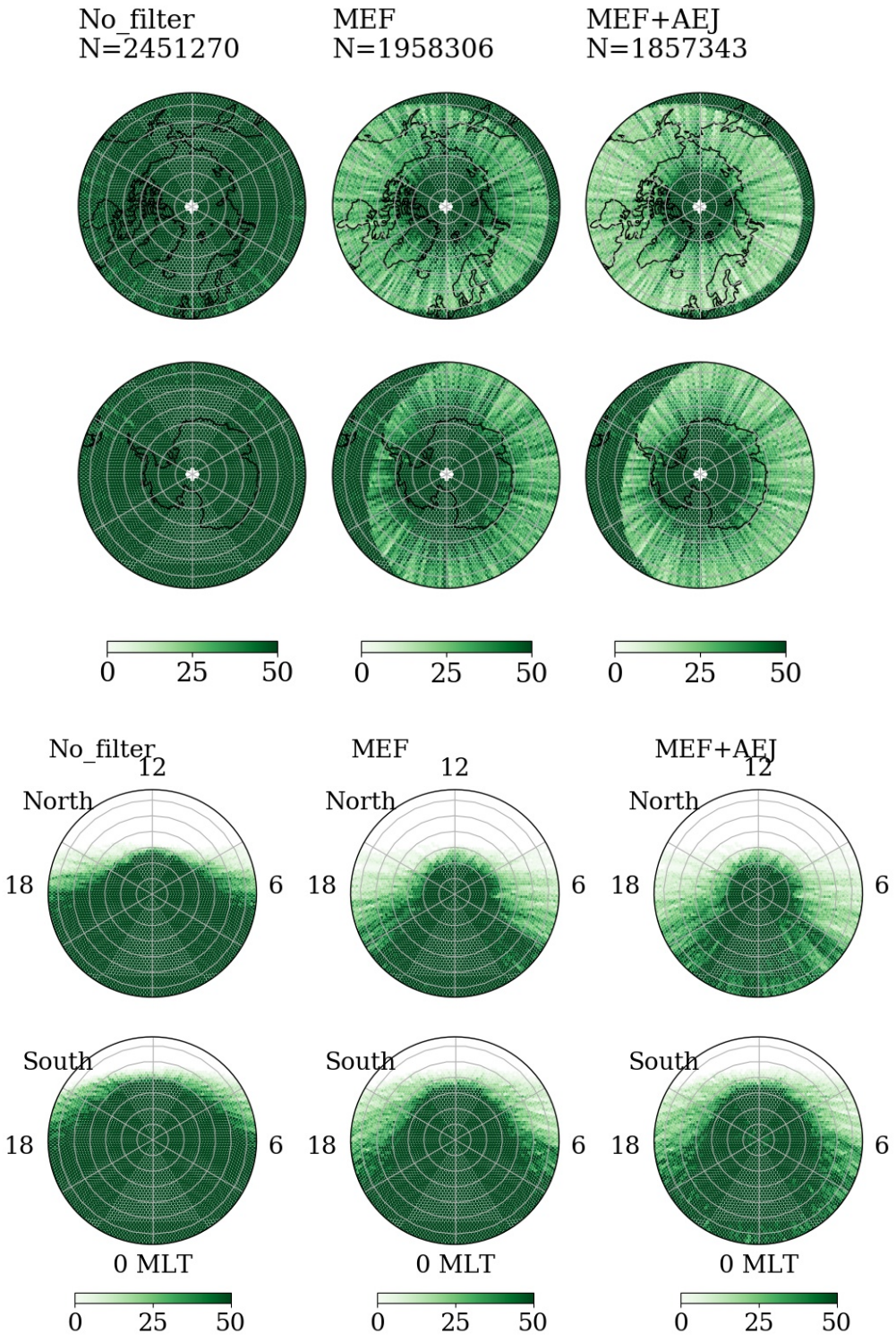

Figure 7.6: Number of data contributing to each bin, corresponding to (top) Figure 7.4 and (bottom) Figure 7.5. The number, N, refers to the total number of remaining data globally.

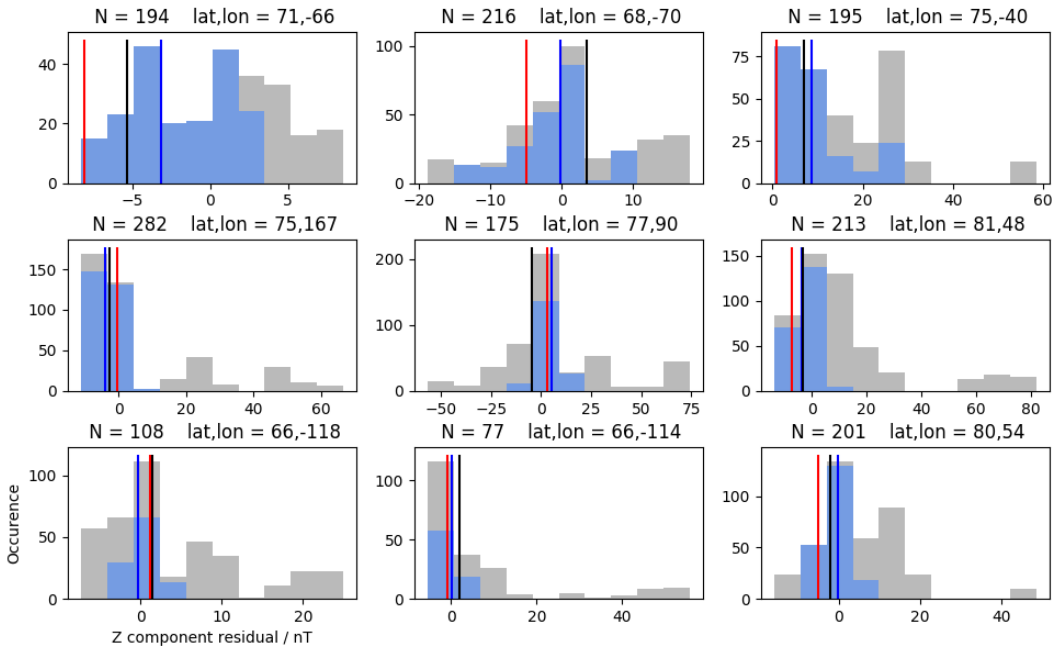

Figure 7.7: Histograms of Z component residual data contributing to nine randomly selected GEO bins in the auroral zone. Grey bars show data before additional data selection and the blue after, with the vertical blue line showing the new median value. Vertical red and black lines show predictions by LCS-1 and MF7 respectively.

7.3 Correcting for the ionospheric noise

This section explains the methodology which attempts to remove the ionospheric signal from the data, and then a spherical harmonic model is created from the corrected data. The notation used to describe the algorithm is introduced first, and the steps are summarised as a flow chart in Figure 7.8, along with a graphical view of the results in Figures 7.9 & 7.10.

7.3.1 Extending notation

Here I extend the notation described in section 7.1.3.

IONO_0 gives an estimate of the unmodelled ionospheric signal which is present in the input data, being more accurate when the spread of residuals in this grid, $(\boldsymbol{d} - \boldsymbol{m}_{C,M,L})_j\,|_{std}$, is low. It therefore follows that we can improve LITH_0 by subtracting this estimate from the input data, $\boldsymbol{d}$:

$$(\text{LITH}_1)_i = (\boldsymbol{d} - \boldsymbol{m}_{C,M} - (\text{IONO}_0)_j)_i \Big|_{med}, \tag{7.4}$$

where each input residual is identified by its position in the QDMLT grid (j) and adjusted according to the value of $(\text{IONO}_0)_j$ at that point.

It is instructive to describe these reduced data in terms of the source and noise fields they contain. LITH_0 contains contributions from the real target lithospheric field, $\boldsymbol{L}$, unmodelled core and magnetospheric fields originating from the CHAOS model (where we also include large scale induced fields), $\boldsymbol{\epsilon}^{(0)}_{C,M}$, ionospheric field, $\boldsymbol{\epsilon}^{(0)}_{I}$, and other unmodelled sources and random noise, $\boldsymbol{\epsilon}^{(0)}_{r}$, so that

$$(\text{LITH}_0)_i = \left(\boldsymbol{L} + \boldsymbol{\epsilon}^{(0)}_{C,M} + \boldsymbol{\epsilon}^{(0)}_{I} + \boldsymbol{\epsilon}^{(0)}_{r}\right)_i \Big|_{med}, \tag{7.5}$$

and

$$(\text{LITH}_1)_i = \left(\boldsymbol{L} + \boldsymbol{\epsilon}^{(1)}_{C,M} + \boldsymbol{\epsilon}^{(1)}_{I} + \boldsymbol{\epsilon}^{(1)}_{r}\right)_i \Big|_{med}. \tag{7.6}$$

Since IONO_0 is subtracted within the formulation of LITH_1, it is expected that $\boldsymbol{\epsilon}^{(1)}_{I} < \boldsymbol{\epsilon}^{(0)}_{I}$, and is hopefully closer to random noise scattered around zero. It follows that LITH_1 should be closer to $\boldsymbol{L}$.

Similarly,

$$(\text{IONO}_0)_j = \left(\boldsymbol{I} + \boldsymbol{\epsilon}^{(I,0)}_{C,M,L} + \boldsymbol{\epsilon}^{(I,0)}_{I} + \boldsymbol{\epsilon}^{(I,0)}_{r}\right)_j \Big|_{med}, \tag{7.7}$$

where $\boldsymbol{I}$ is the true ionospheric field. Note that the noise sources here are different from before because they are instead collected within the QDMLT bins, $\{j\}$.

The effect of the correction made between LITH_0 and LITH_1, i.e. the effect of the part of $\boldsymbol{\epsilon}_I^{(0)}$ which is not part of $\boldsymbol{\epsilon}_I^{(1)}$, can be inspected by looking at the difference, $(\mathrm{LITH}_1)_i - (\mathrm{LITH}_0)_i$. This is the compound effect within GEO coordinates of $\boldsymbol{\epsilon}_I^{(0)}$, itself being more coherently organised within QDMLT coordinates.

The effect of $\boldsymbol{\epsilon}_I^{(1)} + \boldsymbol{\epsilon}_r^{(1)}$, that is, the noise remaining after the ionospheric correction, can be inspected by looking at the standard deviations of the data contributing to LITH_1,

$$(\boldsymbol{d} - \boldsymbol{m}_{C,M} - (\mathrm{IONO}_0)_j)_i \Big|_{std}, \tag{7.8}$$

as well as:

$$(\mathrm{LITH}_1)_j = (\boldsymbol{d} - \boldsymbol{m}_{C,M} - (\mathrm{IONO}_0)_j)_j \Big|_{med,std}, \tag{7.9}$$

which shows the organisation of the input data in the QDMLT grid, and:

$$(\boldsymbol{d} - \boldsymbol{m}_{C,M} - (\mathrm{IONO}_0)_j - (\mathrm{LITH}_1)_i)_j \Big|_{med}, \tag{7.10}$$

which shows the organisation of the unaccounted signal after removing our estimates of both the ionospheric and lithospheric fields.

7.3.2 Demonstration of algorithm and results

Figures 7.9 (medians) & 7.10 (standard deviations) show the gridded data at different steps in the process (downwards component from Swarm Alpha). The plots for the other components and for Swarm Bravo are in Appendix B. At this point the data have had the more stringent selection criteria applied (MEF and AEJ), but strong ionospheric contamination remains. The first column shows these data gridded in GEO, comparable to the data used in the previous chapter (albeit with the additional data selection applied). The second column has had the full CHAOS model subtracted, including the lithospheric part, before gridding in QDMLT. This approximates the external field bias in the data over average quiet conditions, containing an auroral oval feature and a large scale hemispheric bias as described previously. The third column shows the result of subtracting this bias field from the input data and then gridding in GEO, $(\mathrm{LITH}_1)_i$, which is later used to derive a spherical harmonic model. Comparing the

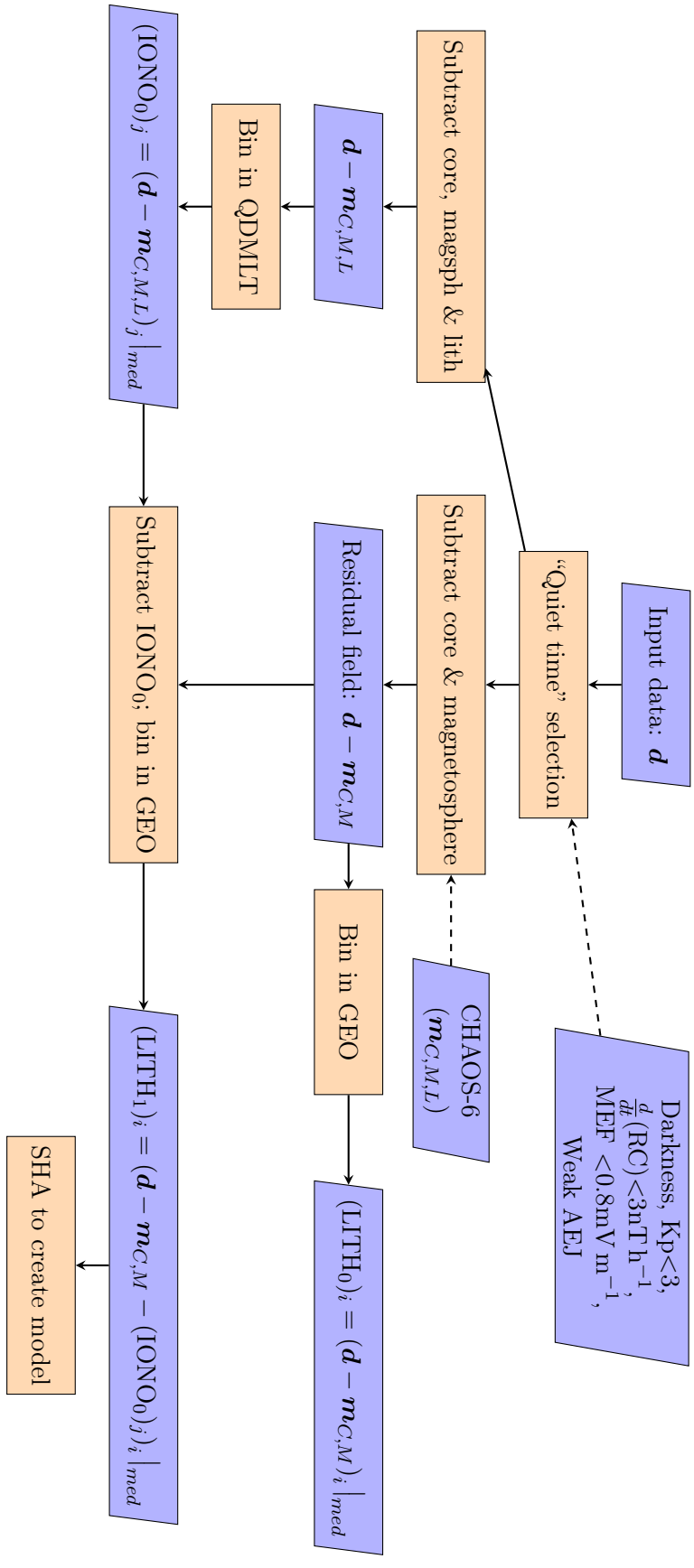

Figure 7.8: Flow chart showing the overall procedure used to reduce Swarm data to create a lithospheric field model, including correcting by the ionospheric field

standard deviations in the first and third column shows a slight reduction in their sizes, indicating some reduction of the variability of data at each GEO grid point due to the samples of data contributing from different local times. This effect appears stronger in the Northern Hemisphere.

The fourth column shows the "corrected" data gridded instead in QDMLT, where the prominent auroral oval and hemispheric biases have been removed. Some weak latitudinal banding appears which could be related to the subtraction of the degree 16 part of the CHAOS model in creating $(\mathrm{IONO}_0)_j$. The fifth column shows the difference between the uncorrected and corrected lithospheric signal, $(\mathrm{LITH}_1)_i - (\mathrm{LITH}_0)_i$. This shows the average effect of the external fields on the input data which at each GEO grid point contain a range of data collected at different local times, and is particularly strong around the auroral oval. The remaining columns show the organisation of the gridded residuals after removing both $(\mathrm{IONO}_0)_j$ and $(\mathrm{LITH}_1)_i$ from the input data. In GEO coordinates this is zero everywhere by definition, and in QDMLT this is generally of magnitude < 1nT.

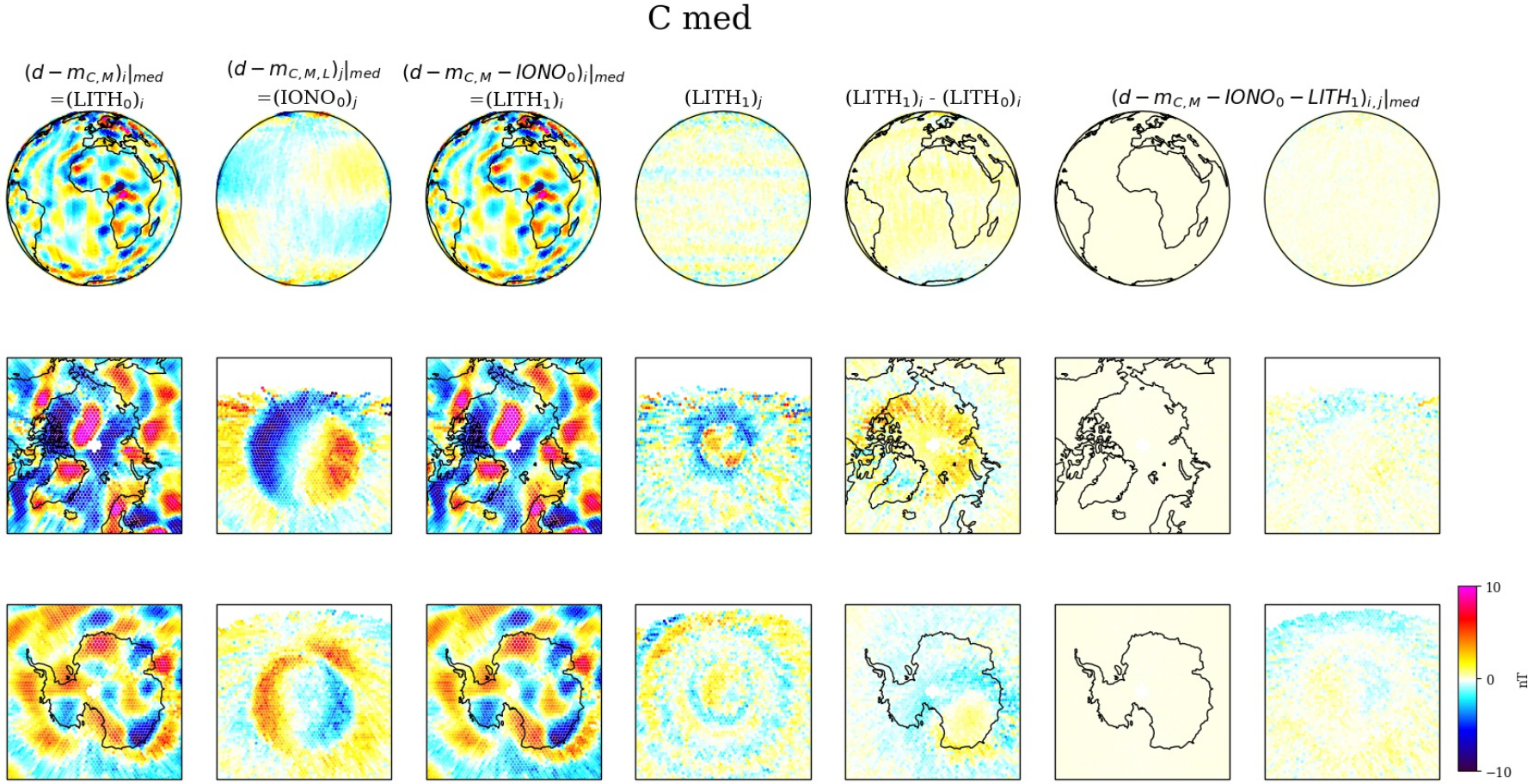

Figure 7.9: The downwards component (C / Z) medians from different procedures - see column titles and refer to text for their meanings. Each column depicts the data processed in different ways, showing (top) a view over the hemisphere centred on the Greenwich Meridian or 0 MLT, (middle row) the Northern Hemisphere, and (bottom) the Southern Hemisphere. The maps with continents show data gridded in GEO coordinates. The maps without continents are in QDMLT coordinates, where the nightside view (centred on 0 MLT) is shown at the top, and the Northern and Southern views below have midnight to the bottom, dawn to the right, and dusk to the left.

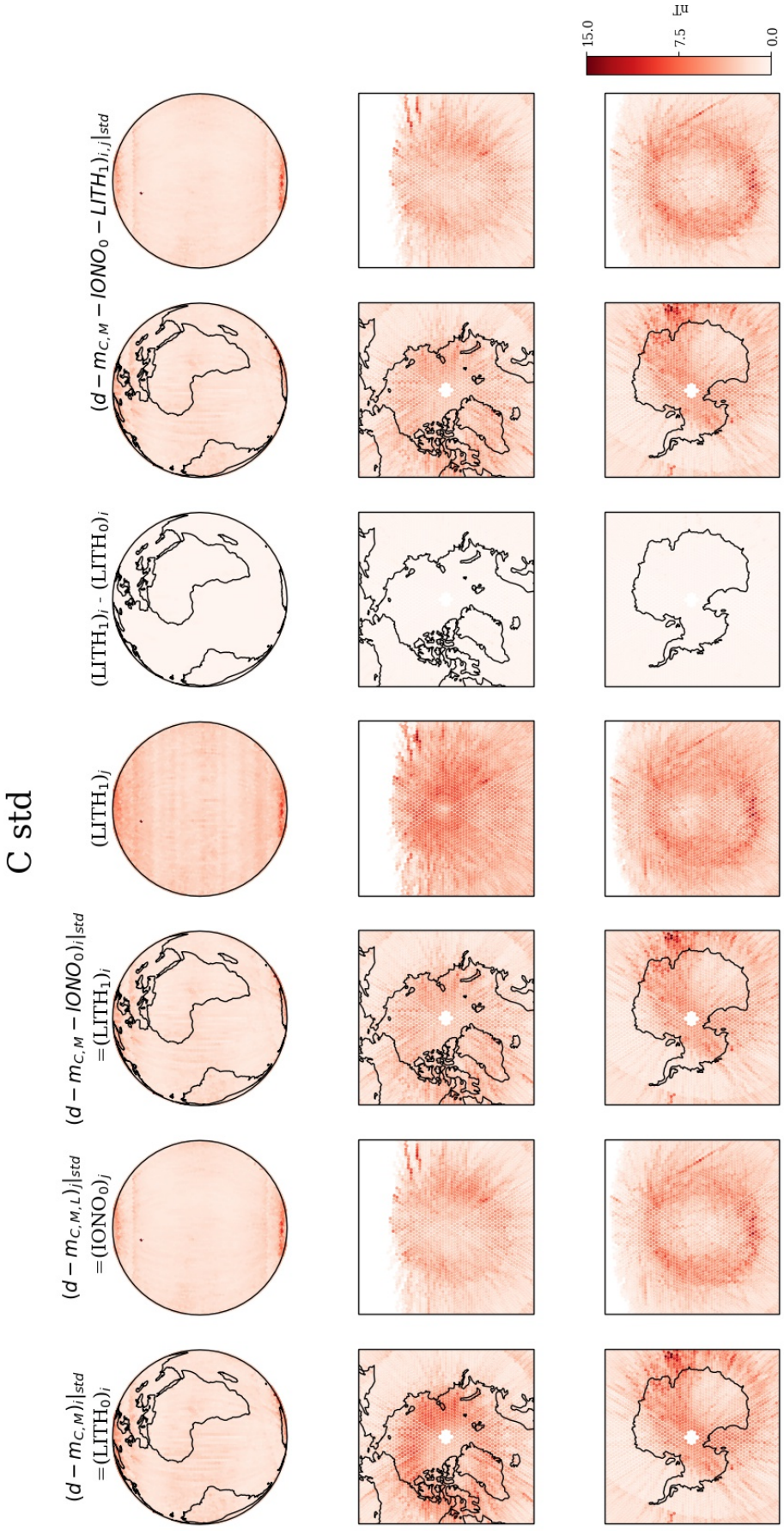

Figure 7.10: The corresponding standard deviations for Figure 7.9

7.4 A new spherical harmonic model

7.4.1 Inversion procedure and comparison of models

In this section the new gridded data (before and after additional data selection by MEF and AEJ, and after correcting with IONO_0) are inverted for spherical harmonic models. These are analysed and compared against each other and against published models.

Figures 7.11 & 7.12 show the power spectra of an ensemble of models that were derived while exploring options for the inversion procedure. Models produced from four input gridded data sets are termed "model 0, 1, 2, & 3", respectively for:

- (0) before the additional data selection described in this chapter,
- (1) for low MEF conditions,
- (2) for low MEF and low AEJ activity,
- (3) after the IONO_0-correction.

A range of inversion procedures were tried, shown in each subplot, labelled:

- (0) Least squares fitting (L2), as in Equation 6.7, but with $\boldsymbol{W}^{\boldsymbol{\sigma}} = \boldsymbol{I}$
- (a) Least squares fitting (L2) with each point weighted by the variance of the contributing data
- (b) Least squares fitting (L2) with the weights normalised to limit their extreme range
- (c) Least squares fitting (L2) without weights, but including a regularisation matrix to damp the power at high degrees
- (d) Least squares fitting (L2) with both weights and damping
- (e) Least squares fitting (L2) with normalised weights and damping
- (f) Least squares fitting (L2) with weaker damping
- (g) Including variance weights; Iteratively reweighted least squares (IRLS) to implement the L1-norm
- (h) Weights, IRLS, and damping, i.e. Equation 6.10

Figure 7.11 contains models derived from data (four years of Swarm Alpha) that include gaps at the poles, and in Figure 7.12 the gaps were filled using values from LCS-1. The models of Figure 7.12 also include data from Swarm Bravo over the same time period from which a new gridded dataset (at a higher altitude) is derived and inverted together with the set from Alpha, but only a minor improvement was noted. For each model,

the L2-norm misfit, χ, is calculated as

$$\chi = \sqrt{\frac{1}{N}\sum_{i=1}^{N}\left[\frac{d_i - \tilde{d}_i}{\sigma_i}\right]^2}, \tag{7.11}$$

where d_i are the data inputs (i.e. the medians of binned values at each grid point), $\tilde{d}_i$ are the model predictions at the same locations, σ_i are the standard deviations of data within each bin, and N is the number of points (e.g. as in Stockmann et al., 2009).

For the data with polar gaps, when using the variance weights directly in both the L2 and L1 inversions without damping, the power spectra increase in strength and oscillate (with larger power in the even terms), for models 0, 1, and 2. The lower misfits of these models, and the fact that the disturbance disappears in the other models (and in model 3, where input data variances are lower), indicate that the inversion is overfitting. Both damping the models and infilling the gaps are independently able to remove this artefact successfully. Infilling the gaps should also reduce the likelihood of other artefacts.

The damped IRLS procedure (h) appears to be the most effective at producing stable models which have the most similar power spectra to each other when using different input data. This is expected because minimising the L1-norm reduces the effect of the outliers caused by the large magnitude external field noise on the smoothly varying model being generated, and has previously been shown to be appropriate for geomagnetic field modelling (Walker and Jackson, 2000). The procedure of evaluating medians will itself also reduce the presence of outliers before inversion.

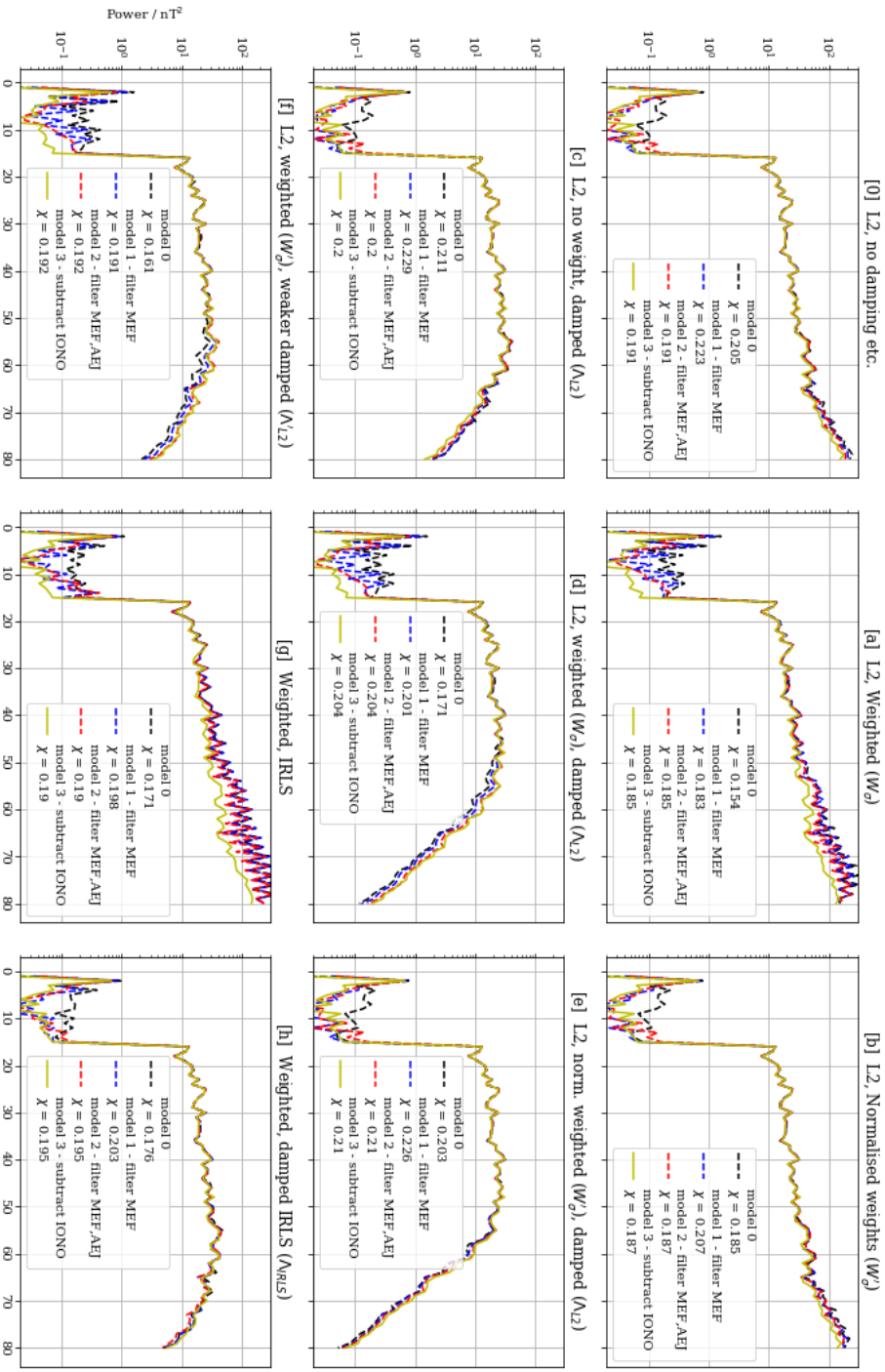

Figure 7.1.1: Power spectra of an ensemble of models. Each subplot shows models produced from a different inversion procedure. Within each subplot, each coloured line shows the resulting model from a different input data set. "Model 0" (black) is from data without the additional data selection. "Model 1" (blue) data are selected for low MEF. "Model 2" data are also selected for low AEJ detections. "Model 3" data are corrected by ($IONO_0$.

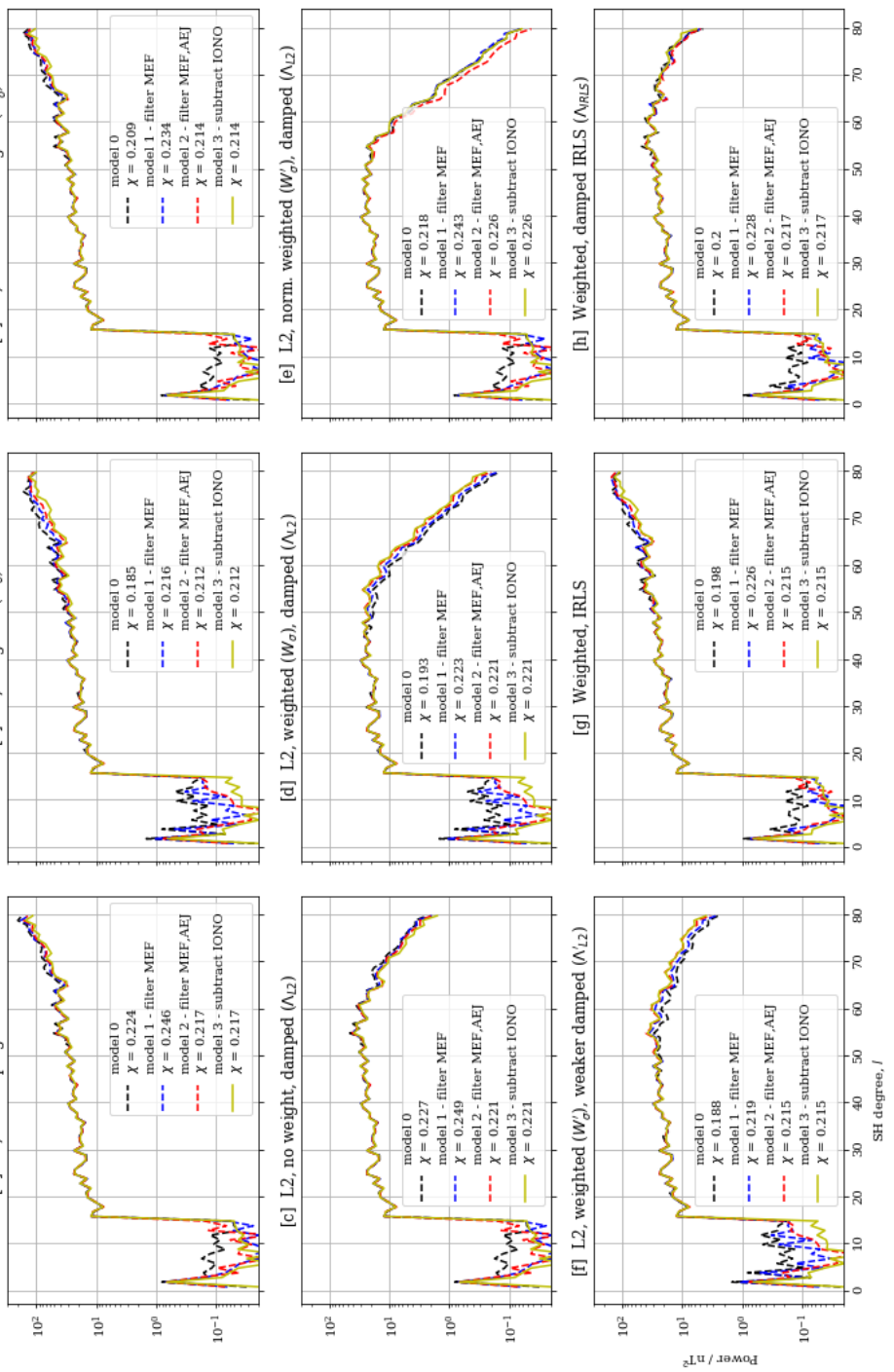

Figure 7.12: As for Figure 7.11 but derived from input with the polar gaps infilled with LCS-1 values, as well as Swarm Bravo data.

7.4.2 Assessment of final model

Figure 7.13 shows the residuals between the final models (i.e. 0, 1, 2, 3 (h) from the lower-right subplot of Figure 7.12) and the gridded data input to them. The residuals are successively reduced, indicating the successive reduction of noise in the input data and that the model (which is spatially smooth) is better able to capture the (fairly smooth) lithospheric signal which is overlaid by noise (which is more granular). In each case, the polar gaps are infilled with LCS-1 values, to which there are large residuals at the North poles. This appears to be due to the inability of my models to fit the small-scale large-amplitude field predicted by LCS-1, and the models being poorly behaved at the poles.

Figure 7.14 shows the power spectra and degree correlation of the models 2 and 3 (h) (i.e. before and after the IONO_0-correction) compared to LCS-1, MF7 and CHAOS-6. They both show a reasonable agreement to these models up to degree 60, beyond which the damping dominates. Weaker damping may well be feasible but this was not explored further. Model 3h exhibits a weak but consistently better agreement, indicating some success in correcting for the ionospheric field. Most notably, the other models are able to resolve higher degrees because of the inclusion of the lower altitude data from CHAMP, and in the case of LCS-1, the use of gradients. The point here is to demonstrate the efficacy of the ionospheric correction technique.

The vertical components of LCS-1, evaluated to its full degree 185 and to degree 80, are shown in comparison to models 2h and 3h in Figure 7.15. The most notable deficiency of my models is North-South banding originating from the along-track correlated noise, i.e. the appearance of satellite tracks in the data. This is obvious over the oceans where the crustal field is weaker, and could be the origin of spurious features in some regions. LCS-1 resolves features more clearly since it extends to higher degree (even when the evaluation is truncated to degree 80): the edges of features are unphysically smoother in my models.

The differences between each of models 2h and 3h, and LCS-1, and between themselves, are shown in Figure 7.16. This shows the regions where my models have unphysical signals. The strongest of these features outside of polar regions are around the Bangui anomaly, south of the Indian Ocean, over Ukraine near the Kursk anomaly, over eastern Russia, and over the North Atlantic west of Portugal. In the case of the Bangui and Kursk anomalies, this is probably because of the difficulty of capturing the strong

sharp features in spherical harmonics, and the fact that my models are heavily damped at degrees 60-80. Looking at the polar regions, the ionospheric correction makes its strongest improvement north of Hudson Bay, but other large differences (to LCS-1) remain along the auroral ovals and at the poles. There is a low degree latitudinal banding visible in the differences between my models and LCS-1 because in the derivation of LCS-1 the core field was subtracted up to degree 14 whereas I included degree 15.

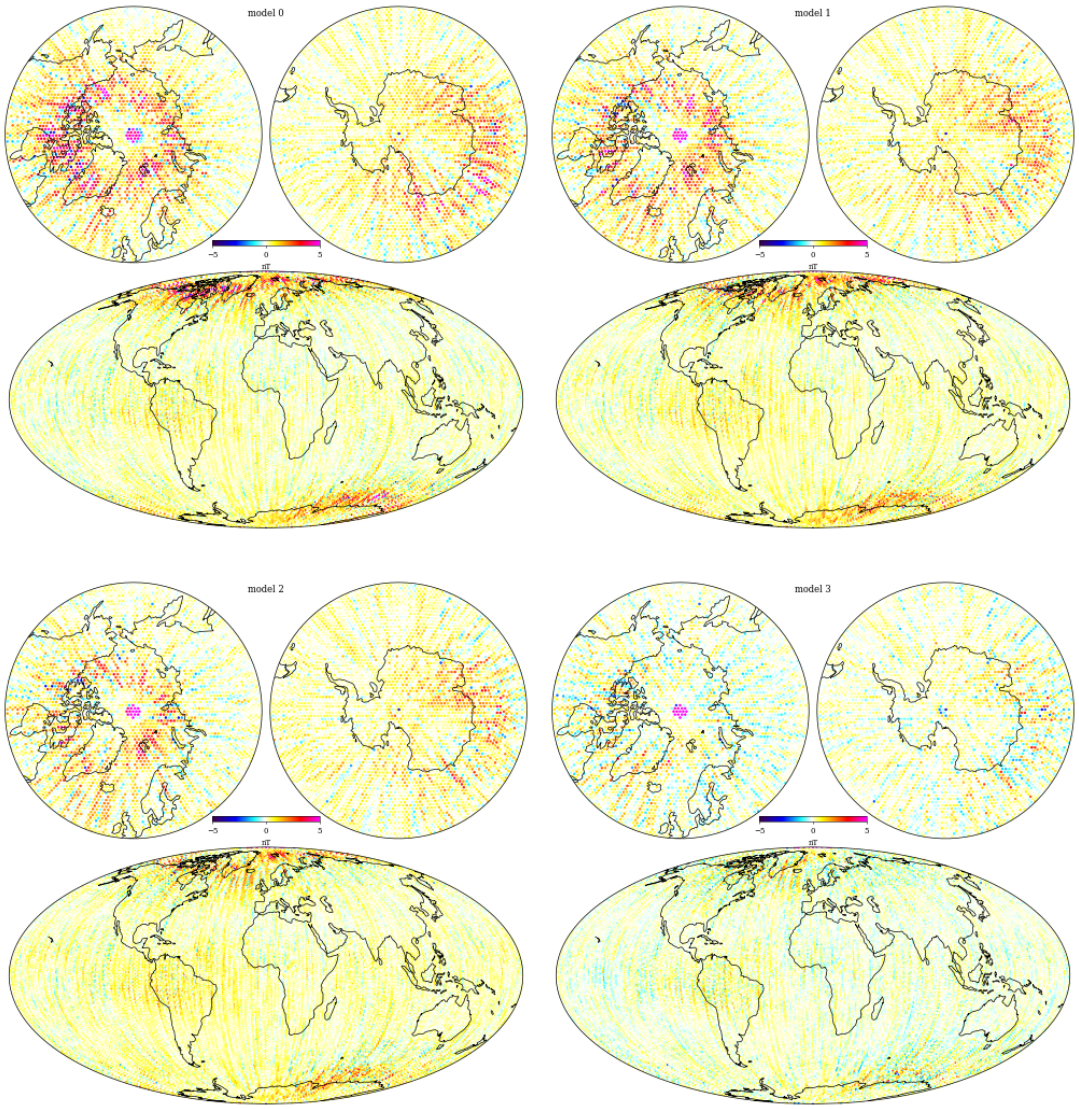

Figure 7.13: Residuals between the input gridded data and the model values, from the four models produced from the different levels of data selection/correction.

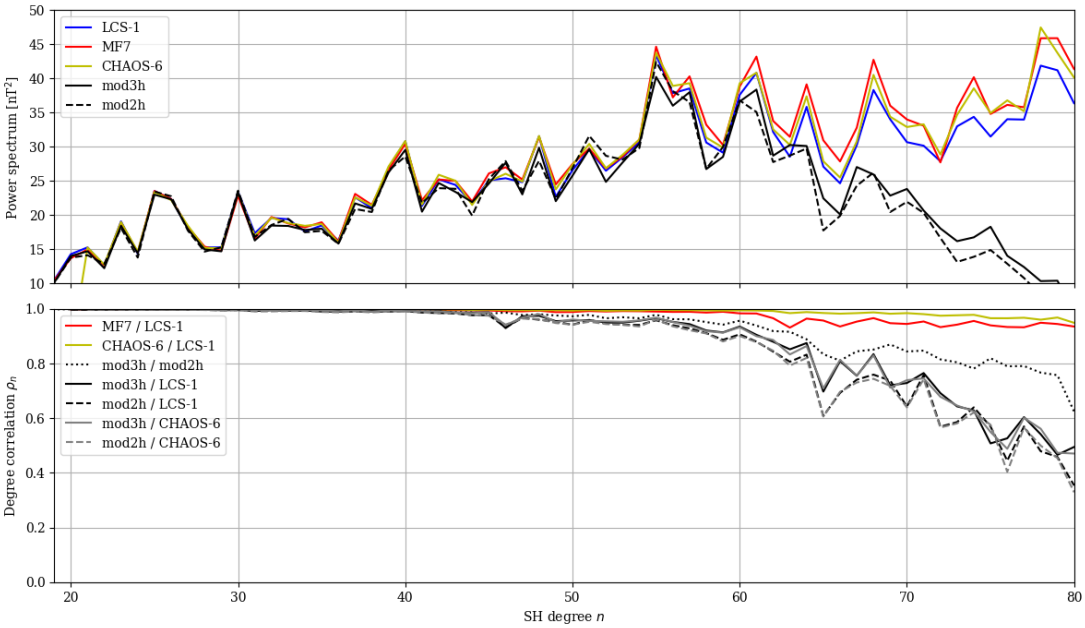

Figure 7.14: (Top) Power spectra of selected models. (Bottom) Spherical harmonic degree correlation.

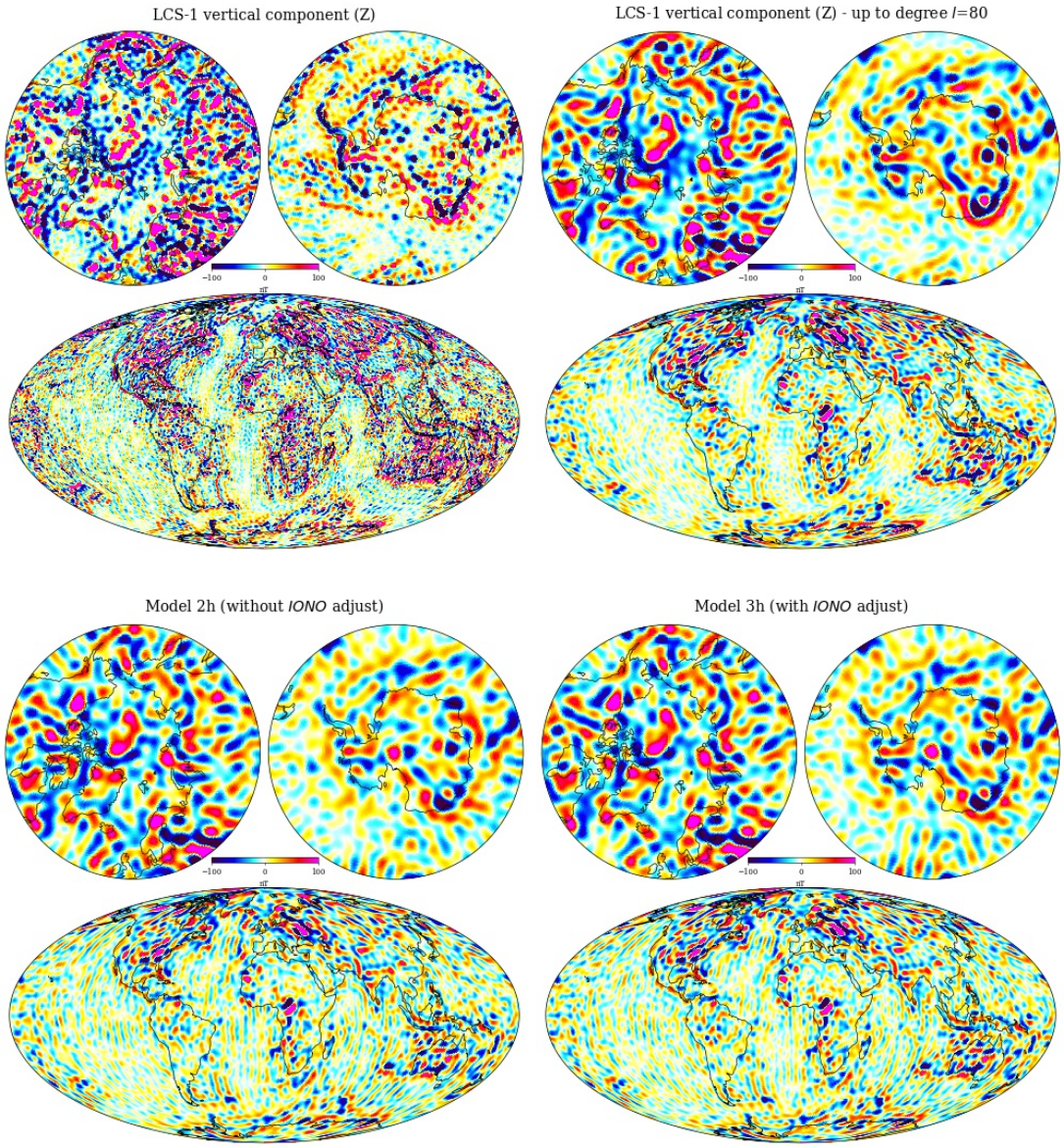

Figure 7.15: The vertical downwards (Z) component evaluated from LCS-1 (top left to degree 185, top right to degree 80), model 2h (before the ionospheric correction, bottom left), and model 3h (after the ionospheric correction).

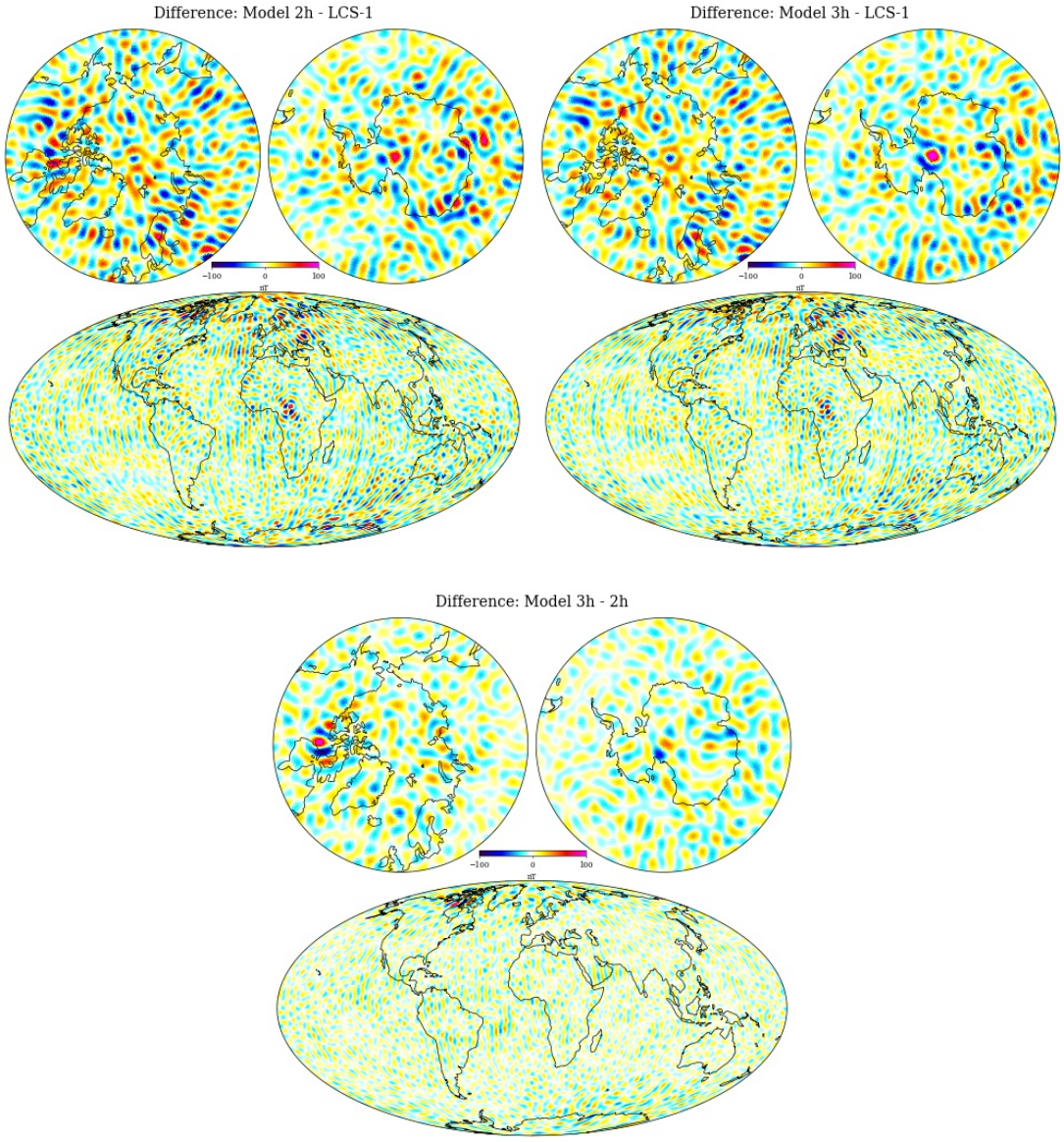

Figure 7.16: Differences in the vertical downwards (Z) component; (top left) between LCS-1 (truncated at degree 80) and model 2h, (top right) between LCS-1 and model 3h; (bottom) between model 2h and 3h.

Chapter 8

Discussion

This chapter reviews some of the key points of the previous three chapters and the connections between them. I start with a reflection on the study of the auroral electrojets of Chapter 5 and the binning technique of Chapters 6 & 7, and suggest some future research directions that might provide better descriptions of polar ionospheric fields. This is followed by a discussion about retrieving both the ionospheric and lithospheric fields, and how better understanding of the drivers of ionospheric activity should help this. Finally I suggest some extensions that could readily be applied to improve the lithospheric model of Chapter 7.

8.1 Quantifying drivers of ionospheric activity

In Chapter 5, the time/space behaviour of the auroral electrojets was investigated. As just one component of the horizontal ionospheric currents, they do not represent the full complexity of the three-dimensional system. They are, however, strongly indicative of the overall ionospheric response to solar wind driving, and represent a large proportion of the energy dissipation in the atmosphere from the magnetosphere. I demonstrated how the system, as a function of local time, responds to solar wind conditions, and longer term trends related to season, solar cycle phase, and secular variation due to change in the main field. A particular focus was hemispheric asymmetries in current strengths, due to 1) asymmetry in the core field providing differently shaped auroral regions and differing insolation patterns over each, and 2) twisting of the magnetosphere with the IMF-By component. Such intertwined issues complicate the interpretation of any particular observed variation.

Other studies have shown similar effects, and through more sophisticated methods are able to describe more of the full current system (e.g. Coxon et al., 2016; Juusola et al., 2009; Laundal et al., 2016a, 2018; Shore et al., 2017). Through synthesis of data from arrays of observatories (on ground and in LEO), and by sampling of different conditions over time, it is possible to describe the large-scale behaviour of ionospheric currents. This enables the creation of predictive models for ionospheric magnetic fields in terms of location and solar wind conditions, which can be used to probe magnetospheric/ionospheric processes, or, for example, for data correction in internal field modelling.

Shore et al. (2017, 2019) used ground observatory data and, by applying empirical orthogonal functions (EOF) and graph theory, systematically resolved the current systems into four dominant modes that arise from different physical drivers: DPY (magnetosphere twisting driven by IMF-By), DP2 (Dungey cycle convection driven by southward IMF-Bz), NBZ (reverse cell convection under northward IMF-Bz), and DP1 (substorm activity) - see Shore et al. (2019), their Figure 1. They investigated how these modes respond to IMF conditions at different lag times, finding that they have peaks in response at different times, from ten minutes to several hours. These can be explained in terms of different processes responding either promptly to solar wind input, or lagged through magnetospheric processes. Similarly, Milan et al. (2018), used principal component analysis (PCA) of FACs derived from the AMPERE experiment to explore the differing lagged responses of dayside and nightside FACs.

The "Average Magnetic field and Polar current System" (AMPS) model of Laundal et al. (2018) provides a good description of the overall ionospheric magnetic field in terms of solar wind conditions, and becomes very accurate when considering longer time scales (hence the "average" in its name). However, Shore et al. (2019) note that, due to its reliance on global (spherical harmonic) functions that must respond simultaneously everywhere (mitigated by temporally smoothed [20 minutes] solar wind inputs), the AMPS model cannot account for differing lag times in different locations (or indeed for lag times changing under different solar wind conditions, when the solar-wind-magnetosphere interaction will be different and when different current systems will dominate).

An example of relating the ionospheric field to solar wind conditions is shown in Figure 8.1. This shows the correlation coefficients between the magnetic field residuals

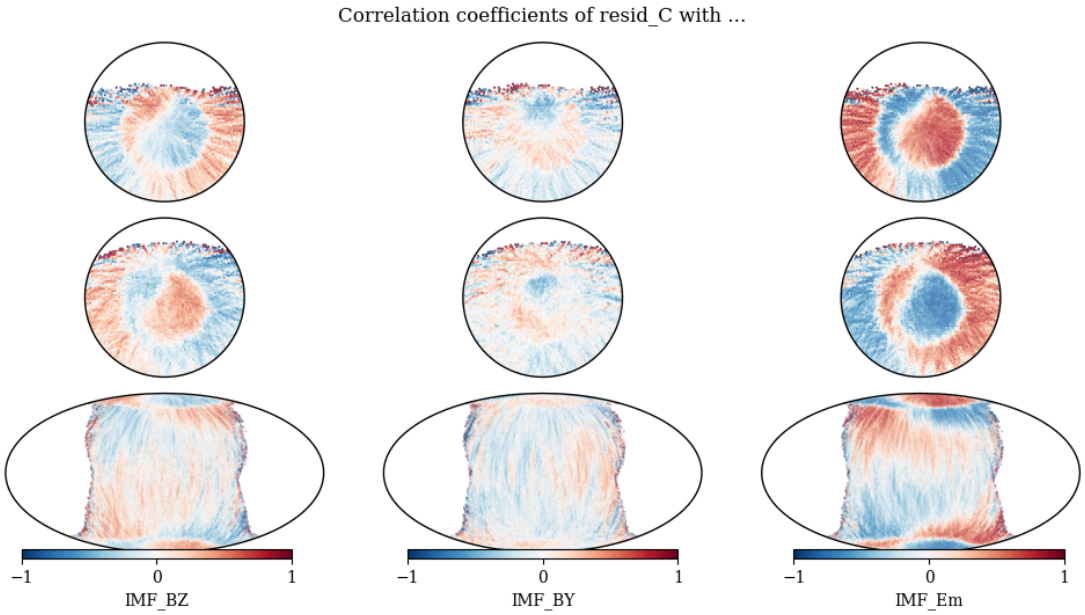

Figure 8.1: Correlation coefficients calculated at each QDMLT bin between the vertical downwards magnetic field component residuals (after selecting for quiet nightside conditions, and subtracting the core and magnetospheric field) and the IMF conditions: with (left) IMF-Bz 20-minute average, (middle) IMF-By 20-minute average, (right) 2-hour weighted average of merging electric field (Em / MEF).

binned in QDMLT (as in the previous chapter) and each of IMF-Bz, IMF-By, and MEF. The strong correlations with MEF demonstrate that it is a good predictor of ionospheric activity, and why using it for further data selection is so effective. It also shows correlation at mid-latitudes, backing up the claim that disturbances here are at least partially due to the far-field effect of FACs, as they are related to solar wind conditions. This shows that it may be possible to account for this ionospheric field with a linear function of MEF, rather than simply removing times when it is large. However, the differing patterns in relation to IMF-Bz and IMF-By demonstrate that the response of the system is more subtle and such a simplistic approach may not be very successful. As the previously mentioned studies have shown, this is due to the overlapping of different current systems, and the solar wind modifying the types of response that the magnetosphere has. It may be possible to build a more sophisticated predictor that incorporates information from IMF-Bx,y,z, solar wind velocity, and their time history, as well as variation of the response across QDMLT, and considering the current systems DP1, DP2, DPY, NBZ.

There are a large number of systems science approaches, based on empirical relations, neural networks, and other tools, which have already been used to predict space

weather effects of the solar wind, mostly in relation to the ring current. Some of these are reviewed by Ganushkina et al. (2017), their section 3 - these are contrasted with methods using physics-based simulations. A promising tool which is similar to neural networks is the nonlinear auto-regressive moving average model with exogenous inputs (NARMAX; Leontaritis and Billings, 1985), whose outputs can be represented as physically interpretable polynomial functions. This has been used in developing coupling functions, and predicting the Kp and Dst indices (e.g. Ayala Solares et al., 2016; Beharrell and Honary, 2016; Boaghe et al., 2001; Boynton et al., 2011a,b).

To explore and test the notion that polar currents occur with certain discrete modes under different solar wind driving, the procedures shown in Figure 8.1 and Figures 7.1-7.3 could be repeated for subselected datasets under different solar wind conditions, and with different IMF time lagging and averaging. This could be used to identify conditions where the system is closer to steady-state and, conversely, where it is more unsettled.

Another aspect to consider is the fact that the ionosphere behaves differently within and outwith the polar cap (i.e. whether the main field lines map out into the solar wind or into the magnetosphere). Chisham (2017) presented a methodology to account for this in model development by ordering data according to the open/closed field line boundary (OCB), with Python code made available (see Burrell and Chisham, 2018). This may also be appropriate in developing data selection routines for internal field modelling.

8.2 The inter-relation of extracting ionospheric and lithospheric signals

Lithospheric modelling typically requires strong data selection, in the absence of ability to capture very precisely the much larger magnitude and highly variable and spatially and temporally complex external fields. Removing the most contaminated data, leaving data with smaller external field contributions, makes it possible to model the weak lithospheric signal. With the development of more accurate external field models, it may be possible to relax the data selection and so include more data to be able to derive more robust models. Nevertheless, whether correcting for the "noise" with the use of models or reducing its effect by using fewer data, there will always be some

level of contamination. Is it possible to model this contamination? What biases does this contamination introduce? To what extent do inaccurate lithospheric models affect the accuracy of ionospheric models? Advances will need to come both in modelling techniques and in our understanding of the ionospheric processes.

Ionospheric field models can be derived independently of data that are used to construct internal field models (or at least partially independent, once further data selection is taken into account). Such models can be used to remove the external field signal to isolate the internal field signal in the data. Similarly, both internal and external fields can be simultaneously co-estimated from the same input data (e.g. as is common for the core and magnetospheric parts, and for all sources with the CI models). This can work reasonably well for the long wavelength parts of the ionosphere (i.e. targeting the core field). Firstly, this is because the core field is much stronger than the ionospheric fields and so they can more easily be distinguished. Secondly, the large scale morphology of external currents is reasonably well known, and can be described well be spherical harmonics, and thus can be relatively successfully parameterised and removed (providing that the external field models are not affected too much by inaccuracy in the core field model due to incomplete source separation). Another issue here is that, for core field modelling, it is important to include more data so as to provide greater continuity in time, and removing an ionospheric field model is a necessary but imperfect step to take in order to include the more contaminated dayside data (e.g. Barrois et al., 2018; Hammer and Finlay, 2019). However, this is unlikely to be successful at present with nightside and polar data, which are more controlled by the solar wind interaction.

In the case of isolating the high latitude lithospheric field, it is harder to remove the ionospheric field. This is firstly because the amplitudes of these sources are similar, so a higher level of ionospheric model accuracy is necessary in order to at least bring the signal to noise ratio above unity. Secondly, while the long spatial wavelengths of the ionospheric field may be predictable from solar wind conditions and the global magnetospheric state, the shorter wavelengths relevant to lithospheric modelling are more complicated. At small scales, more chaotic processes are likely, due to the interaction with the neutral atmosphere and localised effects on conductivity through magnetosphere-ionosphere coupling. To account for the "unpredictable" small scale behaviour, one should interrogate the same data used to derive the lithospheric model, rather than seeking independent predictions. It can reasonably be assumed that such

behaviour has some QDMLT dependence, and my spatial binning method could be used to investigate this.

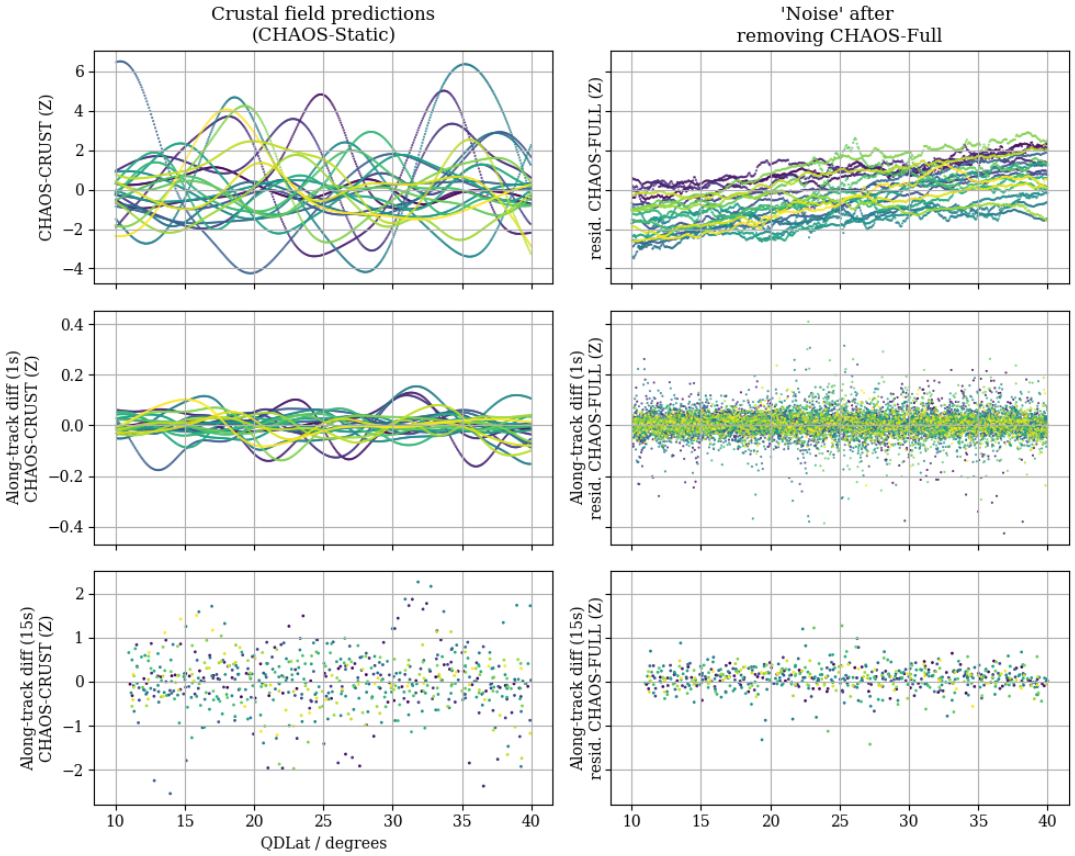

Figure 8.2: Vertical downwards components of: (left) crustal field predictions from CHAOS-6, and (right) residuals between measurements and the full CHAOS model (core + magnetosphere + crust), along nightside mid-latitude parts of orbits from two days of Swarm Alpha data (01-02/01/2018). Colours represent different orbits. (Top) 1Hz data, (middle) along-track differences, (bottom) along-track 15s differences.

Figure 8.2 shows mid-latitude nightside orbital passes from two days of Swarm data, showing the vertical component of lithospheric field predictions from CHAOS-6, and data residuals after removing the full CHAOS model (i.e. core plus magnetosphere plus crust) to approximate the unmodelled (mostly external field) contamination. This is compared with the along-track 1-second differences, and 15-second differences (as used to construct the LCS-1 model; Olsen et al., 2017). This demonstrates the similar magnitudes of the lithospheric and ionospheric field, and the success of using data differences to eliminate the bias introduced by the large-scale unmodelled fields (the upwards trend in the top right panel, varying from orbit to orbit, versus the apparently random noise scattered around zero in the bottom two right panels).

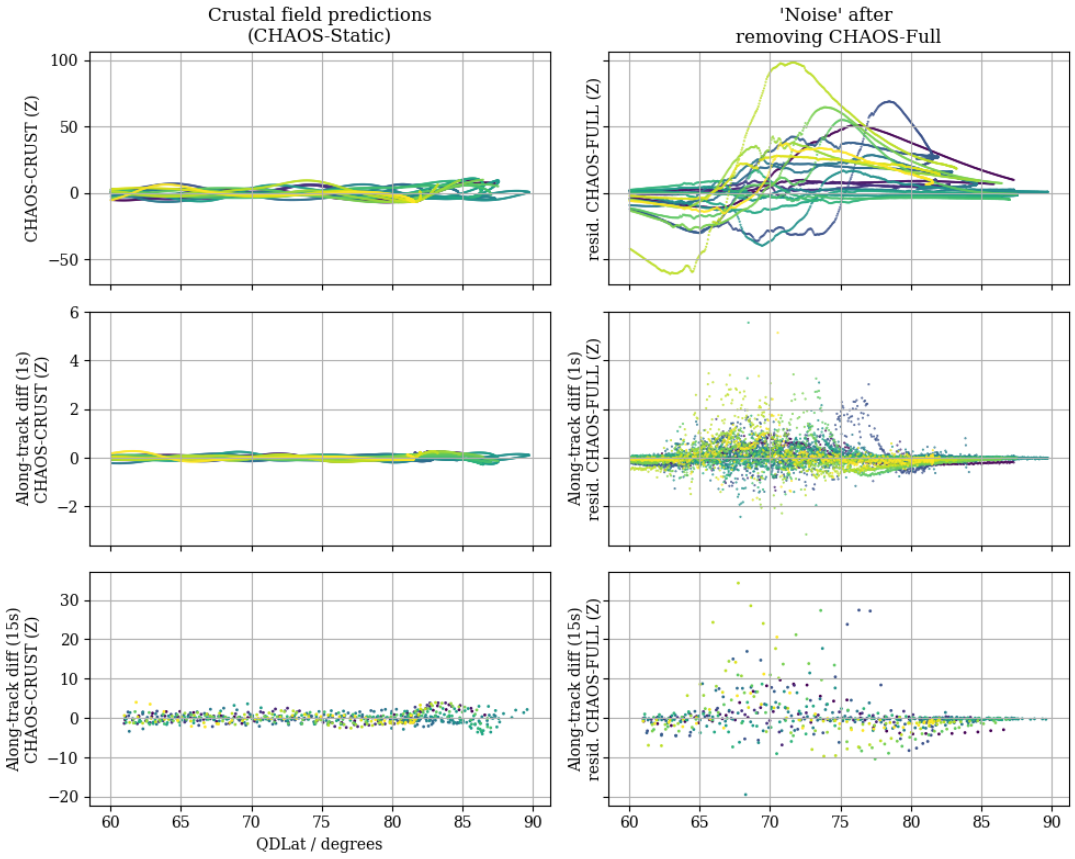

Figure 8.3: As for 8.2 but at polar latitudes.

Figure 8.3 shows the same as Figure 8.2 but at polar latitudes. This shows the much larger "noise" introduced by the auroral electrojets. This noise is still large, and organised, when looking at the along-track differences, and indeed is the signal used to study the electrojets in Chapter 5. Its effect is greatly reduced by stringent data selection, and one may then attempt to model its quiescent state. However, this poses the circular problem of modelling each of these sources separately having supposedly removed the effect of the other, and so should also be approached by co-estimated models. This is the motivation of the gridding procedure of Chapters 6 & 7, to organise their respective signals logically according to their governing frames, GEO and QDMLT.

Figure 8.4 demonstrates the effects of incomplete separation of sources on the study of Chapter 5. When the lithospheric field is not removed at all, sharp gradients in it cause artificial detections of the electrojets. Even after the lithospheric model is removed, it is hard to know where its inaccuracy could be affecting the electrojet signal. There appears to be an excess of detections over the coastline of Antarctica between 90° to 180° longitude. This could be due to the lithospheric model not resolving the sharp

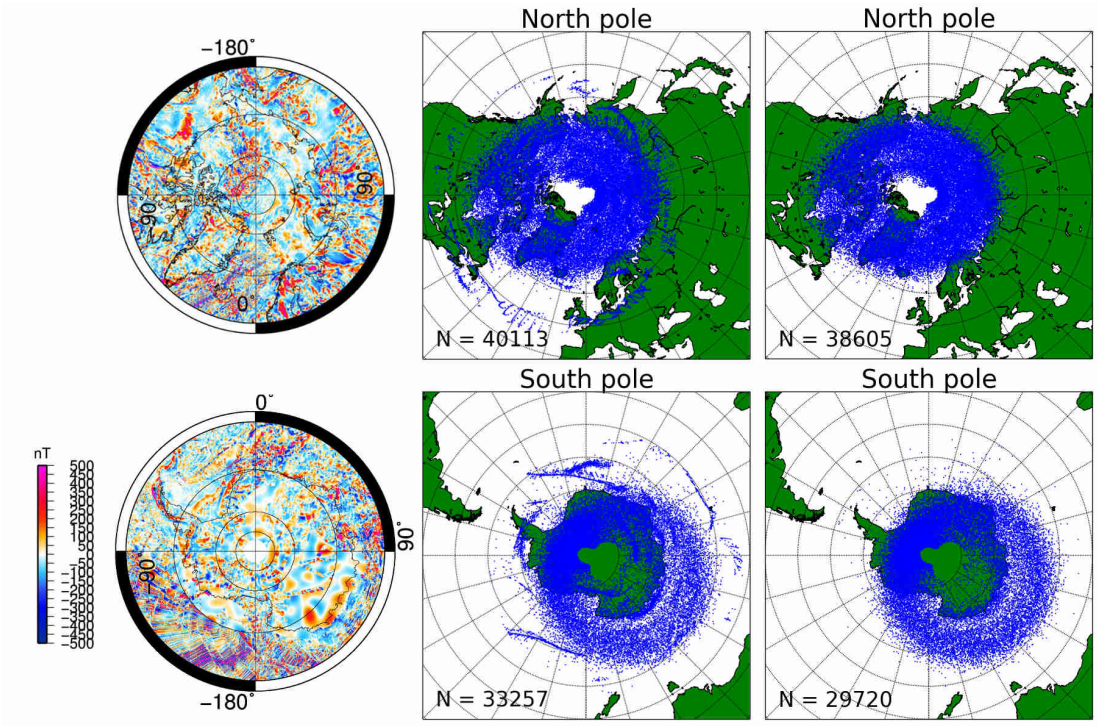

Figure 8.4: (Left) Ground level intensity of the WDMAM model. (Center) Auroral electrojet detections from Chapter 5, but after only removing the core field but not the lithospheric field, and (right) after also removing the lithospheric field

boundary here. Equally this could be a preferential location of the electrojets, secondary to the typical auroral oval latitude, e.g. from pseudo-breakups (Pulkkinen, 1996). In fact, it appears to be due to the higher latitude AEJs on the dayside, associated with the "Region 0" FACs - this can be seen in Figure A.2.

8.3 Improving the lithospheric modelling technique

There are a number of things that could be done to improve the lithospheric model derived in the previous chapter, building on the technique that was developed. Firstly it is obvious that including CHAMP data will improve it due to the lower altitude sampling available (closer to and so more sensitive to the signal), although it will also be closer to the ionospheric signal. This does however raise the question of how to deal with data taken at different altitudes over time. This was neglected in my analysis, instead fixing the altitude of the reduced data to the median altitude in each bin, which is reasonable due to the smaller change in altitude over the time span of the Swarm data used. It would also be good to include the other magnetic field components, but probably only in non-polar regions since the polar regions are so strongly contaminated by FACs.

It would be interesting to explore the use of gradient data, both along-track and cross-track (from Swarm Alpha and Charlie). This would provide the benefit of reducing large-scale field contamination, and hopefully reduce the along-track correlated noise that currently appears to so negatively affect the model presented. The binning method would need to be adapted accordingly. At this point, the method of reducing data to a grid of values should be improved. In this study, the median values within each bin were used, which worked surprisingly well, but something more sophisticated should be explored. Perhaps the same method used in the Virtual Observatory approaches can be used: fitting a potential locally within each bin.

Further data selection is possible, but may not be beneficial if there are not enough data remaining afterwards (see Figure 7.6). A potential novel idea is to apply different data selection in each hemisphere, to account for the asymmetric response to IMF-By, i.e. because the ionospheric currents may be weaker for By<0 in the North, and for positive By>0 in the South (Figure 7.3).

Moving in the other direction, of instead including more data, it will be necessary to better account for the ionospheric field. This may be achieved by a combination of models such as AMPS and by (or instead exclusively by) co-estimating better predictions of the field, as described in Section 8.1.

Beyond being a tool to reduce data and derive a model, the binning technique also offers the possibility of attaching model uncertainties to given locations and conditions.

Within each bin there is a set of measurements which contribute. After the various cleaning routines have been applied, the deviation between the median value and the model prediction, together with the distribution of the values within the bin, can be used to give an estimate of the model accuracy at each location. These uncertainties should be considered when making any geological interpretations based on the model. Similarly, the spread in values in each bin after different data selections have been applied can be used to give predictions of magnetic disturbance, i.e. how disturbed magnetic measurements are likely to be at different times. A model could be built which gives the typical disturbance at each geographical location, for example as a function of local time and geomagnetic activity (e.g. characterised by Kp). With the appropriate real-time data feeds, which could include future predictions of Kp, this would be useful extra information for models used operationally such as the World Magnetic Model.

8.4 Regarding programming and use of VirES

At this point I would like to mention some of the software tools that I have used. Most of my workflow has used the Python programming language and the common stack of libraries for scientific use cases: numpy, scipy, matplotlib, pandas etc. I have also heavily relied on two newer libraries:

- xarray (Hoyer and Hamman, 2017) which provides convenient data structures for N-dimensional labelled arrays
- cartopy (Met Office, 2010) which helps to produce maps based on matplotlib

For domain-specific computation and data access, I have used:

- SpacePy (Morley et al., 2010)
- PYSAT (Stoneback et al., 2018)
- ApexPy (Meeren et al., 2018)
- ChaosMagPy (Kloss, 2019)
- pyAMPS (Laundal and Toresen, 2018)

During the final year of my work, I was able to use the "VirES for Swarm" service to access Swarm data and model evaluations. This is a service developed for ESA by EOX IT Services. Programmatic (i.e. scriptable) access to the service was made possible by a Python package called viresclient (Smith and Pačes, 2019), which I developed together with EOX. VirES is a server/client architecture where up-to-date data and models are

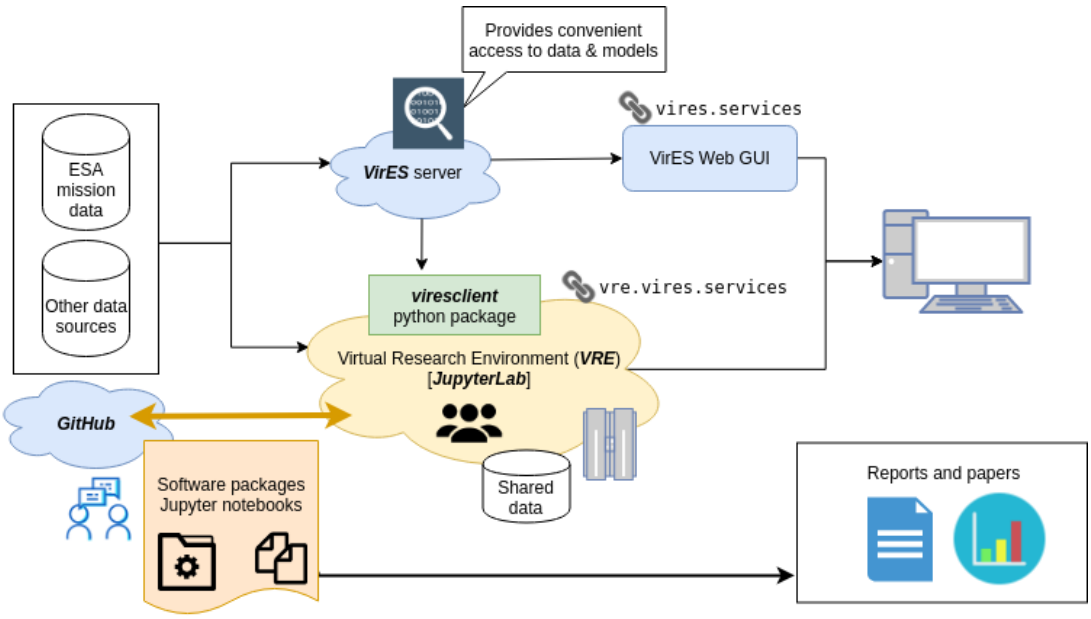

Figure 8.5: Server/client architecture of VirES. VRE refers to the "Virtual Research Environment", an ESA cloud service in development, which elastically spawns containerised instances of JupyterLab on demand for registered users.

processed on the server and custom datasets are delivered through a client interface - either the web-based GUI at `https://vires.services` or the Python interface (Figure 8.5). Code to generate results and figures from this thesis will be made available through my GitHub page (`https://github.com/smithara`). The workflow I developed is shown in overview in Figure 8.6.

Further development on viresclient will make Swarm products more accessible and easier to integrate with other data and software, such as those reviewed by Burrell et al. (2018) for heliophysics. These efforts are important in order to reduce barriers that delay the progress of science in geospace and to democratise scientific analysis (McGranaghan et al., 2017).

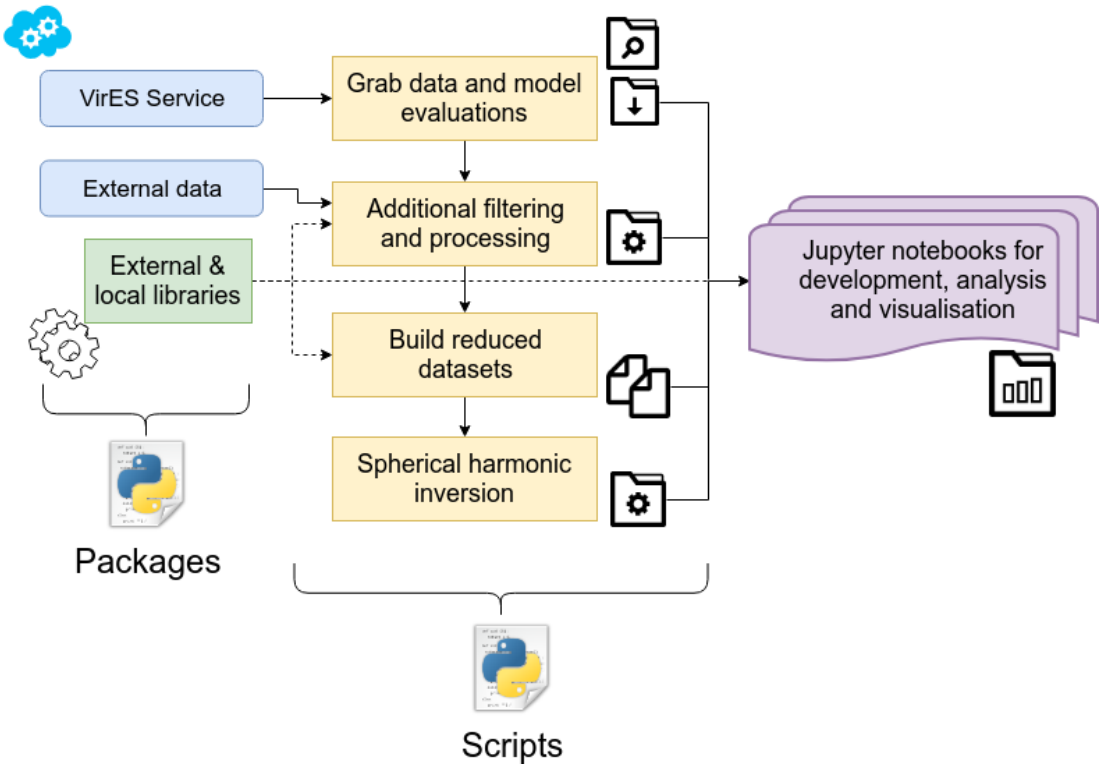

Figure 8.6: Overview of processing pipeline and interactive usage through Jupyter tools.

Chapter 9

Conclusion

This research has made use of data from the Swarm mission and related satellites to explore new techniques to study the geomagnetic field. It has focused on two aspects: the auroral electrojets (AEJs) and the lithospheric field, and ways to reduce the contamination from the AEJs in lithospheric field modelling. Some insight was gained about the AEJs which is relevant to internal field modelling: seasonal and solar cycle trends, and interhemispheric differences in response to the solar wind. By building a lithospheric model, I explored the "noise" created by the AEJs, and demonstrated a new method which attempts to remove their effect. In the final chapter I suggested some ways in which we might better describe the complexity of the solar wind's effect on magnetic measurements made at low Earth orbit, which in turn would help to improve both internal and external field models.

Chapter 5 presented a simple method to capture the activity of the AEJs from each satellite pass by tracking maxima in the along-track gradient of magnetic field intensity. Despite the simplicity of the approach, many climatological features can be extracted when a large number of detections are analysed together. The key findings were of hemispheric asymmetries (where often the system is considered as symmetric) and of long-term trends in the AEJ strength and location (related to season, solar cycle, and main field secular variation) that are not captured by ground-derived geomagnetic activity indices. These motivate the development and exploitation of new satellite-derived indices both for space weather studies and for internal field modelling. These may be simply satellite-pass-specific measures of activity based on measurements from a given pass such as those shown in this thesis, or potentially synthesised from multiple satellites with a number of quantities specified at each point in time to encompass the

complexity of the AEJs across local time and location.

Hemispheric asymmetry of the AEJs in response to IMF conditions was identified: weaker Northern Hemisphere AEJs were found for IMF-By < 0 than for IMF-By > 0, whereas the reverse was observed in the Southern Hemisphere. This prompts asymmetric treatment of data from each hemisphere for internal field modelling, such as by using different data selection criteria for IMF-By for data taken in each hemisphere. The long-term trends in AEJ strength and location suggest that there are unaccounted-for biases in data used to construct main field models and that a dedicated study of their effects is necessary. Possible tests for this include repeating field modelling using data from different local time sectors (where external field contamination is different), and modelling using synthetic data sets which contain a forward model of the long-term ionospheric variation.

In Chapters 6 & 7, a gridding procedure was used to inspect satellite data under different selection criteria and after subtracting different combinations of models. Two grids, one in GEO (latitude and longitude) and one in QDMLT (quasi-dipole latitude and magnetic local time) coordinates, were used to organise signals from the solid Earth and from the ionosphere respectively. In each case, the medians and standard deviations of data contributing at each grid point were evaluated. This was an effective way of summarising large volumes of data and exploring them graphically, without artefacts that may be introduced by spherical harmonic analysis.

The gridding procedure also showed promise as the basis of a new approach to field modelling, providing a simple way to suppress the ionospheric noise present within a lithospheric field modelling context. To extend this approach further, the QDMLT binning could be performed under different data selection and the magnetic field at each QDMLT location related to upstream solar wind conditions with techniques as described in Section 8.1. This could lead to a model to predict the ionospheric magnetic field at satellite altitude based on a complex combination of the solar wind conditions and varying lag times at each QDMLT location. Such a model could itself be used to remove the ionospheric effect on internal field models, though attention should be paid to the circular nature of having to subtract a prior lithospheric field model prediction as part of building the new model. Ultimately a true co-estimation of sources should be made, but its accuracy and applicability will be affected by the input data selection and model parameterisation.

Methodological improvements and deeper understanding of the various geomagnetic field sources will continue to improve our ability to model their behaviour with greater accuracy. Nevertheless, to support these endeavours we rely on the continued and uninterrupted provision of high quality measurements from observatories both on the ground and in space. We must ensure that these facilities endure as vital assets for monitoring Earth. The ongoing Swarm mission and increasing synergies with other initiatives will no doubt be essential for Earth and space scientists, far beyond the applications in this thesis, and I hope that these have the ongoing support and success that they deserve.

Bibliography

Aakjær, C. D., N. Olsen, and C. C. Finlay (2016). "Determining polar ionospheric electrojet currents from Swarm satellite constellation magnetic data". In: *Earth, Planets and Space* 68.1, p. 140. DOI: 10.1186/s40623-016-0509-y.

Akasofu, S.-I. (1964). "The development of the auroral substorm". In: *Planetary and Space Science* 12, pp. 273–282. DOI: 10.1016/0032-0633(64)90151-5.

Akasofu, S.-I. (2017). "Auroral Substorms: Search for Processes Causing the Expansion Phase in Terms of the Electric Current Approach". In: *Space Science Reviews* 212.1-2, pp. 341–381. DOI: 10.1007/s11214-017-0363-7.

Alken, P., S. Maus, P. Vigneron, O. Sirol, and G. Hulot (2013). "Swarm SCARF equatorial electric field inversion chain". In: *Earth, Planets and Space* 65.11, pp. 1309–1317. DOI: 10.5047/eps.2013.09.008.

Alken, P., A. Maute, and A. D. Richmond (2016). "The F-Region Gravity and Pressure Gradient Current Systems: A Review". In: *Space Science Reviews* 206.1-4, pp. 1–19. DOI: 10.1007/s11214-016-0266-z.

Amm, O. (1997). "Ionospheric elementary current systems in spherical coordinates and their application". In: *Earth, Planets and Space* 49.7, pp. 947–955. DOI: 10.5636/jgg.49.947.

Ayala Solares, J. R., H.-L. Wei, R. J. Boynton, S. N. Walker, and S. A. Billings (2016). "Modeling and prediction of global magnetic disturbance in near-Earth space: A case study for Kp index using NARX models". In: *Space Weather* 14.10, pp. 899–916. DOI: 10.1002/2016SW001463.

Backus, G. E. (1970). "Non-uniqueness of the external geomagnetic field determined by surface intensity measurements". In: *Journal of Geophysical Research: Space Physics* 75. DOI: 10.1029/JA075i031p06339.

Backus, G. E., R. Parker, and C. Constable (1996). *Foundations of Geomagnetism*. Cambridge University Press. ISBN: 0-521-41006-1.

Barrois, O., M. D. Hammer, C. C. Finlay, Y. Martin, and N. Gillet (2018). "Assimilation of ground and satellite magnetic measurements: inference of core surface magnetic and velocity field changes". In: *Geophysical Journal International* 215.1, pp. 695–712. DOI: 10.1093/gji/ggy297.

Bartels, J., N. H. Heck, and H. F. Johnston (1939). "The three-hour-range index measuring geomagnetic activity". In: *Journal of Geophysical Research* 44.4, p. 411. DOI: 10.1029/te044i004p00411.

Baumgardner, J. R. and P. O. Frederickson (1985). "Icosahedral Discretization of the Two-Sphere". In: *SIAM Journal on Numerical Analysis* 22.6, pp. 1107–1115. DOI: 10.1137/0722066.

Baumjohann, W. and R. Treumann (1997). *Basic Space Plasma Physics*. Imperial College Press. DOI: 10.1142/p015.

Baumjohann, W. and R. Nakamura (2007). "Magnetospheric Contributions to the Terrestrial Magnetic Field". In: *Treatise on Geophysics*. Vol. 5. Elsevier, pp. 77–92. DOI: 10.1016/B978-044452748-6.00088-2.

Beggan, C. and K. Whaler (2008). "Core flow modelling assumptions". In: *Physics of the Earth and Planetary Interiors* 167.3-4, pp. 217–222. DOI: 10.1016/j.pepi.2008.04.011.

Beharrell, M. J. and F. Honary (2016). "Decoding solar wind-magnetosphere coupling". In: *Space Weather* 14.10, pp. 724–741. DOI: 10.1002/2016SW001467.

Birkeland, K. (1908). *The Norwegian Aurora Polaris Expedition 1902-1903 Vol. 1.* URL: https://archive.org/details/norwegianaurorap01chririch.

Boaghe, O. M., M. A. Balikhin, S. A. Billings, and H. Alleyne (2001). "Identification of nonlinear processes in the magnetospheric dynamics and forecasting of Dst index". In: *Journal of Geophysical Research: Space Physics* 106.A12, pp. 30047–30066. DOI: 10.1029/2000ja900162.

Bouffard, J., R. Floberghagen, and N. Olsen (2019). "The Swarm Satellite Trio Studies Earth and Its Environment". In: *Eos* 100. DOI: 10.1029/2019eo123269.

Boynton, R. J., M. A. Balikhin, S. A. Billings, A. S. Sharma, and O. A. Amariutei (2011a). "Data derived NARMAX Dst model". In: *Annales Geophysicae* 29.6, pp. 965–971. DOI: 10.5194/angeo-29-965-2011.

Boynton, R. J., M. A. Balikhin, S. A. Billings, H. L. Wei, and N. Ganushkina (2011b). "Using the NARMAX OLS-ERR algorithm to obtain the most influential coupling functions that affect the evolution of the magnetosphere". In: *Journal of Geophysical Research: Space Physics* 116.5, pp. 1–8. DOI: 10.1029/2010JA015505.

Browett, S. D., R. C. Fear, A. Grocott, and S. E. Milan (2017). "Timescales for the penetration of IMF By into the Earth's magnetotail". In: *Journal of Geophysical Research: Space Physics* 122.1, pp. 579–593. DOI: 10.1002/2016JA023198.

Burrell, A. G., A. J. Halford, J. Klenzing, R. A. Stoneback, S. K. Morley, A. M. Annex, et al. (2018). "Snakes on a Spaceship - An Overview of Python in Heliophysics". In: *Journal of Geophysical Research: Space Physics*, pp. 1–19. DOI: 10.1029/2018JA025877.

Burrell, A. G. and G. Chisham (2018). *aburrell/ocbpy: Beta Release.* DOI: 10.5281/ZENODO.1217177.

Chapman, S. and V. C. A. Ferraro (1931). "A new theory of magnetic storms". In: *Terrestrial Magnetism and Atmospheric Electricity* 36.

Chappell, C. R. (2015). "The Role of the Ionosphere in Providing Plasma to the Terrestrial Magnetosphere—An Historical Overview". In: *Space Science Reviews*, pp. 5–25. DOI: 10.1007/s11214-015-0168-5.

Chisham, G. (2017). "A new methodology for the development of high-latitude ionospheric climatologies and empirical models". In: *Journal of Geophysical Research: Space Physics*, pp. 1–16. DOI: 10.1002/2016JA023235.

Chulliat, A., P. Vigneron, E. Thébault, O. Sirol, and G. Hulot (2013). "Swarm SCARF dedicated ionospheric field inversion chain". In: *Earth, Planets and Space* 65.11, pp. 1271–1283. DOI: 10.5047/eps.2013.08.006.

Chulliat, A. and S. Maus (2014). "Geomagnetic secular acceleration, jerks, and a localized standing wave at the core surface from 2000 to 2010". In: *Journal of Geophysical Research: Solid Earth*, n/a–n/a. DOI: 10.1002/2013JB010604.

Chulliat, A., S. Macmillan, P. Alken, C. Beggan, M. Nair, B. Hamilton, et al. (2015). *The US/UK World Magnetic Model for 2015-2020: Technical Report.* Tech. rep. National Geophysical Data Center, NOAA. DOI: 10.7289/V5TB14V7.

Chulliat, A., P. Vigneron, and G. Hulot (2016a). "First results from the Swarm Dedicated Ionospheric Field Inversion chain". In: *Earth, Planets and Space* 68.1, p. 104. DOI: 10.1186/s40623-016-0481-6.

Chulliat, A., J. Matzka, A. Masson, and S. E. Milan (2016b). "Key Ground-Based and Space-Based Assets to Disentangle Magnetic Field Sources in the Earth's Environment". In: *Space Science Reviews*, pp. 1–34. DOI: 10.1007/s11214-016-0291-y.

Clark, D. A. (1997). "Magnetic petrophysics and magnetic petrology: aids to geological interpretation of magnetic surveys". In: *AGSO Journal of Australian Geology and Geophysics* 17.2, pp. 83–103.

Cnossen, I. and J. Matzka (2016). "Changes in solar quiet magnetic variations since the Maunder Minimum: A comparison of historical observations and model simulations". In: *Journal of Geophysical Research: Space Physics*, pp. 783–785. DOI: 10.1002/2016JA023362.

Cnossen, I. (2017). "The Impact of Century-Scale Changes in the Core Magnetic Field on External Magnetic Field Contributions". In: *Space Science Reviews* 206, pp. 259–280. DOI: 10.1007/s11214-016-0276-x.

Cowley, S. W. H. and M. Lockwood (1992). "Excitation and decay of solar wind-driven flows in the magnetosphere-ionosphere system". In: *Annales Geophysicae* 10, pp. 103–115.

Cowling, T. (1976). *Magnetohydrodynamics*. Hilger. ISBN: 0852743009.

Coxon, J. C., S. E. Milan, J. A. Carter, L. B. N. Clausen, and H. Korth (2016). "Seasonal and diurnal variations in AMPERE observations of the Birkeland currents compared to modelled results". In: *Journal of Geophysical Research: Space Physics* 121, pp. 4027–4040. DOI: 10.1002/2015JA022050.

Davis, T. and M. Sugiura (1966). "Auroral electrojet activity index AE and its universal time variations". In: *Journal of Geophysical Research* 71.3, pp. 785–801. DOI: 10.1029/JZ071i003p00785.

Denton, M. H., J. E. Borovsky, M. Stepanova, and J. A. Valdivia (2016). "Preface: Unsolved Problems of Magnetospheric Physics". In: *Journal of Geophysical Research: Space Physics* 121. DOI: 10.1002/2016JA023362.

DTU (2019). *Swarm Level1b Processor Algorithms*. URL: https://earth.esa.int/web/guest/document-library/browse-document-library/-/article/swarm-level-1b-processor-algorithms.

Dungey, J. W. (1961). "Interplanetary magnetic field and the auroral zones". In: *Physical Review Letters* 6.2, pp. 47–48. DOI: 10.1103/PhysRevLett.6.47.

Dunlop, D. and Ö. Özdemir (2007). "Magnetizations in Rocks and Minerals". In: *Treatise on Geophysics*. Vol. 5, pp. 277–336. ISBN: 9780444527486. DOI: 10.1016/B978-044452748-6.00093-6.

Eastwood, J. P. (2008). "The science of space weather". In: *Philosophical transactions of the Royal Society* 366.1884, pp. 4489–500. DOI: 10.1098/rsta.2008.0161.

Emmert, J. T., A. D. Richmond, and D. P. Drob (2010). "A computationally compact representation of magnetic-apex and Quasi-Dipole coordinates with smooth base vectors". In: *Journal of Geophysical Research: Space Physics* 115.8. DOI: 10.1029/2010JA015326.

ESA (2018). *Swarm trio becomes a quartet*. URL: https://www.esa.int/Our_Activities/Observing_the_Earth/Swarm/Swarm_trio_becomes_a_quartet.

Farquharson, C. G. and D. W. Oldenburg (1998). "Non-linear inversion using general measures of data misfit and model structure". In: *Geophysical Journal International* 134.1, pp. 213–227. DOI: 10.1046/j.1365-246x.1998.00555.x.

Finch, I. and M. Lockwood (2007). "Solar wind-magnetosphere coupling functions on timescales of 1 day to 1 year". In: *Annales Geophysicae* 25.2, pp. 495–506. DOI: 10.5194/angeo-25-495-2007.

Finlay, C. C., M. Dumberry, A. Chulliat, and M. A. Pais (2010). "Short timescale core dynamics: Theory and observations". In: *Space Science Reviews* 155.1-4, pp. 177–218. DOI: 10.1007/s11214-010-9691-6.

Finlay, C. C., N. Olsen, and L. Tøffner-clausen (2015). "DTU candidate field models for IGRF-12 and the CHAOS-5 geomagnetic field model". In: *Earth, Planets and Space* 67. DOI: 10.1186/s40623-015-0274-3.

Finlay, C. C., N. Olsen, S. Kotsiaros, N. Gillet, and L. T. Clausen (2016). "Recent geomagnetic secular variation from Swarm and ground observatories as estimated in the CHAOS-6 geomagnetic field model". In: *Earth, Planets and Space* 68, p. 112. DOI: 10.1186/s40623-016-0486-1.

Finlay, C. C., V. Lesur, E. Thébault, F. Vervelidou, A. Morschhauser, and R. Shore (2017). "Challenges Handling Magnetospheric and Ionospheric Signals in Internal Geomagnetic Field Modelling". In: *Space Science Reviews* 206, pp. 157–189. DOI: 10.1007/s11214-016-0285-9.

Fratter, I., J.-M. Léger, F. Bertrand, T. Jager, G. Hulot, L. Brocco, et al. (2016). "Swarm Absolute Scalar Magnetometers first in-orbit results". In: *Acta Astronautica* 121, pp. 76–87. DOI: 10.1016/J.ACTAASTRO.2015.12.025.

Friis-Christensen, E. and J. Wilhjelm (1975). "Polar Cap Currents for Different Directions of the Interplanetary Magnetic Field in the Y-Z Plane". In: *Journal of Geophysical Research* 80.10, pp. 1248–1260. DOI: 10.1029/JA080i010p01248.

Friis-Christensen, E., H. Luhr, and G. Hulot (2006). "Swarm: A constellation to study the Earth's magnetic field". In: *Earth, Planets and Space* 58, pp. 351–358. DOI: 10.1186/BF03351933.

Friis-Christensen, E., C. C. Finlay, M. Hesse, and K. M. Laundal (2017). "Magnetic Field Perturbations from Currents in the Dark Polar Regions During Quiet Geomagnetic Conditions". In: *Space Science Reviews* 206.1-4, pp. 281–297. DOI: 10.1007/s11214-017-0332-1.

Friis-Christensen, E. (2018). "Global Change, Space Weather, and Climate". In: *Global Change and Future Earth*. Cambridge University Press. ISBN: 9781316761489. DOI: 10.1017/9781316761489.005.

Fukushima, N. (1976). "Generalized theorem of no ground magnetic effect of vertical currents connected with Pedersen currents in the uniform conducting ionosphere". In: *Rep. Ionos. Space Res. Jpn.* 30, pp. 35–40. URL: https://ci.nii.ac.jp/naid/10003532648/.

Gaina, C., S. C. Werner, R. Saltus, and S. Maus (2011). "Chapter 3 Circum-Arctic mapping project: new magnetic and gravity anomaly maps of the Arctic". In: *Geological Society, London, Memoirs*. Vol. 35. 1, pp. 39–48. DOI: 10.1144/M35.3.

Ganushkina, N. Y., A. Jaynes, and M. Liemohn (2017). "Space Weather Effects Produced by the Ring Current Particles". In: *Space Science Reviews* 212.3-4, pp. 1315–1344. DOI: 10.1007/s11214-017-0412-2.

Ganushkina, N. Y., M. W. Liemohn, and S. Dubyagin (2018). "Current Systems in the Earth's Magnetosphere". In: *Reviews of Geophysics* 56. DOI: 10.1002/2017RG000590.

Garland, G. D. (1979). "The contributions of Carl Friedrich Gauss to geomagnetism". In: *Historia Mathematica* 6.1, pp. 5–29. DOI: doi:10.1016/0315-0860(79)90100-9.

Gaunt, C. T. (2016). "Why Space Weather Is Relevant to Electrical Power Systems". In: *Space Weather* 14.1, pp. 2–9. DOI: 10.1002/2015SW001306.

Gauss, C. F. (1838). "Allgemeine Theorie des Erdmagnetismus". In: *Werke*. Berlin, Heidelberg: Springer Berlin Heidelberg, pp. 119–193. DOI: 10.1007/978-3-642-49319-5_5.

Gillet, N., V. Lesur, and N. Olsen (2010). "Geomagnetic core field secular variation models". In: *Space Science Reviews* 155.1-4, pp. 129–145. DOI: 10.1007/s11214-009-9586-6.

Gillet, N., O. Barrois, and C. C. Finlay (2015). "Stochastic forecasting of the geomagnetic field from the COV-OBS.x1 geomagnetic field model, and candidate models for IGRF-12". In: *Earth, Planets and Space* 67.1, p. 71. DOI: 10.1186/s40623-015-0225-z.

Gjerloev, J. W. (2012). "The SuperMAG data processing technique". In: *Journal of Geophysical Research: Space Physics* 117.A9. DOI: 10.1029/2012JA017683.

Glassmeier, K.-H., H. Soffel, and J. Negendank (2009). *Geomagnetic Field Variations*. Ed. by K. H. Glassmeier, H. Soffel, and J. Negendank. Springer Berlin. DOI: 10.1007/978-3-540-76939-2.

Glassmeier, K.-H. and B. T. Tsurutani (2014). "Carl Friedrich Gauss – General Theory of Terrestrial Magnetism – a revised translation of the German text". In: *History of Geo- and Space Sciences* 5.1, pp. 11–62. DOI: 10.5194/hgss-5-11-2014.

Glatzmaier, G. A. and P. Olson (2005). "Probing the Geodynamo". In: *Scientific American* 292. DOI: 10.1038/scientificamerican0405-50.

Golynsky, A. V., F. Ferraccioli, J. K. Hong, D. A. Golynsky, R. R. B. von Frese, D. A. Young, et al. (2018). "New Magnetic Anomaly Map of the Antarctic". In: *Geophysical Research Letters*. DOI: 10.1029/2018GL078153.

Grocott, A., S. E. Milan, S. M. Imber, M. Lester, and T. K. Yeoman (2012). "A quantitative deconstruction of the morphology of high-latitude ionospheric convection". In: *Journal of Geophysical Research: Space Physics* 117.5, pp. 1–16. DOI: 10.1029/2012JA017580.

Gubbins, D. (2004). *Time Series Analysis and Inverse Theory for Geophysicists*. Cambridge University Press. ISBN: 0521525691.

Haaland, S., G. Paschmann, M. Förster, J. M. Quinn, R. B. Torbert, C. E. McIlwain, et al. (2007). "High-latitude plasma convection from Cluster EDI measurements: method and IMF-dependence". In: *Annales Geophysicae* 25, pp. 239–253. DOI: 10.5194/angeo-25-239-2007.

Hamilton, B. (2013). "Rapid modelling of the large-scale magnetospheric field from Swarm satellite data". In: *Earth, Planets and Space* 65.11, pp. 1295–1308. DOI: 10.5047/eps.2013.09.003.

Hamilton, B., V. A. Ridley, C. D. Beggan, and S. Macmillan (2015). "The BGS magnetic field candidate models for the 12th generation IGRF". In: *Earth, Planets and Space* 67. DOI: 10.1186/s40623-015-0227-x.

Hammer, M. D. and C. C. Finlay (2019). "Local averages of the core–mantle boundary magnetic field from satellite observations". In: *Geophysical Journal International* 216.3, pp. 1901–1918. DOI: 10.1093/gji/ggy515.

Hamoudi, M., Y. Quesnel, J. Dyment, and V. Lesur (2011). "Aeromagnetic and Marine Measurements". In: *Geomagnetic Observations and Models*. Dordrecht: Springer Netherlands, pp. 57–103. DOI: 10.1007/978-90-481-9858-0_4.

Hapgood, M. A. (1992). "Space physics coordinate transformations: A user guide". In: *Planetary and Space Science* 40.5, pp. 711–717. DOI: 10.1016/0032-0633(92)90012-D.

Hardy, C. M. and J. Wong (2019). "Stably stratified layers within Earth's core". In: *Astronomy & Geophysics* 60. DOI: 10.1093/astrogeo/atz148.

He, M., J. Vogt, H. Lühr, E. Sorbalo, A. Blagau, G. Le, et al. (2012). "A high-resolution model of field-aligned currents through empirical orthogonal functions analysis (MFACE)". In: *Geophysical Research Letters* 39.17, pp. 1–6. DOI: 10.1029/2012GL053168.

Hinze, W. J., R. R. von Frese, and D. N. Ravat (1991). "Mean magnetic contrasts between oceans and continents". In: *Tectonophysics* 192.1-2, pp. 117–127. DOI: 10.1016/0040-1951(91)90250-V.

Horning, B. L., R. L. McPherron, and D. D. Jackson (1974). "Application of linear inverse theory to a line current model of substorm current systems". In: *Journal of Geophysical Research* 79.34, pp. 5202–5210. DOI: 10.1029/ja079i034p05202.

Hoyer, S. and J. J. Hamman (2017). "xarray: N-D labeled Arrays and Datasets in Python". In: *Journal of Open Research Software* 5, pp. 1–6. DOI: 10.5334/jors.148.

Huang, C.-S., G. J. Sofko, A. V. Koustov, D. A. Andre, J. M. Ruohoniemi, R. A. Greenwald, et al. (2000). "Evolution of ionospheric multicell convection during northward interplanetary magnetic field with | B z / B y | > 1". In: *Journal of Geophysical Research: Space Physics* 105.A12, pp. 27095–27107. DOI: 10.1029/2000ja000163.

Huber, P. J. (1964). "Robust Estimation of a Location Parameter". In: *The Annals of Mathematical Statistics* 35.1, pp. 73–101. DOI: 10.1214/aoms/1177703732.

Hulot, G., T. J. Sabaka, and N. Olsen (2007). "The Present Field". In: *Treatise on Geophysics*. Vol. 5, pp. 33–75. ISBN: 9780444527486. DOI: 10.1016/B978-044452748-6.00087-0.

Hulot, G., C. C. Finlay, C. G. Constable, N. Olsen, and M. Mandea (2010). "The Magnetic Field of Planet Earth". In: *Space Science Reviews* 152.1-4, pp. 159–222. DOI: 10.1007/s11214-010-9644-0.

Hulot, G., J. M. Leger, P. Vigneron, T. Jager, F. Bertrand, P. Coïsson, et al. (2018). "The NanoMagSat Nanosatellite High-Precision Magnetic Project". In: *American Geophysical Union, Fall Meeting 2018, abstract #A41K-3116*. URL: http://adsabs.harvard.edu/abs/2018AGUFM.A41K3116H.

Iijima, T. and T. a. Potemra (1978). "Large-scale characteristics of field-aligned currents associated with substorms". In: *Journal of Geophysical Research* 83.A2, p. 599. DOI: 10.1029/JA083iA02p00599.

Jackson, A., A. R. Jonkers, and M. R. Walker (2000). "Four centuries of geomagnetic secular variation from historical records". In: *Philosophical Transactions of the Royal Society A: Mathematical, Physical and Engineering Sciences* 358.1768, pp. 957–990. DOI: 10.1098/rsta.2000.0569.

Jones, C. A., M. J. Thompson, and S. M. Tobias (2010). "The solar dynamo". In: *Space Science Reviews* 152.1-4, pp. 591–616. DOI: 10.1007/s11214-009-9579-5.

Juusola, L., O. Amm, and A. Viljanen (2006). "One-dimensional spherical elementary current systems and their use for determining ionospheric currents from satellite measurements". In: *Earth, Planets and Space* 58.5, pp. 667–678. DOI: 10.1186/BF03351964.

Juusola, L., K. Kauristie, O. Amm, and P. Ritter (2009). "Statistical dependence of auroral ionospheric currents on solar wind and geomagnetic parameters from 5 years of CHAMP satellite data". In: *Annales Geophysicae* 27.3, pp. 1005–1017. DOI: 10.5194/angeo-27-1005-2009.

Juusola, L., S. E. Milan, M. Lester, a. Grocott, and S. M. Imber (2014). "Interplanetary magnetic field control of the ionospheric field-aligned current and convection distributions". In: *Journal of Geophysical Research: Space Physics* 119.4, pp. 3130–3149. DOI: 10.1002/2013JA019455.

Juusola, L., K. Kauristie, H. Vanham??ki, A. Aikio, and M. van de Kamp (2016). "Comparison of auroral ionospheric and field-aligned currents derived from Swarm and ground magnetic field measurements". In: *Journal of Geophysical Research: Space Physics* 121.9, pp. 9256–9283. DOI: 10.1002/2016JA022961.

Kan, J. and L. Lee (1979). "Energy coupling function and solar wind-magnetosphere dynamo". In: *Geophysical Research Letters* 6. DOI: 10.1029/GL006i007p00577.

Kauristie, K., A. Morschhauser, N. Olsen, C. C. Finlay, R. L. McPherron, J. W. Gjerloev, et al. (2017). "On the Usage of Geomagnetic Indices for Data Selection in Internal Field Modelling". In: *Space Science Reviews* 206, pp. 61–90. DOI: 10.1007/s11214-016-0301-0.

Keiling, A., O. Marghitu, and M. Wheatland (2018). *Electric Currents in Geospace and Beyond*. ISBN: 978-0-87590-429-0. DOI: 10.1029/164GM03.

Kepko, L., R. L. McPherron, O. Amm, S. Apatenkov, W. Baumjohann, J. Birn, et al. (2014). "Substorm Current Wedge Revisited". In: *Space Science Reviews*, pp. 1–46. DOI: 10.1007/s11214-014-0124-9.

Kloss, C. (2019). *ChaosMagPy*. URL: https://github.com/ancklo/ChaosMagPy.

Kotsiaros, S. and N. Olsen (2012). "The geomagnetic field gradient tensor". In: *GEM - International Journal on Geomathematics* 3, pp. 297–314. DOI: 10.1007/s13137-012-0041-6.

Kotsiaros, S. (2016). "Toward more complete magnetic gradiometry with the Swarm mission". In: *Earth, Planets and Space* 68.1, p. 130. DOI: 10.1186/s40623-016-0498-x.

Kuvshinov, A. V. (2008). "3-D global induction in the oceans and solid earth: Recent progress in modeling magnetic and electric fields from sources of magnetospheric, ionospheric and oceanic origin". In: *Surveys in Geophysics* 29.2, pp. 139–186. DOI: 10.1007/s10712-008-9045-z.

Lakhina, G. S. and B. T. Tsurutani (2016). "Geomagnetic storms: historical perspective to modern view". In: *Geoscience Letters* 3.1. DOI: 10.1186/s40562-016-0037-4.

Langel, R. A. and W. J. Hinze (1998).
Magnetic Field of the Earths Lithosphere: The Satellite Perspective.
Cambridge: Cambridge University Press. ISBN: 9780511629549.
DOI: 10.1017/CBO9780511629549.

Larmor, J. (1919). "How could a rotating body such as the Sun become a magnet?"
In: *Reports of the British Association* 87, pp. 159–160.

Laundal, K. M., C. C. Finlay, and N. Olsen (2016a). "Sunlight effects on the 3D polar current system determined from low Earth orbit measurements".
In: *Earth, Planets and Space* 68.1, p. 142. DOI: 10.1186/s40623-016-0518-x.

Laundal, K. M., J. W. Gjerloev, N. Østgaard, J. P. Reistad, S. Haaland, K. Snekvik, et al. (2016b). "The impact of sunlight on high-latitude equivalent currents".
In: *Journal of Geophysical Research: Space Physics* 121, pp. 2715–2726.
DOI: 10.1002/2015JA022236.

Laundal, K. M. and A. D. Richmond (2017). "Magnetic Coordinate Systems".
In: *Space Science Reviews* 206.1, pp. 27–59. DOI: 10.1007/s11214-016-0275-y.

Laundal, K. M., I. Cnossen, S. E. Milan, S. E. Haaland, J. Coxon, N. M. Pedatella, et al. (2017). "North-South Asymmetries in Earth's Magnetic Field".
In: *Space Science Reviews* 206.1, pp. 225–257. DOI: 10.1007/s11214-016-0273-0.

Laundal, K. M. and M. Toresen (2018). "klaundal/pyAMPS: pyAMPS 0.1.0". In:
DOI: 10.5281/ZENODO.1182931.

Laundal, K. M., C. C. Finlay, N. Olsen, and J. P. Reistad (2018). "Solar Wind and Seasonal Influence on Ionospheric Currents From Swarm and CHAMP Measurements".
In: *Journal of Geophysical Research: Space Physics* 123. DOI: 10.1029/2018JA025387.

Leontaritis, I. J. and S. A. Billings (1985). "Input-output parametric models for non-linear systems Part I: deterministic non-linear systems".
In: *International Journal of Control* 41.2, pp. 303–328. DOI: 10.1080/0020718508961129.

Lesur, V., I. Wardinski, M. Rother, and M. Mandea (2008). "GRIMM: The GFZ Reference Internal Magnetic Model based on vector satellite and observatory data".
In: *Geophysical Journal International* 173.2, pp. 382–394.
DOI: 10.1111/j.1365-246X.2008.03724.x.

Lesur, V., N. Olsen, and A. W. Thomson (2011).
"Geomagnetic Core Field Models in the Satellite Era".
In: *Geomagnetic Observations and Models*. Dordrecht: Springer Netherlands, pp. 277–294.
DOI: 10.1007/978-90-481-9858-0_11.

Lesur, V., M. Hamoudi, Y. Choi, J. Dyment, and E. Thébault (2016). "Building the second version of the World Digital Magnetic Anomaly Map (WDMAM)". en.
In: *Earth, Planets and Space* 68.1, p. 27. DOI: 10.1186/s40623-016-0404-6.

Livermore, P. W., R. Hollerbach, and C. C. Finlay (2016).
"An accelerating high-latitude jet in Earth's core". In: *Nature Geoscience* 1.December.
DOI: 10.1038/ngeo2859.

Lockwood, M. (2013). "Reconstruction and prediction of variations in the open Solar Magnetic Flux and interplanetary conditions". In: *Living Reviews in Solar Physics* 10.
DOI: 10.12942/lrsp-2013-4.

Lockwood, M. (2016). "Jim Dungey, The Open Magnetosphere, and Space Weather".
In: *Space Weather* 14.6, pp. 380–383. DOI: 10.1002/2016SW001438.

Lockwood, M., M. J. Owens, L. A. Barnard, S. Bentley, C. J. Scott, and C. E. Watt (2016).
"On the Origins and Timescales of Geoeffective IMF".
In: *Space Weather* 14.6, pp. 406–432. DOI: 10.1002/2016SW001375.

Lockwood, M., M. J. Owens, L. A. Barnard, C. J. Scott, and C. E. Watt (2017).
"Space climate and space weather over the past 400 years: 1. The power input to the magnetosphere". In: *Journal of Space Weather and Space Climate* 7, A25.
DOI: 10.1051/swsc/2017019.

Lockwood, M., A. Chambodut, L. A. Barnard, M. J. Owens, E. Clarke, and V. Mendel (2018a). "A homogeneous aa index: 1. Secular variation".
In: *Space Weather and Space Climate* 8. DOI: 10.1051/swsc/2018038.

Lockwood, M., M. J. Owens, L. A. Barnard, C. J. Scott, C. E. Watt, and S. Bentley (2018b). "Space climate and space weather over the past 400 years: 2. Proxy indicators of geomagnetic storm and substorm occurrence". In: *Journal of Space Weather and Space Climate* 8, A12. DOI: 10.1051/swsc/2017048.

Lotko, W. (2017). "The Unifying Principle of Coordinated Measurements in Geospace Science". In: *Space Weather* 15.4, pp. 553–557. DOI: 10.1002/2017SW001634.

Lowes, F. J. (1974). "Spatial power spectrum of the main geomagnetic field". In: *Geophys. J. R. Astr. Soc.* 36, pp. 717–730.

Lowes, F. J. (2007). "Measuring magnetic field in the 'diamagnetic' ionosphere". In: *Geophysical Journal International* 171.1, pp. 115–118. DOI: 10.1111/j.1365-246X.2007.03506.x.

Lowrie, W. (2007). *Fundamentals of Geophysics*. Cambridge University Press. ISBN: 9780521859028.

Lühr, H., C. Xiong, N. Olsen, and G. Le (2017). "Near-Earth Magnetic Field Effects of Large-Scale Magnetospheric Currents". In: *Space Science Reviews* 206.1-4, pp. 521–545. DOI: 10.1007/s11214-016-0267-y.

Macmillan, S. (2007a). "Observatories, Overview". In: *Encyclopedia of Geomagnetism and Paleomagnetism*. Ed. by D. Gubbins and E. Herrero-Bervera. Dordrecht: Springer Netherlands, pp. 708–711. ISBN: 978-1-4020-4423-6. DOI: 10.1007/978-1-4020-4423-6_224.

Macmillan, S. (2007b). "Repeat Stations". In: *Encyclopedia of Geomagnetism and Paleomagnetism*. Dordrecht: Springer Netherlands, pp. 858–859. DOI: 10.1007/978-1-4020-4423-6_276.

Macmillan, S. and C. Finlay (2011). "The International Geomagnetic Reference Field". In: *Geomagnetic Observations and Models*. Dordrecht: Springer Netherlands, pp. 265–276. DOI: 10.1007/978-90-481-9858-0_10.

Mandea, M. and N. Olsen (2006). "A new approach to directly determine the secular variation from magnetic satellite observations". In: *Geophysical Research Letters* 33.15, pp. 1–5. DOI: 10.1029/2006GL026616.

Mandea, M. and M. Purucker (2018). "The Varying Core Magnetic Field from a Space Weather Perspective". In: *Space Science Reviews* 214.1, p. 11. DOI: 10.1007/s11214-017-0443-8.

Maus, S., F. Yin, H. Lühr, C. Manoj, M. Rother, J. Rauberg, et al. (2008). "Resolution of direction of oceanic magnetic lineations by the sixth-generation lithospheric magnetic field model from CHAMP satellite magnetic measurements". In: *Geochemistry, Geophysics, Geosystems* 9.7, pp. 1–10. DOI: 10.1029/2008GC001949.

Maus, S. (2008). "The geomagnetic power spectrum". In: *Geophysical Journal International* 174.1, pp. 135–142. DOI: 10.1111/j.1365-246X.2008.03820.x.

Maus, S. (2010a). "An ellipsoidal harmonic representation of Earth's lithospheric magnetic field to degree and order 720". In: *Geochemistry, Geophysics, Geosystems* 11.6, pp. 1–12. DOI: 10.1029/2010GC003026.

Maus, S. (2010b). *Magnetic field model MF7*. URL: http://www.geomag.us/models/MF7.html.

Maus, S., C. Manoj, J. Rauberg, I. Michaelis, and H. Lühr (2010). "NOAA/NGDC candidate models for the 11th generation International Geomagnetic Reference Field and the concurrent release of the 6th generation Pomme magnetic model". In: *Earth, Planets and Space* 62.10, pp. 729–735. DOI: 10.5047/eps.2010.07.006.

Mayaud, P. N. (1980). *Derivation, Meaning, and Use of Geomagnetic Indices*. American Geophysical Union. ISBN: 0875900224. DOI: 10.1029/GM022.

McGranaghan, R. M., A. Bhatt, T. Matsuo, A. J. Mannucci, J. L. Semeter, and S. Datta-Barua (2017). "Ushering in a New Frontier in Geospace Through Data Science". In: *Journal of Geophysical Research: Space Physics* 122.12, pp. 12586–12590. DOI: 10.1002/2017JA024835.

McPherron, R. L., C. T. Russell, and M. P. Aubry (1973). "Satellite studies of magnetospheric substorms on August 15, 1968: 9. Phenomenological model for substorms". In: *Journal of Geophysical Research* 78.16, pp. 3131–3149. DOI: 10.1029/ja078i016p03131.

McPherron, R. L. (2005). "Magnetic pulsations: Their sources and relation to solar wind and geomagnetic activity". In: *Surveys in Geophysics* 26.5, pp. 545–592. DOI: 10.1007/s10712-005-1758-7.

Meeren, C. v. d., A. G. Burrell, and K. M. Laundal (2018). *ApexPy*. DOI: 10.5281/ZENODO.1214207.

Menvielle, M. and A. Marchaudon (2007). "Geomagnetic Indices in Solar-Terrestrial Physics and Space Weather BT - Space Weather: Research Towards Applications in Europe". In: ed. by J. Lilensten. Dordrecht: Springer Netherlands, pp. 277–288. ISBN: 978-1-4020-5446-4. DOI: 10.1007/1-4020-5446-7_24.

Menvielle, M., T. Iyemori, A. Marchaudon, and M. Nosé (2011). "Geomagnetic Indices". In: *Geomagnetic Observations and Models*. Dordrecht: Springer Netherlands, pp. 183–228. DOI: 10.1007/978-90-481-9858-0_8.

Met Office (2010). "Cartopy: a cartographic python library with a Matplotlib interface". In: URL: http://scitools.org.uk/cartopy.

Meyer, B., A. Chulliat, and R. Saltus (2017). "Derivation and Error Analysis of the Earth Magnetic Anomaly Grid at 2 arc min Resolution Version 3 (EMAG2v3)". In: *Geochemistry, Geophysics, Geosystems* 18.12, pp. 4522–4537. DOI: 10.1002/2017GC007280.

Milan, S. E., L. B. N. Clausen, J. C. Coxon, J. A. Carter, M.-T. Walach, K. Laundal, et al. (2017). "Overview of Solar Wind–Magnetosphere–Ionosphere–Atmosphere Coupling and the Generation of Magnetospheric Currents". In: *Space Science Reviews* 206, pp. 547–573. DOI: 10.1007/s11214-017-0333-0.

Milan, S. E., J. A. Carter, H. Sangha, K. M. Laundal, N. Østgaard, P. Tenfjord, et al. (2018). "Timescales of Dayside and Nightside Field-Aligned Current Response to Changes in Solar Wind-Magnetosphere Coupling". In: *Journal of Geophysical Research: Space Physics* 123.9, pp. 7307–7319. DOI: 10.1029/2018JA025645.

Milan, S., J. Wild, a. Grocott, and N. Draper (2006). "Space- and ground-based investigations of solar wind–magnetosphere–ionosphere coupling". In: *Advances in Space Research* 38.8, pp. 1671–1677. DOI: 10.1016/j.asr.2005.08.009.

Moretto, T., N. Olsen, P. Ritter, and G. Lu (2002). "Investigating the auroral electrojets with low altitude polar orbiting satellites". In: *Annales Geophysicae* 20.7, pp. 1049–1061. DOI: 10.5194/angeo-20-1049-2002.

Morley, S. K., D. T. Welling, J. Koller, B. A. Larsen, M. G. Henderson, and J. Niehof (2010). "SpacePy-A Python-based library of tools for the space sciences". In: *Proceeding of the 9th Python in Science Conference* Scipy, pp. 39–45. URL: http://conference.scipy.org/proceedings/scipy2010/pdfs/morley.pdf.

Newell, P. T., T. Sotirelis, K. Liou, C. I. Meng, and F. J. Rich (2007). "A nearly universal solar wind-magnetosphere coupling function inferred from 10 magnetospheric state variables". In: *Journal of Geophysical Research: Space Physics* 112.1, pp. 1–16. DOI: 10.1029/2006JA012015.

Newell, P. T., T. Sotirelis, and S. Wing (2010). "Seasonal variations in diffuse, monoenergetic, and broadband aurora". In: *Journal of Geophysical Research* 115, A03216. DOI: 10.1029/2009JA014805.

Newell, P. T. and J. W. Gjerloev (2011). "Substorm and magnetosphere characteristic scales inferred from the SuperMAG auroral electrojet indices". In: *Journal of Geophysical Research: Space Physics* 116.A12. DOI: 10.1029/2011JA016936.

Nishida, A. (1968). "Coherence of geomagnetic DP 2 fluctuations with interplanetary magnetic variations".

In: *Journal of Geophysical Research* 73.17, pp. 5549–5559. DOI: 10.1029/ja073i017p05549.

Olsen, N. (1996). "A new tool for determining ionospheric currents from magnetic satellite data". In: *Geophysical Research Letters* 23.24, pp. 3635–3638. DOI: 10.1029/96GL02896.

Olsen, N., T. Moretto, and E. Friis-Christensen (2002). "New approaches to explore the Earth's magnetic field". In: *Journal of Geodynamics* 33.1-2, pp. 29–41. DOI: 10.1016/S0264-3707(01)00052-7.

Olsen, N., F. Primdahl, L. Tøffner-Clausen, T. Sabaka, P. Brauer, J. Merayo, et al. (2003). "Calibration of the Ørsted vector magnetometer". In: *Earth, Planets and Space* 55.1, pp. 11–18. DOI: 10.1186/BF03352458.

Olsen, N., T. J. Sabaka, and F. Lowes (2005). "New parameterization of external and induced fields in geomagnetic field modeling, and a candidate model for IGRF 2005". In: *Earth, Planets and Space* 57.12, pp. 1141–1149. DOI: 10.1186/BF03351897.

Olsen, N. (2007). "Natural Sources for Electromagnetic Induction Studies". In: *Encyclopedia of Geomagnetism and Paleomagnetism*. Ed. by D. Gubbins and E. Herrero-Bervera. Springer, pp. 696–700. ISBN: 978-1-4020-3992-8. DOI: 10.1007/978-1-4020-4423-6.

Olsen, N., G. Hulot, and T. J. Sabaka (2010a). "Measuring the Earth's magnetic field from space: Concepts of past, present and future missions". In: *Space Science Reviews* 155, pp. 65–93. DOI: 10.1007/s11214-010-9676-5.

Olsen, N., K. H. Glassmeier, and X. Jia (2010b). "Separation of the magnetic field into external and internal parts". In: *Space Science Reviews* 152.1-4, pp. 135–157. DOI: 10.1007/s11214-009-9563-0.

Olsen, N. and C. Stolle (2012). "Satellite Geomagnetism". In: *Annu. Rev. Earth Planet. Sci* 40. DOI: 10.1146/annurev-earth-042711-105540.

Olsen, N., E. Friis-Christensen, R. Floberghagen, P. Alken, C. D. Beggan, A. Chulliat, et al. (2013). "The Swarm satellite constellation application and research facility (SCARF) and Swarm data products". In: *Earth, Planets and Space* 65.11, pp. 1189–1200. DOI: 10.5047/eps.2013.07.001.

Olsen, N., H. Lühr, C. C. Finlay, T. J. Sabaka, I. Michaelis, J. Rauberg, et al. (2014). "The CHAOS-4 geomagnetic field model". In: *Geophysical Journal International* 197.2, pp. 815–827. DOI: 10.1093/gji/ggu033.

Olsen, N., D. Ravat, C. C. Finlay, and L. K. Kother (2017). "LCS-1: A high-resolution global model of the lithospheric magnetic field derived from CHAMP and Swarm satellite observations". In: *Geophysical Journal International* October, pp. 1461–1477. DOI: 10.1093/gji/ggx381.

Olsen, N. and C. Stolle (2017). "Magnetic Signatures of Ionospheric and Magnetospheric Current Systems During Geomagnetic Quiet Conditions - An Overview". In: *Space Science Reviews* 206, pp. 5–25. DOI: 10.1007/s11214-016-0279-7.

Østgaard, N., B. K. Humberset, and K. M. Laundal (2011). "Evolution of auroral asymmetries in the conjugate hemispheres during two substorms". In: *Geophysical Research Letters* 38.3. DOI: 10.1029/2010GL046057.

Østgaard, N., J. P. Reistad, P. Tenfjord, K. M. Laundal, K. Snekvik, S. Milan, et al. (2016). "Mechanisms that Produce Auroral Asymmetries in Conjugate Hemispheres". In: *Auroral Dynamics and Space Weather, Geophysical Monograph Book Series*. Vol. 215, pp. 131–143. ISBN: 9781118978719. DOI: 10.1002/9781118978719.ch10.

Parker, E. N. (1955). "Hydromagnetic Dynamo Models". In: *Astrophysical Journal* 122.

Parker, E. N. (1958). "Dynamics of the interplanetary gas and magnetic fields". In: *Astrophysical Journal* 128. DOI: 10.1086/146579.

Parkinson, W. (1983). *Introduction to Geomagnetism*. Scottish Academic Press. ISBN: 707302927.

Pilipenko, V. A. (1990). "ULF waves on the ground and in space". In: *Journal of Atmospheric and Terrestrial Physics* 52.12, pp. 1193–1209. DOI: 10.1016/0021-9169(90)90087-4.

Pirjola, R. (2005). "Space weather risk". In: *Space Weather* 3.2. DOI: 10.1029/2004SW000112.

Pulkkinen, A., O. Amm, and A. Viljanen (2003). "Ionospheric equivalent current distributions determined with the method of spherical elementary current systems".
In: *Journal of Geophysical Research: Space Physics* 108.A2. DOI: 10.1029/2001ja005085.

Pulkkinen, T. I. (1996). "Pseudobreakup or substorm?"
In: *Proceedings of the 3rd International Conference on Substorms (ICS-3)*.
URL: https://ui.adsabs.harvard.edu/abs/1996ESASP.389..285P.

Purucker, M. E. and K. A. Whaler (2006). "Crustal Magnetism". In: *Treatise on Geophysics*. Vol. 5. July 2013. Elsevier, pp. 1–85. DOI: 10.1016/B978-0-444-53802-4.00100-7.

Purucker, M. E. and D. A. Clark (2011).
"Mapping and Interpretation of the Lithospheric Magnetic Field".
In: *Geomagnetic Observations and Models*. Dordrecht: Springer Netherlands, pp. 311–337.
DOI: 10.1007/978-90-481-9858-0_13.

Rasson, J. L., H. Toh, and D. Yang (2011). "The Global Geomagnetic Observatory Network".
In: *Geomagnetic Observations and Models*. Dordrecht: Springer Netherlands, pp. 1–25.
DOI: 10.1007/978-90-481-9858-0_1.

Reay, S. J., D. C. Herzog, S. Alex, E. P. Kharin, S. McLean, M. Nosé, et al. (2011).
"Magnetic Observatory Data and Metadata: Types and Availability".
In: *Geomagnetic Observations and Models*. Dordrecht: Springer Netherlands, pp. 149–181.
DOI: 10.1007/978-90-481-9858-0_7.

Richmond, A. D. (1995). "Ionospheric Electrodynamics Using Magnetic Apex Coordinates".
In: *J. Geomag. Geoelectr.* 47. DOI: 10.5636/jgg.47.191.

Ritter, P., A. Viljanen, H. Lühr, O. Amm, and N. Olsen (2003). "Ionospheric currents from CHAMP magnetic field data comparison with ground based measurements".
In: *First CHAMP mission results for gravity, magnetic and atmospheric studies*.
Ed. by C. Reigber, H. Luhr, and P. Schwintzer. Springer Berlin, pp. 347–352.
ISBN: 978-3-540-38366-6. DOI: 10.1007/978-3-540-38366-6_50.

Ritter, P., L. Hermann, H. Luhr, J. Rauberg, and L. Hermann (2013).
"Determining field-aligned currents with the Swarm constellation mission".
In: *Earth, Planets and Space* 65.11, pp. 1285–1294. DOI: 10.5047/eps.2013.09.006.

Roberts, P. H. and E. M. King (2013). "On the genesis of the Earth's magnetism."
In: *Reports on progress in physics. Physical Society (Great Britain)* 76.9, p. 096801.
DOI: 10.1088/0034-4885/76/9/096801.

Rostoker, G. and C.-G. Fälthammar (1967). "Relationship between changes in the interplanetary magnetic field and variations in the magnetic field at the Earth's surface".
In: *Journal of Geophysical Research* 72.23, pp. 5853–5863.
DOI: 10.1029/jz072i023p05853.

Rother, M., V. Lesur, and R. Schachtschneider (2013).
"An algorithm for deriving core magnetic field models from the Swarm data set".
In: *Earth, Planets and Space* 65.11, pp. 1223–1231. DOI: 10.5047/eps.2013.07.005.

Russell, C. T. and R. L. McPherron (1973). "Semiannual variation of geomagnetic activity".
In: *Journal of Geophysical Research* 78.1, pp. 92–108. DOI: 10.1029/JA078i001p00092.

Russell, C. T., J. G. Luhmann, and R. J. Strangeway (2016). *Space Physics*.
Cambridge University Press. ISBN: 978-1-107-09882-4.

Sabaka, T. J., L. Tøffner-Clausen, and N. Olsen (2013).
"Use of the comprehensive inversion method for Swarm satellite data analysis".
In: *Earth, Planets and Space* 65.11, pp. 1201–1222. DOI: 10.5047/eps.2013.09.007.

Sabaka, T. J., N. Olsen, R. H. Tyler, and A. Kuvshinov (2014).
"CM5, a pre-Swarm comprehensive geomagnetic field model derived from over 12 yr of CHAMP, Ørsted, SAC-C and observatory data".
In: *Geophysical Journal International* 200.3, pp. 1596–1626. DOI: 10.1093/gji/ggu493.

Sabaka, T. J., R. H. Tyler, and N. Olsen (2016). "Extracting ocean-generated tidal magnetic signals from Swarm data through satellite gradiometry".
In: *Geophysical Research Letters* 43, pp. 3237–3245.
DOI: 10.1002/2016GL068180.Received.

Sabaka, T. J., L. Tøffner-Clausen, N. Olsen, and C. C. Finlay (2018). "A comprehensive model of Earth's magnetic field determined from 4 years of Swarm satellite observations". In: *Earth, Planets and Space* 70. DOI: 10.1186/s40623-018-0896-3.

Sandhu, J. K., T. Walach, and C. Watt (2019). "A global view of storms and substorms". In: *Astronomy & Geophysics* 60, pp. 13–19. URL: 10.1093/astrogeo/atz144.

Schuster, A. (1889). "The diurnal variation of terrestrial magnetism". In: *Philosophical Transactions of the Royal Society* 180, pp. 467–518. DOI: 10.1098/rsta.1889.0015.

Shoemake, K. (1985). "Animating Rotation with Quaternion Curves". In: *SIGGRAPH*. ISBN: 0-89791-166-0.

Shore, R. M., M. P. Freeman, J. A. Wild, and J. W. Gjerloev (2017). "A high-resolution model of the external and induced magnetic field at the Earth's surface in the northern hemisphere". In: *Journal of Geophysical Research: Space Physics*. DOI: 10.1002/2016JA023682.

Shore, R. M., M. P. Freeman, and J. W. Gjerloev (2019). "Interplanetary magnetic field control of polar ionospheric equivalent current system modes". In: *Space Weather*, 2019SW002161. DOI: 10.1029/2019SW002161.

Shue, J.-H., J. K. Chao, H. C. Fu, C. T. Russell, P. Song, K. K. Khurana, et al. (1997). "A new functional form to study the solar wind control of the magnetopause size and shape". In: *Journal of Geophysical Research* 102.1, p. 9497. DOI: 10.1029/97JA00196.

Smith, A. R. A., C. D. Beggan, S. Macmillan, and K. A. Whaler (2017). "Climatology of the auroral electrojets derived from the along-track gradient of magnetic field intensity measured by POGO, Magsat, CHAMP, and Swarm". In: *Space Weather* 15. DOI: 10.1002/2017SW001675.

Smith, A. R. A. and M. Pačes (2019). "ESA-VirES/VirES-Python-Client: Release for VirES v3.0". In: DOI: 10.5281/ZENODO.2800802.

Southwood, D., S. W. H. Cowley, and S. Mitton (2015). *Magnetospheric Plasma Physics: The Impact of Jim Dungey's Research*. Ed. by D. Southwood, S. W. H. Cowley, and S. Mitton. Springer, pp. 33–64. ISBN: 9783319183596. DOI: 10.1007/978-3-319-18359-6_2.

Stauning, P. (2013). "The Polar Cap index: A critical review of methods and a new approach". In: *Journal of Geophysical Research: Space Physics* 118.8, pp. 5021–5038. DOI: 10.1002/jgra.50462.

Stevenson, D. J. (2008). "Planetary magnetic fields". In: *Earth and Planetary Science Letters* 208.1. DOI: 10.1088/0034-4885/46/5/001.

Stockmann, R., C. C. Finlay, and A. Jackson (2009). "Imaging Earth's crustal magnetic field with satellite data: a regularized spherical triangle tessellation approach". In: *Geophysical Journal International* 179.2, pp. 929–944. DOI: 10.1111/j.1365-246X.2009.04345.x.

Stoneback, R. A., A. G. Burrell, J. Klenzing, and M. Depew (2018). "PYSAT: Python Satellite Data Analysis Toolkit". In: *Journal of Geophysical Research: Space Physics*. DOI: 10.1029/2018JA025297.

Sugiura, M. (1964). "Hourly values of equatorial Dst for the IGR". In: *Ann. Int. Geophys. Yr.* 35. URL: https://www.osti.gov/biblio/4554034.

Teanby, N. A. (2006). "An icosahedron-based method for even binning of globally distributed remote sensing data". In: *Computers and Geosciences* 32.9, pp. 1442–1450. DOI: 10.1016/j.cageo.2006.01.007.

Tenfjord, P., N. Østgaard, K. Snekvik, K. M. Laundal, J. P. Reistad, S. Haaland, et al. (2015). "How the IMF B y induces a B y component in the closed magnetosphere and how it leads to asymmetric currents and convection patterns in the two hemispheres". In: *Journal of Geophysical Research: Space Physics* 120, pp. 9368–9384. DOI: 10.1002/2015JA021579.

Thébault, E., M. Purucker, K. A. Whaler, B. Langlais, and T. J. Sabaka (2010). "The Magnetic Field of the Earth's Lithosphere". In: *Space Science Reviews* 155.1-4, pp. 95–127. DOI: 10.1007/s11214-010-9667-6.

Thébault, E., P. Vigneron, S. Maus, A. Chulliat, O. Sirol, and G. Hulot (2013). "Swarm SCARF Dedicated Lithospheric Field Inversion chain". In: *Earth, Planets and Space* 65.11, pp. 1257–1270. DOI: 10.5047/eps.2013.07.008.

Thébault, E., C. C. Finlay, C. D. Beggan, P. Alken, J. Aubert, O. Barrois, et al. (2015). "International Geomagnetic Reference Field: the 12th generation". en. In: *Earth, Planets and Space* 67.1, p. 79. DOI: 10.1186/s40623-015-0228-9.

Thébault, E., V. Lesur, K. Kauristie, and R. Shore (2017). "Magnetic Field Data Correction in Space for Modelling the Lithospheric Magnetic Field". In: *Space Science Reviews* 206.1-4, pp. 191–223. DOI: 10.1007/s11214-016-0309-5.

Thomson, A. W. P., B. Hamilton, S. Macmillan, and S. J. Reay (2010). "A novel weighting method for satellite magnetic data and a new global magnetic field model". In: *Geophysical Journal International* 181.1, pp. 250–260. DOI: 10.1111/j.1365-246X.2010.04510.x.

Troitskaya, V. A. and A. V. Gul'elmi (1967). "Geomagnetic micropulsations and diagnostics of the magnetosphere". In: *Space Science Reviews* 7.5-6, pp. 689–768. DOI: 10.1007/BF00542894.

Troshichev, O. A. and V. G. Andrezen (1985). "The relationship between interplanetary quantities and magnetic activity in the southern polar cap". In: *Planetary and Space Science* 33.4, pp. 415–419. DOI: 10.1016/0032-0633(85)90086-8.

Tsurutani, B. T. and G. S. Lakhina (2014). "An extreme coronal mass ejection and consequences for the magnetosphere and Earth". In: *Geophysical Research Letters* 41. DOI: 10.1002/2013GL058825.

Tsyganenko, N. A. (1995). "Modeling the Earth's magnetospheric magnetic field confined within a realistic magnetopause". In: *Journal of Geophysical Research* 100, pp. 5599–5612. DOI: 10.1029/94JA03193.

Tsyganenko, N. A. (2019). "Secular drift of the auroral ovals: How fast do they actually move?" In: *Geophysical Research Letters*, pp. 3017–3023. DOI: 10.1029/2019GL082159.

Tyler, R. H., S. Maus, and H. Lu (2003). "Satellite Observations of Magnetic Fields Due to". In: *Science* 239, pp. 239–242. DOI: 10.1126/science.1078074.

Unsworth, M. (2007). "Magnetotellurics". In: *Encyclopedia of Geomagnetism and Paleomagnetism*. Dordrecht: Springer Netherlands, pp. 670–673. DOI: 10.1007/978-1-4020-4423-6_207.

Vennerstrom, S. and T. Moretto (2013). "Monitoring auroral electrojets with satellite data". In: *Space Weather* 11.9, pp. 509–519. DOI: 10.1002/swe.20090.

Vervelidou, F. and V. Lesur (2018). "Unveiling Earth's hidden magnetization". In: *Geophysical Research Letters* 45. DOI: 10.1029/2018GL079876.

Walker, M. R. and A. Jackson (2000). "Robust modelling of the Earth's magnetic field". In: *Geophysical Journal International* 143.3, pp. 799–808. DOI: 10.1046/j.1365-246X.2000.00274.x.

Wasilewski, P. J., H. H. Thomas, and M. A. Mayhew (1979). "The Moho as a magnetic boundary". In: *Geophysical Research Letters* 6. DOI: 10.1029/GL006i007p00541.

Werner, S. M., C. J. Rodger, and N. R. Thomson (2005). "Identifying power line harmonic radiation from an electrical network". In: *Annales Geophysicae* 23.6, pp. 2107–2116. DOI: 10.5194/angeo-23-2107-2005.

Whaler, K. A. (2007). "Geomagnetism in the satellite era". In: *Astronomy and Geophysics* 48.2, pp. 23–29. DOI: 10.1111/j.1468-4004.2007.48223.x.

Yamazaki, Y. and A. Maute (2017). "Sq and EEJ—A Review on the Daily Variation of the Geomagnetic Field Caused by Ionospheric Dynamo Currents". In: *Space Science Reviews* 206.1-4, pp. 299–405. DOI: 10.1007/s11214-016-0282-z.

Yin, F. and H. Lühr (2011). "Recalibration of the CHAMP satellite magnetic field measurements". In: *Measurement Science and Technology* 22.5. DOI: 10.1088/0957-0233/22/5/055101.

Appendices

Appendix A

AEJ detections and climatology

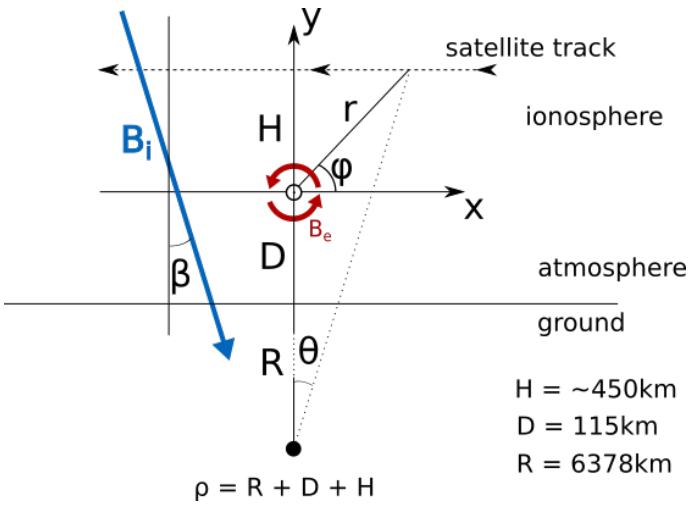

Figure A.1: An elevation view to show the various angles involved. The satellite path is described in polar coordinates by r and ϕ with $0 < \phi < \pi$, and is equivalently described by a transformation to the Cartesian x, y coordinates. For the part of the path with significant perturbation caused by the electrojet, ϕ is close to $\frac{\pi}{2}$ so the path and Earth curvature is ignored. The path passes through a small change in latitude (θ) so the path length is given by $x = \rho\theta$. The angle between the internal field direction and the vertical is β.

By modelling the electrojet as a single horizontal line current along a circle of magnetic latitude, the maximum in the along-track gradient (being approximately perpendicular to magnetic latitude circles, i.e. along a line of magnetic longitude) indicates the location and strength of the current. The field produced by an infinite line current is:

$$\boldsymbol{B} = \frac{\mu_0 I}{2\pi r}\hat{\boldsymbol{\phi}} \tag{A.1}$$

given in polar coordinates in a plane perpendicular to the current, with r and ϕ the distance and angle to the current (see Figure A.1). If the satellite passes along the x-direction at a height H, then the path can be described by ϕ and r such that $sin(\phi) = \frac{H}{r}$. The coordinate systems are related by $\hat{\boldsymbol{\phi}} = -sin(\phi)\hat{\boldsymbol{x}} + cos(\phi)\hat{\boldsymbol{z}}$ and so $\boldsymbol{B}$ can be re-expressed as:

$$\boldsymbol{B} = \frac{\mu_0 I}{2\pi H} sin(\phi)\left(-sin(\phi)\hat{\boldsymbol{x}} + cos(\phi)\hat{\boldsymbol{z}}\right) \tag{A.2}$$

The arc length travelled by the satellite as it subtends an angle of θ with the Earth's centre (corresponding to a change of $\sim \theta$ in latitude) is $x = \rho\theta$ where ρ is the orbital radius. Since $tan(\phi) = \frac{H}{x}$, we get

$$\theta = \frac{H}{\rho} cot(\phi), \tag{A.3}$$

$$v = \frac{d\theta}{dt} = \frac{H}{\rho}\frac{d\phi}{dt} cosec^2(\phi). \tag{A.4}$$

Rearranging gives

$$\frac{d\phi}{dt} = -\frac{\rho}{H} v sin^2(\phi) \tag{A.5}$$

where the angular orbital velocity, $v = \frac{d\theta}{dt} \approx \frac{2\pi}{60*90} s^{-1}$, assuming an orbit takes 90 minutes to complete.

If the internal field is inclined with respect to the z-direction at an angle β then the component of the field detected, resolved parallel to the internal field, is given as

$$B_{\parallel} = B_z cos(\beta) + B_x sin(\beta) \tag{A.6}$$

$$= \frac{\mu_0 I}{2\pi H}\left(sin(\phi)cos(\phi)cos(\beta) - sin^2(\phi)sin(\beta)\right) \tag{A.7}$$

where B_z and B_x are the z and x components of Equation A.2.

The along-track gradient for the parallel component is then given by

$$\frac{dB_{\parallel}}{dt} = \frac{\mu_0 I}{2\pi H}\left(cos(\beta)\frac{d}{dt}\left(sin(\phi)cos(\phi)\right) - sin(\beta)\frac{d}{dt}\left(sin^2(\phi)\right)\right) \tag{A.8}$$

$$= \frac{\mu_0 I}{2\pi H}\frac{d\phi}{dt}\left(cos(\beta)\left(1-2sin^2(\phi)\right) - sin(\beta)\left(2sin(\phi)cos(\phi)\right)\right) \tag{A.9}$$

$$= -\frac{\mu_0 I \rho}{2\pi H^2} v sin^2(\phi)\left(cos(\beta)\left(1-2sin^2(\phi)\right) - sin(\beta)\left(2sin(\phi)cos(\phi)\right)\right) \tag{A.10}$$

where $\frac{d\phi}{dt}$ has been substituted using Equation A.5. For $\beta = 0$, the case where the field points directly along z, the maximum $\frac{dB_{\parallel}}{dt}$ occurs at $\phi = \frac{\pi}{2}$, where the satellite is exactly above the line current (i.e. at the same latitude), and the current required to produce the observed maximum can be found by rearranging Equation A.10 to give

$$I = \frac{2\pi H^2}{\mu_0 \rho v}\frac{dB_{\parallel}}{dt}|_{max}. \tag{A.11}$$

When $\beta \neq 0$ is considered, $\frac{dB_{\parallel}}{dt}|_{max}$ is offset from the current location. By setting $\frac{d^2 B_{\parallel}}{dt^2} = 0$, this is found as

$$cot(\beta) = tan(\phi)\left(\frac{4cos^2(\phi)-1}{4cos^2(\phi)-3}\right) \tag{A.12}$$

and the associated current strength, I, is found accordingly from Equation A.10.

After subtracting a main field model from the scalar data, F, measured by the satellite, the maximum in its gradient over a polar-region pass thus indicates the position electrojet and the current strength can be calculated from the size of the maximum. The data is therefore segregated into ascending and descending segments above 50^o magnetic latitude and the maximum (either negative or positive) gradient is selected above a threshold of 0.1nT/s (corresponding to an electrojet of ∼10kA). The method is robust in that it can usually pick out a clear signal and has low requirements on data availability and quality but it does not show the latitudinal extent or complexity of the electrojet. This is particularly a problem when the electrojet is less concentrated and is spread across a larger latitudinal extent, where this method will simply identify a weaker current.

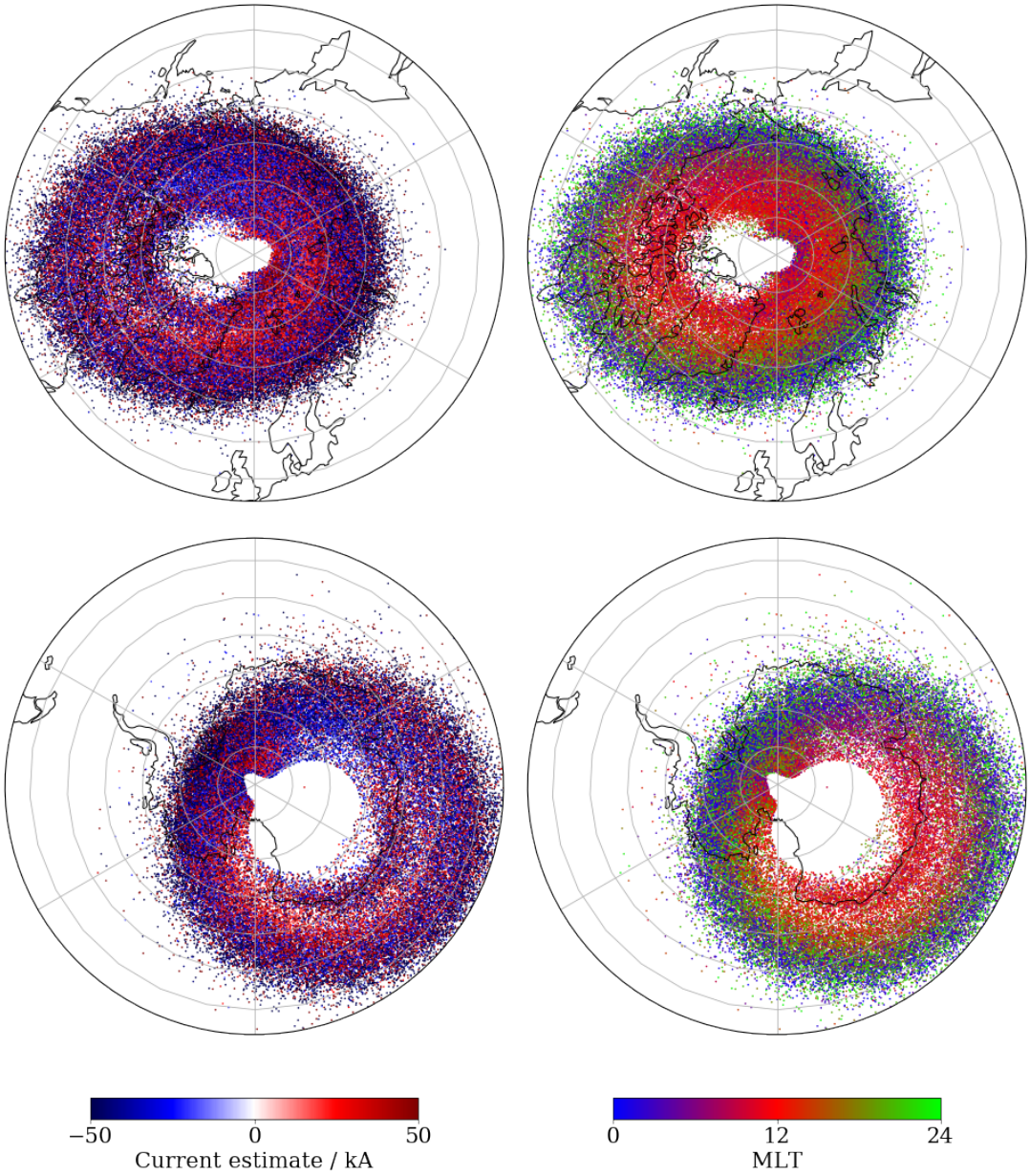

Figure A.2: AEJ detections as in Figure 5.4, showing (left) the assigned current direction, and (right) the magnetic local time of each detection.

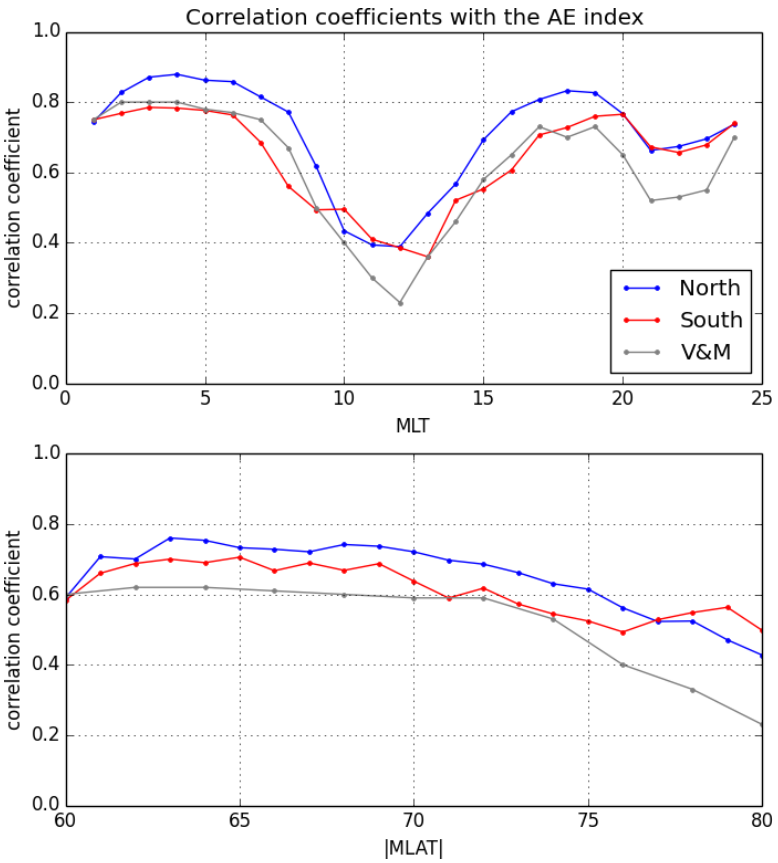

Figure A.3: Correlation coefficients between my AEJ measurement and the AE index, binned according to the magnetic local time (top) and magnetic latitude (bottom) of the AEJ measurements. The different lines correspond to measurements in the Northern Hemisphere (blue) and measurements in the Southern Hemisphere (red), and the original results by Vennerstrom and Moretto (2013) (grey). The correlation is stronger in the North at latitudes typical of the observatories which contribute to the AE index (60-70° MLAT), at the MLTs where the stations are more likely to be contributing because the electrojets are stronger here (dawn/dusk).

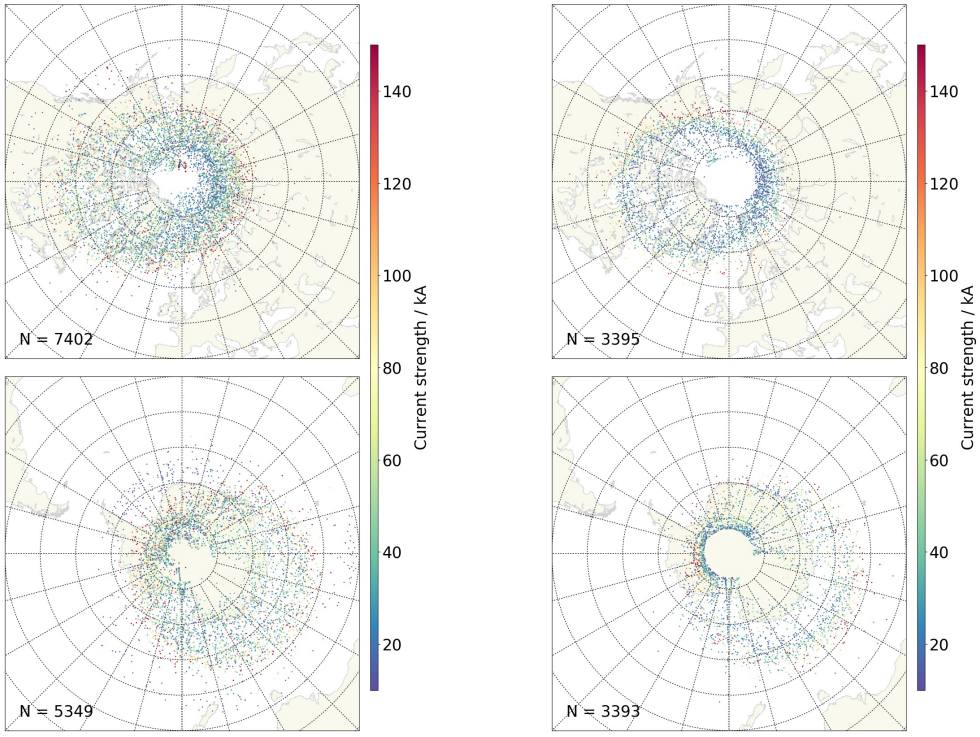

Figure A.4: AEJ detections as in 5.4, but for (left) POGO and (right) Magsat data.

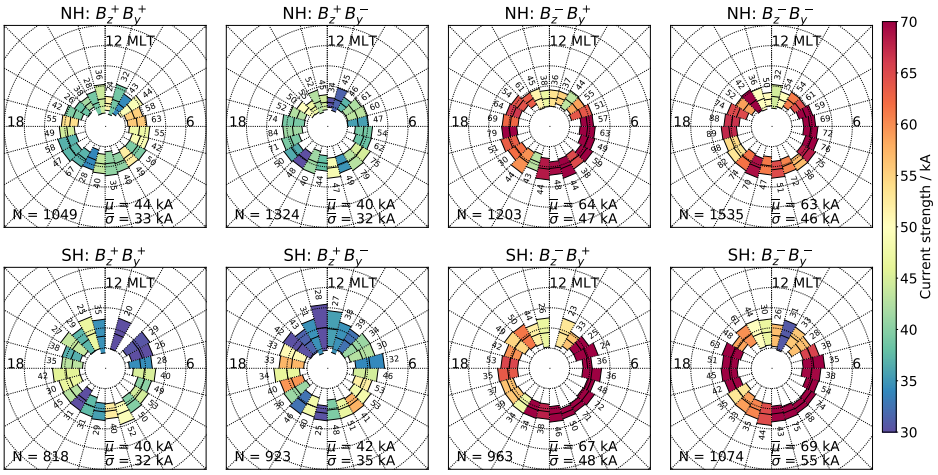

Figure A.5: As for Figure 5.5 but for POGO data

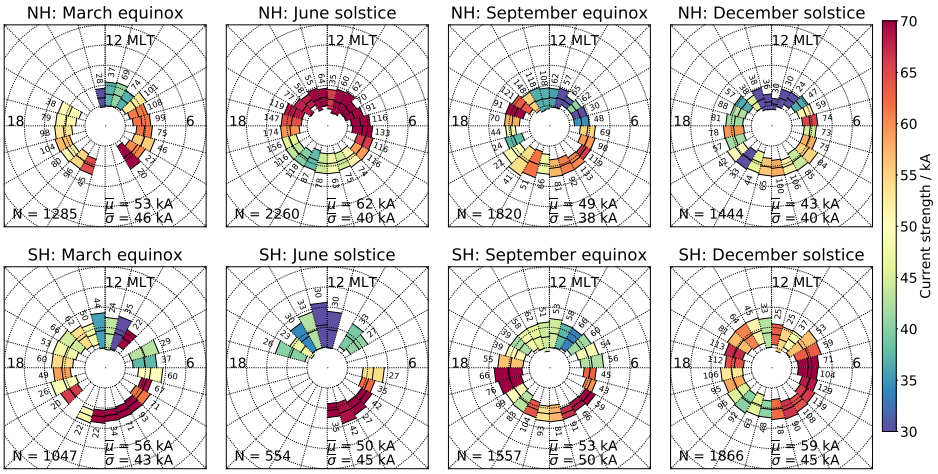

Figure A.6: As for Figure 5.6 but for POGO data

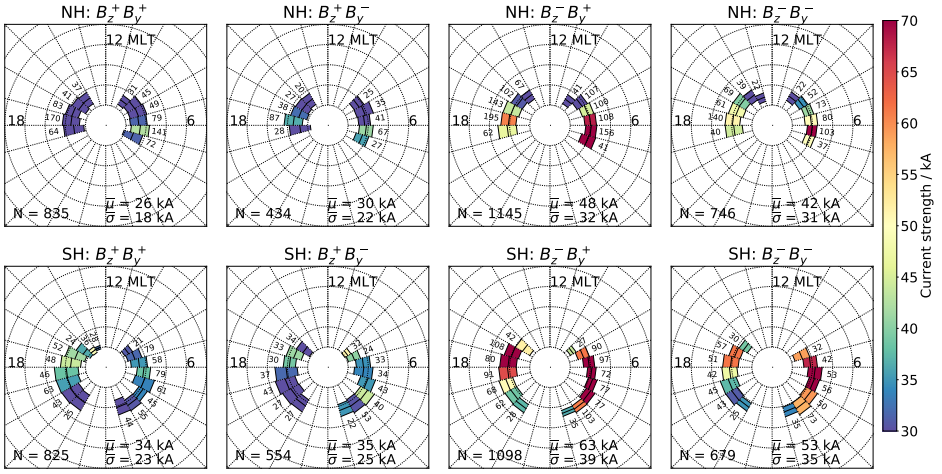

Figure A.7: As for Figure 5.5 but for Magsat data

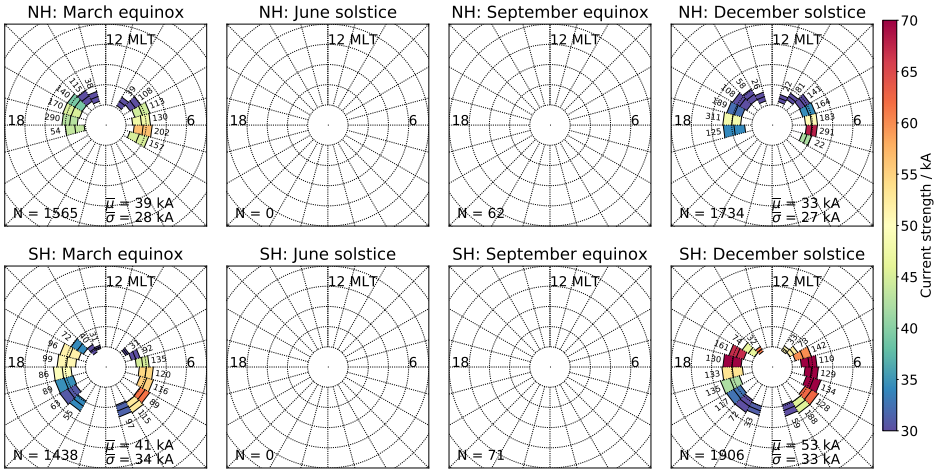

Figure A.8: As for Figure 5.6 but for Magsat data

Appendix B

Lithospheric model algorithm for other components

The following figures show additional information for Chapter 7. They show the algorithm steps as in Figures 7.9 & 7.10, but for all components (NEC), first for Swarm Alpha, then for Swarm Bravo.

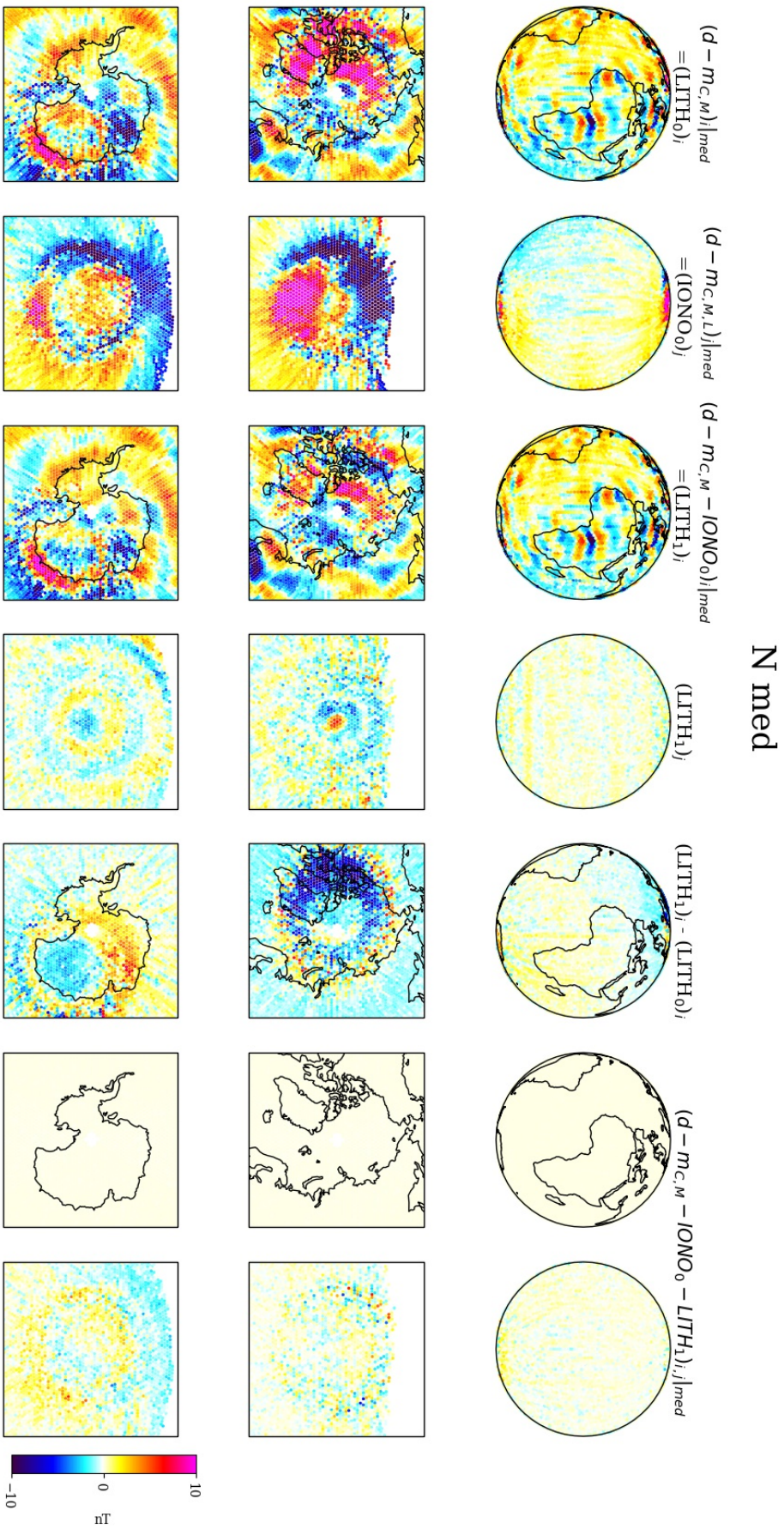

Figure B.1: Swarm Alpha North (X) component medians

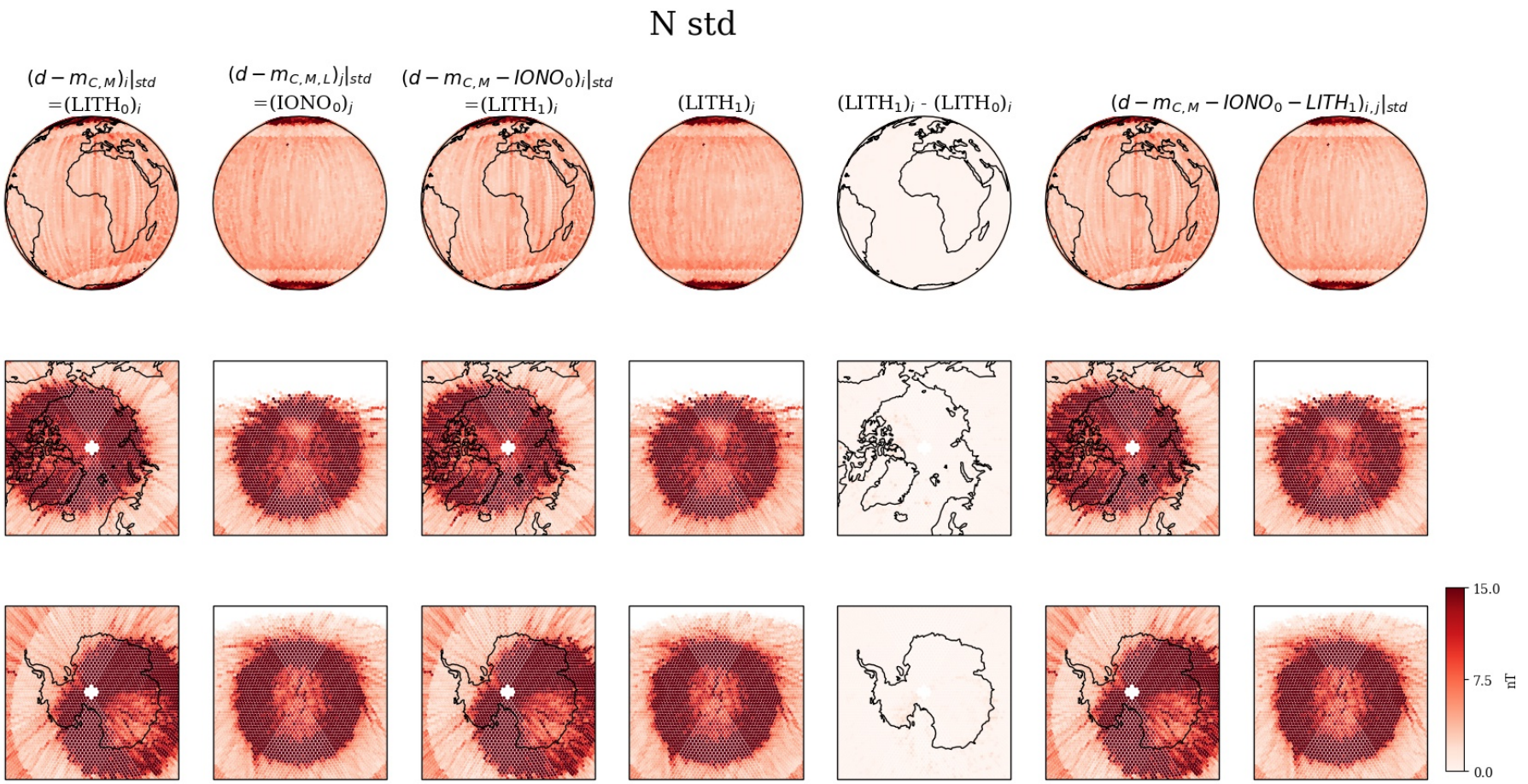

Figure B.2: Swarm Alpha North (X) component standard deviations

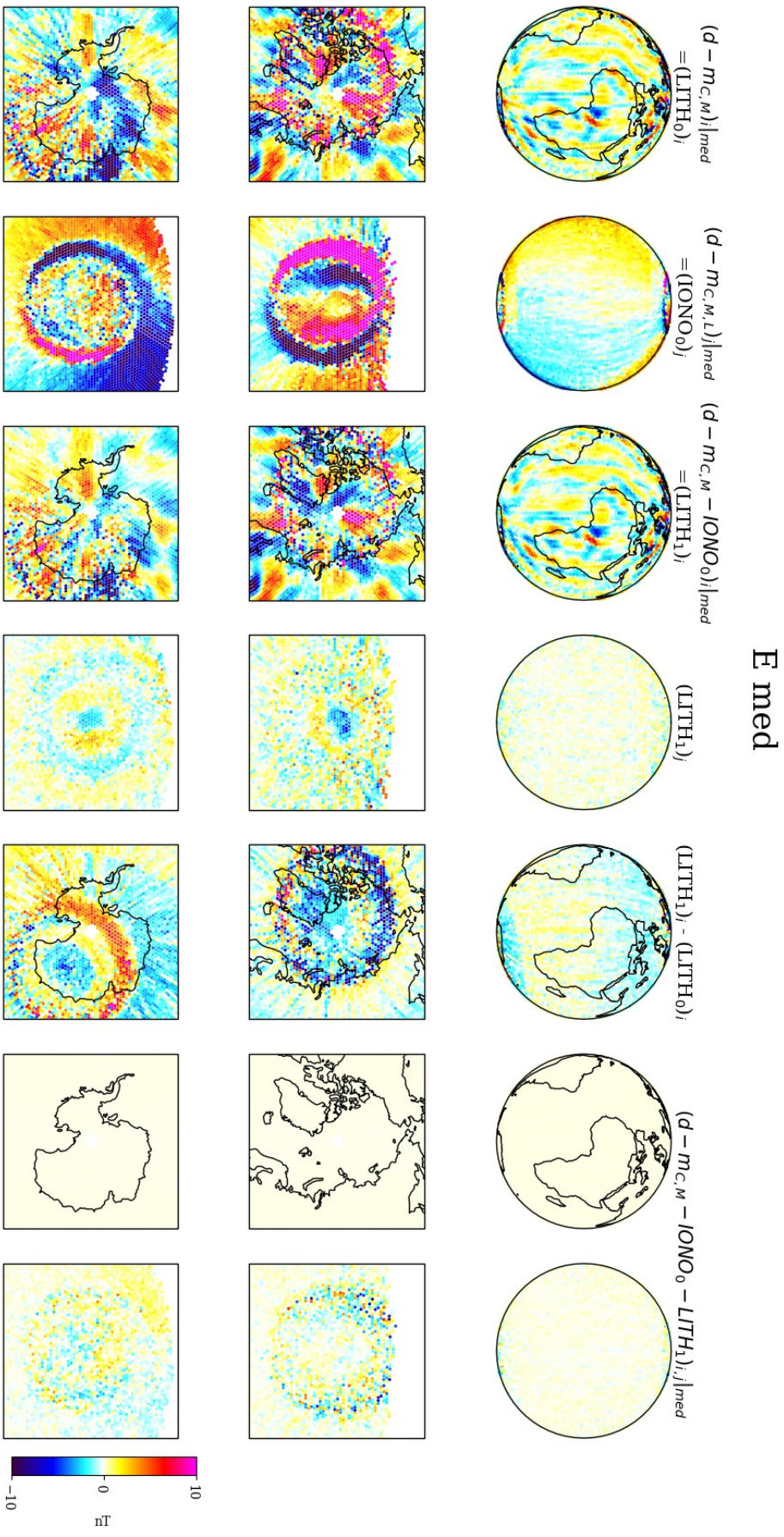

Figure B.3: Swarm Alpha East (Y) component medians

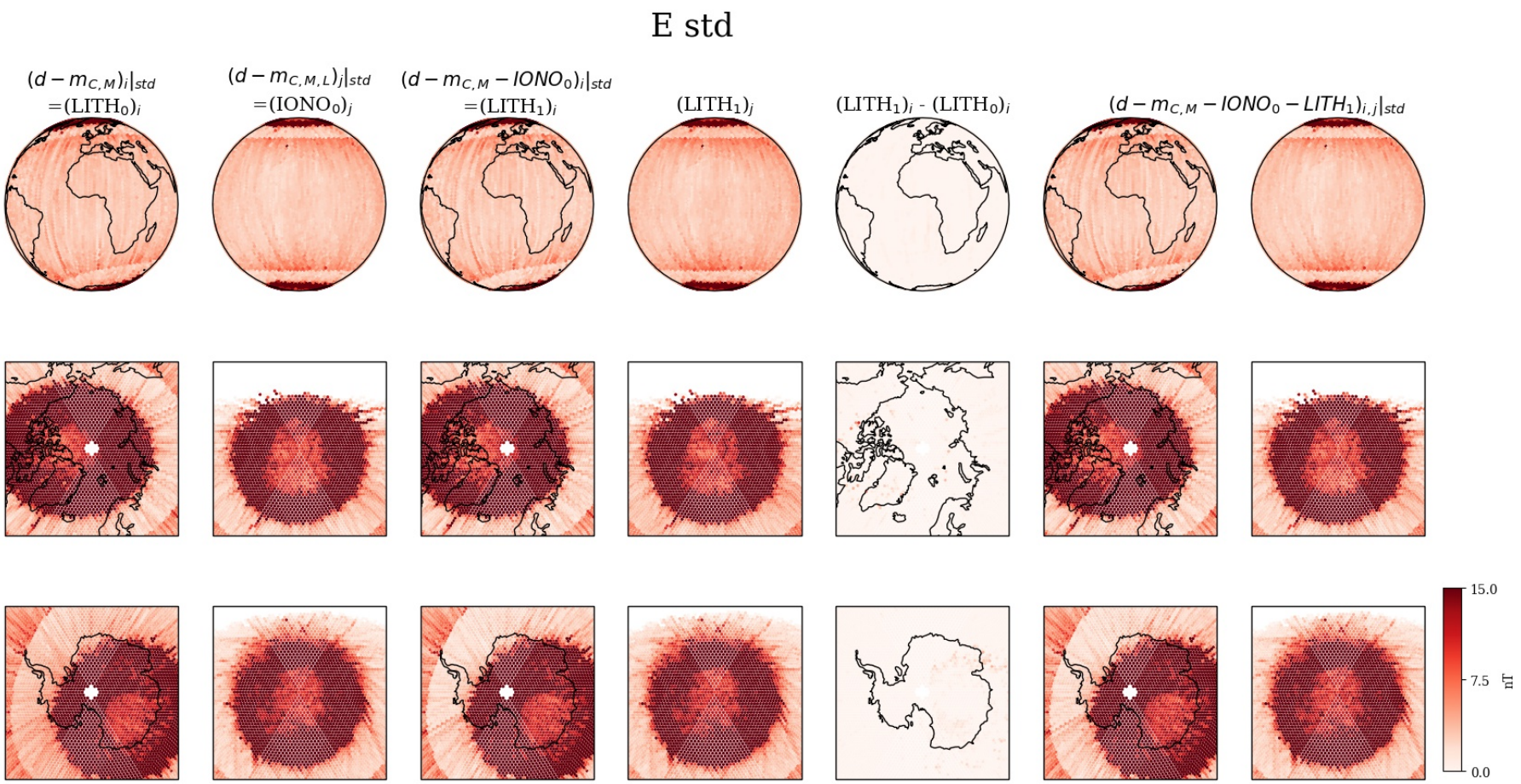

Figure B.4: Swarm Alpha East (Y) component standard deviations

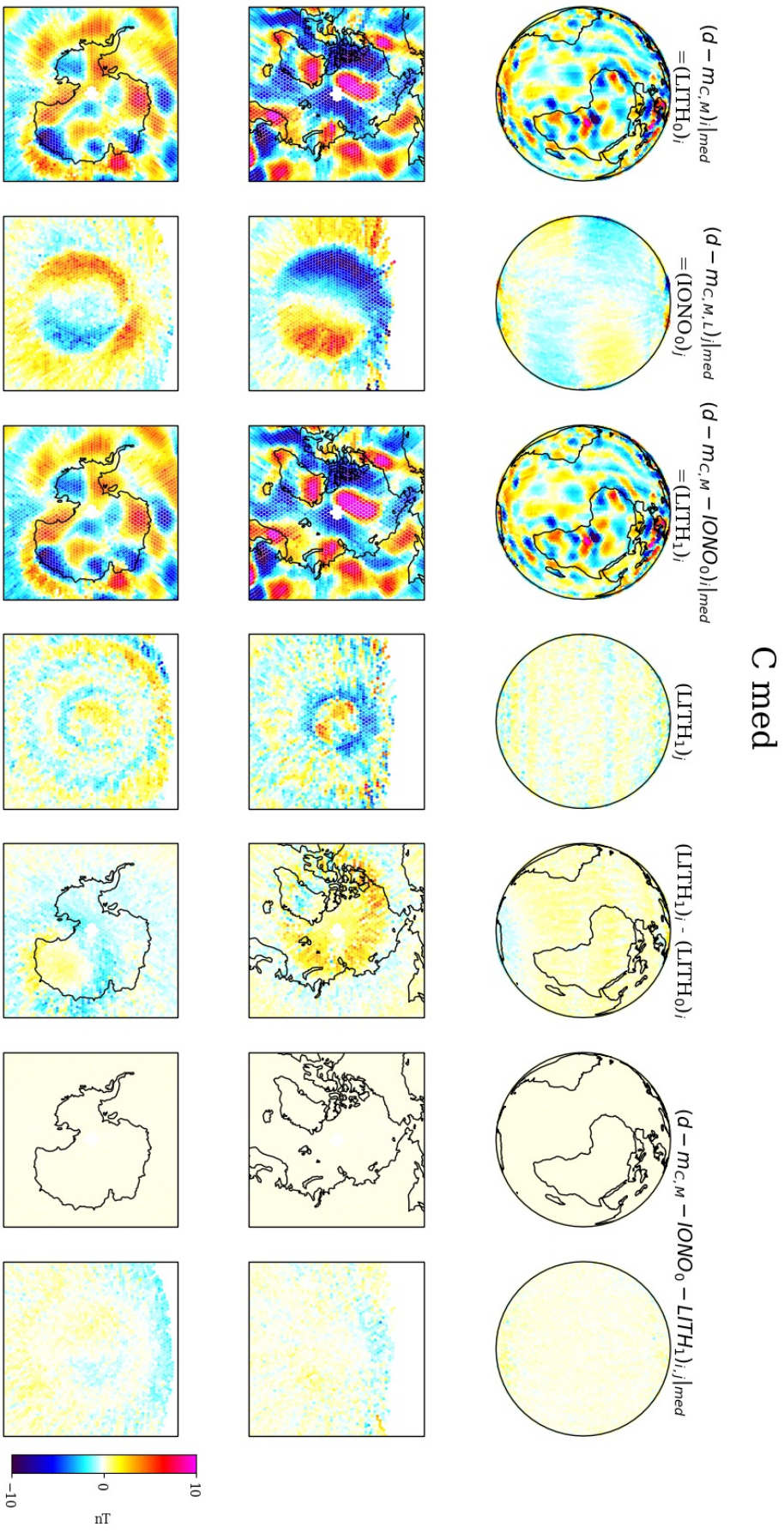

Figure B.5: Swarm Alpha Centre (Z) component medians

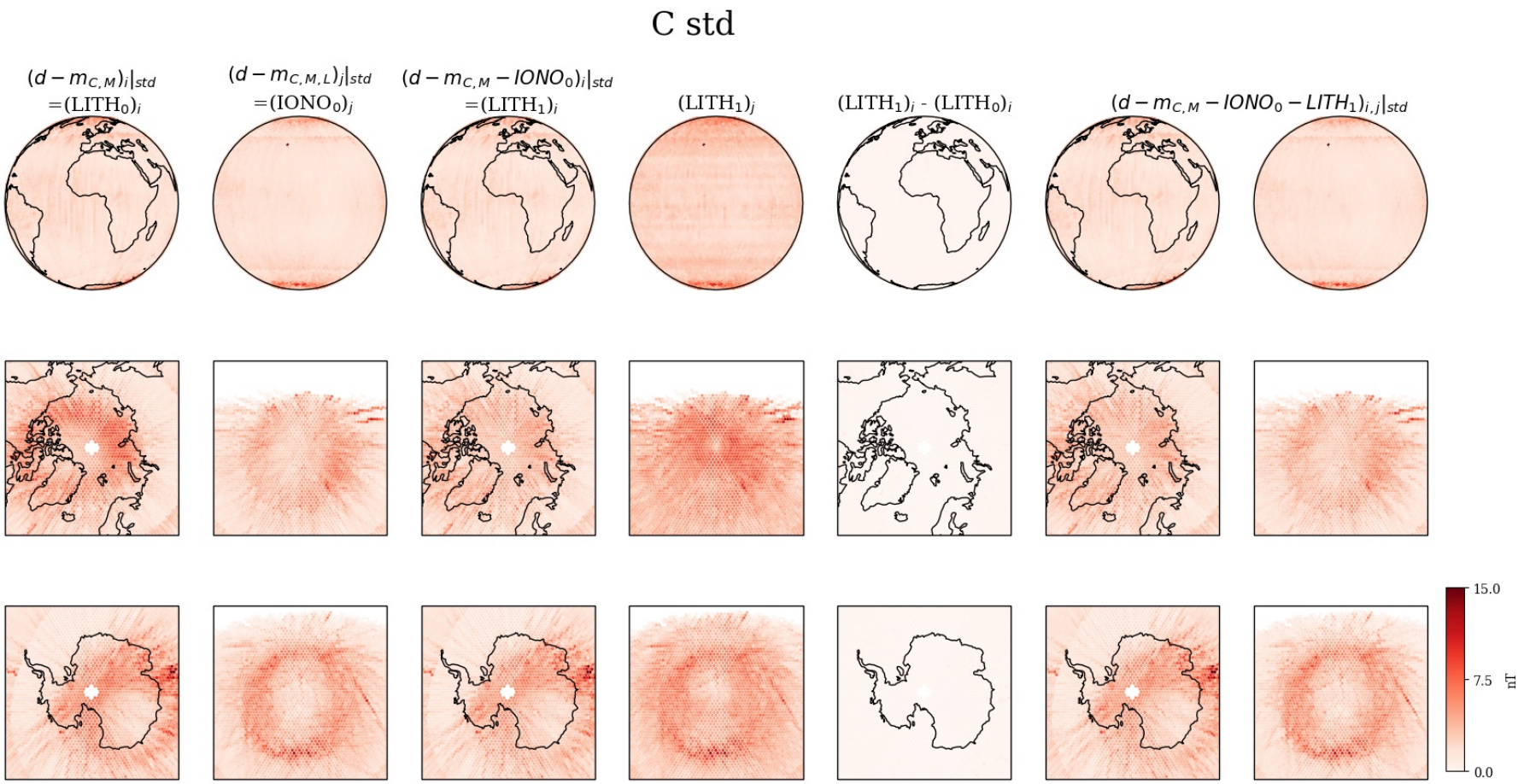

Figure B.6: Swarm Alpha Centre (Z) component standard deviations

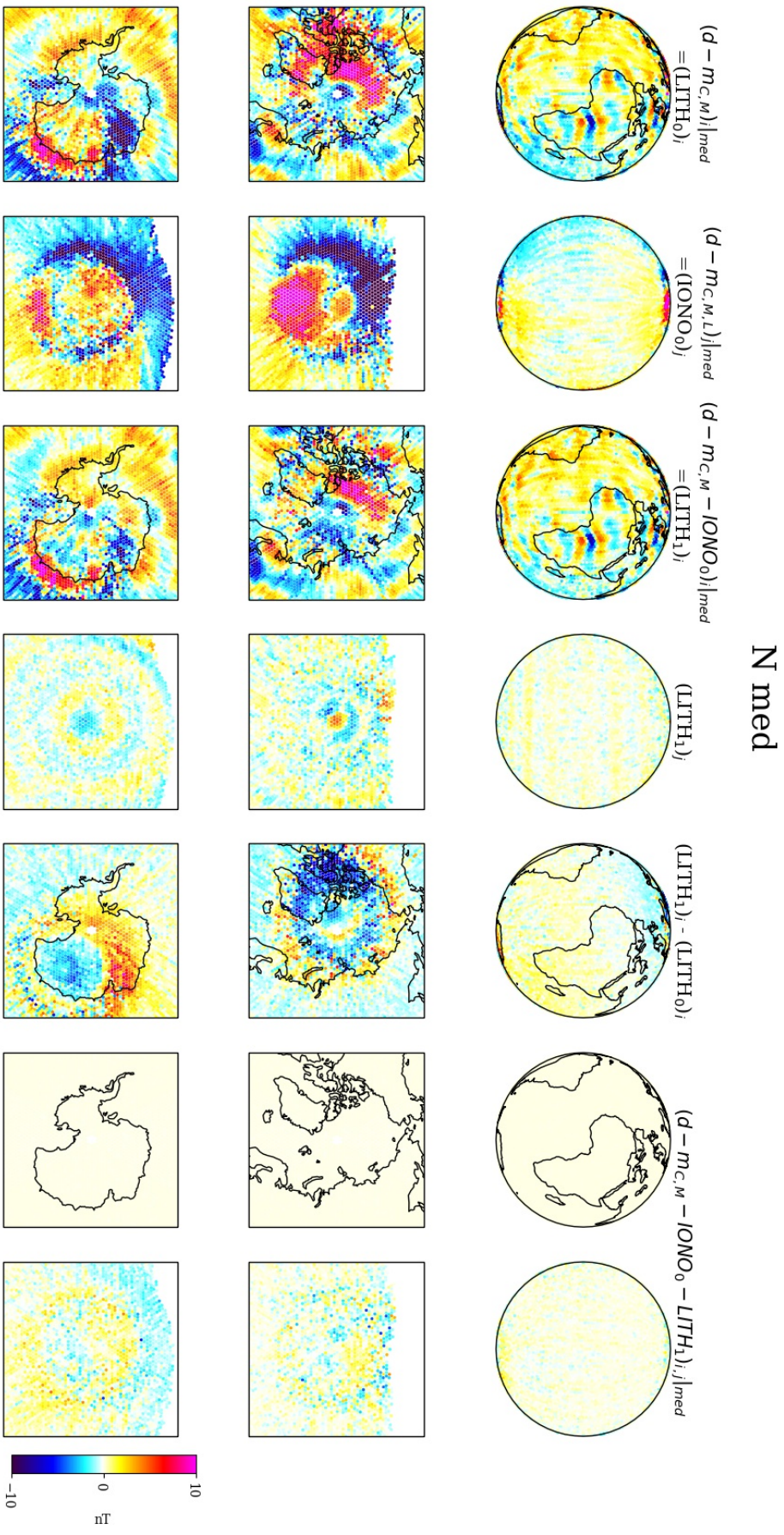

Figure B.7: Swarm Bravo North (X) component medians

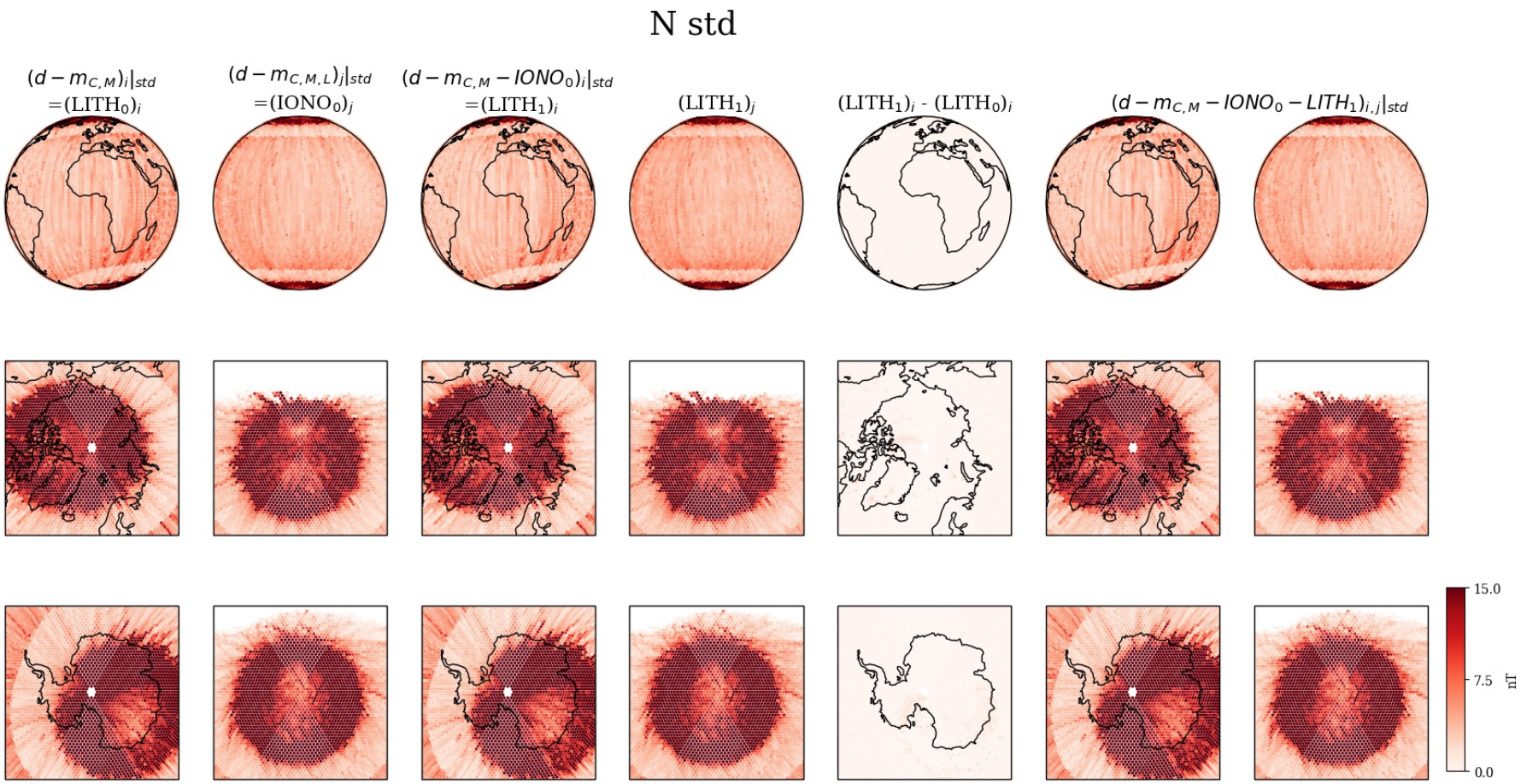

Figure B.8: Swarm Bravo North (X) component standard deviations

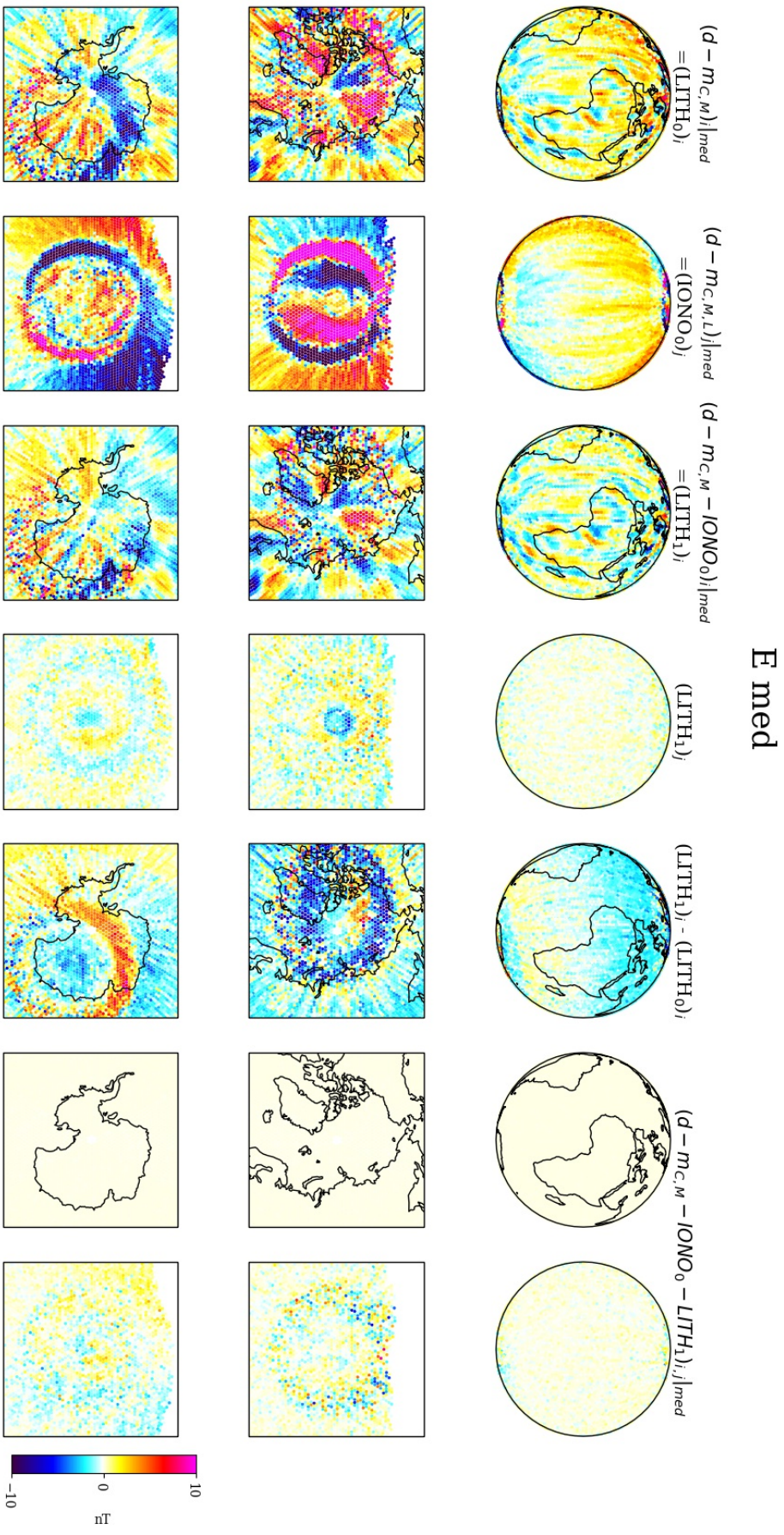

Figure B.9: Swarm Bravo East (Y) component medians

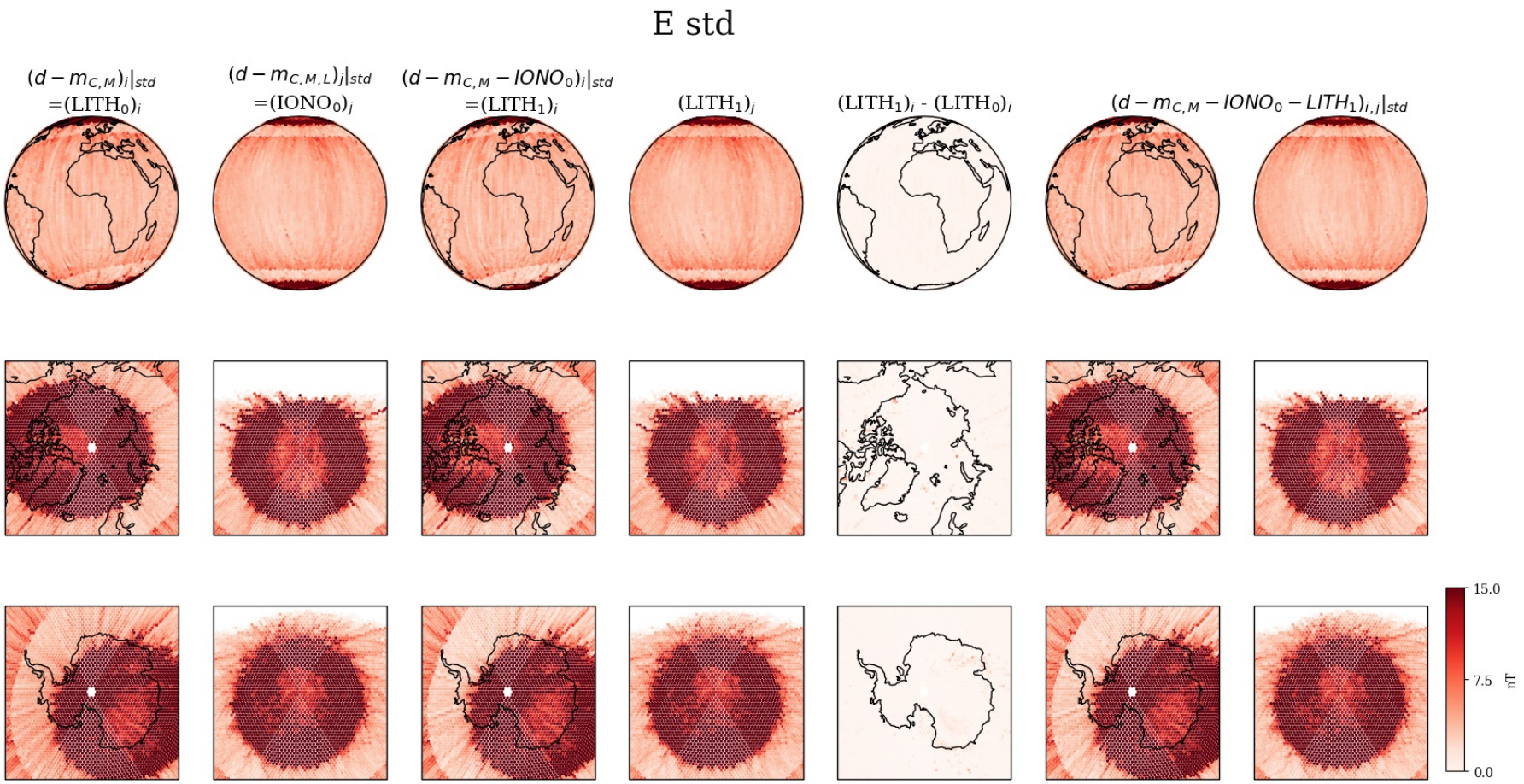

Figure B.10: Swarm Bravo East (Y) component standard deviations

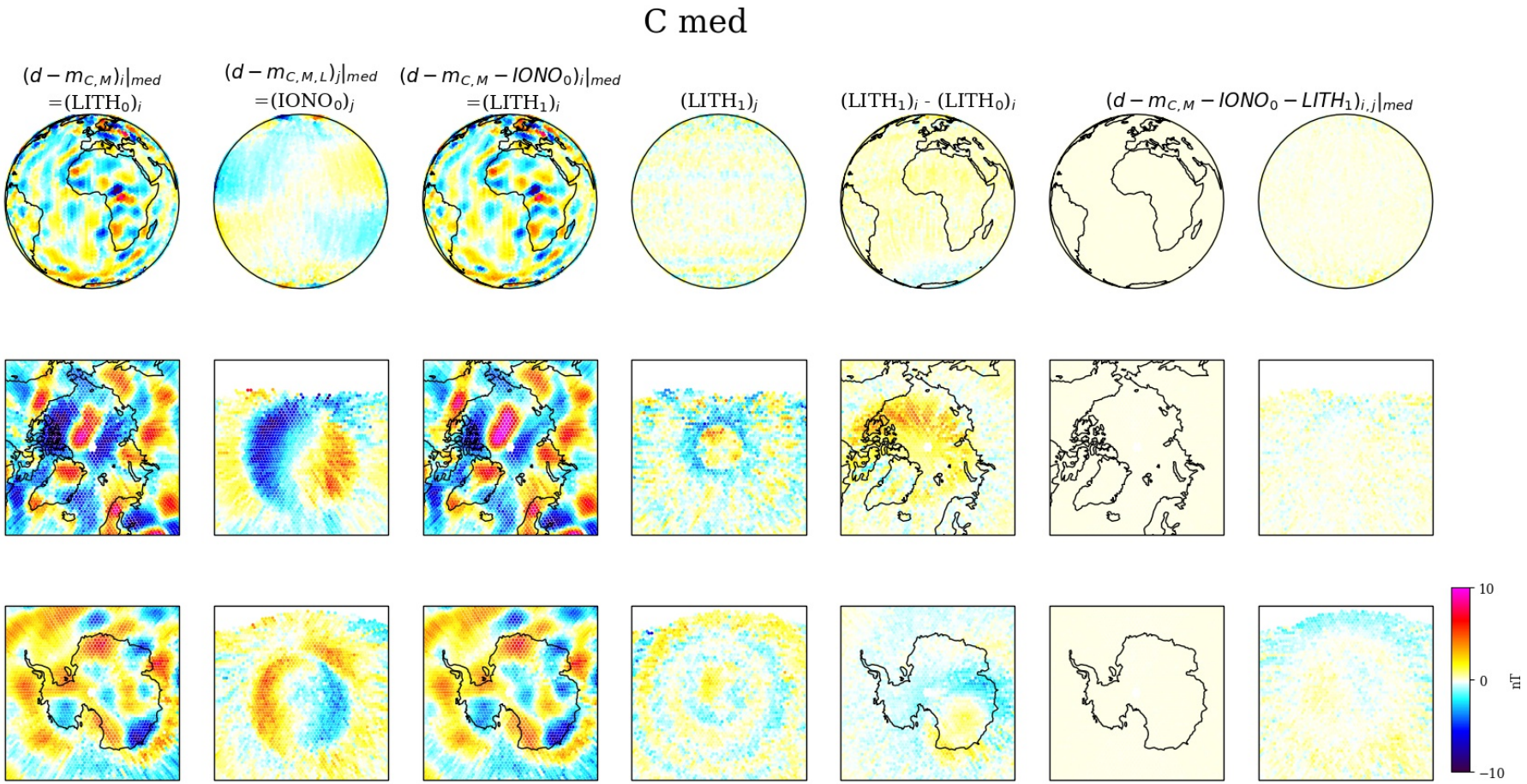

Figure B.11: Swarm Bravo Centre (Z) component medians

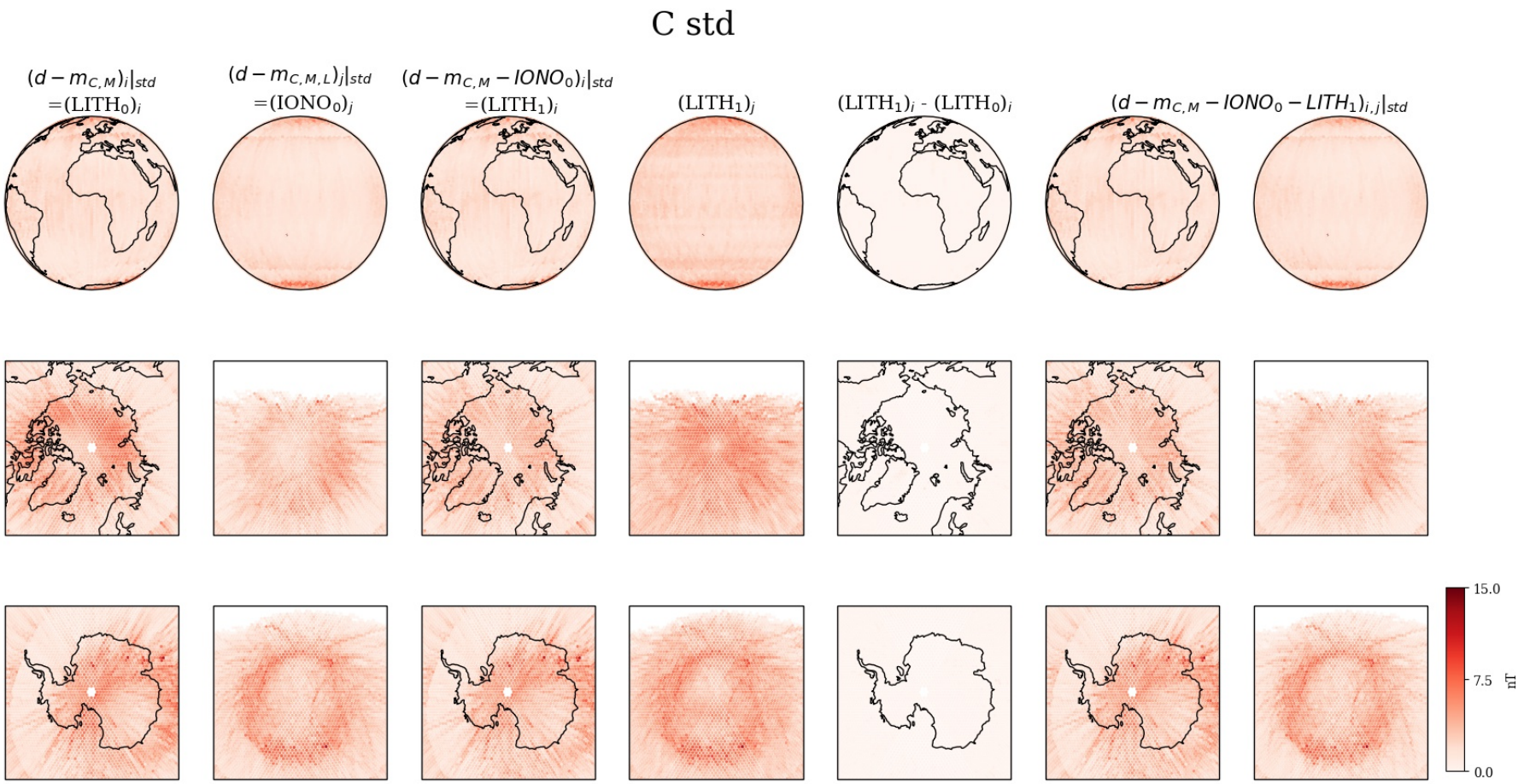

Figure B.12: Swarm Bravo Centre (Z) component standard deviations